**UNIVERSITY OF SOUTHAMPTON**

FACULTY OF NATURAL AND ENVIRONMENTAL SCIENCES

Chemistry

# Anions & the Bilayer. Structural & Mechanistic Studies Towards Synthetic Anion Carriers for Therapeutic Applications.

by

Michael James Spooner

Thesis for the degree of Doctor of Philosophy

February 2017

**UNIVERSITY OF SOUTHAMPTON**

# ABSTRACT

FACULTY OF NATURAL AND ENVIRONMENTAL SCIENCES

Chemistry

Doctor of Philosophy

# ANIONS & THE BILAYER. STRUCTURAL & MECHANISTIC STUDIES TOWARDS SYNTHETIC ANION CARRIERS FOR THERAPEUTIC APPLICATIONS.

By Michael James Spooner

Synthetic transmembrane anion transporters have attracted a great deal of interest due to their potential as therapeutic agents for the treatment of channelopathies such as cystic fibrosis or in the treatment of cancer. Despite a great deal of progress in the field over recent years, there are currently several hurdles that need to be overcome before anionophores become genuine therapeutic candidates. These include knowledge of how carriers behave in more cell-like bilayer systems, what molecular properties govern the rate determining step of the transport process and issues with solubility and deliverability. This thesis aims to explore some of these areas to help overcome some of these future barriers.

The effect of lipid environment on the transport ability of a series of alkyl-substituted thioureas was investigated. The series covered a wide range of lipophilicity, to determine whether the optimum lipophilic range varied depending on the composition of the bilayer. Despite the different lipids appearing to modulate the overall transport rate, the relative order of the transporter efficacy appeared unaffected.

Data is also presented demonstrating the use of dynamic covalent chemistry to generate an active transporter molecule *in situ* within the membrane. The compound formed by DCC was observed by measuring its transport response from vesicle experiments after the addition of two precursors (which do not facilitate transport alone) to the membrane. Comparison of the transport ability of the pre-formed compound and the rate of the DCC reaction measured by NMR spectroscopy gave insight into the balance required between these two factors in the design of these compounds.

Finally, the effect of the fluorination of alkyl chains in tripodal tris-thiourea receptors was explored. Vesicle assays with and without accompanying protonophores to couple to the transport process were carried out to determine the mechanism of the transport process and discover whether fluorination had any effect on the selectivity of the transporter molecules. The activity of the compounds in FRT-YFP cell assays was also determined and comparison with the vesicle data gave insights into the vesicle tests required to accurately predict the transporters' efficacy in cell epithelia.

*"Have we vanquished an enemy? None but ourselves. Have we gained success? That word means nothing here. Have we won a kingdom? No… and yes. We have achieved an ultimate satisfaction… fulfilled a destiny. To struggle and to understand - never this last without the other; such is the law."*

George Mallory

# Table of Contents

# Table of Figures

# Acknowledgments

This work would not have been possible without the help and support of so many people. Firstly, I'd like to extend my thanks to my supervisor, Prof. Phil A Gale. Thank you for the opportunity to work with you for the past few years, for all the support and ideas, and most of all for the encouragement that helped me find my feet as time has gone on.

I have to say a special thanks to the rest of the Gale group, who've been an amazing little family guiding me, helping me and keeping me entertained during innumerable tea breaks. Thanks especially to Jenny for generally being a mother hen and convincing me that I was actually good at this! To Nathalie and Xin, without whose help and ideas I don't think I'd have got this far, and Wim for the late-night drunken careers advice. Also thanks to Ethan for supporting and pushing me right at the end when I didn't think I would get this done; I will repay you in future belays when I visit Australia!

Thanks to my fellow PhDs over the years, to Issy and Lou for being incredibly welcoming and looking after me when I first started, and Stu, Laura and Harriet for the vesicles room parties, brightening up the lab and being great friends. You guys have all made the last few years' hard work a pleasure. And thanks for the cake, I'm not sure I'd have lasted 3 years without this group's obsession with baked goods!

To my family, Mum, Dad, Joe & Helen, thanks for always being there. Always supportive, always looking out for me. Plus I can always rely on you guys for general weirdness and unnaturally high levels of banter, don't ever change. Although Mum, now I've written this all down it'd be nice if you could explain my PhD properly to other people from now on, you'll be getting your own copy.

Thanks also to my friends and housemates, Robin, Conrad and especially Jon who've had to put up with my whinging and grumpiness. And finally thanks to all my friends, too many to mention, who've joined me on adventures climbing, mountaineering and generally exploring the outdoors. Every hour outdoors has kept me motivated me to work hard and get back into the lab, thanks for keeping me sane.

# Abbreviations

| | |
|---|---|
| **ATP** | Adenosine triphosphate |
| **CFTR** | Cystic fibrosis transmembrane conductance regulator |
| **CHOL** | Cholesterol |
| **ClogP** | Calculated log P (P is the octanol/water partition coefficient) |
| **Cy** | Cyclohexyl |
| **DCC** | Dynamic covalent chemistry |
| **DCM** | Dichloromethane |
| **DFT** | Density functional theory |
| **DMSO** | Dimethyl sulphoxide |
| **dppp** | 1,3-Bis(diphenylphosphino)propane |
| **EXT** | External buffer |
| **FA** | Fatty acid |
| **FRT-YFP** | Fischer rat thyroid expressing yellow fluorescent protein (cell line) |
| **Gr** | Gramicidin-A |
| **H-bond(ing)** | Hydrogen bond(ing) |
| **HPTS** | 8-Hydroxypyrene-1,3,6-trisulphonic acid |
| **INT** | Internal buffer |
| **ISE** | Ion-selective electrode |
| **NBD** | Nucleotide binding domain |
| **NOESY** | Nuclear overhauser effect spectroscopy |
| **NMR** | Nuclear magnetic resonance |
| **NMDG** | N-Methyl-D-glucamine |
| **POPC** | 1-Palmitoyl-2-oleoyl-sn-glycero-3-phosphocholine |
| **POPE** | 1-Palmitoyl-2-oleoyl-sn-glycero-3-phospho-ethanolamine |
| **POPG** | 1-Palmitoyl-2-oleoylphosphatidylglycerol |
| **QSAR** | Quantitative structure-activity relationship |
| **RBF** | Round-bottomed flask |
| **RDS** | Rate-determining step |
| **RP-UHPLC** | Reverse-phase ultra-high performance liquid chromatography |
| **RT** | Retention time |
| **TBA** | tetra-Butyl ammonium |
| **THF** | Tetrahydrofuran |
| **vdW** | van der Waals |
| **X-bond(ing)** | Halogen bond(ing) |

$pK_b$ refers to the $pK_a$ of the conjugate acid of the basic compound in question.

# 1 Introduction

## 1.1 Anions in Nature

The concentrations of anions in nature vary widely between intra- and extra-cellular solutions, between cell types and between different organelles[1]. Variations in concentration play a vital role in maintaining cell homeostasis, including maintaining pH gradients[2], preserving cellular volume[3] or assisting in inter cellular signalling[4].

Central to maintaining concentration gradients of different anions is the movement of anions across bilayer membranes in cells. The phospholipid bilayer forms a hydrophobic barrier between the extracellular medium and the cell interior, over which ions and hydrophilic molecules cannot pass[5]. Nature achieves the flux of anions across this barrier using several different processes, including channel, relay and mobile carrier mechanisms (Figure 1.1)[1, 6].

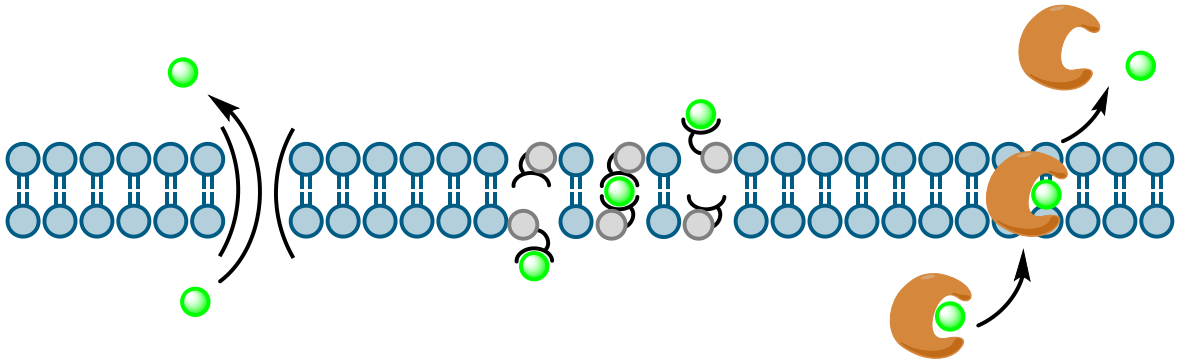

**Figure 1.1** Schematic showing the channel (**A**), relay (**B**) and mobile carrier (**C**) mechanisms of transport.

Problems with the regulation of anion gradients have been implicated in diseases known as 'channelopathies'[7]. A key example of this type of disease is cystic fibrosis. There are multiple mutations and underlying causes which lead to degradation, misfolding, inability to locate in the membrane, reduced transcription or faulty regulatory domains of the CFTR chloride channel; all pathways however lead to CFTR dysfunction the inability of cell epithelia within airways to secrete chloride[8]. The osmotic imbalance this causes leads to the build-up of thick mucus in the airway, causing many of the symptoms of the disease including shortness of breath, wheezing and recurrent lung infections.

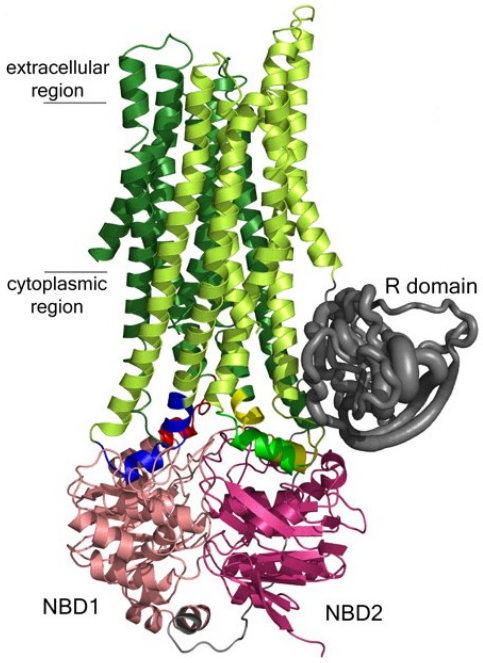


**Figure 1.2** Model of CFTR reproduced from A. W. R Serohijos et. al. 2008[9], showing the two membrane spanning domains (green) which form the chloride channel, the two nucleotide binding domains (NBD, pink) which bind ATP and the regulatory region (R domain, grey).

Currently there is only one drug on the market, Ivacaftor, which treats the root cause of CFTR dysfunction. Unfortunately it is only able to target those with the G551D mutation[10], which is present in approximately 4-5% of sufferers[8] and the drug is currently priced in excess of $300,000 a year[11]. It has been suggested that using small molecules to replace the function of the CFTR protein, and regulate movement of chloride across the bilayer, could be a route to developing new treatments for this disease[6, 12].

In addition to protein based anion channels, natural examples of small, mobile anion carriers have also been discovered. One of the best studied is prodigiosin **1**, a compound produced by *Serratia* and *Streptomyces* bacteria[13]. It is an $H^+/Cl^-$ symporter, but its protonated form can also bind other anions to facilitate an antiport (exchange) mechanism[14]. This $H^+/Cl^-$ transport ability gives it the ability to de-acidify acidic compartments within cells[15, 16].

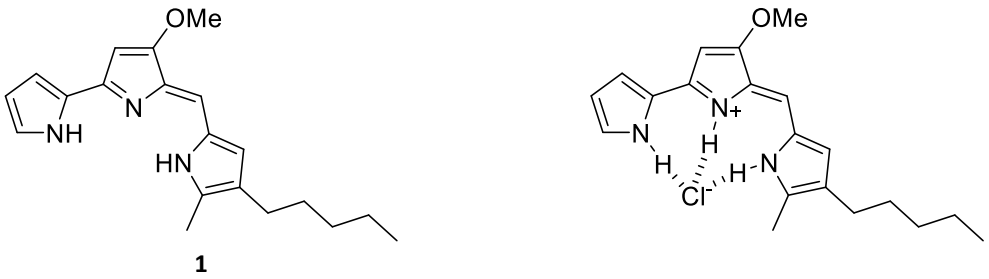


**1**

**Figure 1.3** Structure of prodigiosin and its HCl complex.

Prodigiosin has been shown to induce apoptosis in cancer cells[17]. Although the mechanism of action is unclear, studies of prodigiosin analogues suggest a strong correlation between their transport activity and cytotoxicity[18]. This and other studies have led to the suggestion that synthetic anion transporters that can de-acidify cellular compartments could be potential targets as anti-cancer agents[6].

## 1.2 Anion Receptor Chemistry

The first examples of anion receptors emerged in the late 60s. Shriver and Biallas reported chelation of negatively charged oxygen species (such as methoxide, **2**) by a bidentate Lewis base moeity in 1967[19]. This was the first example of an anionic complex based on the traditionally prepared analogous adducts from a bidentate Lewis base and a cationic metal ion.

The following year, Park and Simmons reported the synthesis of a series of diazabicyclo[n,n,n]alkane-ammonium ions[20]. The larger ions in the series (n = 3 or 4) showed a stabilisation of the in-in isomer, with both N-H groups pointing into the compound's cavity, consistent with binding a halide inside the cavity (later confirmed by X-ray crystallography[21]). Both n = 3 & 4 showed binding of $Cl^-$ and $Br^-$, whilst only n = 4, with a larger internal cavity, was able to bind to $I^-$. For n = 1 or 2, with small internal cavities, no binding events were observed. This concept of optimum spatial fit to govern receptor specificity would become a central theme in future anion receptor studies.


**2** **3**

**Figure 1.4** Structures of the chelate adducts prepared by Shriver & Biallas and Park & Simmons diazabicyclo[n,n,n]alkane-ammonium ions.

Following these early examples, it took a great deal of time for anion receptor chemistry to develop, with the number of examples lagging behind the number of reported receptors for cations. This has been attributed to the innate difficulties in binding anions compared to cations, including their increased size and more diffuse nature (limiting the utility of electrostatic interactions for example), pH sensitivity and wide variety of geometries[22]. Over time, a number of scaffolds have been developed that bind anions using a variety of non-covalent interactions, including electrostatics, hydrogen bonding, hydrophobic and metal or Lewis acid coordination.

Schmidtchen published examples of cationic quaternary ammonium cages (eg. **4**) that were able to bind iodide with purely electrostatic interactions[23]. These compounds suffered from competition from their counterions for the binding site, hence zwitterionic analogues such as **5** were developed[24], which had much increased anion association constants in water.

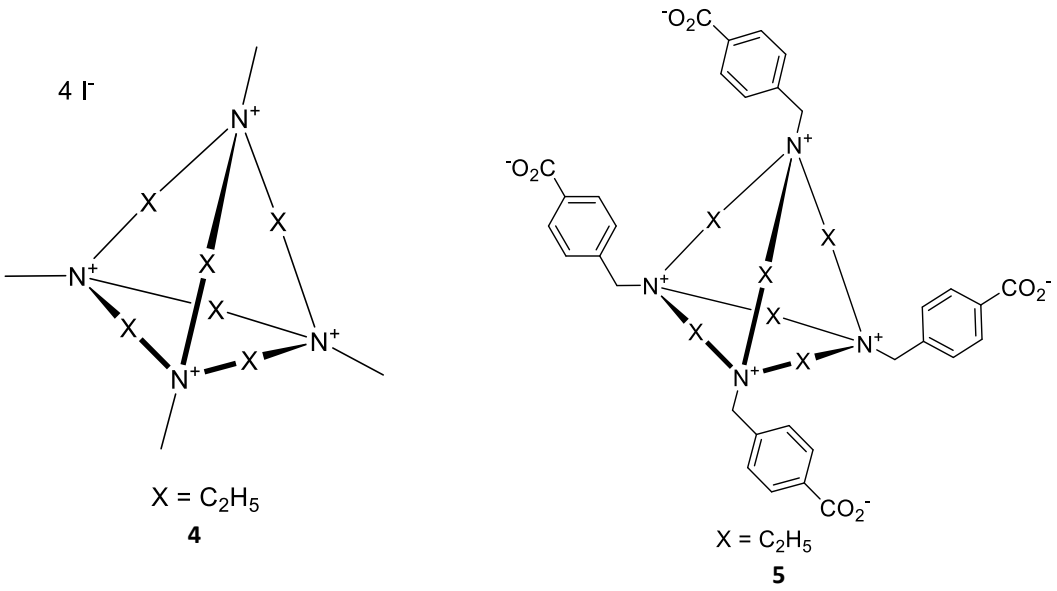


**Figure 1.5** Structures of cationic and zwitterionic quaternary ammonium cages reported by Schmidtchen.

E. Graf and J. M. Lehn used a combination of electrostatic interactions and hydrogen bonding in the development of their macrotricyclic spheroidal ligands[25]. They described a macrotricyclic cryptate effect in the binding of spherical halides. Ligand **6** showed much higher stability and very high $Cl^-/Br^-$ selectivity over **7**, which was attributed to the more closed and rigid cavity, a property that might be referred to as better pre-organisation in modern terminology. They suggest this effect stemmed from deformation resistance (increasing size selectivity), organisation of the N-H binding groups and hindrance of N-H hydration.

Ligand **6**'s selectivity for $Cl^-/Br^-$ over other halides was attributed to the optimal size of the molecule's cavity[25]. In contrast, ligand **8** displayed selectivity for anions based on shape[26]. The more ellipsoidal cavity prearranges the binding N-H sites in a configuration complementary to the shape of a linear anion such as azide. Hence, this compound shows much higher stability constants for the inclusion of $N_3^-$ in aqueous solution, over spherical anions such as chloride and bromide.

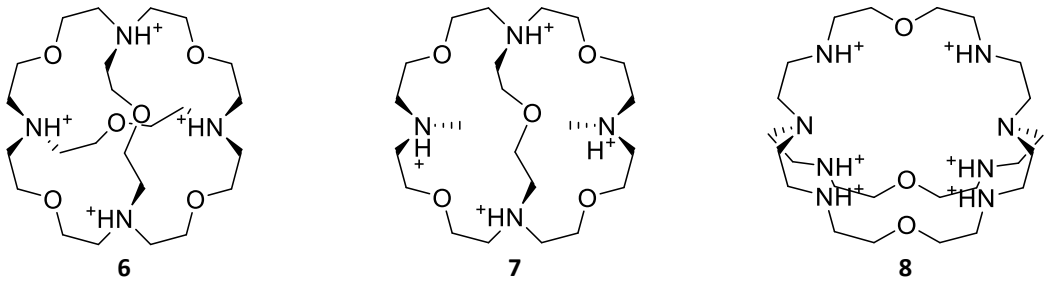


**Figure 1.6** Macrocyclic anion cryptand receptors developed by Graf & Lehn.

A drawback of these and other electrostatic plus hydrogen-bonding receptors is the need to have the correct pH conditions to ensure protonation of the binding groups[22]. Pascal and co-workers reported the first example of a neutral hydrogen bonding (H-bonding) receptor that did not require protonation[27]. Their (1,3,5)-cyclophane **9** formed a central cavity with 3 amide N-H bonds pointing approximately inwards towards the centre. The authors found preliminary NMR evidence that the compound could bind to fluoride.

In 1993 Reinhoudt and co-workers demonstrated the binding of $H_2PO_4^-$ using hydrogen bonding from amide N-H bonds arranged on a tripodal tren-based scaffold such as **10**[28]. The configuration of the hydrogen bond donors was postulated to be a better configuration for the binding of tetrahedral anions, demonstrated by the compounds much higher binding constants for $H_2PO_4^-$ compared to $Cl^-$. Exchanging amide groups for sulphonamide groups dramatically increased the binding strength to $H_2PO_4^-$ by about an order of magnitude, which was attributed to the increase in electrophilicity of the more acidic sulphonamide N-H.

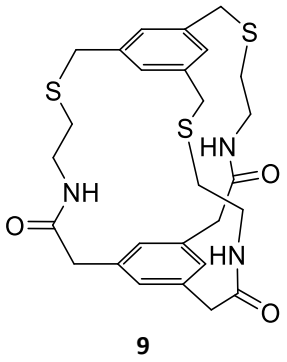


**9**

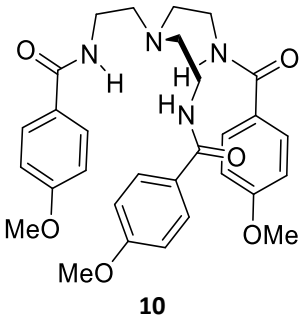


**10**

**Figure 1.7** The structures of the first examples of neutral hydrogen bonding anion receptors.

Following these examples, many new hydrogen bond donors were explored in anionophore design. Ureas were first used by Kelly & Kim[29]. They demonstrated that receptors such as **11** had a high affinity for carboxylate and related structures, with two parallel H-bond donors being well configured for binding to the Y-shaped anion. Umezawa and co-workers demonstrated the use of bis-thioureas such as compound **12**[30]. The pre-organised nature of these receptors gave them a significant selectivity in binding dihydrogenphosphate over acetate and chloride. Similar effects have been seen using structurally analogous secondary squaramides, such as **13**, with parallel H-bond donors again well arranged to bind acetate strongly in competitive DMSO-based media[31].

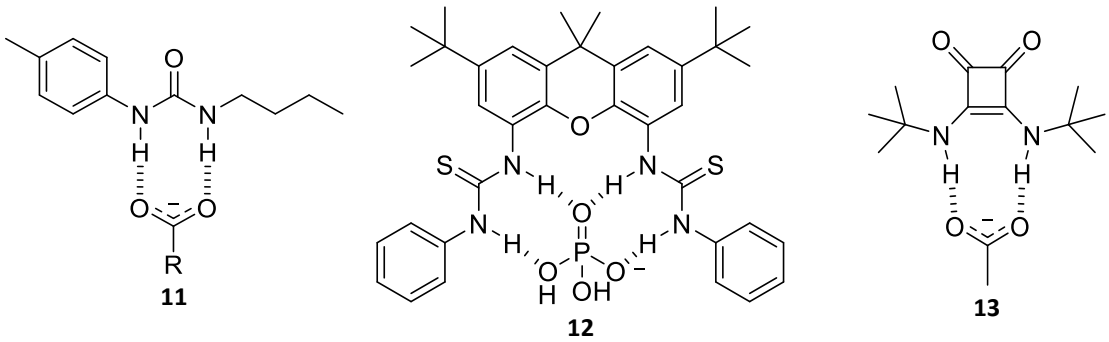


**Figure 1.8** Examples of early receptors using urea and thiourea hydrogen bond donors, and their arrangement for binding their preferred anions.

Hydrogen bond donors from nitrogen containing heterocycles have also been employed in anion receptors[32]. A key example of these are the calix[4]pyrroles, such as **14**, first reported in 1886[33] and shown by Gale and Sessler to be strong receptors for fluoride and chloride[34]. The compound is able to flip from a 1,3-alternate configuration to a cone conformation, pre-organising the N-H donors to bind the halide.

Hydroxyl groups have also been used as H-bond donors by Smith and co-workers to bind halides[35]. Simple catechol **15a** is able to bind chloride with a binding constant of 1570 $M^{-1}$ in acetonitrile. This is an order of magnitude stronger than its *meta*-substituted analogue resorcinol **15b**, an effect the authors attributed to *ortho*-OH groups in catechol having the optimum "bite angle" for chloride binding. NMR evidence also showed that the C-H group between the two O-H groups in resorcinol was involved in a binding interaction with the halide.

C-H bonds have been identified as having minor, weak interactions with anionic guests in many systems but they have also been used as the sole donor of H-bonds in anion receptors. Flood and Li reported macrocycle **16**, containing four mutually planar 1,2,3-triazole rings[36]. The compound is able to bind chloride strongly in chloroform, with downfield shifts associated with a binding interaction detectable for all central C-H protons. The authors suggest the strength of the interaction stems from the pre-organisation of the macrocycle (hence no energy cost in conformational change on binding) and the strong dipole in the 1,2,3-triazoles allowing the C-H bonds on these rings to act as unusually strong H-bond donors.

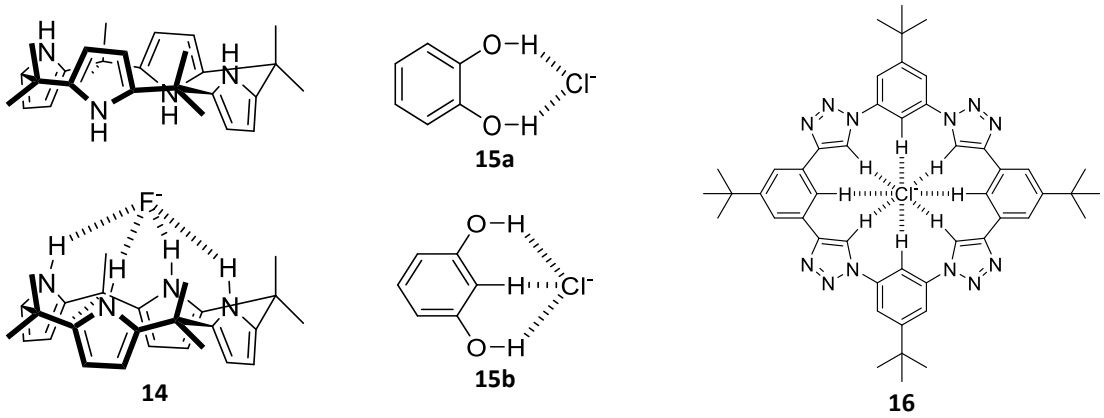


**Figure 1.9** Various structures of compounds using different H-bond donors in anion complexation.

Halogen bonding (X-bonding) has only relatively recently been exploited in the binding of anions. These bonds involve the donation of electron density from the anion into a 'σ-hole' of electron deficiency opposite a C-X bond[37]. The first example of halogen bonding in an anion receptor was reported by Resnati and co-workers[38]. They developed ditopic receptor **17** which formed complexes with NaI; the sodium was bound by 5 O atoms and an N in the pocket formed by the arms of the receptor with the iodide bound by halogen bonding to the *para*- iodines on the phenyl ring. In the solid state the iodide ions formed halogen bonded bridges between two receptor molecules.

The tridentate receptor **18** reported by Taylor and co-workers is a neutral receptor able to bind halides by pure halogen bonding without an additional cation[39]. Using *ortho*-substituted iodotetrafluorobenzene groups they were able to arrange the receptor to form a pocket of the correct geometry to bind spherical halides. The receptor exhibited strong binding affinity for $Cl^-$>$Br^-$ >$I^-$ which the authors attributed to the ability of the anions to act as an X-bond acceptor rather than any size selectivity in the relatively flexible receptor.

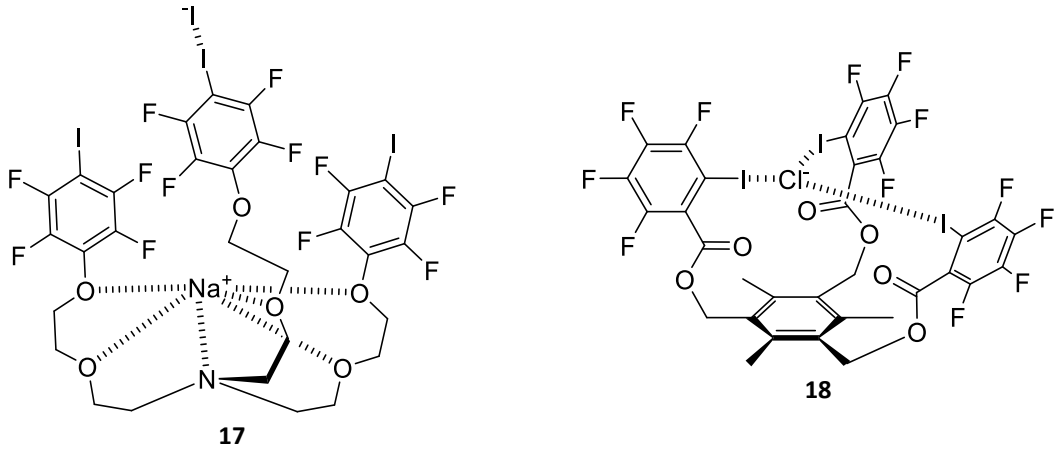


**Figure 1.10** Structures of compounds using halogen bonding to bind anions.

The hydrophobic effect has also been harnessed to produce anion receptors. Cyclodextrins, such as β-cyclodextrin **19**, are commonly studied supramolecules that are able to bind anions in this way. It has been shown for example that the inclusion of naphthalene acetates and sulphonates in the cyclodextrin pocket is primarily caused by the hydrophobic effect[40], driven by the release of ordered water from the cavity on anion inclusion.

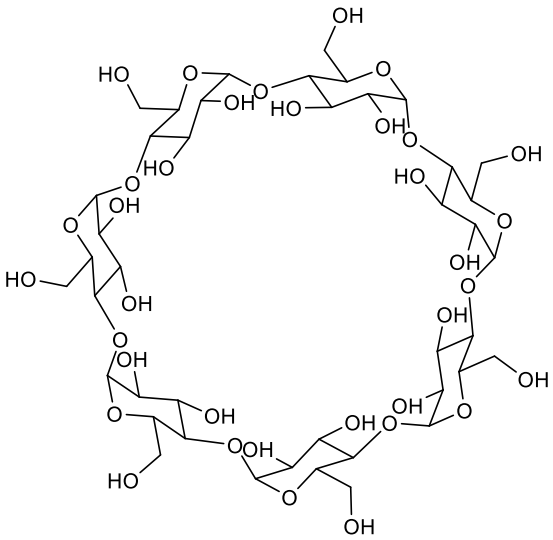

**19**

**Figure 1.11** Structure of β-cyclodextrin.

Finally, coordination to metal centres is another motif used for the complexation of anions. The first example of this was the use of tin macrocycles such as **20** to bind chloride[41]. The tin dichloride moiety gives the receptors the ability to act as Lewis acids and the compounds are thus able to strongly bind chloride in acetonitrile. The binding appeared to fit a 1:2 (host:guest) model and the smaller receptors show a slight size selectivity effect over the larger macrocycles.

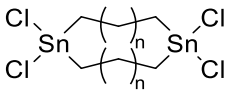

n = 6, 8, 10

**20**

**Figure 1.12** Structure of dialkyltin dichloride macrocylic receptors for $Cl^-$.

Using this range of anion binding motifs, a number of applications of this chemistry appeared. Some of the more remarkable/seminal examples are discussed here for interest, for further examples the reader is referred to a comprehensive review of the subject[42].

Appending a fluorophore to an anion receptor can produce synthetic sensors for anions. For example compound **21**, reported by Haley & Johnson[43], is based on 2,6-ethynylpyridine and contains electron withdrawing groups appended to its two urea hydrogen binding groups. This yields a non-emissive unbound compound which shows a switch-on fluorescence response on $Cl^-$ binding.

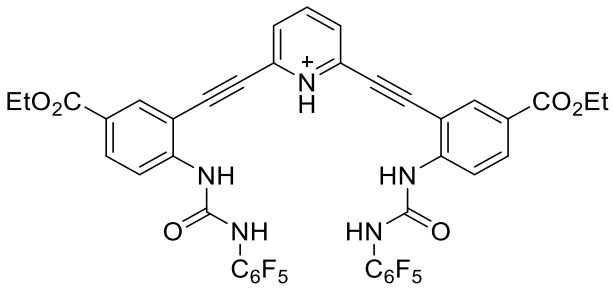


**21**

**Figure 1.13** Switch-on $Cl^-$ fluorescent sensor reported by Haley & Johnson.

Anion receptors can also be designed for anion extraction. For example, the polymer **22** reported by Flood et. al.[44] contains aryl triazole chains, with C-H trizole H-bond donors. $^1$H NMR titrations showed the ability of the polymer to bind chloride in chloroform and it was demonstrated that the modified polymer was able to extract tetrapropylammonium chloride from water into DCM twice as effectively as the unmodified parent poly(methyl methacrylate) polymer alone.

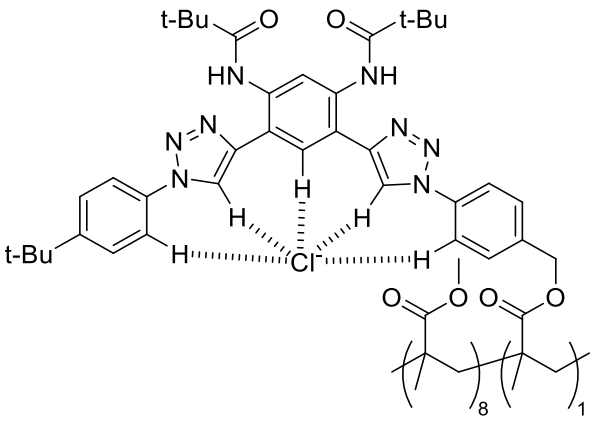


**22**

**Figure 1.14** Structures of aryl trazole-modified poly(methyl methacrylate) polymer reported by Flood et. al.

Anion binding chemistry has also been applied to produce supramolecular structures that respond to external anion stimuli. For example, compound **23** is a low molecular weight supramolecular gelator that forms supramolecular gels in acetone[45]. Addition of external anions including halides and acetate caused destruction of the gel. The minimum anion concentration required to destroy the gel was proportional to the binding constant with that anion measured by $^1$H NMR titration in acetone.

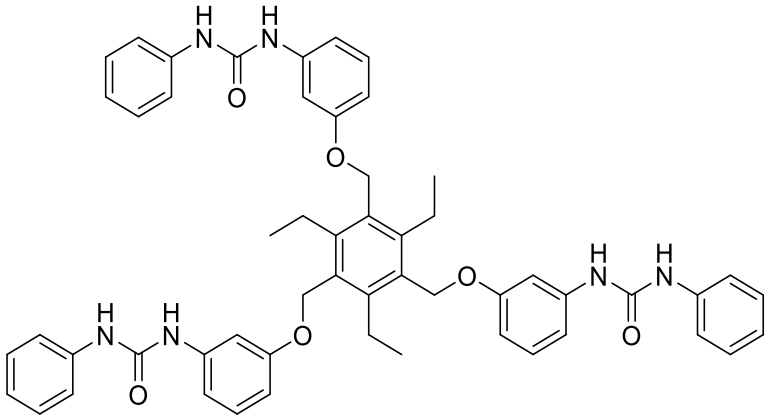

**23**

**Figure 1.15** Structure of an anion-responsive low molecular weight supramolecular gelator reported by Itagaki et. al.

Anion complexation has also been used as a method to template larger macro structures. Lehn and co-workers demonstrated this with circular double helicate structure **24**[46]. The structure was formed from 5 pseudo-octahedral $Fe^{2+}$ ions complexed to 5 tris-2,2′-bipyridine (bipy) H-bond acceptor ligands. A central chloride ion templated the structure, forming the helicate unit, the anion stabilised by C-H hydrogen bonding from the inner bipy units. In the presence of sulphate the metal and ligand instead self-assembled into a hexameric structure templated around the larger anion[47].

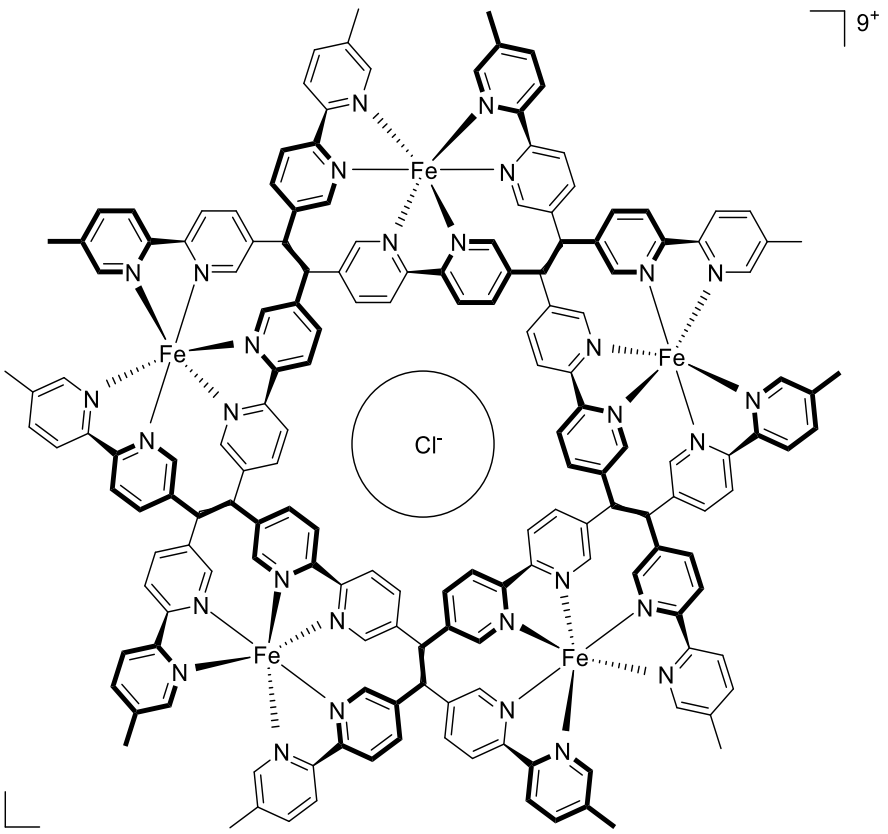


**24**

**Figure 1.16** Structure of Lehn and co-workers' $Cl^-$ templated circular double helicate.

Anion templating has also been used in the assembly of mechanical bonds. Beer and co-workers demonstrated this in the formation of rotaxane **25**[48]. The rotaxane thread and macrocycle precursor form a $Cl^-$ binding site. The binding of chloride brings the two components together, enabling the closure of the macrocycle by ring-closure metathesis. By comparison, analogous structures without H-bond donors to form the binding site yielded no mechanically linked rotaxane product. After removal of the template, the rotaxane-$PF_6$ salt retains excellent anion receptor properties, with an order of magnitude increase in $Cl^-$ binding strength over the free thread and vastly increased selectivity for $Cl^-$ over other anions such as acetate.

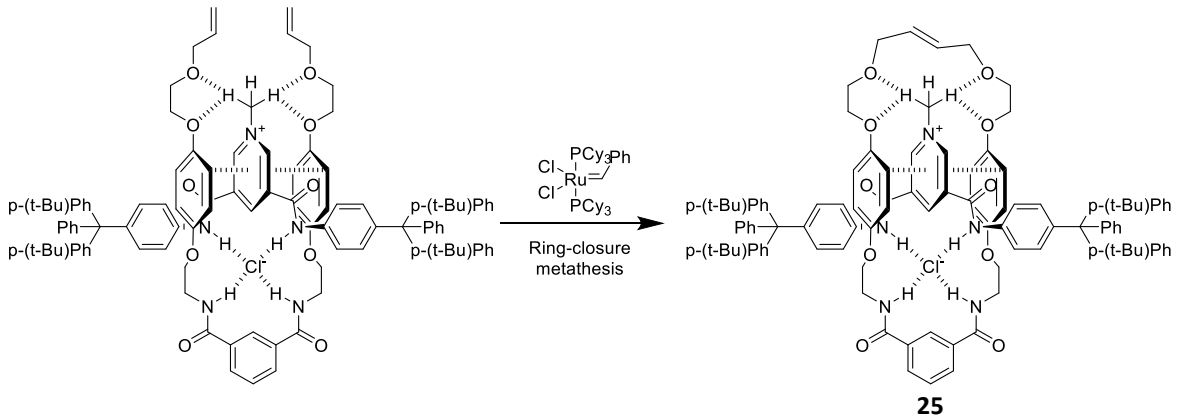


**25**

**Scheme 1.1** $Cl^-$ used as a template in rotaxane synthesis.

Additionally, synthetic anion receptors have also been used to promote organocatalysis. In a seminal example, Jacobsen reported chiral thiourea **26**. This compound is able to catalyse Pictet-Spengler cyclisations. The thiourea is able to bind a chloride counteranion, which interacts with an iminium cationic intermediate. The chiral nature of the ligand directs the product formation, giving a 93 % enantiomeric excess of the chiral product, compared with the racemate achieved using more forcing conditions.

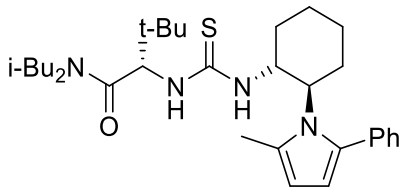


**26**

**Figure 1.17** Structure of an anion-responsive low molecular weight supramolecular gelator reported by Itagaki et. al.

## 1.3 Synthetic Anion Receptors as Transporters

The development of anion receptor chemistry produced the toolbox required for supramolecular chemists to explore the creation of synthetic anionophores that could transport anions across lipid bilayers. The ability to synthesise synthetic lipid vesicles reproducibly, with easily variable interior and external solutions[49] has allowed simple, routine screening of synthetic carriers within the laboratory. Chloride transport, for example, can be monitored easily using ion-selective electrode techniques[50] or fluorescent reporters such as lucigenin[51]. Transport rate is most often quantified by fitting efflux curves to find the initial rate of transport or calculating $EC_{50}$ values (effective concentration to elicit 50 % response) using Hill analysis[52-54] (discussed in detail in Chapter 3.3).

There are several examples of synthetic anion channels in the literature; Matile's rigid rods, such as **27**, are an early example of compounds able to facilitate $Cl^-/OH^-$ exchange[55]. Synthetic relay mechanisms have also been exploited in receptors such as the modified phospholipid **28**, developed by Smith and co-workers[56].

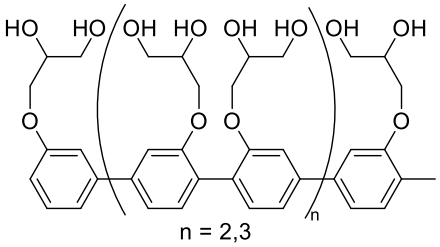


**27**

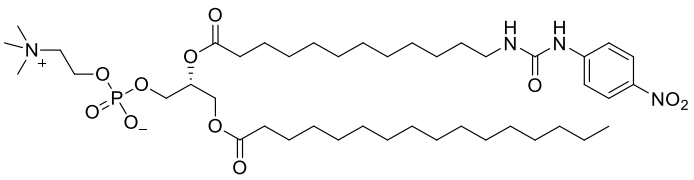


**28**

**Figure 1.18** Example structures of synthetic anion channels and relays.

There are many further examples of synthetic anionophores that exploit these mechanisms, and the literature is well reviewed[42, 57]. As the focus of this work is on molecules that exploit a mobile carrier mechanism however, and more specifically interact with anions via hydrogen bonding interactions, this class of synthetic transporter will be discussed in detail here.

Sessler and co-workers developed several synthetic variations on prodigiosin, such as **29a**, as well as some truncated dipyrromethene based structures, **29b**[18]. All exhibited an HCl co-transport mechanism similar to prodigiosin. It is interesting to note that **29b** exhibited very similar transport efficacy to **29a**, despite lacking one additional H-bond donor. Crystal structure data revealed that the HCl complexes of the prodigiosin mimics were twisted with two N-H bonds longer than the third whilst those of the truncated structures were planar with H-bonds of equal length, perhaps suggesting greater pre-organisation of this receptor. The anticancer activity of these compounds in A549 and PC3 human cell lines appeared to correlate with anion transport ability in vesicles.

Many synthetic transporter scaffolds have been designed as prodigiosin (**1**) mimics. Gale & Smith reported an amidopyrrole based receptor, **30**[58]. This compound contained two N-H hydrogen bonding groups and one further protonatable nitrogen on the imidazole, much like **1**. Hence **30** was able to facilitate HCl efflux from POPC/cholesterol vesicles.

Quesada & co-workers first reported the transport activity of the tambjamine class of anionophores **31**[59]. These included naturally occurring analogues, such as **31a,** and novel synthetic analogues with aryl substitutions such as **31b**. Again, these share the same central binding group as prodigiosin (**1**) with two N-H donors and a protonatable N. The authors showed that the carriers could elicit both $Cl^-/HCO_3^-$ and $Cl^-/NO_3^-$ exchange. Unlike prodigiosin, little HCl co-transport was observed, which was suggested to stem from the high $pK_a$ of the tambjamines (~10), meaning they would likely stay protonated at pH 7.2. Acridine Orange assays performed with the compounds in GLC4 lung cancer cells showed the most active transporters de-acidifying cell compartments, which the authors attributed to $HCO_3^-$ influx into the lysosomes.

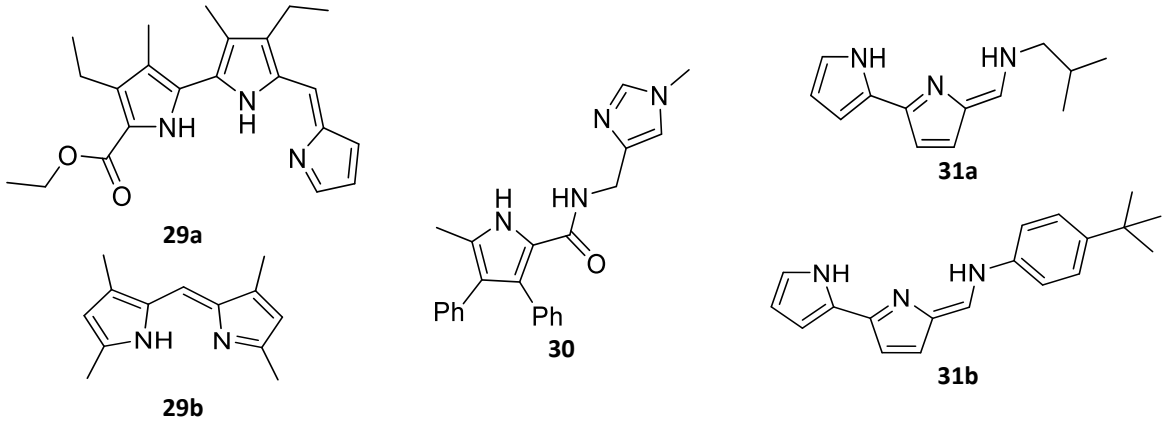


**Figure 1.19** Early examples of synthetic anionophore scaffolds mimicking the structure of prodigiosin **1**.

Davis and co-workers have described large steroidal scaffolds for use as anion carriers, the cholapods[60]. These large, lipophilic backbones are used as scaffolds to hold converging urea groups, with N-H hydrogen bond donors oriented to facilitate anion binding. Compound **32** outperformed other analogues tested in $Cl^-/NO_3^-$ exchange assays, the results of which correlated with anion binding strength.

The Davis group has developed further lipophilic scaffolds that are highly pre-organised for anion binding. The diaxial decalins were based on the cholapods but were more compact and less lipophilic[61]. The long octyl tail and the electron withdrawing effect of the bis-$CF_3$ substituted aryl group enabled decalin **33** to achieve measurable chloride efflux at loadings of 4 x $10^{-4}$ mol % (with respect to lipid). The group took this simplification one step further with the introduction of a cyclohexane scaffold, which compromised slightly on pre-organisation of the binding groups in

exchange for being more synthetically accessible[62]. Cyclohexane **34** was over 3 times more active than an electronically similar cholapod in transport assays, despite reduced $Cl^-$ binding affinity. The authors suggest that the greater conformational freedom of **34** increases the kinetics of binding whilst lowering overall affinity, increasing its turnover rate in transport.

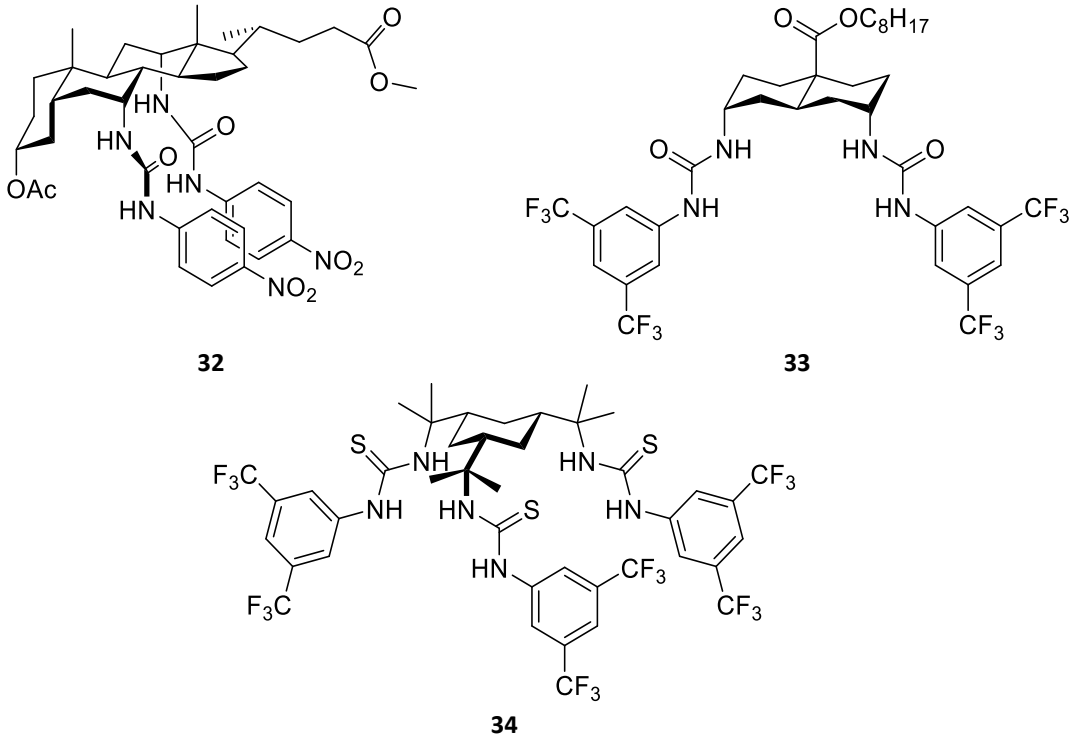


**Figure 1.20** Assorted structures of anionophores containing large lipophilic backbones.

A tren-based scaffold has also been used to pre-organise urea and thiourea hydrogen bonding groups for chloride and bicarbonate transporters **35**[63]. Bicarbonate transport was detected directly in a $^{13}C$ NMR experiment using vesicles loaded with $H^{13}CO_3^-$. The thiourea variants were significantly more active than the urea compounds, likely due to the greater acidity and more charge-diffuse nature of this binding group.

Gale & co-workers have also demonstrated that very simple, single thiourea receptors **36** can show transport activity[64]. The most active indole-substituted compound was able to facilitate $Cl^-/HCO_3^-$ exchange faster than tripodal analogues **35**, remarkable given its fewer binding groups and less encapsulated binding site. The indolyl analogue was also the most active compounds in $Cl^-/NO_3^-$ exchange, which was attributed to its better affinity for the anions afforded by the extra indolyl H-bond donor and the geometry of its binding site. Urea analogues of the series were inactive, again attributed to the less polar, more lipophilic character of the thiourea.

As isosteres of urea and thiourea groups, squaramides were also natural candidates for simple anion carriers. Again, Gale & co-workers demonstrated that squaramides, such as **37**, are superior

transporters to both its urea and thiourea analogues[65]. This effect was attributed to the much higher anion binding strength of the squaramides (an order of magnitude stronger than ureas and thioureas in DMSO-$d_6$), an effect of the more convergent H-bonding geometry. The authors suggested that the squaramides resistance to nucleophilic attack could make them better drug candidates due to lower toxicity.

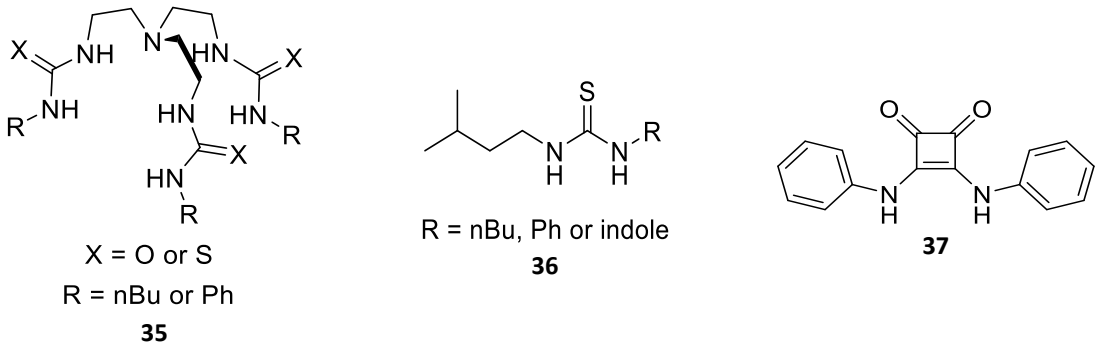


**Figure 1.21** Small-molecule urea, thiourea and squaramide based anion carriers.

Chloride has also been transported as an ion pair. In the first report of transport mediated by these compounds, calixpyrrole **14** facilitated the efflux of CsCl from POPC vesicles[66]. Cation dependence assays showed no transport with NaCl, KCl or RbCl, nor was there any dependence on external anion, suggesting a CsCl symport mechanism. The binding of the anion to the pyrrole N-H groups pre-organises into the pyrrole rings forming a cup, allowing inclusion of the cation and transport of the salt as an ion pair.

Although much of the focus in anion transport has been on transporting $Cl^-$ and $HCO_3^-$, due to the biological relevance of these anions discussed above, receptors have also been reported for other anions. The transport of $SO_4^{2-}$, for example, was a difficult prospect due to its large size and charge diffuse nature, but also its high hydration energy[67]. Joliffe, Gale & co-workers demonstrated that compound **38** was able to transport sulphate across a bilayer preferentially over chloride and nitrate, with direct evidence from a $^{33}S$ NMR assay[68]. They suggested that its transport ability stemmed from high affinity for the large anion, plus optimally-sized strap, to effectively shield the charge from the hydrophobic bilayer whilst allowing fast movement of the anion in and out of the complex.

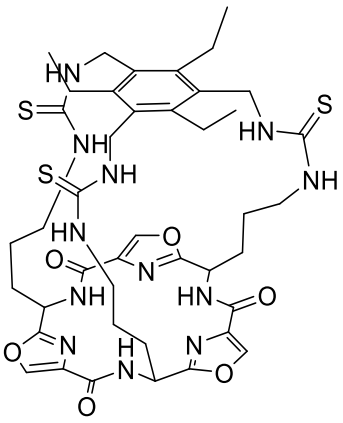

**38**

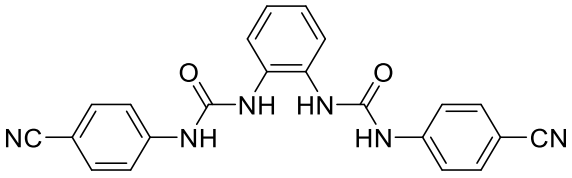

**39**

**Figure 1.22** Various structures of transporters for anions other than chloride.

Anionophores have also been reported that are capable of transporting carboxylates. *ortho*-Phenylenediamine based bisurea **39** has been screened for its ability to transport the natural carboxylates fumarate and maleate[69]. The compounds showed apparent ability to only transport the carboxylate in their mono-anionic form, hence due to differences in $pK_a$ of the anions, only maleate was able to be transported at pH 7.2.

Gale and co-workers have also reported transporters that are selective for certain natural carboxylates over others[70]. Compound **40** transports pyruvate faster than lactate, presumably as lactate is more hydrophilic (binding affinity is actually greater for lactate in DMSO/$H_2O$ 0.5 %). With the introduction of an amide on the indole ring in compound **41** however, this trend is reversed. The authors attributed this to the capability of an additional H-bond to be formed between the amide carbonyl and lactate OH, giving greater complex stability and better shielding within the membrane.

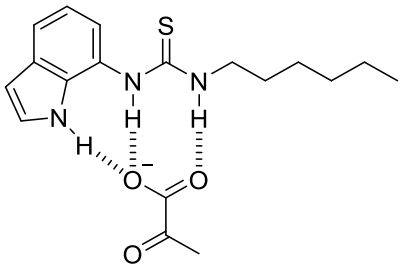

**40**

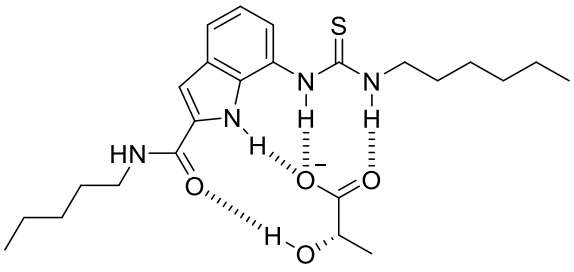

**41**

**Figure 1.23** Structures of transporters selective for natural carboxylates.

Anionophores have also been shown to exhibit 'flippase' activity; that is the binding of a phospholipid head group and translocating it across the bilayer. This has been shown using scaffolds such as tren-based tris-amides by Boon & Smith[71, 72] as well as with cholapod-based transporters developed by Davis et. al.[73].

In addition to hydrogen-bonded complexes, other methods of anion binding have been employed in transport. Matile reported anion transport mediated by halogen bonding compounds such as perfluoroiodohexane **42**[74]. X-ray structures showed that several X-bonding units surrounded the anion to shield the charge, and high Hill coefficients[53] in analysis of the transport data supported the hypothesis that this also took place in the membrane.

Finally, there have been limited reports of transport facilitated by metal complexes. One such example is palladium complex **43**, which is able to transport chloride by $Cl^-/OH^-$ exchange[75]. Evidence for this mechanism was inferred from observation of acidification of the vesicle interior (using HPTS pH-sensitive fluorophore) with $Cl^-$ influx, and a significantly reduced activity in conditions for $Cl^-/NO_3^-$ exchange. The authors proposed that the active form of the complex was a $[Pd(dppp)]^{2+}$ species.

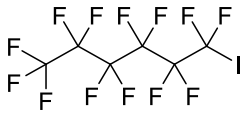


**42**

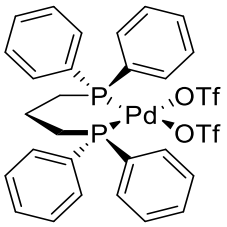


**43**

**Figure 1.24** Structures of halogen bonded and metal complexed transporters.

## 1.4 Structure-Activity Relationships in Transport

Following the development of a wealth of scaffolds on which synthetic anionophores could be built, many studies looking at the effects of structural modifications to carriers on their transport ability followed.

Davis, Gale and Quesada demonstrated the power of pre-organisation of the binding groups in modulating transport activity[76]. Compound **44b** showed an increase in the association constant of greater than one order of magnitude for binding $Cl^-$, $Br^-$ and $I^-$ in $CD_3CN$. The intramolecular hydrogen bonds between the *ortho*-OH groups and the amide carbonyls contributed to the pre-organisation of the N-H H-bond donors into a convergent configuration. Conversely, **44c** demonstrated no appreciable anion binding properties at all, the methoxy substituents this time accepting an H-bond from the amide N-Hs, tying up the binding site. These trends were reflected in the anion transport properties of the compounds, both **44a** & **44c** were inactive in $Cl^-/NO_3^-$ exchange whereas **44b** was a potent $Cl^-$ transporter. The major conformations in Figure 1.25 were confirmed by X-ray crystallography.

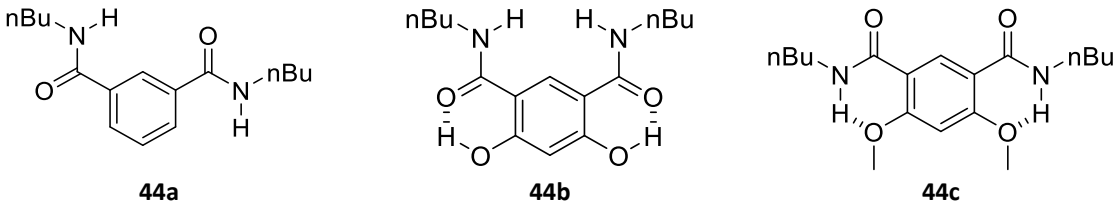


**Figure 1.25** Major conformations of pre-organised isophthalamide transporters.

Intramolecular hydrogen bonds were also exploited in the development of acylthioureas[77]. In these structures the additional carbonyl group is able to hydrogen bond to one of the thiourea N-H groups (Scheme 1.2), visible in the X-ray structures of the compound. As a result, the lipophilicity of the compounds was much increased (evidenced by longer retention times on a C18 HPLC column) by the hydrogen bond shielding the hydrophilic hydrogen bonding group, despite the additional polar atoms in the molecule. This effect increased the activity of the compounds within the membrane and yielded an order of magnitude improvement in $EC_{50\,(270\,s)}$ for **45** in $Cl^-/NO_3^-$ exchange experiments over the analogous thiourea.

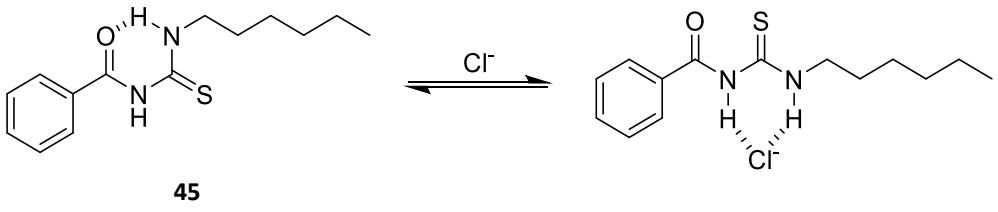


**Scheme 1.2** The intra-molecular bond formed in unbound acylthiourea anion carriers.

Structure-activity relationships studies have been carried out with many of the different anion carrier scaffolds. It has been mentioned already how for the cholapod scaffolds (such as **32**) the transport activity and anion binding activity of the carriers were correlated[60, 78] when considering electronic changes around the binding group. It has also been shown that the encapsulation of the binding site can greatly increase transport efficacy[79]. For example **46b** showed an order of magnitude improvement in initial rate of $Cl^-$ transport over **46a**, with little difference in anion binding affinity.

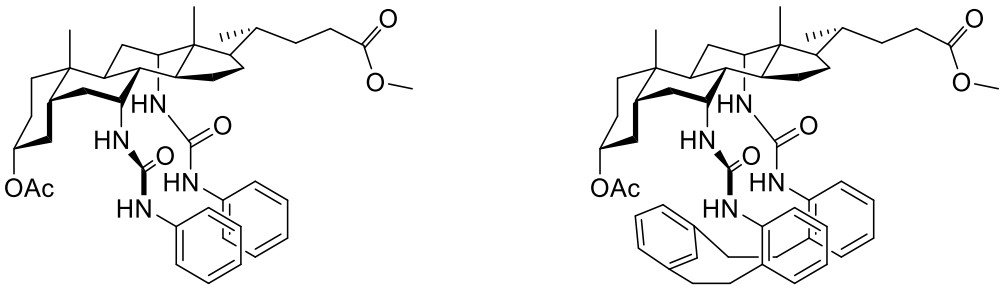


**Figure 1.26** Structures of encapsulated cholaphane **46b** and its analogous cholapod **46a**.

Encapsulation has also been explored in the structure of calix[4]pyrroles[80]. The modification of *meso*-octamethylcalix[4]pyrrole **14** with a triazole strap increased $Cl^-$ binding affinity by an order of magnitude in acetonitrile. Where calixpyrrole **14** was only able to facilitate $Cl^-$ transport in combination with caesium, **47** was able to facilitate transport with sodium, potassium, rubidium and caesium chlorides, although transport was still fastest with the larger cations. The authors suggested this was because the compound was capable of both MCl co-transport and $Cl^-/NO_3^-$ antiport. The extra C-H hydrogen bond yielded by the 1,2,3-triazole ring and the shielding of the charge itself assist this compounds additional binding affinity. A similar effect has been shown using a fluorinated analogue **48**, which again shows increased anion affinity over **14** due to the electron withdrawing fluorine substituents, which again leads to a loss of cation dependence in transport[81].

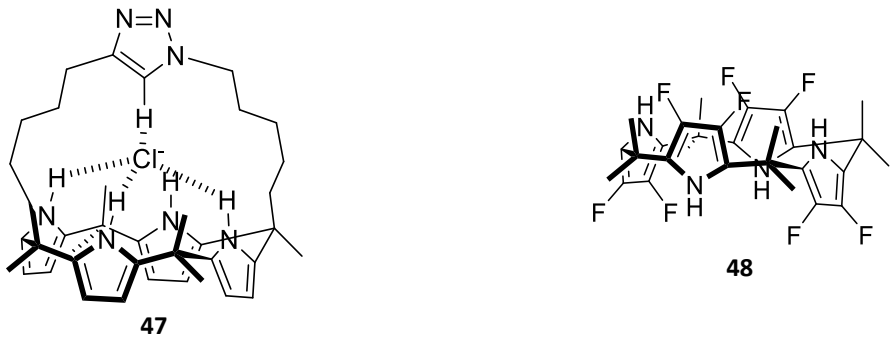


**Figure 1.27** Structural modifications for *meso*-octamethylcalix[4]pyrrole **14** modulating transport activity.

Due to the simplicity of the scaffolds, some very systematic structure-activity studies with small thiourea transporters have been possible using a wide range of compounds. Gale, Félix, Frey and co-workers published a comprehensive QSAR (quantitative structure-activity relationship) study of a series of 22 1-hexyl-3-phenylthioureas, with varying *para*- substituents on the phenyl ring[82]. A training set with 18 of the compounds allowed the development of an equation to predict the transport ability of the four remaining compounds. Successful QSAR prediction of the transport activity of the remaining compounds could be achieved using a term describing the compound's lipophilicity, the Hammet constant for the phenyl substituent (as a measure of its electron withdrawing effect[83], to quantify the effect on anion binding strength) and the calculated relative molecular size.

Thioureas have also been used to study the effect of the location of substituents, not just their lipophilic or electronic effects. Gale and Davis studied thioureas **49**, all with very similar lipophilicities and anion affinities[84]. Remarkably, in $Cl^-/NO_3^-$ exchange experiments **49c** showed an order of magnitude improvement in intital rate of transport and in $EC_{50\,(270\,s)}$ over **49a** & **49b**. The authors rationalised this as an effect of the 'lipophilic balance' of the molecule, where the more asymmetrical compounds are more amphiphile-like in structure, thus better stabilised in the head region of the bilayer and have a greater energy barrier to rearranging and crossing the tail region.

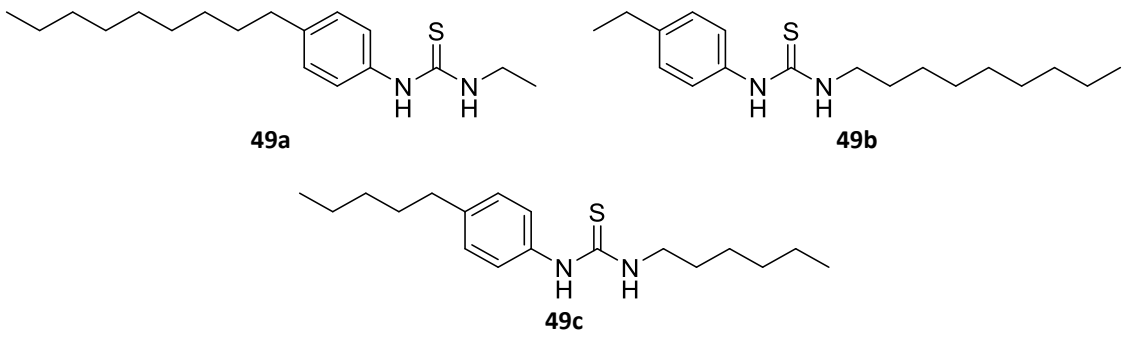


**Figure 1.28** Compounds developed to study the concept of lipophilic balance.

QSAR studies have also been carried out on a large selection of 43 synthetic tambjamine structures[85]. Good fits for the prediction of transport activity based on lipophilicity combined with a large range of further descriptors were obtained. By grouping subsets of the compounds based on the type of substituents involved (eg alkyl, halogen, alkoxide etc.), the authors found that the dependence of transport activity on lipophilicity shifted based on substituent type. They suggested this implies specific interactions between the carriers and the membrane can govern the optimum range of molecular properties, such as lipophilicity, in carrier design.

## 1.5 Advanced Transport – Recent Developments

As the field of anion transport has developed, the methods used to characterise their activity have become more sophisticated, as have the mechanisms carriers exhibit and the methods used to control the transport process. Some specific examples are discussed below.

Gale and co-workers reported a series of thiourea-based $Cl^-$ transporters **50** incorporating a naphthalimide fluorophore[86]. An acidic C-H on the naphthalimide moiety also lends an additional H-bond donor to aid anion complexation. The fluorophore allowed imaging of the localisation of the compounds within intracellular compartments in A549 human lung carcinoma cells.

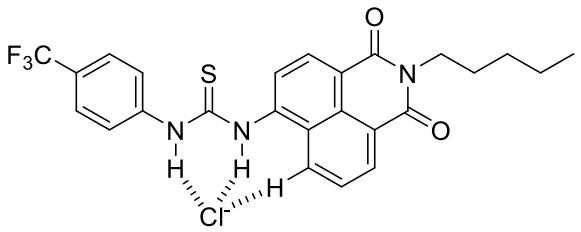

**50**

**Figure 1.29** Thiourea-based fluorescent anion transporter.

Anionophores have been used to bind and transport zwitterionic amino acids in combination with an electrophilic aldehyde[87]. The aldehyde forms a dynamic covalent bond to the ammonium moiety, shielding the positive charge and a squaramide anion carrier binds to the carboxylic acid moiety, shielding the negative charge. This then facilitates diffusion of the complex across the membrane (Scheme 1.3). The transport activity of the two compounds was shown to be synergistic (greater than the sum of the transport mediated by either compound separately) and the mechanism elucidated by comparison with the transport of substrates lacking the ability to form hemiaminals or imines, thus disproving the 'activation' of squaramide carboxylic acid transport by the aldehyde.

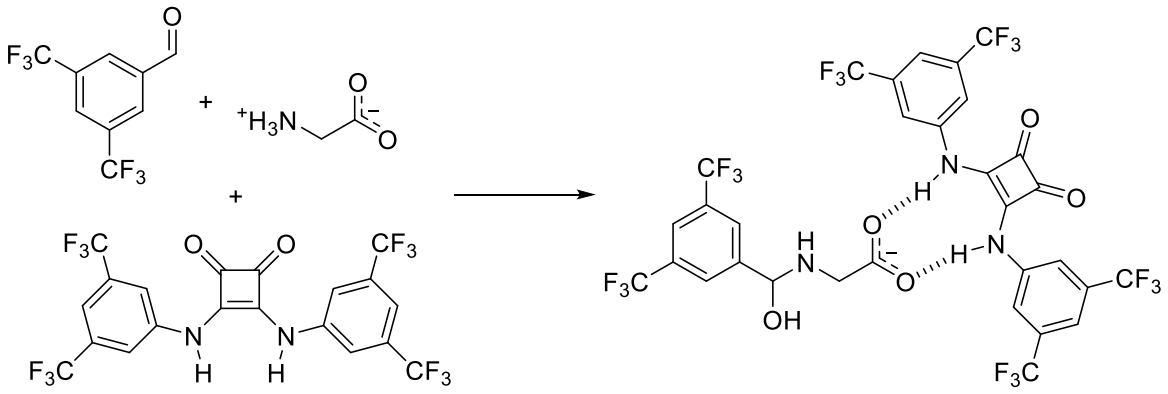

**Scheme 1.3** Using dynamic covalent bonding plus an anionophore to bind and transport glycine.

Further control of the transport mechanism has been achieved with the development of pH-switchable anionophores. A good example of these structures are the thiosquaramides, which were developed to enhance the anion affinity of the squaramides in an analogous way to the advantages of the thioureas over ureas[88]. It was discovered that the $pK_a$s of these compounds were much lower than those of the comparable squaramides, eg. **51** has an experimental $pK_a$ of 7.3, compared to 11.7 for the conventional squaramide (**37**). Hence at pH 7.2, **51** was too inactive in $Cl^-/NO_3^-$ exchange assays to allow Hill analysis of the transport activity, as a large proportion of the compound was deprotonated and thus unable to bind $Cl^-$. The compound showed an acidic switch-on effect, and achieved an $EC_{50\,(270\,s)}$ of 0.0125 mol % (wrt. lipid) at pH 4.0. The thiosemicarbazones are another series of compounds that have shown promising pH-switchable behaviour at biologically relevant pHs[89], these are discussed in detail in Chapter 3.

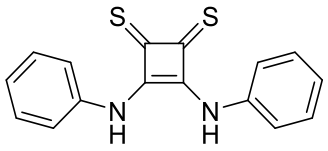


**51**

**Figure 1.30** Structure of a pH-switchable thiosquaramide.

Given the evidence that the anti-cancer activity of the prodigiosins is related to their ability to facilitate HCl co-transport (discussed above), the anti-cancer activity of many anionophore classes has been investigated. Often, compounds are tested using Hoechst staining assays to show that the origin of cytotoxic activity is apoptosis and acridine orange straining is used to show the de-acidification of cellular compartments. This has been demonstrated with the tambjamines by Quesada, Pérez-Tomás and co-workers[90] and with a series of aromatic tren-based tris-ureas and thioureas[91].

In the treatment of cystic fibrosis however, cytotoxicity is not desired, just an ability to transport chloride across cell membranes well enough to compensate to lost activity of CFTR. With this is mind, Davis, Sheppard and co-workers reported a cell-based assay using modified Fischer rat thyroid (FRT) cell epithelia[92]. FRT cells do not express natural $Cl^-$ channels such as CFTR, and were modified to express a halide-sensitive yellow fluorescent protein (YFP). Hence anion transport into the cell mediated by a synthetic anionophore added via the extracellular solution could be monitored by fluorescence microscopy. Thus, in combination with XTT toxicity assays showing a lack of cytotoxic activity, they demonstrated that potent anionophores such as **52** could exhibit the transport properties required of potential cystic fibrosis therapeutics.

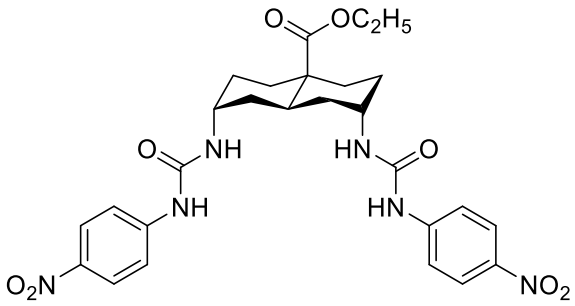

**52**

**Figure 1.31** Structure of non-toxic decalin **52**, highly active in FRT-YFP assays.

With this incentive to develop anionophores which can selectively transport chloride, more attention has been given to accurately determining and describing the selectivity of synthetic carriers. Recent work by Gale, Davis, Sheppard and co-workers identified the need to differentiate between an anionophore's electrogenic transport activity over other transport pathways[93]. Electrogenic transport processes involve solely the movement of a charged species across the membrane, which would otherwise cause a build-up of charge on one side of the membrane without a coupling process to dissipate this. This is in contrast to an electroneutral process which would cause no net build-up of charge alone (eg. HCl co-transport or functionally equivalent $Cl^-/OH^-$ exchange).

The authors described a series of carefully designed assays using the natural $K^+$ transporter valinomycin or $K^+/H^+$ antiporter monensin. This allowed the elucidation of the electrogenic or electroneutral character of the transport mechanism of a range of different anionophores, by the identifying which accompanying processes the carriers were able to couple to[93]. A further set of assays allowed the determination of the level of $Cl^-/OH^-$ selectivity of the compounds, and the investigation of whether they were able to facilitate $H^+/OH^-$ transport alone. The authors demonstrated that the greatest level of any selectivity was correlated with the greatest level of encapsulation of the anion, and that electrogenic tren-based transporter **53** was able to effectively transport $Cl^-$ in cells without affecting the pH of intracellular compartments.

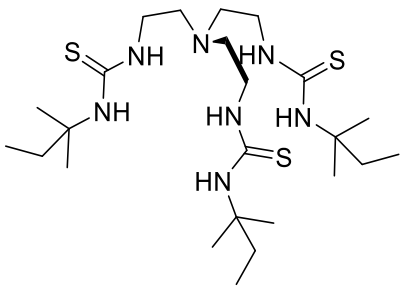

**53**

**Figure 1.32** Structure of an electrogenic tris-thiourea transporter.

## 1.6 Current Challenges in Anionophore Development

The development of synthetic anion transporters is a field that has begun to mature. There are now a wealth of scaffolds and templates available to supramolecular chemists which have shown promise as anionophores, as has been discussed above. The rules governing the ability of these compounds to transport anions are now clearer, with the principles of optimum anion binding (optimum spatial fit, H-bond donor acidity etc.), binding site encapsulation, balance of optimum lipophilicity etc. becoming well-established.

There still exists, however, several hurdles to overcome before it will be possible to develop anionophores that represent genuine therapeutic candidates and demonstrate that principles demonstrated in the lab will be applicable in *in vivo* applications.

Firstly, little to no work has been done to determine how anionophores behave in different lipid environments. Given the complexity of the make-up of natural cell membranes[5, 94], this is clearly a necessary issue to address. Any work that has been done (eg. comparing POPC and POPC/Cholesterol membranes) has given ambiguous or inconclusive results (see discussion in Chapter 2.5.2). Hence the effect of different lipids on the transport process should be explored to determine whether conclusions made in vesicle experiments will hold in real membrane applications.

Secondly, deliverability of anionophores is an inherent problem; by definition, active compounds must be lipophilic but this has an impact on the compounds' solubility, and thus many scaffolds do not adhere to Lipinski's rule of 5 for 'drug-like' molecules[95] (for example). Exploration of novel methods of transporter delivery to the membrane or new ways to subvert solubility issues are thus interesting avenues for anionophore development.

Finally, given the advances in the knowledge of the mechanisms carriers can operate by, and in the methods by which they can be monitored[93], discussed above, old rules for and explanations of structure-activity effects in anion transporters can be viewed in a new light. Exploring the transport process in more detail than previous work can allow a deeper understanding of the effects structural changes have on how anion carriers operate.

This thesis aims to address some of these issues and each is discussed in greater detail in the chapters that follow.

# 2 The Bilayer Environment and the Effects of Lipophilicity

The work in this chapter has been previously published as M. J. Spooner and P. A. Gale (2015). "Anion transport across varying lipid membranes - the effect of lipophilicity." *Chemical Communications* **51**(23): 4883-4886 and is reproduced with permission from the Royal Society of Chemistry.

## 2.1 Introduction

Biological membranes are a complex mixture of different phospholipids, sterols, proteins and various other molecules[5, 94]. The make-up of membranes varies greatly not only between cells of different kingdoms, but also cell types within an organism and even between different organelles within the same cell. The proportion of different lipids within cell membranes alters the physical properties of the membrane[5, 96, 97] and can affect cellular processes such as protein folding and activity[96-98] or be involved in cell signalling[94, 99].

The vast majority of studies on synthetic anion transporters have been carried out in model POPC or POPC/Cholesterol membranes however[6], and seemingly little work had been done to investigate the effect of the lipid environment on transporter efficacy. The condensing effect of cholesterol on the bilayer is well known[100] and previous studies have used the comparison of transport efficacy in the presence and absence of cholesterol as evidence of a mobile carrier mechanism[101, 102] (the logic being that a small molecule will diffuse more slowly across the more ordered membrane in the presence of cholesterol, presenting as slower measured transport rate). Given the variation in composition of lipid membranes *in vivo,* it is important that the effect of lipid environment should be addressed as a natural step to developing synthetic anion carriers as viable therapeutic agents.

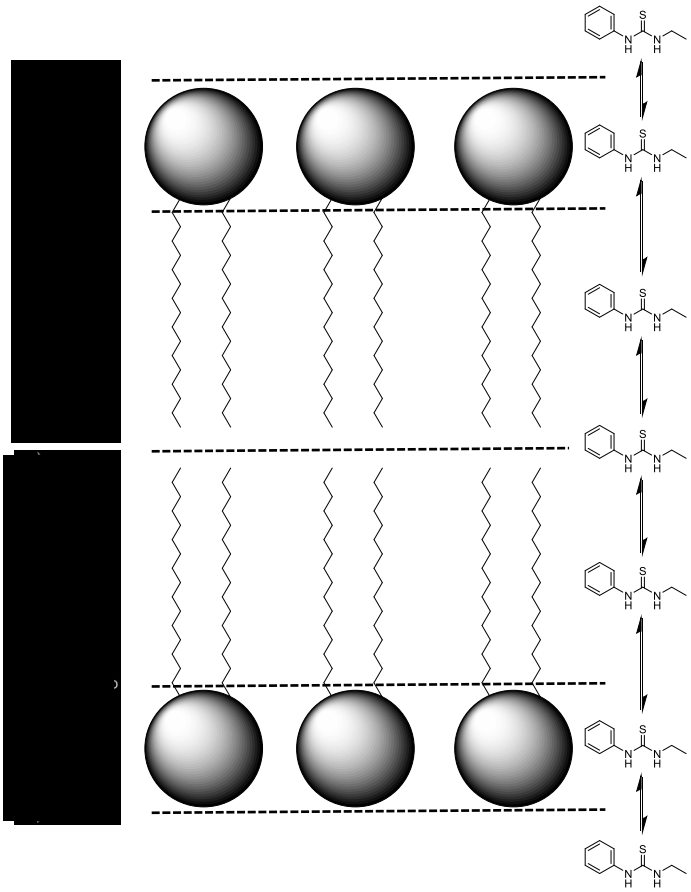

**Figure 2.1** Schematic of the bilayer structure, showing examples of regions where a small molecule may partition.

The bilayer can be considered as several distinct regions with different properties (Figure 2.1). From the bulk solution (the aqueous phase) the first region entered would be the head groups, a relatively polar environment due to the proximity of the polar phosphate moieties in the lipid. The alkyl tail region forms a more hydrophobic region, before reaching the centre of the membrane between the two tails where there is a degree of free space. A molecule diffusing across the bilayer can be considered as being in equilibrium between each region to aid interpretation of transport processes.

Computational studies have allowed the calculation of the free energy profiles of small solutes moving across the bilayer[103]. In particular, it has been shown that different energy barriers exist for different small solutes across the bilayer, with hydrophilic solutes encountering a significant barrier in the tail region, whilst hydrophobic solutes experience a significant barrier in the head region, with a minimum free energy in the centre of the bilayer[104]. These maxima and minima vary in magnitude depending on the lipid forming the bilayer and the fraction of cholesterol incorporated in the membrane.

It was decided to investigate whether similar effects were present when small-molecule anion transporters were tested in systems composed of several different common lipids (Figure 2.2). The lipids were chosen as systematic variations in structure from POPC (1-palmitoyl-2-oleoyl-*sn*-glycero-3-phosphocholine), the most commonly used and readily available lipid used in laboratory vesicle assays.

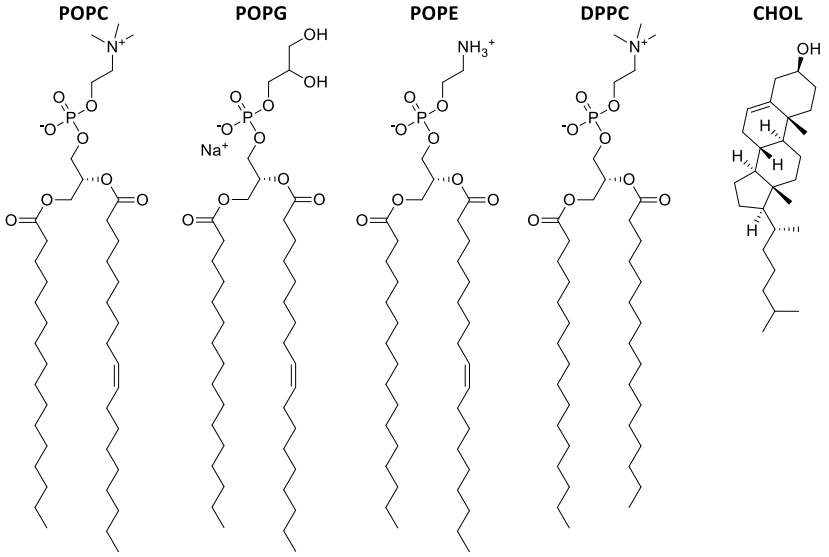


**Figure 2.2** Structures of the four phospholipids discussed in this section and cholesterol (CHOL).

Some initial data was obtained from indole- and carbazole- substituted squaramides **54** & **55** (Figure 2.3). Their transport activity was assayed for $Cl^-/NO_3^-$ exchange from vesicles of binary mixtures of POPC with either POPG or POPE (Figure 2.3). Hill analysis[52-54] of the % chloride efflux observed after 270 s at least 6 concentrations of receptor was used to obtain an $EC_{50\ 270\ s}$ value (effective receptor concentration required to achieve 50 % efflux after 270 s), a quantitative measure of transport activity.

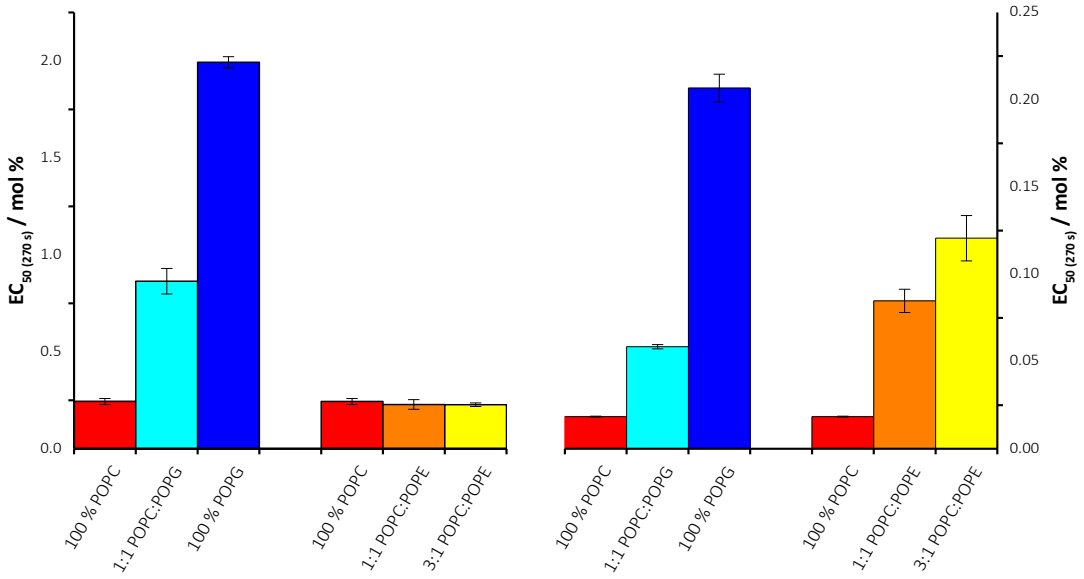


**Figure 2.3** Structures of and $EC_{50\ 270\ s}$ values for compounds **54** & **55** for $Cl^-/NO_3^-$ exchange at pH 7.2 from vesicles of varying ratios of POPC, POPG and POPE.

For both compounds, the $EC_{50}$ increased with increasing fraction POPG in the bilayer, indicating less effective transport performance. Considering the negative charge of POPG at pH 7.2, it is likely that this increases the energy barrier for a negatively charged $Cl^-$ complex to form and cross the head group region in the bilayer.

With an increasing fraction of POPE, the effect is less well defined. Compound **55** exhibited a similar effect, with increasing fraction of POPE inhibiting the transport process. For **54** however, the $EC_{50}$ remained the same in the bilayers tested. This suggests that the rate-determining step (RDS) for the transport process for each compound is different. Changing the head group appears not to affect the rate or transport for **54** suggesting that crossing the tail region may be the RDS. For **55**, the RDS appears to be affected by the changing head group, perhaps the more polar environment or greater availability of hydrogen bonds from the head group disfavours the compound picking up a chloride in the head region.

One of the key differences in the two compounds is the increased lipophilicity of **55** afforded by the extra ring in the carbazole substituents. The calculated log P (Clog P, P is the octanol/water partition coefficient) value (by the ALOGPS method[105]) of **54** is 3.81, compared to 5.57 for **55**. It was theorised that the increased lipophilicity could explain why changes in the structure of the head group affects this compound more than for **54**, which appears to be limited by its crossing of the tail region.

The importance of lipophilicity in anion transporter design is well known[91, 102]. Clog P has been shown to be a key indicator of transport activity in simple thioureas[82] and it has been shown that an optimum range of log P exists for the tambjamine class of transporters[106]. Further QSAR work studying the effect of different substitutions on the tambjamines showed that the optimum log P range depended on the type of substituent present (eg. alkyl/halide etc.), suggesting that this range is dependent on specific interactions between the membrane and the anionophore[85].

A study was designed to probe the relationship between log P and transport rate in different lipid environments. The aim was to use a series of simple transporters covering a wide range of lipophilicity to test how different lipids affected the transport rate and whether the optimum log P range changed depending on the constitution of the bilayer.

## 2.2 Thiourea Series

A series of simple thioureas (Figure 2.4) was designed to carry out this work. The thiourea binding motif has been studied in detail previously[82, 84] and the compounds are easy to synthesise from commercially available starting materials and can be easily modified by varying the substituents in the starting materials (Scheme 2.1). The appropriate aniline and isothiocyanate were stirred in pyridine or dry DCM under $N_2$ atmosphere overnight, heating if necessary. Purification was achieved by removal of starting materials with an Isolute® SCX-2 cation exchange column then flash chromatography. Yields ranged from 9 – 90 %. Full synthetic procedures and spectroscopic data are appended (Appendix I).

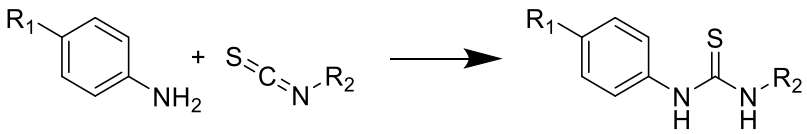


**Scheme 2.1** General synthesis of the simple thiourea series. Reactions carried out under $N_2$, reaction solvents, temperatures and timings varied, see Appendix I.

Fifteen compounds in total were synthesised, with increasing length of alkyl chains in the $R_1$ and $R_2$ positions, from $C_1$ – $C_8$. Carbon atoms were added symmetrically in keeping with the principle of lipophilic balance[84]. In this way, a large range of lipophilicity was covered without greatly affecting the electronics of the binding moiety.

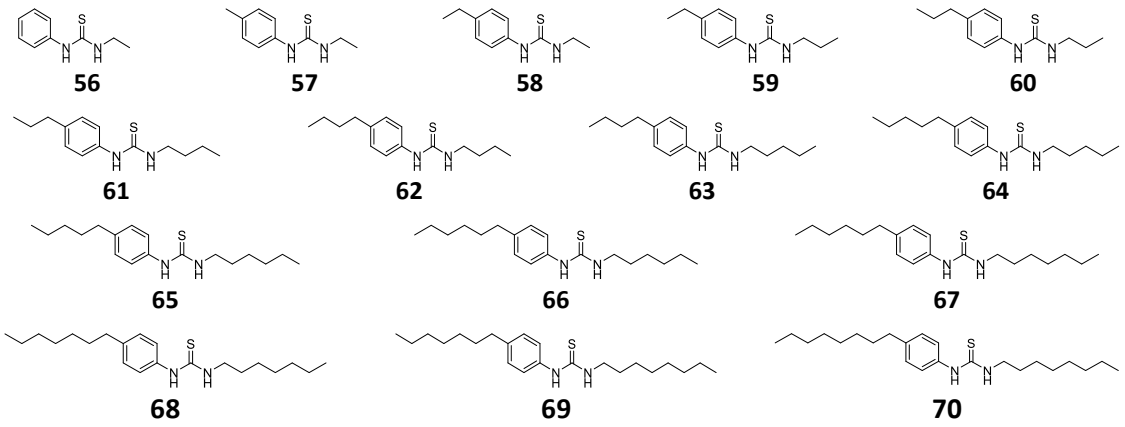


**Figure 2.4** Structure of the thiourea series.

## 2.3 Log P Calculation & Evaluation

The calculated log P values (P = octanol/water partition coefficient) for each compound were calculated using various methods, using open online calculation tools[105, 107] or algorithms built into common programs such as ACD/LogP and Chemdraw. The obtained values are listed in Table 2.1.

| # | RT /min | Chemdraw | VCCLab Cons. | ALOGPs | AClogP | ALOGP | MLOGP | KOWWIN | XLOGP2 | XLOGP3 | ACD/LogP |
|---|---|---|---|---|---|---|---|---|---|---|---|
| **56** | 0.27 | 1.41 | 1.81 | 1.50 | 2.11 | 2.19 | 1.95 | 1.91 | 1.59 | 1.42 | 1.42 |
| **57** | 0.30 | 1.91 | 2.19 | 1.74 | 2.42 | 2.68 | 2.25 | 2.46 | 2.03 | 1.78 | 1.88 |
| **58** | 0.35 | 2.44 | 2.65 | 2.45 | 2.78 | 3.14 | 2.54 | 2.95 | 2.49 | 2.22 | 2.41 |
| **59** | 0.41 | 2.97 | 3.16 | 2.87 | 3.24 | 3.66 | 2.82 | 3.44 | 2.85 | 3.22 | 2.94 |
| **60** | 0.52 | 3.50 | 3.62 | 3.33 | 3.71 | 4.12 | 3.09 | 3.93 | 3.42 | 3.76 | 3.47 |
| **61** | 0.68 | 4.03 | 4.07 | 3.86 | 4.17 | 4.57 | 3.36 | 4.42 | 3.99 | 4.12 | 4.01 |
| **62** | 0.93 | 4.55 | 4.54 | 4.37 | 4.64 | 5.03 | 3.61 | 4.91 | 4.56 | 4.66 | 4.54 |
| **63** | 1.28 | 5.08 | 4.99 | 4.77 | 5.10 | 5.49 | 3.86 | 5.40 | 5.12 | 5.20 | 5.07 |
| **64** | 1.85 | 5.61 | 5.45 | 5.20 | 5.57 | 5.94 | 4.11 | 5.89 | 5.69 | 5.74 | 5.60 |
| **65** | 2.67 | 6.14 | 5.91 | 5.71 | 6.03 | 6.40 | 4.34 | 6.38 | 6.26 | 6.28 | 6.13 |
| **66** | 3.99 | 6.67 | 6.38 | 6.20 | 6.49 | 6.85 | 4.57 | 6.88 | 6.83 | 6.82 | 6.66 |
| **67** | 5.91 | 7.20 | 6.70 | 6.74 | 6.96 | 7.31 | 4.80 | 7.37 | 6.35 | 7.37 | 7.19 |
| **68** | 8.93 | 7.73 | 7.25 | 7.15 | 7.42 | 7.77 | 5.94 | 7.86 | 6.70 | 7.91 | 7.72 |
| **69** | 13.44 | 8.26 | 7.69 | 7.52 | 7.89 | 8.22 | 6.16 | 8.35 | 7.27 | 8.45 | 8.26 |
| **70** | 20.55 | 8.79 | 8.10 | 7.87 | 8.35 | 8.68 | 6.37 | 8.84 | 7.63 | 8.99 | 8.79 |

**Table 2.1** Clog P values for the thiourea series, plus isocratic retention times (RT).

Each method was evaluated by studying the quality of the correlation between the retention times for the compounds obtained by HPLC with the Clog P values. Compounds were eluted from a C18 RP-HPLC column isocratically over 30 minutes with 60% acetonitrile/water. The retention factor k' is calculated from the retention time (RT) of each compound and the column dead time (the time taken for an unretained compound to pass through the column, $t_0$).

$$k' = \frac{RT - t_0}{t_0} \quad (1)$$

The dead time ($t_0$) of the column was determined by comparison of the relative retention times of the compounds. As the series is homologous, plotting the RT($n_c$) (retention time, number of carbons = n) against RT($n_{c+1}$) gives a straight line allowing $t_0$ to be calculated as given in equation (2)[108]. The retention time values from the RP-HPLC are given in Table 2.1 and the plot in Figure 2.6.

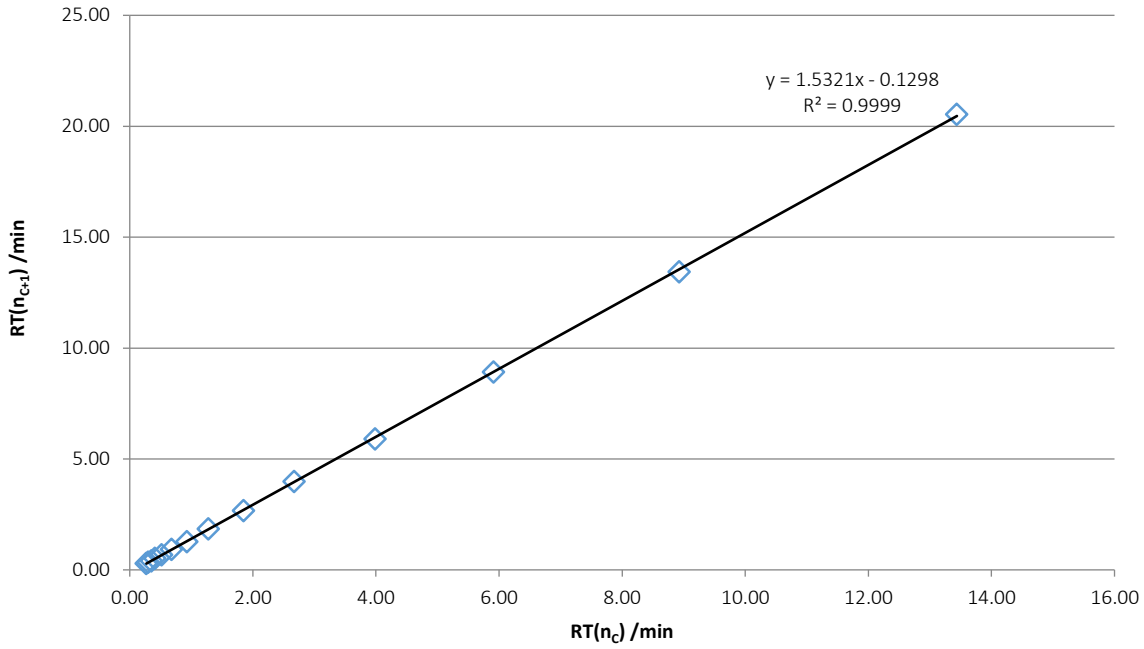


**Figure 2.5** Determining $t_0$ for the RP-HPLC experiments. Retention times plot plus calculation steps. Method adapted from [108].

$$RT(N_{C+1}) = A * RT(N_C) + (1 - A)t_0 \tag{2}$$

$$A = 1.5321 \qquad (1 - A)t_0 = -0.1298 \qquad \Rightarrow t_0 = 0.2439\, min$$

With $t_0$ = 0.2439 min, k′ could be calculated for each compound. As log k′ from isocratic HPLC data correlates linearly with log P[108, 109], the values were plotted against the Clog P values from the tested calculation methods.

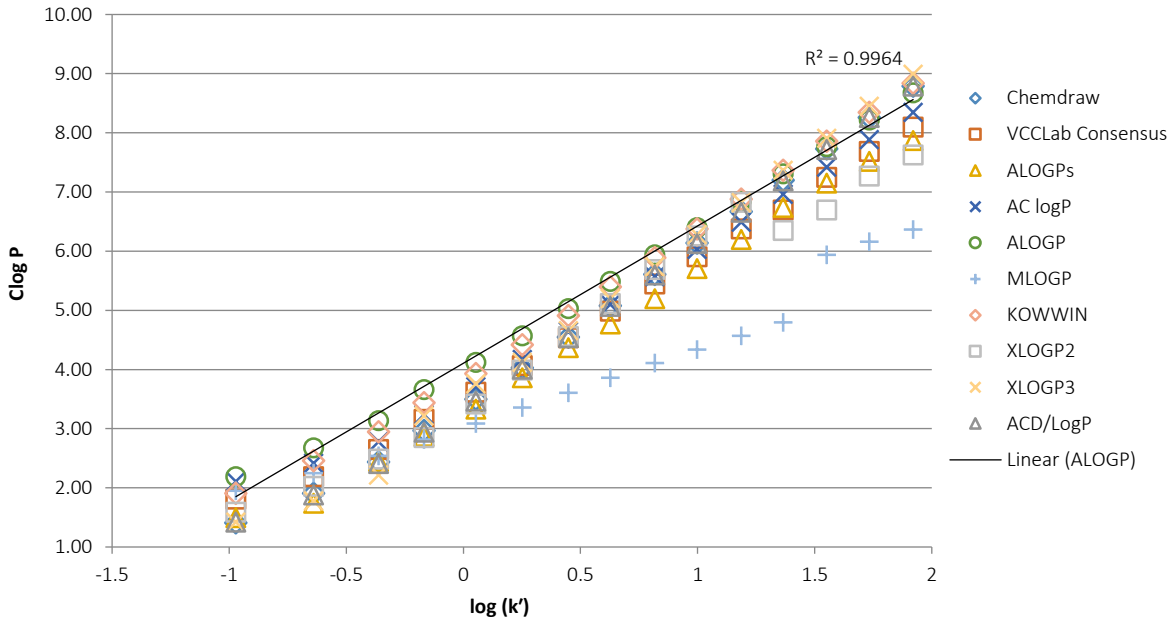


**Figure 2.6** Plot of log (k') against calculated log P from various computational methods. Black line represents the linear fit of the data from the ALOGP model, with the correlation coefficient.

Although several methods gave very strong correlations, the ALOGP model (Ghose-Crippen) was chosen as it gave the highest correlation coefficient ($R^2 = 0.9964$). It should be noted, that even between methods that showed very strong correlations ($R^2 > 0.99$), Clog P values from different methods for the same molecule could vary by up to 1 log P unit. Although clearly Clog P values are desirable for the prediction of compound properties before their synthesis, this shows that care must be taken when comparing values reported from different sources. A direct log P measurement would be more desirable to allow better comparison between reported compounds.

## 2.4 Anion Binding

The anion binding properties of the compounds were studied by $^1$H NMR titration. Briefly, aliquots of an ~0.16 M solution of the TBA salt of the anionic guest in 0.5 % $H_2O$/DMSO-$d_6$ were added to an ~0.01 M solution of the receptor 0.5 % $H_2O$/DMSO-$d_6$. $^1$H NMR spectra were obtained for each titre, with approx. 20 spectra obtained from 0 to 6 equivalents of guest to host. The chemical shift of the two N-H protons over the course of the titration was plotted against the concentration of the anionic guest and the data fitted to a 1:1 Binding model using WINEQNMR2[110]. Fit curves and sample stack plots are appended (Appendix III.1.2).

| Guest | Proton | 56 | 62 | 70 |
|---|---|---|---|---|
| TBA Cl | N-H Aryl | 16 | 17 | 17 |
| | N-H Alkyl | 14 | 17 | 16 |
| TBA $NO_3$ | N-H Aryl | <10 | <10 | <10 |
| | N-H Alkyl | <10 | <10 | <10 |
| TBA $H_2PO_4$ | N-H Aryl | 200 | 253 | 186 |
| | N-H Alkyl | 181 | 333 | 157 |
| $TBA_2$ $SO_4$ | N-H Aryl | 2782 | 3389 | 4299 |
| | N-H Alkyl | 3045 | 3384 | 5035 |

**Table 2.2** Binding constants ($K^{-1}$) obtained from $^1$H NMR titrations for compounds **56**, **62** & **70**. All constants from 1:1 binding model as calculated by WINEQNMR2[110]. All errors <10 %.

The binding constants for TBA Cl, TBA $NO_3$ and $TBA_2$ $SO_4$ are all very similar across the series, mostly falling within error (~10 %) of each other, suggesting no significant difference in the strength of binding to these anions. Only with TBA $H_2PO_4$ is a significant difference in binding strength observed, with compound **62** binding more strongly that the compounds at the extremes of the series. The difference however, although significant in terms of lying outside of experimental error, is still small. It is therefore unlikely that significant differences in the transport rate observed in subsequent experiments could be attributable to differences in anion binding strength.

## 2.5 Transport Rate Screening

### 2.5.1 POPC Vesicles & Plot Methodology

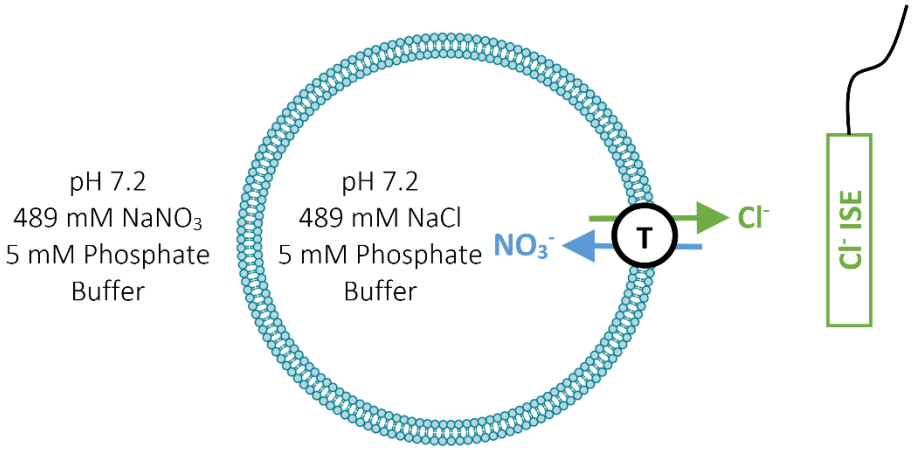


**Figure 2.7** Schematic showing the setup of the $Cl^-/NO_3^-$ exchange assay. T = the anionophore being tested.

To obtain the baseline for comparison with other lipid mixtures, the full series was tested in standard vesicle models of POPC loaded with NaCl, suspended in a solution of $NaNO_3$ and buffered to pH 7.2. An $Cl^-$ selective ion-selective electrode (ISE) was used to monitor the efflux of chloride from the vesicles after the addition of the transporter as a solution in DMSO. After 5 minutes a detergent was added (1 g polyoxyethylene-(8)-lauryl ether in 8 ml 7:1 water:DMSO) to lyse the vesicles and calibrate to 100 % efflux. The total chloride efflux after 270 s was plotted against the Clog P values from the ALOGP calculation method.

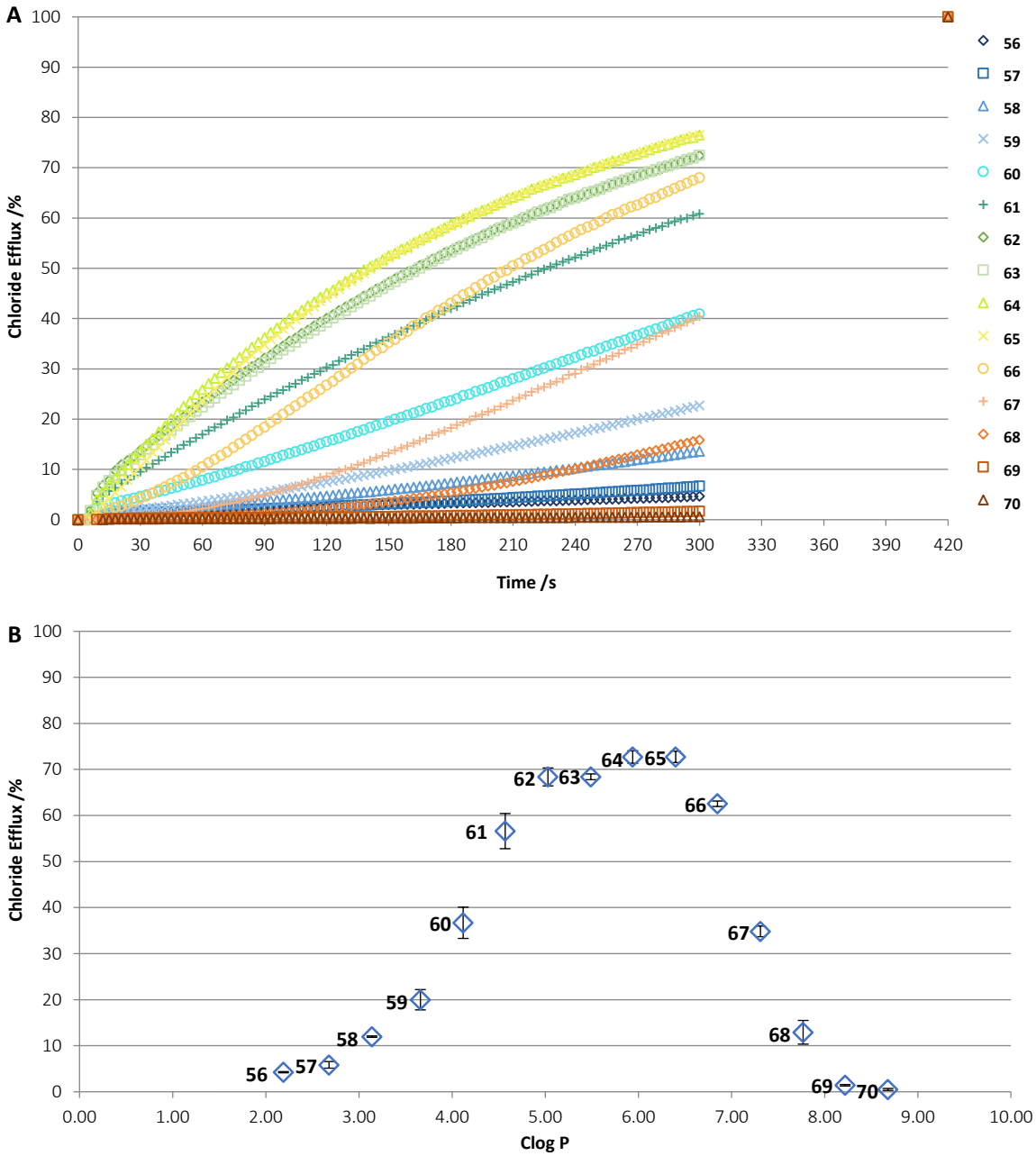


**Figure 2.8** **A**: Chloride release from POPC vesicles over time for **56** - **70**. **B**: Chloride efflux at 270 s for **56** - **70**, plotted against calculated log P of each compound. Each point in both plots represents the average of 3 trials.

The plots show a peak in activity for compounds of moderate lipophilicity, as expected[106]. Interestingly, the curves representing the release of chloride over time from the vesicles show differing shapes; this could be due to different mechanisms or factors limiting transport across the bilayer or effects of delays to partitioning into the membrane, (a problem investigated below).

As a directly comparable measure of the transport efficiency of the compounds, the initial rate of transport was quantified. Various attempts to fit the trial curves to various sigmoidal/exponential/growth/decay functions yielded unsatisfactory results. Errors on calculated

values were large, especially for compounds at either end of the series, and consistently-shaped plots of residual errors suggested that the models attempted were fundamentally describing the wrong relationship.

Instead, an approach similar to that used by Quesada et. al.[106] was used to quantify the initial rate. The data point for the first 30 seconds of each run were considered to be approximately linear and the rate taken as the gradient obtained by performing a linear regression on the data. This gave a good value for the initial rate with a reasonable error, with the $r^2$ value for the regression analysis always being greater than 0.88, with the majority of values (ie those not at the extremes of lipophilicity) in excess of 0.94.

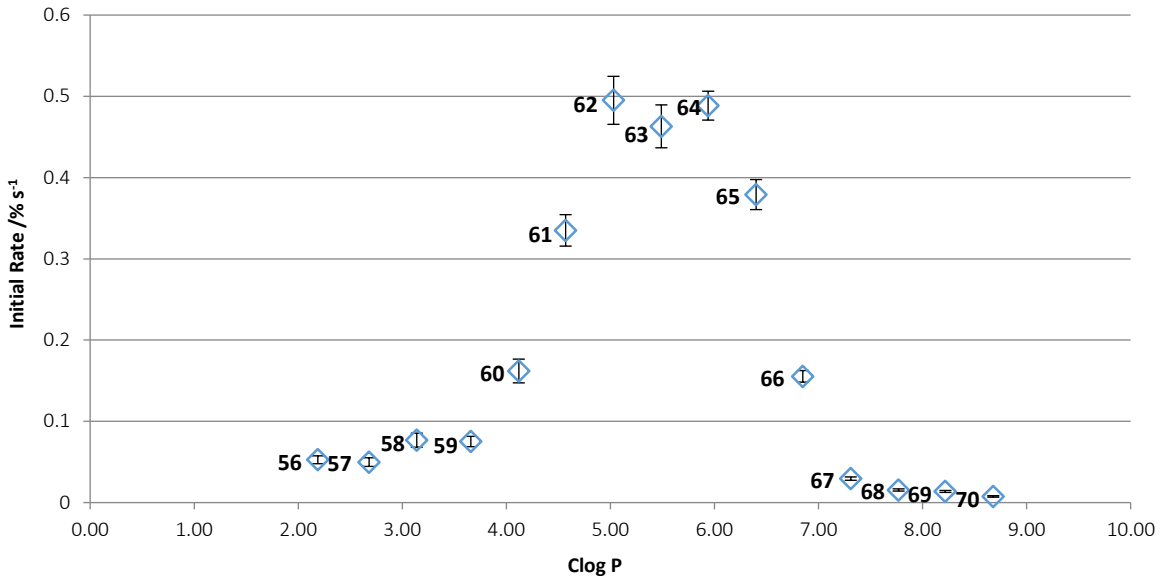


**Figure 2.9** Plot of the initial rate of $Cl^-/NO_3^-$ transport for **56** - **70** in POPC vesicles.

These data suggest an ideal Clog P range of approximately 5-6 for maximum $Cl^-$ transport efficiency for these simple thioureas. This is considerably different to the range of 3.4 ± 0.5 previously reported for the tambjamine class of anionophores[106,*]. Traditional rationalisation of the optimum log P range suggests the effect arises from having to strike a balance between the receptor being lipophilic enough to cross the tail region of the membrane, without being so lipophilic as to be confined there. This would suggest that the range should be the same within the same lipid system, these results however imply that the effect is more complex.

To check for any changes in carrier delivery, transport assays were repeated using vesicles dispersed in 162 mM $Na_2SO_4$ solution. The very hydrophilic nature of the sulphate ion[67] means that

[*] The value quoted in the paper is 4.2 ± 0.5, based on the VCC Lab consensus log P. The values have been recalculated using the ALOGP method for consistency with calculations used in this work.

it is generally assumed that will not be transported by anion carriers[82]. After 2 minutes a spike of $NaNO_3$ solution is added to initiate transport. This allows time for the carriers to equilibrate within the membrane, removing any possible effects on transport from delays in carrier partitioning. The results are shown in Figure 2.10.

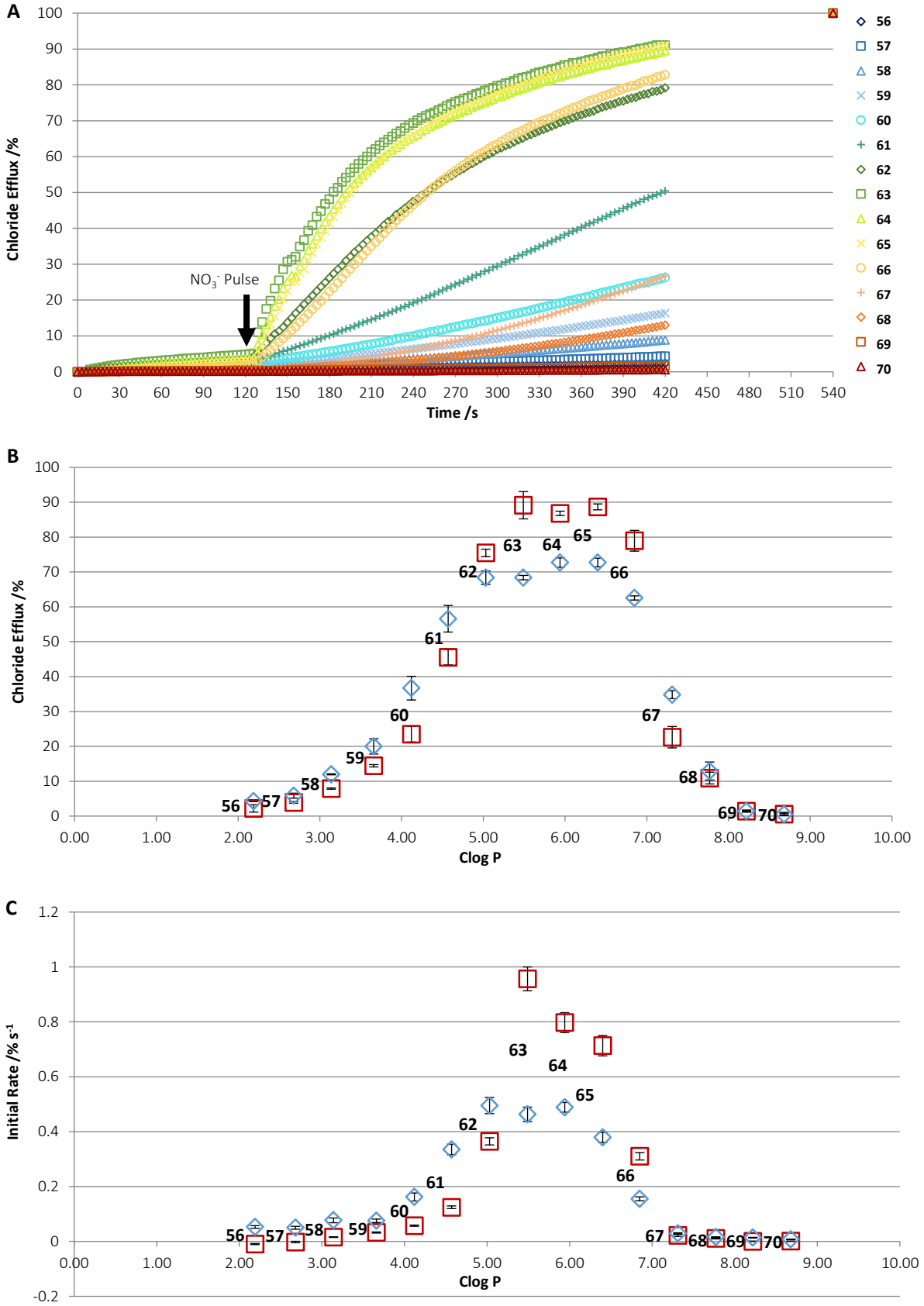


**Figure 2.10** **A**: Transport curves for POPC vesicles over time for **56** - **70** in $SO_4^{2-}/NO_3^-$ spike experiments. **B**: Chloride efflux at 270 s/390 s for **56** - **70**, plotted against calculated log P of each compound. **C**: Initial rate of chloride transport after $NO_3^-$ addition. Blue diamonds - $Cl^-/NO_3^-$ trials. Red squares – $SO_4^{2-}/NO_3^-$ spike trials. Each point in all plots represents the average of 3 trials.

These results show that the trend in relative activity across the series does not vary between the $SO_4^{2-}$ experiments and the normal $Cl^-/NO_3^-$ trials. The most active compounds in the centre of the series appear to increase in activity in the $SO_4^{2-}$ trials; this is likely due to the expected effect of allowing the transporters to fully partition into the membrane before transport starts, thus the initial rate and the final efflux value increase.

For the less active compounds **56** - **61** and **67** - **70** at the extremes of the series, transport activity appears to be lower in the $SO_4^{2-}$ trials. For the more hydrophobic compounds, this may be rationalised by their faster partitioning into the tail region of the membrane, where they are likely confined. The hydrophilic compounds may be binding more competitively with the lipid head groups or potentially complexing $SO_4^{2-}$ in solution; the binding affinity for sulphate is higher than the other anions present (Table 2.2). If complexes between sulphate and the hydrophilic receptors are stable in solution, it is even less favourable for the receptors to locate in the membrane, and fewer will be available for transport.

### 2.5.2 7:3 POPC:Cholesterol

Cholesterol is known to increase the viscosity, rigidity and ordering of the bilayer[111-114] and thus has been added to bilayers in transport studies to provide evidence of a mobile carrier mechanism (the logic being that slower transport through a more rigid membrane suggest a mobile carrier over channel formation)[101, 102]. This has however occasionally led to confusing results, with some series of compounds showing increased transport in the presence of cholesterol[65, 115].

It was theorised that the lipophilicity of the compounds tested may have a bearing on the effect seen in cholesterol vesicles in comparison to pure POPC, as it had been suggested that increased partitioning of transporters into cholesterol-containing bilayers may explain the increases seen[65]. Hence the screening was repeated in vesicles of 7:3 POPC:Cholesterol.

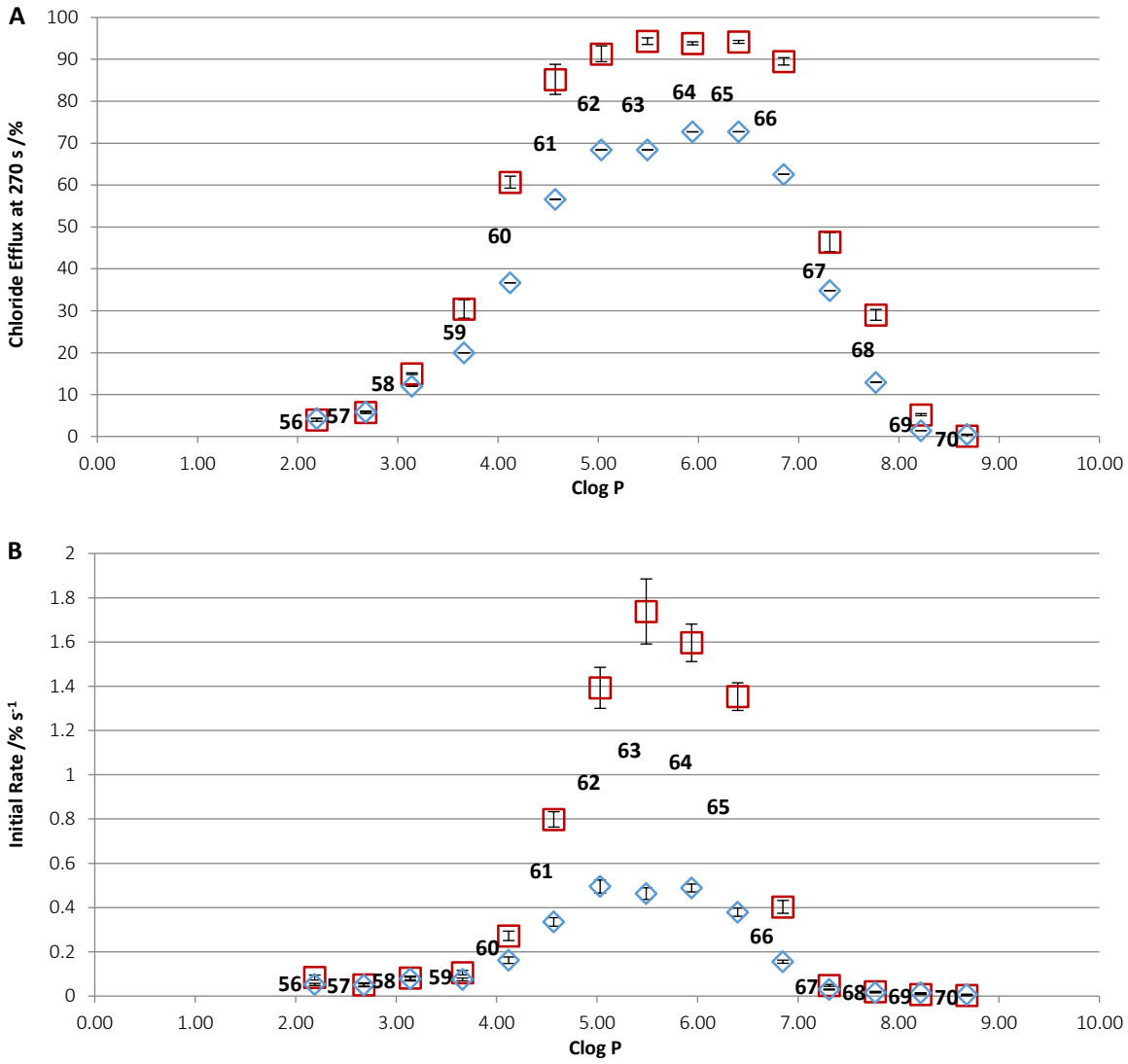


**Figure 2.11** **A**: Chloride efflux at 270 s for **56** - **70**, plotted against transporter Clog P. **B**: Initial rate of chloride transport. Blue diamonds – 100% POPC. Red squares – 7:3 POPC:CHOL. Each point in all plots represents the average of 3 trials.

Across the whole series, transport activity is increased with the addition of cholesterol to the lipid bilayer, with more compounds reaching close to 100 % efflux after 270 s and initial rate increasing for every compound. Importantly, the peak or 'ideal' lipophilicity does not move for cholesterol vesicles, the fastest compounds in POPC remain the fastest for 7:3 POPC:CHOL.

This result along with others previously[65, 115] show that the assumption that the more ordered membrane would slow diffusion and therefore transport does not hold for all transporter classes. For this class of compounds, regardless of the lipophilicity of the molecule, an increase in activity is always observed. This suggests that the cholesterol effect is not determined by a compound's partitioning into the membrane (from purely hydrophobic effects). Rather it may be an intrinsic property of the compound class and specific interactions between the binding moiety and the membrane.

The experiments were also repeated as $SO_4^{2-}$ experiments (Figure 2.12). Almost all compounds showed a decrease in activity in the $SO_4^{2-}$ trials, the exceptions being **65** (same activity, within error) and **66** & **67** (which showed an activity increase). Again, this may be due to similar effects as discussed above, which will require further investigation. In all cases activity remained higher than the $SO_4^{2-}$ runs with 100% POPC.

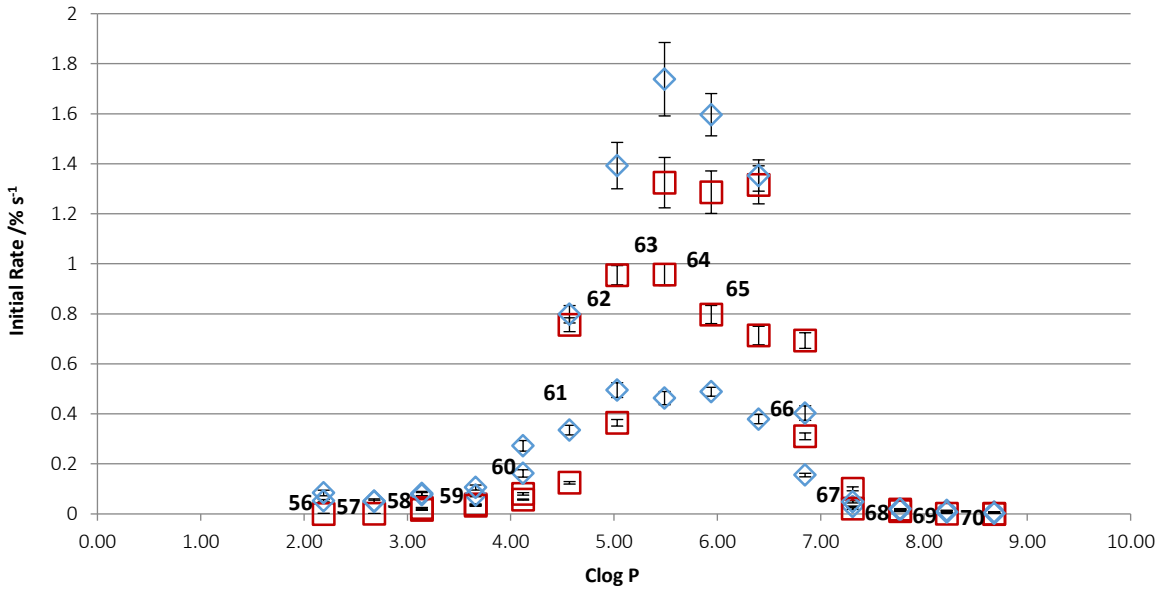


**Figure 2.12** Initial rate of chloride transport for $SO_4^{2-}/NO_3^-$ spike trials with **56** - **70** in 100 % POPC and 7:3 POPC:CHOL vesicles. Blue diamonds – 100% POPC. Red squares – 7:3 POPC:CHOL. Faded points are standard $Cl^-/NO_3^-$ trials given for comparison. Each point in all plots represents the average of 3 trials.

### 2.5.3 POPG vesicles

Phosphatidyl glycerol is a lipid that is rare in mammalian cells but is common in bacterial cells, constituting up to 20 % of *E. Coli* cell membranes[5]. POPG has a very similar structure to POPC, the only difference is that the choline moiety is replaced with a glycerol, giving the molecule an overall negative charge.

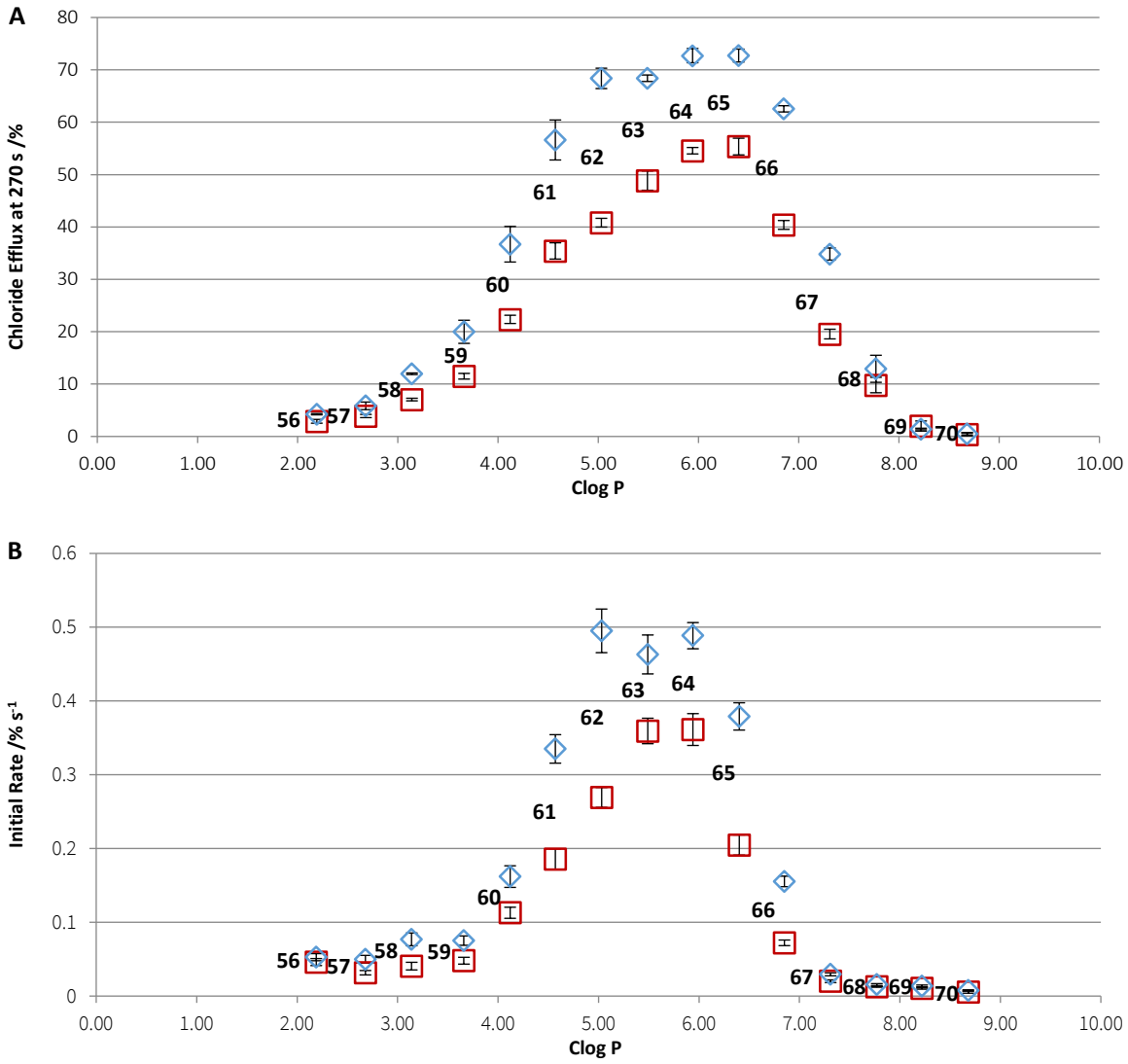


**Figure 2.13** **A**: Chloride efflux at 270 s for **56** - **70**, plotted against transporter Clog P. **B**: Initial rate of chloride transport. Blue diamonds – 100% POPC. Red squares – 100 % POPG. Each point in all plots represents the average of 3 trials.

The transport activity is quite clearly lower across the entire series, again with no obvious shift in peak activity with respect to lipophilicity. This may be down to one of two effects. The increased polarity in the head region due to the negative charge on the POPG head groups may be giving a higher energy barrier to all compounds, confining them more to the tail region and disfavouring diffusion to the head region to pick up / release a chloride ion. The negative charge would most likely disfavour the negatively charged anion complex. The effect could also be rationalised by increased competitive binding of the carriers to the lipid head group, which could be strengthened by the increased negative charge or a more optimal spatial fit of the phosphoglycerol moiety. Titration data of the relative binding strengths of the transporters to the lipid molecules could offer insight into the more likely mechanism.

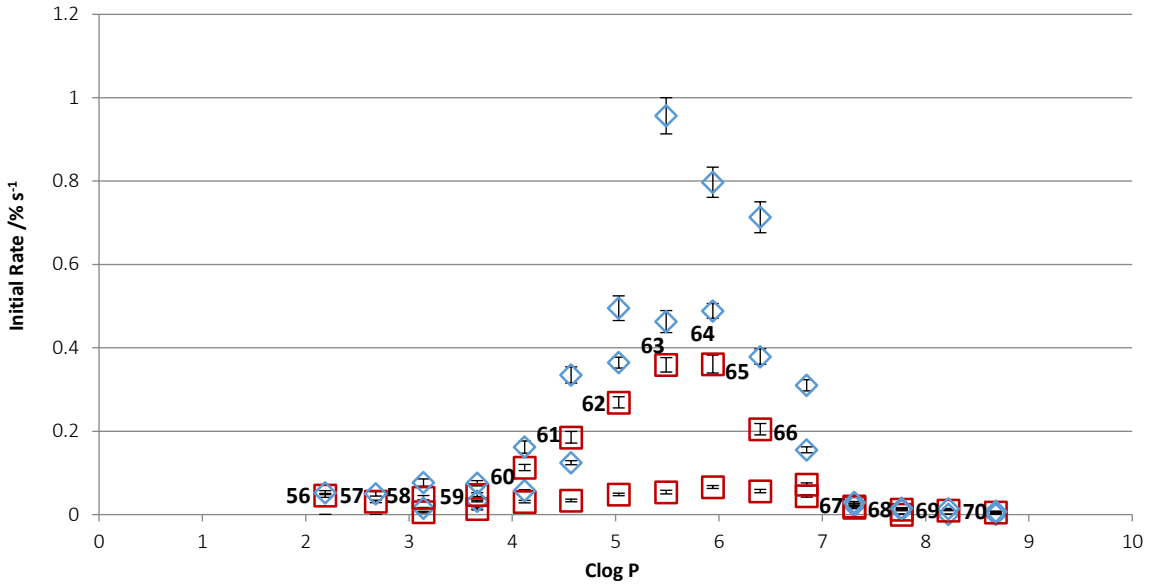


**Figure 2.14** Initial rate of chloride transport for $SO_4^{2-}/NO_3^-$ spike trials with **56** - **70** in 100 % POPC and 100 % POPG vesicles. Blue diamonds – 100% POPC. Red squares – 100 % POPG. Faded points are standard $Cl^-/NO_3^-$ trials given for comparison. Each point in all plots represents the average of 3 trials.

$SO_4^{2-}/NO_3^-$ spike experiments were also carried out in 100 % POPG as before; transport activity was greatly reduced across the whole series. Interestingly, the increase observed in POPC for the most active compounds was not observed here, suggesting that speed of initial partitioning into the membrane is not rate-limiting.

The reduction in activity can be rationalised in a similar way to before, if the compounds are binding more competitively to $SO_4^{2-}$ over $Cl^-$ and $NO_3^-$. This could conceivably decrease transport rate, as despite higher binding affinity the carriers would likely be unable to fully desolvate the $SO_4^{2-}$ ion and transport it, thus having no overall contribution to the antiport process.

### 2.5.4 3:1 POPE:POPC Vesicles

The transport screening was repeated with phosphoethanolamine (PE) vesicles. PE constitutes up to 75% of *E. Coli* membranes[116], and has the same head-group structure as POPC, save for the lack of methyl groups around the choline nitrogen. POPE was tested as a 3:1 mixture with POPC, as POPE will not form vesicles on its own (due to the higher transition temperature for this lipid and the likelihood of forming a combination of gel and liquid crystalline phases at the concentrations used in these experiments[117]).

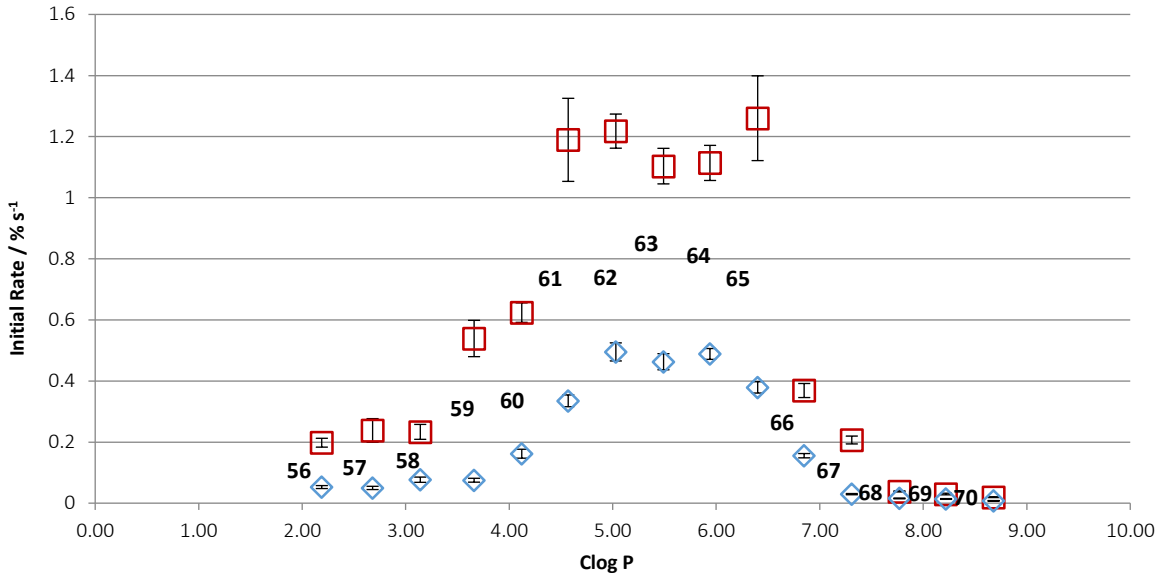


**Figure 2.15** Initial rate of chloride transport for **56** - **70**, plotted against transporter Clog P. Blue diamonds – 100% POPC. Red squares – 3:1 POPE:POPC. Each point in all plots represents the average of 3 trials.

For all compounds, the presence of POPE increased the rate of chloride transport observed in the experiment, in the case of the most active compounds the rate almost doubling. Again, no shift in peak activity with respect to lipophilicity was observed. It might have been expected that the decreased bulk around the charged ammonium group would give a more polar environment in the head region that would increase the energy barrier to the lipophilic transporter molecules diffusing to the head region. It appears however that the opposite effect is the case. This could be due to the increased free space in the head region due to the less bulky head group, or potentially different H-bonding interactions with the head groups decreasing the energy barrier to picking up a chloride ion (either allowing $Cl^-$ to diffuse further into the membrane or stabilising the anionophore in the head region).

It is interesting to note that the opposite effect has been observed here as was observed with the indole-squaramides (Figure 2.3). Where compounds **56** - **70** were all enhanced in the presence of POPE, the activity of **55** was decreased whilst **54** appeared unaffected. This range of effects is further evidence that the rate-determining step for transport is specific to the structure of the transporter family. It is clear however that the effect observed is not a function of the simple log P of the anionophore.

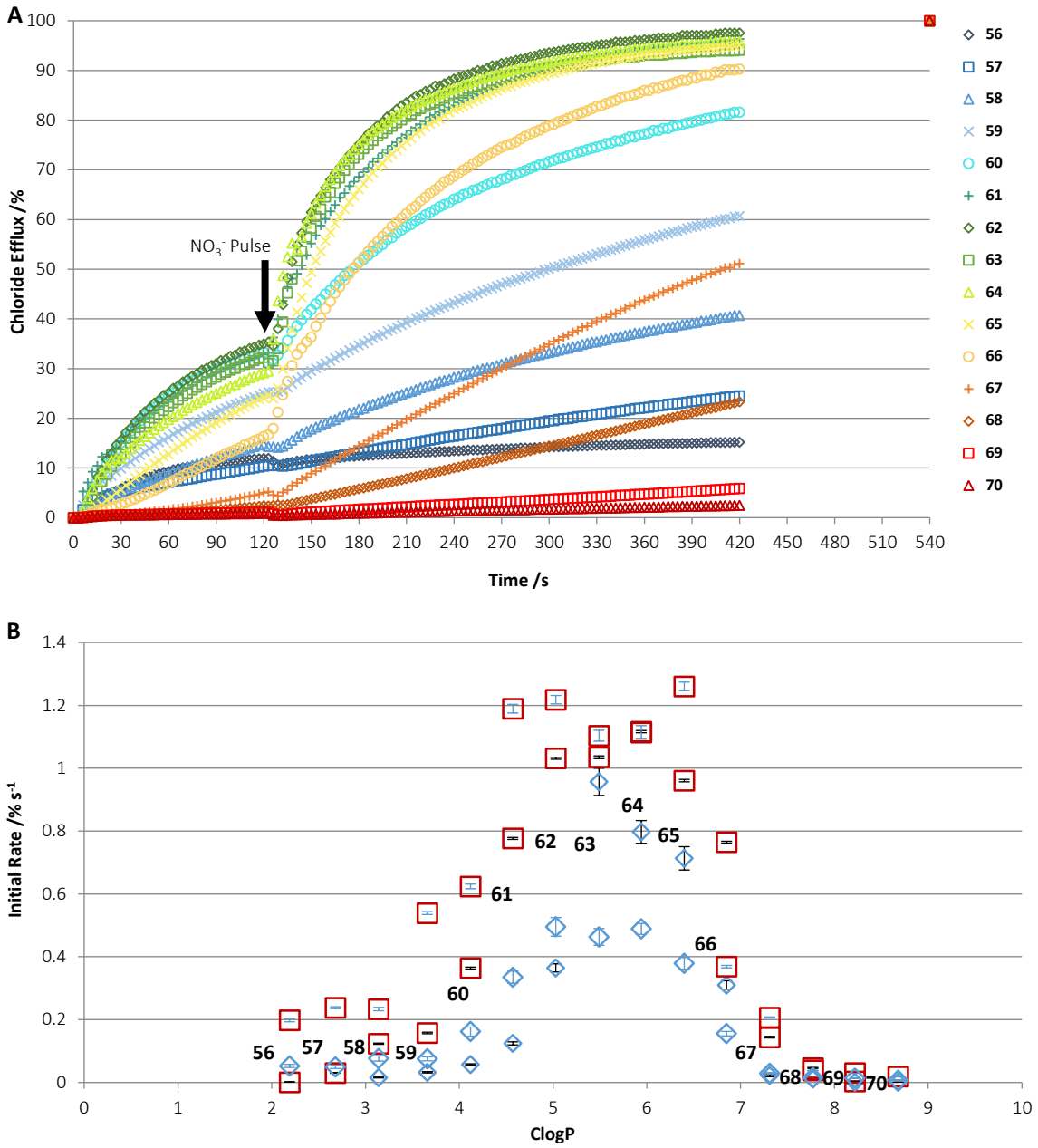


**Figure 2.16** **A**: Transport curves for 3:1 POPE:POPC vesicles over time for **56** - **70** in $SO_4^{2-}/NO_3^-$ spike experiments. **B**: Initial rate of chloride transport after $NO_3^-$ addition. Blue diamonds - $Cl^-/NO_3^-$ trials. Red squares – $SO_4^{2-}/NO_3^-$ spike trials. Faded points are standard $Cl^-/NO_3^-$ trials given for comparison. Each point in all plots represents the average of 3 trials.

The $SO_4^{2-}/NO_3^-$ spike experiments were also conducted for POPE (Figure 2.16). The trends observed were broadly the same as observed previously, however up to 30% chloride efflux was observed before nitrate addition for the most active compounds. Further assays were conducted to determine the mechanism of the observed transport, the results of which are appended (Appendix III.1.3).

No evidence of $SO_4^{2-}$ transport was observed, nor was there any leakage from the vesicles. A slight counter cation dependence was observed however, suggesting a contribution of MCl co-transport. Slight de-acidification of the vesicle was also observed in a HPTS pH assay, suggesting a small

component of HCl transport (or functionally equivalent $OH^-/Cl^-$ antiport, although these small transporters are unlikely to be able to dehydrate $OH^-$). These two mechanisms may explain the effect seen in this system accounting for the additional efflux seen before nitrate addition. It is possible that the PE head groups are more porous to protons and cations due to the extra free space available, hence the effect is only seen in this system.

### 2.5.5 DPPC Vesicles

Finally, the transport rate was assayed in 100 % DPPC vesicles. DPPC has the same structure as POPC, with the replacement of the unsaturated oelyl tail with a fully saturated palmitoyl tail. Due to the higher transition temperature of DPPC[118], vesicle synthesis and transport experiments were carried out at 55°C and a new baseline for POPC obtained.

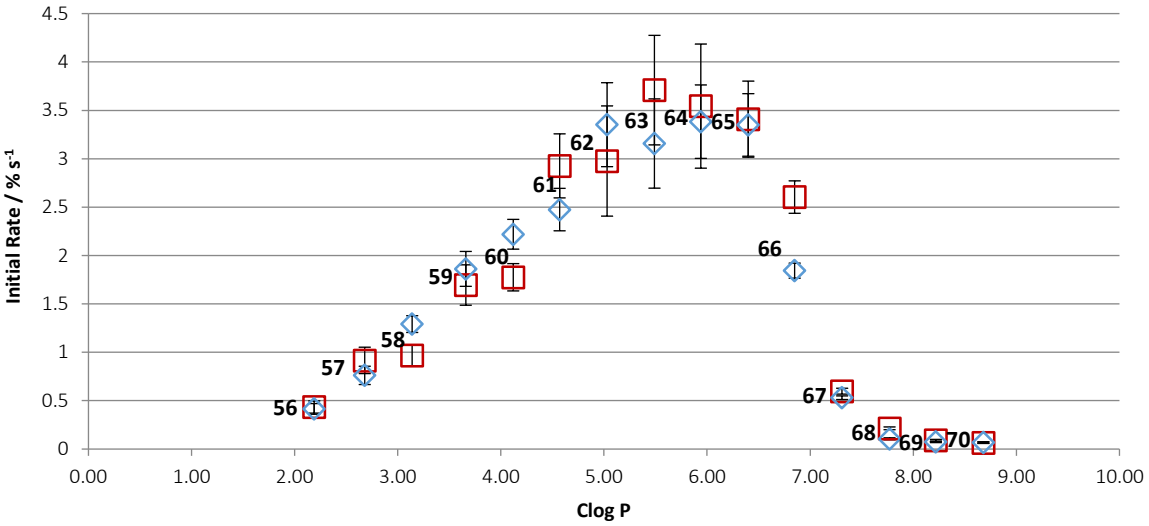


**Figure 2.17** Initial rate of chloride transport at 55°C for **56** - **70**, plotted against transporter Clog P. Blue diamonds – 100% POPC. Red squares – 100 % DPPC. Each point in all plots represents the average of 3 trials.

The transport rate appeared unaffected by the increased saturation in the tail group region, with most points remaining within error of each other on both systems. This further suggests that for these compounds, the rate-determining step is not diffusion across the tail region, hence differing results seen when varying the lipid head group.

## 2.6 Conclusions

These results have shown that the lipophilicity of a transporter does not influence the relative effect of differing lipid environments on the transport rate in vesicle models. The ideal range of lipophilicity for a transporter series does not appear to change in the different systems tested. Crucially this means that compounds optimised for lipophilicity in one series should remain the most active of a series across lipid systems.

Lipophilicity remains a vital indicator which should be tuned to achieve maximum efficacy from a series of anionophores. The lipid environment clearly has an effect on the absolute rate of transport, but from this series of compounds it appears that the relative order of efficacy is retained. Specific interactions in the membrane seem to determine the rate-determining step of transport. Currently, it is difficult to predict whether a compound will show an increase or decrease in transport activity in different bilayers, and a deeper understanding of what transporter features will be important for future transporter design.

In addition to other reported examples[65, 115], these results also show that the 'Cholesterol Test' is not a reliable method for demonstrating a mobile carrier mechanism. It's clear that not all transporters are rate-limited by tail group diffusion, hence the logic of this test does not hold. Using the u-tube method showing transport of anions through an organic layer that is far too large for channel formation would be more useful for this purpose.

# 3 Transporter Synthesis *in situ* by Dynamic Covalent Chemistry

Compounds **73** - **86** were synthesised by Ethan Howe in as yet unpublished results, $^{1}$H NMR spectra are appended for reference. DCC transport fluorescence experiments were carried out by project student Anna Tassie and anion binding data was obtained by project student Alice Moysiadi.

## 3.1 Introduction

The deliverability of synthetic anion carriers is a significant barrier to their eventual application as therapeutics. By their very nature, carriers have to be lipophilic in order to partition into the lipid bilayer. This clearly compromises their solubility in water and makes it difficult to achieve 'drug-likeness', for example in accordance with Lipinski's rule of 5[95].

Davis, Sheppard and co-workers considered the deliverability of large lipophilic cholapod and decalin-based anionophores whilst developing an assay for measuring chloride efflux directly in cell epithelia[92]. The compounds were graded A-D based on the difference in activity between pre-incorporating the compounds in the membrane in vesicle transport studies and their delivery externally as a methanol solution. A-graded compounds showed little to no difference in the two methods, whilst D-graded compounds showed more than 5 times decrease in initial rate. When assayed in cells (with compounds introduced into the extracellular medium), it was those compounds that scored highest for deliverability that performed the best.

This inherent disparity between the molecular properties required to be a highly active transporter and those required to be a potent drug candidate provides an incentive to explore novel methods of introducing a synthetic anionophore into a target membrane. One such method could be a dynamic approach to forming a transporter *in situ*.

Dynamic covalent chemistry has already been applied in anion transport by the use of a squaramide and an electrophilic aldehyde to bind zwitterionic amino acids[87] (see Scheme 1.3). In this case, the aldehyde formed a dynamic covalent bond with the terminal $NH_3^+$, forming a hemiaminal and shielding the positive charge on the amino acid, whilst the squaramide bound the carboxylate to shield the negative charge.

The approach in this work was to use a dynamic covalent reaction to synthesise an active transport molecule within the membrane itself. The aim was to show that it was possible to initiate transport by the addition of two precursors to the transporter to the extra-vesiclular solution, which would then diffuse into the membrane, react to form the anionophore which could then bind and transport chloride. This method could open up new pathways for designing anionophores which could be produced *in situ* from components that are far more drug-like than the active compound.

It could also allow the design of combinatorial libraries of precursors, as has been demonstrated previously[119] for the design of novel transport compounds.

Dynamic covalent systems are under thermodynamic control, favouring the formation of the most stable product[120]. For this to be the case, the formation of the covalent bond must be reversible, and often a catalyst is required to ensure equilibrium is reached fast enough. The product distribution is sensitive to all manner of external factors such as temperature, pressure, concentration and other components in the system. If a target site is used for selection, the product with the best (or most stable) binding or recognition is generally favoured[120, 121].

Phenythiosemicarbazones are a class of pH-switchable electroneutral anionophores[89]. They are strict HCl symporters, the same transport mechanism of the natural anionophore prodigiosin (**1**). Their pH-switchable behaviour originates from a conformation change on protonation of the imine nitrogen, breaking an intramolecular hydrogen bond between the aryl thioureas N-H and the imine nitrogen (Figure 3.1). Compound **73** has the highest switchability of the compounds at the pHs tested, as the $pK_a$ of the conjugate acid form is the highest of the series, thus a higher proportion of the molecules will be protonated at pH 4.0.

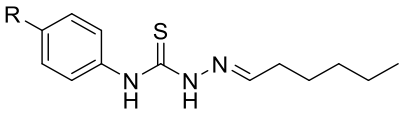

| Compound | R | $EC_{50}$ pH 4.0 /mol % | $EC_{50}$ pH 7.2 /mol % | pH 7.2 / 4.0 Ratio |
|---|---|---|---|---|
| **71** | $-CF_3$ | 0.13 | >>10 | >>77 |
| **72** | $-OCH_3$ | 0.0073 | 1.8 | 250 |
| **73** | -H | 0.0074 | 4.7 | 640 |

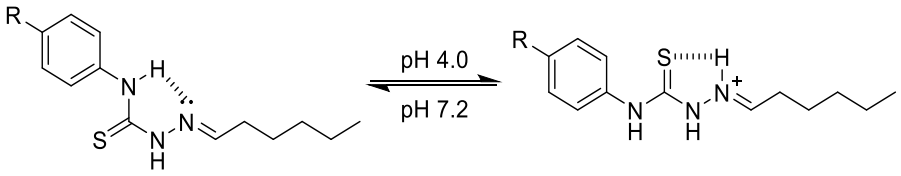


**Figure 3.1** General structure of previously published[89] thiosemicarbazone anion transporters, their $EC_{50}$ value for $Cl^-/NO_3^-$ exchange at pH 4.0 & 7.2 and the conformation switch upon protonation.

The imine moiety in the thiosemicarbazone structure makes it good candidate scaffold to use for production of an active anion transporter *in situ* using DCC, due to the reversible nature of the imine bond formation[120]. The system's pH switchability, which could aid its selectivity for acidic cellular compartments[89], the de-acidification of which has been linked to causing cell death in cancer stem cells[122], also makes it an interesting system for further study.

## 3.2 Thiosemicarbazone Series

A series of thiosemicarbazones was designed to test whether it was possible to form an active anion carrier *in situ* using DCC. A range of 14 compounds was designed (Figure 3.2) to test the how varying substituents on the imine moiety affected the transport rate, interesting as it was known that the $pK_b$ of the imine N determined the transport activity of the previously reported compounds[89]. This also meant that the precursors for the DCC reaction were a wide variety of alkyl and aromatic aldehydes, hence a study of the influence of this reagent on the reaction in the transport experiments was possible.

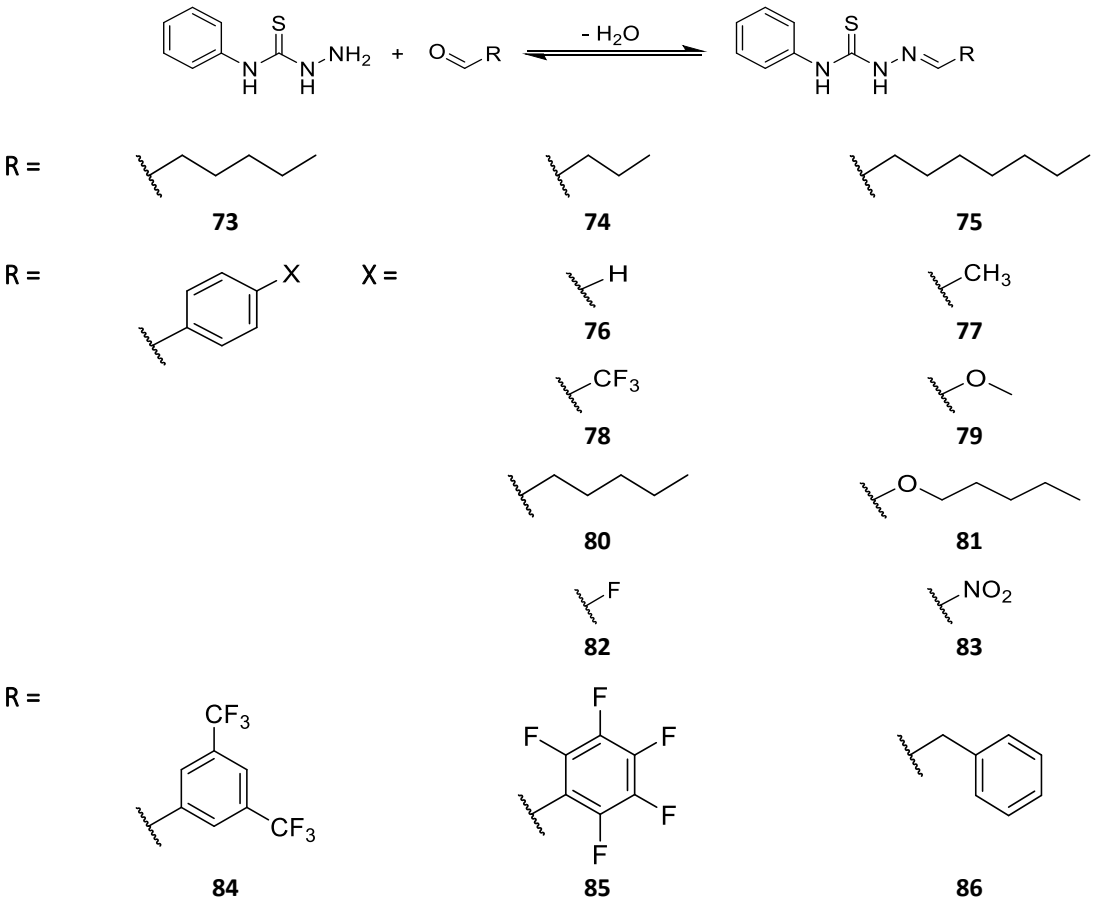


**Figure 3.2** Scheme of the DCC reaction, and structures of the preformed thiosemicarbazone series.

Pre-formed compounds **73** - **86** were synthesised by the previously reported method[89]. N-Phenyl thiosemicarbazide was reacted with the appropriate aldehyde in absolute ethanol under nitrogen atmosphere overnight. The compounds could be obtained after recrystallization from the evaporated reaction mixture and were stored at -20° under $N_2$ to minimise hydrolysis of the product.

The $pK_b$ of the compounds was calculated using the JChem plugin for Marvin[123]. As expected, the alkyl compounds **73** - **75** had the highest $pK_b$ of the series of 3.1. A phenyl substituent lowered the

$pK_b$ to 2.6 and the substituents on the ring increased or decreased the $pK_b$ as would be expected based on the electron withdrawing or donating characteristics of the substituent, with the bis-$CF_3$ and $C_6F_5$ compounds **84** & **85** being the least basic of the compounds by a large margin ($pK_b$s of 0.8 and -1.2 respectively). Adding the methylene space between the phenyl ring and the imine group in **86** reduced the electron-withdrawing influence of the ring to some degree, given this compound has a $pK_b$ of 2.8, directly between the phenyl and alkyl variants.

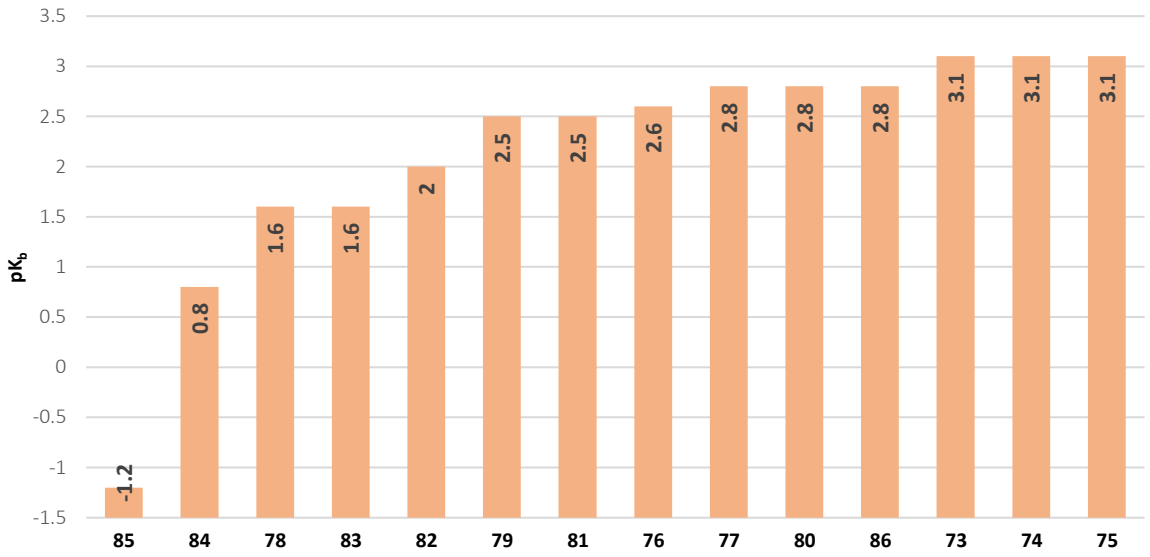


**Figure 3.3** Calculated $pK_b$ values for compounds **73** - **86** from the JChem plugin for Marvin[123].

## 3.3 Anion Transport

To enable evaluation of the transport performance of the compounds being formed by DCC, the transport ability of the preformed compounds was quantified. The transport rate was quantified by a $Cl^-/NO_3^-$ exchange assay.

POPC vesicles were synthesised containing 486 mM NaCl, suspended in a solution of 486 mM $NaNO_3$. The internal and external solutions were buffered to pH 4.5 using 5 mM citrate buffers. A low was required to ensure protonation of the thiosemicarbazones to promote their transport activity; pH 4.5 was chosen in particular as it was the lowest pH at which stable vesicles which did not leak the fluorophores required for future assays (section 3.5) could be made.

Samples were equipped with a chloride-selective ion selective electrode (ISE) to monitor the $Cl^-$ concentration in the external solution. This allowed the recording of the efflux of $Cl^-$ over time after the addition of the test compound as a solution in DMSO. After 5 minutes, the vesicles were lysed with detergent (Triton X-100, 1 g in 8 ml 7:1 water:DMSO) to calibrate to 100 % efflux. All experiments were run in triplicate the results averaged.

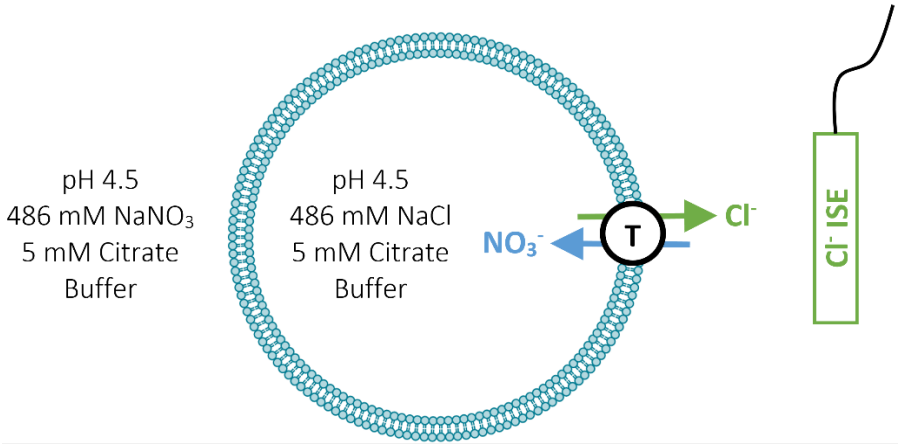


**Figure 3.4** Schematic showing the setup of the $Cl^-/NO_3^-$ ISE experiments. T = the anionophore being tested.

To aid comparison of the anionophores' activity, Hill Plots were obtained to fully quantify transport activity. Transport experiments were run using at least 6 concentrations of transporter. The Hill equation (3) was first proposed by A. V. Hill in 1913 who used it to model the saturation of haemoglobin with oxygen and carbon monoxide[52]. The model has since been widely adopted to describe the self-assembly or supramolecules[53] and for dose-response modelling in pharmacological applications[54].

$$y = \frac{V_{max}[x]^n}{\mathrm{k^n} + x^n} \tag{3}$$

$$EC_{50} = \sqrt[-n]{\frac{-k^{-n}(50 - V_{max})}{50}} \tag{4}$$

Where $V_{max}$ = maximum transporter response ($y_{max}$), n = Hill coefficient, k = concentration of anionophore were y is half of $V_{max}$, x = concentration of anionophore, y = chloride efflux.

A sample Hill plot of compound **74** is given in Figure 3.5. $Cl^-$ efflux curves were obtained at different loadings to ensure a range of values at 270 s was recorded, from ~10 % to ~100 % efflux. This provided sufficient detail for fitting of the data to the Hill equation (Figure 3.5B). The values from the Hill fits are tabulated in Table 3.1. For most compounds, $V_{max}$ was fixed to 100 for the fitting, hence the value of k was equal to the $EC_{50}$. For compounds that did not reach 100 %, $V_{max}$ was allowed to vary and the rearrangement (4) was used to calculate the $EC_{50}$ (see appended individual plots in Appendix III.2.1).

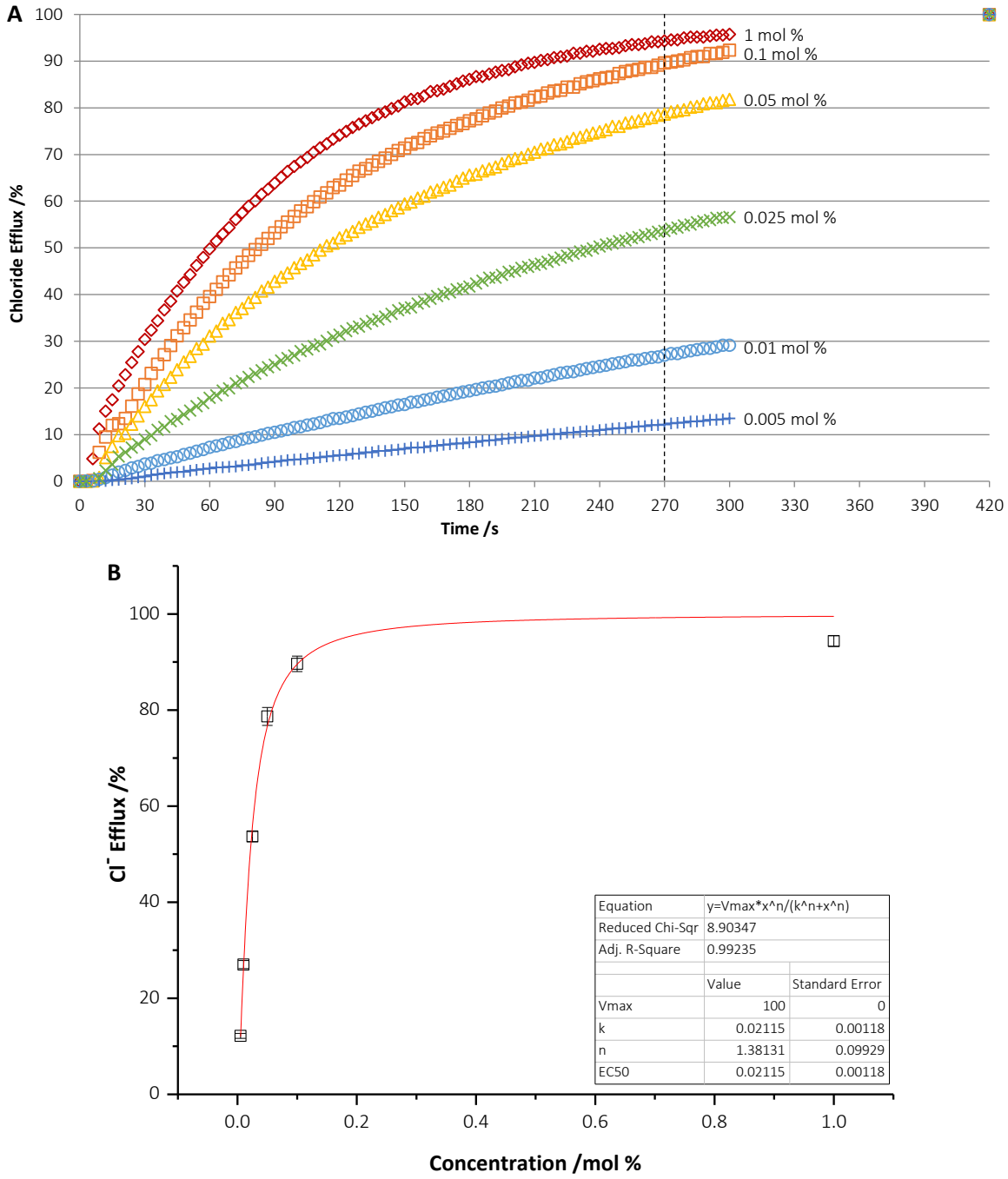


**Figure 3.5** **A**: Plot of the transport curves ($Cl^-$ efflux over time) obtained at various loading concentrations of compound **74** (given in mol % wrt. lipid). Dashed line indicates values at 270 s. **B**: Fitted curve (red) from the fitting of the values of $Cl^-$ efflux at 270 s from **A**, plotted against concentration of **74**. Numerical results of fitting to the Hill equation (4) are given in the table.

| Compound | Substituent | $EC_{50\,(270\,s)}$ /mol % | Hill Coeff. (n) |
|---|---|---|---|
| **73** | n-hexyl | 0.00746 | 1.31 |
| **74** | n-butyl | 0.0212 | 1.38 |
| **75** | n-octyl | 0.00889 | 1.34 |
| **76** | phenyl | 0.0182 | 1.02 |
| **77** | p-Me | 0.00818 | 1.37 |
| **78** | p-$CF_3$ | 0.640 | 0.64 |
| **79** | p-OMe | 0.0386 | 1.32 |
| **80** | p-nPe | 0.0200 | 1.46 |
| **81** | p-nOPe | 0.0561 | 1.63 |
| **82** | p-F | 0.0794 | 0.52 |
| **83** | p-$NO_2$ | N/A[a] | N/A[a] |
| **84** | bis-$CF_3$ | 0.442 | 1.01 |
| **85** | $C_6F_5$ | 0.0749 | 1.08 |
| **86** | benzyl | 0.0683 | 0.99 |

**Table 3.1** $EC_{50\,(270\,s)}$ and Hill Coefficient values for compounds **73** - **86** from $Cl^-/NO_3^-$ exchange ISE assays. [a]Compound **83** was too inactive to allow Hill analysis.

The $EC_{50\,(270\,s)}$ values for the compounds spanned 3 orders of magnitude, indicating a wide range of activity. Alkyl compounds **73** - **75** were among the best performing compounds. Hexyl substituted **73** was fastest with a marginally lower $EC_{50}$ than n-octyl **75** and more than two-fold improvement over n-butyl **74**, suggesting the n-hexyl chain affords a good balance in chain length and lipophilicity. Calculated log P values from the ALOGPs model[105, 107] suggest this the case (**73**: 4.45, **74**: 3.60, **75**: 5.23) and are in line with optimal log P ranges discussed previously (Chapter 2).

Compound **83** was too inactive to allow Hill analysis as 100 % efflux could not be achieved with loadings less than 10 mol %. For the other aryl analogues it appeared that compounds with more electron donating substituents had lower $EC_{50}$s than those with electron withdrawing substituents; for instance methyl **77** is two orders of magnitude more active than $CF_3$ substituted **78**. The electron-withdrawing nature of the substituent has a large impact on the $pK_b$ of the imine N, hence the relationship between the $pK_b$ and $EC_{50}$ was explored (Figure 3.6).

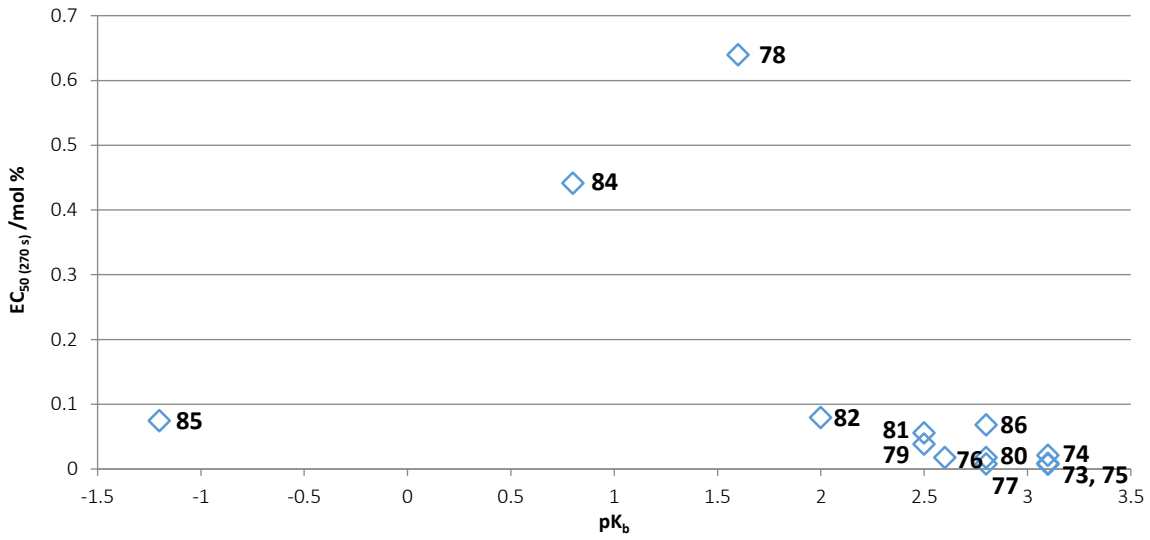


**Figure 3.6** Comparison of the calculated $pK_a$ of compounds **73** - **86** and their $EC_{50\,(270\,s)}$ from $Cl^-/NO_3^-$ exchange assays.

Figure 3.6 clearly shows the correlation between the basicity of the imine nitrogen and the transport activity of the thiosemicarbazones. The higher the $pK_b$ of the compound, the greater proportion of the compound that will be protonated at pH 4.5 and thus the greater proportion of the molecules that will be in the switched-on, protonated conformation to facilitate the transport process.

Between compounds of a similar $pK_b$, the compounds' lipophilicity appears to govern the relative activity of the compound. Compounds **73** - **75** have been discussed above, and the same trend can be observed with **77**, **80** & **86** for example. Benzyl **86** is much less lipophilic (Clog P 4.07, Table 3.2) hence is much less active than both n-pentyl **80** (5.52) and closest to the 'ideal' range methyl **77** (3.99).

Two notable exceptions to the apparent trend visible in Figure 3.6; compounds **84** & **85** are much more active than simple correlation with their $pK_b$ might suggest. This can be rationalised by looking at the anion binding strength of the neutral thiosemicarbazone species (Table 3.2). Binding constants were obtained by NMR titration of the compounds in $CD_3CN$. The binding mode of the thiosemicarbazones in the neutral state clearly involves a shift in a thiourea N-H and the imine C-H; a sample stack plot is shown in (Figure 3.7). These shifts could be fitted to a 1:1 binding model using BindFit v0.5[124, 125].

Bis-$CF_3$ compound **84** & $C_6F_5$ **85** are significantly stronger anion binders than the remainder of the series (constants of 24.0 and 48.6 $M^{-1}$ respectively in comparison to 12.5 $M^{-1}$ for phenyl compound **76** in the neutral state). Therefore, these compounds would be able to bind and transport $Cl^-$ in their neutral form without a protonation event, hence the $pK_b$ dependence is lost for these

compounds. It should also be noted that $NO_2$ compound **83** also has a high binding constant of 27 $M^{-1}$; the zwitterionic nature of the $NO_2$ group however makes the anionophore too polar hence its partitioning into the tail region of the membrane is disfavoured.

| Compound | Substituent | Binding Constant /$M^{-1}$ | Clog P (ALOGPs) |
|---|---|---|---|
| **73** | n-hexyl | 8.2 | 4.45 |
| **74** | n-butyl | 8.3 | 3.60 |
| **75** | n-octyl | 8.3 | 5.23 |
| **76** | phenyl | 12.5 | 3.68 |
| **77** | p-Me | 11.5 | 3.99 |
| **78** | p-$CF_3$ | 23.6 | 4.49 |
| **79** | p-OMe | 11.4 | 3.77 |
| **80** | p-nPe | 11.5 | 5.52 |
| **81** | p-nOPe | 9.6 | 5.24 |
| **82** | p-F | 15.5 | 3.85 |
| **83** | p-$NO_2$ | 27.0 | 3.79 |
| **84** | bis-$CF_3$ | 24.0 | 4.71 |
| **85** | $C_6F_5$ | 48.6 | 3.96 |
| **86** | benzyl | 12.1 | 4.07 |

**Table 3.2** Anion binding constants and calculated log P values for compounds **73** - **86**. Binding constants obtained by NMR titration with TBACl in $CD_3CN$ and fitting of the shift in imine C-H and thiourea N-H to a 1:1 binding model with BindFit v0.5[124, 125]. Clog P values calculated by the ALOGPs applet[105, 107].

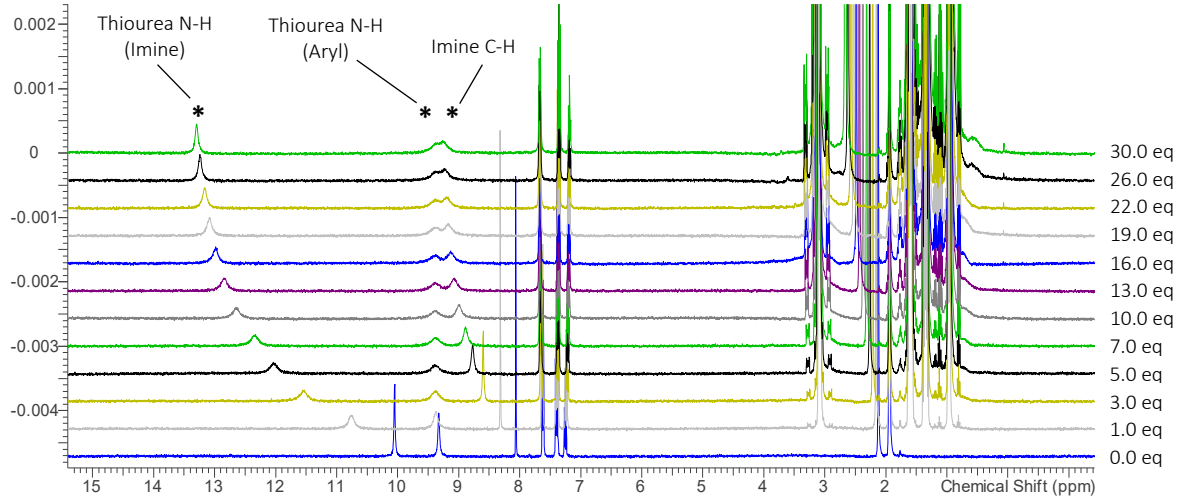


**Figure 3.7** Stack plot showing $^1H$ NMR (400 MHz, $CD_3CN$) titration of **85** with TBA Cl.

Further information on the transport process is given by the Hill coefficient (n). This value is correlated to the stoichiometry of the binding event, value close to 1 indicate a 1:1 binding event[53, 126]. Almost all of the compounds have n equal or slightly greater than 1. Many of the compounds that are $pK_b$ dependent have $1.3 < n < 1.6$. This might suggest a higher stoichiometry in the transport event, however the same effect would be seen by a proportion of the molecules not taking part in the binding and transport; this would be expected given a proportion of the

molecules will be deprotonated thus unable to transport. It is interesting that compounds **84** & **85** have Hill coefficients that are almost exactly 1, suggesting a 1:1 transport stoichiometry and further evidence that these compounds are not pKb dependent. Note that compounds **78** & **82** give hill coefficients of less than 1 (n = 0.64 & 0.52 respectively); this an artefact of the fitting for these compounds whose activity plateaued at less than 100 % efflux at high loadings(see Hill Plots in Appendix III.2.1), likely due to aggregation at high concentrations.

## 3.4 DCC Product Formation Rate

The rate of the formation of the thiosemicarbazones by DCC was monitored by $^1$H NMR spectroscopy. A 20 mM solutions of phenylthiosemicarbazide and the appropriate aldehyde in $CDCl_3$ were combined in an NMR tube (such that the final concentration of each component was 10 mM immediately before loading into the NMR spectrometer. The $^1$H NMR spectrum of the mixture was collected every 60 seconds for 1 hour.

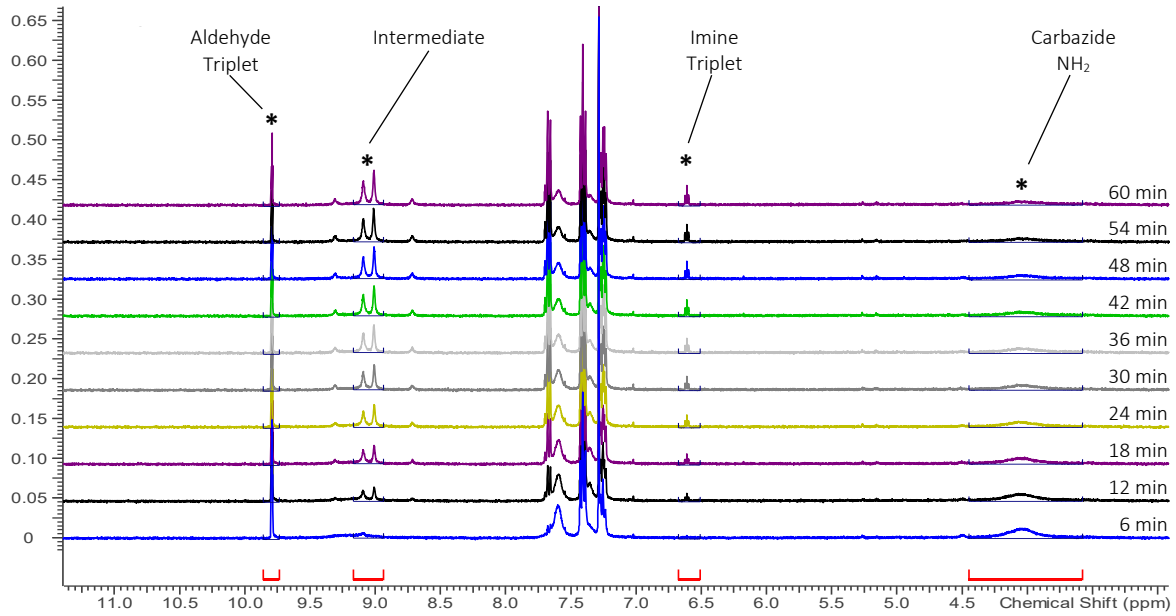


**Figure 3.8** Stack plot of partial $^1$H (400 MHz, $CDCl_3$) spectra showing the formation of **73** over 60 minutes from phenylthiosemicarbazide and hexanal.

The experiments showed different behaviour between the reactions with aliphatic and aromatic aldehydes. The stack plot showing the formation of **73** over time is shown in Figure 3.8. The evolution of the triplet from the imine moiety is visible at δ = ~6.6 ppm. Consumption of the aldehyde (δ = ~9.6 ppm) and starting carbazide (δ = ~4.1 ppm) can also be observed.

The evolution of a signal at δ = ~9.1 ppm can also be observed. This is attributed to the formation of hemiaminal intermediate after the addition of the thiosemicarbazide to the aldehyde. Elimination of water then leads to the final product. It appears for the aliphatic aldehydes that this elimination is a slow step, hence a large proportion of the hemiaminal is visible in the experiments.

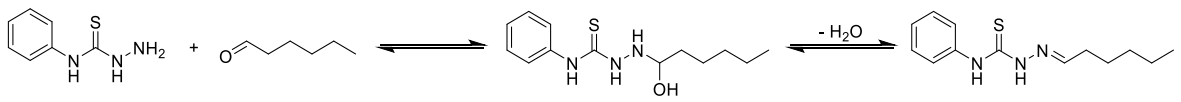


**Scheme 3.1** The two stages of the DCC reaction for aliphatic aldehydes, showing addition of the thiosemicarbazide to aldehyde, then the slow elimination of water to form the product.

The signals were integrated with respect to a fixed signal in the data (in this case the hexyl $CH_3$ protons, unaffected by the DCC reaction) and scaled for the number of nuclei corresponding to the signal. This gave a relative integral, equivalent to the fraction of each component consumed/converted. The kinetic data for the formation of **73** are plotted in Figure 3.9.

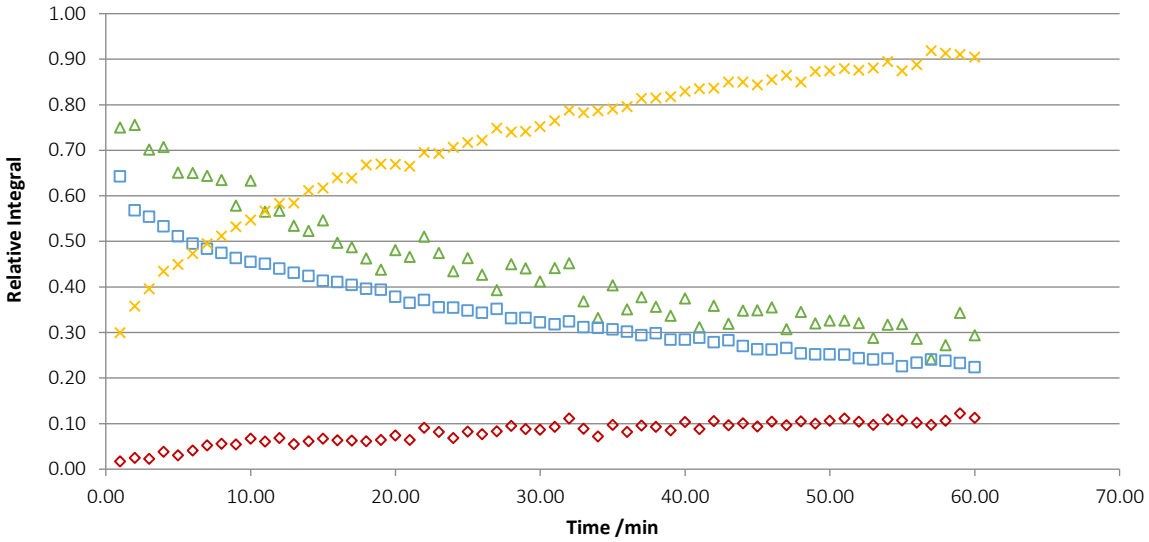


**Figure 3.9** Plot showing the fraction conversion (measured by relative integral) of the starting aldehyde (blue squares) and phenylthiosemicarbazide (green triangles) to hemiaminal intermediate (yellow crosses) and thiosemicarbazone product (red diamonds) for the formation of **73** by DCC over 1 hour.

Interestingly, the experiment showed that the vast majority of reacted aldehyde was converted to intermediate over the course of 1 hour, with only approx. 10 % conversion to final product. This might be expected using chloroform as the solvent, which would disfavour the elimination of water and have few acidic protons to assist the elimination step.

The evolution of the intermediate was observed for all the aliphatic compounds **73** - **75**. In contrast, the intermediate for all the aromatic aldehydes was not evident. It can be inferred from this that addition of the carbazide to the aldehyde is the limiting step in the reaction, as might be expected considering the mesomeric effects of the aromatic ring on the reactivity of the carbonyl.

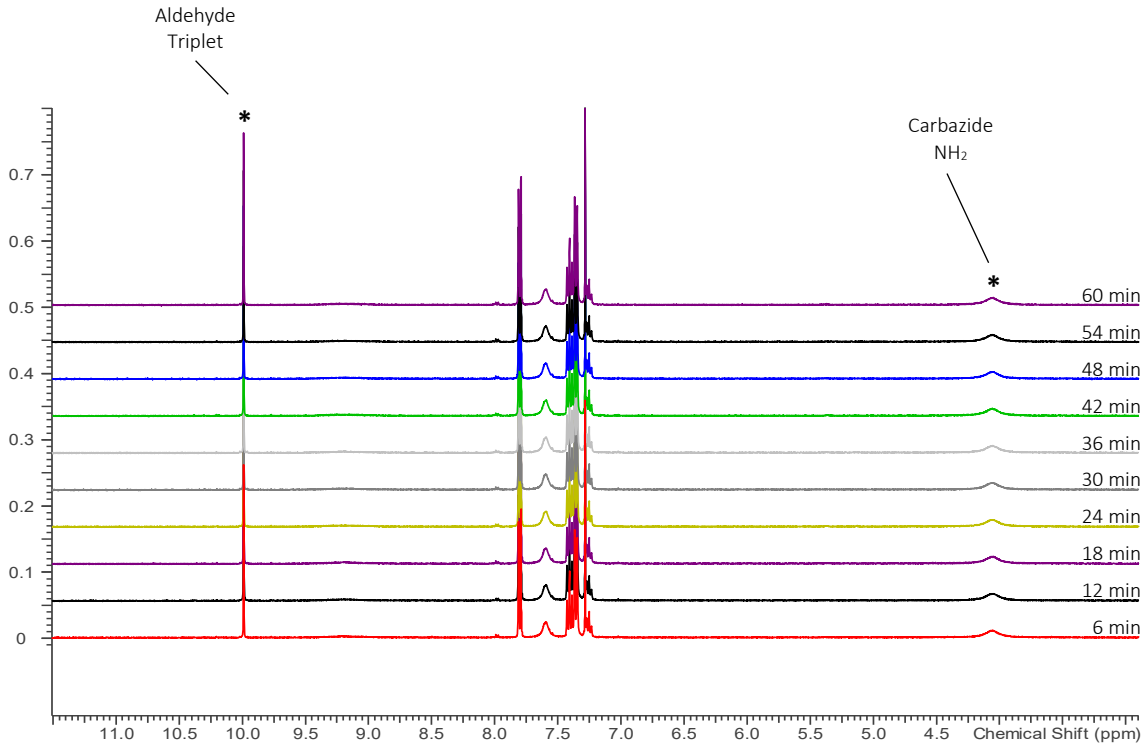


**Figure 3.10** Stack plot of partial $^{1}$H NMR (400 MHz, $CDCl_3$) spectra showing the formation of **77** over 60 minutes from phenylthiosemicarbazide and p-tolyaldehyde.

In almost all cases with the aromatic aldehydes, the evolution of the imine peak was either not detected within the hour of the experiment (Figure 3.10) or the location of the peak overlapped with peaks in the aromatic region of the spectrum. To quantify the progress of the reaction across the whole series, the % consumption of the aldehyde after 1 hour was calculated using the relative integral as before, as the most consistent method of measuring this across the series. These data are presented in Table 3.3. Where is was possible to observe the evolution of the product, these data are also presented.

| Compound | Substituent | % Aldehyde Consumption | % Product Evolution |
|---|---|---|---|
| **73** | hexyl | 78 | 11 |
| **74** | butyl | 36 | -[b] |
| **75** | octyl | 67 | 35 |
| **76** | phenyl | 0 | -[b] |
| **77** | p-Me | 2 | -[b] |
| **78** | p-$CF_3$ | 11 | 9 |
| **79** | p-OMe | -[a] | 27 |
| **80** | p-nPe | 23 | -[b] |
| **81** | p-nOPe | 0 | -[b] |
| **82** | p-F | 0 | -[b] |
| **83** | p-$NO_2$ | 0 | -[b] |
| **84** | bis-$CF_3$ | 10 | -[b] |
| **85** | $C_6F_5$ | 0 | -[b] |
| **86** | benzyl | 25 | -[a] |

**Table 3.3** Data for the consumption of aldehyde starting material in DCC reactions, from relative integral data from $^1$H (400 MHz, $CDCl_3$) experiments. [a]N/A due to peaks overlapping. [b]Product evolution not observed.

Only for the formation of compound **79** from anisaldehyde was the aldehyde peak overlapping sufficiently to prevent its accurate integration. Fortunately this was one of the few compounds for which the generation of the imine signal was clearly observable; allowing the calculation of 27 % conversion to product after 60 minutes, making it the fastest reaction of the series (cf. 9 % product evolution for **78**, after 11 % aldehyde consumption.

Good results are also observed for pentyl compound **80**. Although having electron donating effects would likely decrease the electrophilicity of the aldehyde, it is probably that they accelerate the dehydration of the hemiaminal in the second step, hence the good response seen here.

For the other aromatic aldehydes, the electron-withdrawing **78** & **84** show a significant level of aldehyde consumption. This is likely because the electron withdrawing effect makes the aldehyde more susceptible to nucleophilic attack. For the most electron poor-aromatic aldehydes **84** & **85**, no consumption of aldehyde is observed after 60 minutes, it is possible that the electron withdrawing effects of these compounds is too great, and disfavours the fast second step of the reaction (dehydration of the hemiaminal to form the imine).

Benzyl compound **86** again shows activity more similar the alkyl compounds, giving 25 % consumption after 60 minutes, compared to no reaction for the phenyl **76**. Evidently again, the methylene spacer is successful in shielding the aldehyde/imine form the electron withdrawing effects of the ring.

Looking at the consumption of the aldehyde gives a good indication of the rate of the DCC reaction, which allows interesting comparisons with the rate of transport in DCC experiments discussed

below (section 3.5). There are clearly limitations however due to lack of information on the formation of the product. Further experiments in different solvents are in progress (section 3.6).

## 3.5 DCC Assays in Vesicles

Attempts were made to use the same assay as used in section 3.3 to detect transport by a thiosemicarbazone formed *in situ* by DCC. From some initial data however, it was found not to be possible due to very large background $Cl^-$ efflux, which appeared after the addition of the phenylthiosemicarbazide component. The experiment was repeated with vesicles containing internal and suspended in external $NaNO_3$. In this case no transport should have been possible. Changes in the readings were however still registered on the electrode, which was concluded to stem from interference with the ISE phenylthiosemicarbazide. Ammonia and primary amines are known to be interferences for this brand of electrode[127], hence this is a feasible effect. Unfortunately, the interference was inconsistent and unpredictable, so attempts to quantify it and subtract it from the data were unsuccessful.

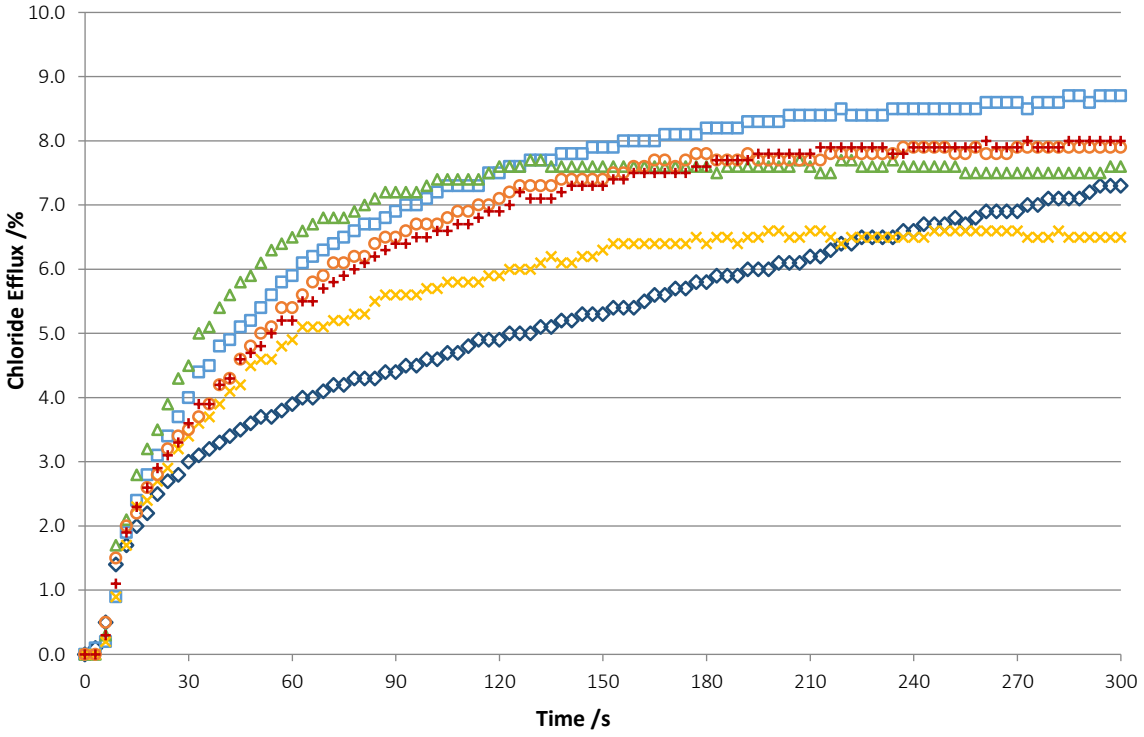


**Figure 3.11** Example plot of control ISE assays at pH 4.5 as section 0, using vesicles containing internal and external $NaNO_3$ using 1 % loading phenylthiosemicarbazide. Curves show 6 individual datasets to indicate in consistency of the interference.

As an alternative method, $Cl^-/NO_3^-$ exchange was measured using a fluorescence assay. Vesicles were loaded with 1 mm lucigenin dye and suspended in a solution of 238 mM $NaNO_3$. Internal & external solutions were buffered to pH 4.5 with 5 mM citrate buffers. Lucigenin is fluorophore with an excitation wavelength at 455 nm and an emission wavelength at 505 nm which is known to be quenched by halides[51]. The combination of reagents or anionophore to be tested was added as a

solution in DMF before initiation transport by a pulse of NaCl, bringing the final external concentration of NaCl to 60 mM.

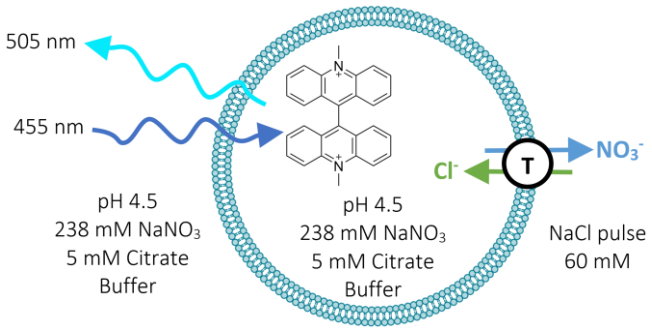


**Figure 3.12** Schematic showing the lucigenin assay. T = the anionophore/reagents being tested.

For each compound a curve for the preformed compound at 5 % loading and a DMF control were obtained. DCC runs were carried out by the addition of phenylthiosemicarbazide then the appropriate aldehyde to a final concentration of 5 mol % of each component. Two DCC curves were obtained, one initiating transport with an NaCl spike after 1 minute, the second with a 5 minute delay. Fluorescence of the sample in all cases was monitored for a total of 15 minutes. Sample fluorescence traces obtained for compound **73** are shown in Figure 3.13, runs were carried out in triplicate and averaged.

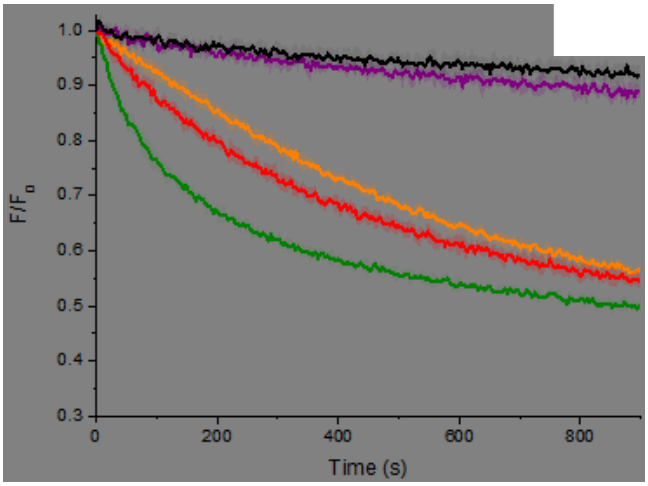


**Figure 3.13** Sample fluorescence trace for transport promoted by **73** in lucigenin experiments by the preformed compound (green trace) and by DCC from its phenylthiosemicarbazide and hexanal precursors after 1 minute (orange trace) and 5 minutes (red trace). Controls of DMF (black), hexanal (blue) and phenylthiosemicarbazide (purple) also shown.

The fluorescence intensity was normalised by dividing the starting intensity by the current intensity. The relationship between normalised intensity and the concentration of a quencher species if given by the Stern-Volmer equation (5) which has been exploited previously in quantifying anion transport in fluorescence assays[128].

$$\frac{F_0}{F} = 1 + \mathrm{k_q}\tau_0[Q] \quad (5)$$

Where F is the fluorescence intensity, $F_0$ is the starting intensity, $k_q$ is the rate coefficient, $\tau_0$ is the lifetime of the excited state, [Q] is the quencher concentration.

Equation (5) implies that the normalised fluorescence is directly proportional to the concentration of the quencher, in this case $Cl^-$. Hence the initial rate of $Cl^-$ transport can be quantified by the slope of the fluorescence traces. The curves were fitted to an exponential or double exponential function, which allowed calculation of the initial rate at time = 0 s. These data are shown in Table 3.1. The background decay from the DMF control was quantified by a linear fit and this rate subtracted for each curve.

| Compound | Substituent | % Aldehyde Cons. | % Product Form. | $EC_{50\,(270\,s)}$ /mol % | DCC-5 Init. Rate ($s^{-1}$) |
|---|---|---|---|---|---|
| **73** | n-hexyl | 78 | 11 | 0.00746 | $1.2 \times 10^{-3}$ |
| **74** | n-butyl | 36 | -[b] | 0.0212 | $2.7 \times 10^{-5}$ |
| **75** | n-octyl | 67 | 35 | 0.00889 | $1.6 \times 10^{-3}$ |
| **76** | phenyl | 0 | -[b] | 0.0182 | -[c] |
| **77** | p-Me | 2 | -[b] | 0.00818 | -[c] |
| **78** | p-$CF_3$ | 11 | 9 | 0.640 | -[c] |
| **79** | p-OMe | -[a] | 27 | 0.0386 | -[c] |
| **80** | p-nPe | 23 | -[b] | 0.0200 | $2.6 \times 10^{-4}$ |
| **81** | p-nOPe | 0 | -[b] | 0.0561 | $3.2 \times 10^{-5}$ |
| **82** | p-F | 0 | -[b] | 0.0794 | -[c] |
| **83** | p-$NO_2$ | 0 | -[b] | N/A[a] | -[c] |
| **84** | bis-$CF_3$ | 10 | -[b] | 0.442 | -[c] |
| **85** | $C_6F_5$ | 0 | -[b] | 0.0749 | -[c] |
| **86** | benzyl | 25 | -[a] | 0.0683 | $2.7 \times 10^{-5}$ |

**Table 3.4** Comparison of $Cl^-/NO_3^-$ exchange activity, rate of DCC reaction and rate of $Cl^-$ transport after 5 minutes of DCC compound generation *in situ* in vesicles. [a]N/A due to peaks overlapping. [b]Product evolution not observed. [c]No DCC transport observed.

Unsurprisingly, the DCC data shows clearly that for most compounds that showed no formation of product in the NMR experiments (**76**, **77**, **82**, **83**, **85**) no response was seen in the DCC experiment. The alkyl aldehydes performed well, with their DCC response seemingly correlating with the transport ability of the parent compound (**75** < **73** << **74**). This should not be too surprising given the rate of the DCC reaction appeared to be faster than for the aromatic aldehydes in the NMR experiments, implying the reaction is likely to be fast in the bilayer and thus the rate is more limited by transport rate.

For the aromatic aldehydes, some interesting, more subtle effects are observed. Interestingly, it is compounds **80** (n-pentyl) & **81** (n-pentoxy) that appear gave the best DCC response. This is despite no product being evident in the NMR assays. Methoxy compound **79**, despite appearing to give the

highest yield of product in the NMR experiment, also gave no response in the DCC assay. This is despite being electronically very similar (Hammet constant $\sigma_p$ = -0.27 for –OMe, $\sigma_p$ = -0.37 for -OPe[83]) and having an $EC_{50}$ of the same order of magnitude as **81**. It would appear that the membrane itself may be helping catalyse the DCC reaction, and the long chains on p-pentyl and p-pentoxy benzadehydes would greatly increase their affinity for the membrane (cf. Clog P = 1.64 for p-methoxybenzaldehyde, 3.49 for p-pentoxybenzaldehyde[105, 107]).

Compounds **78** & **84** were the only other aromatic aldehydes for which any DCC reaction was observed in the NMR, however for these compounds no transport was observed over the 15 minutes of the experiment. It is worth noting that the preformed versions of compounds have some of the lowest $EC_{50}$ values from the ISE experiments, for reasons discussed above. It should be noted that the slowest initial rate observed in the DCC experiments was that of **74** ($2.7 \times 10^{-5}$), which was of the same order of magnitude as the background quenching from the DMF control. The $EC_{50}$ of both **78** & **84** are an order of magnitude lower than **74**, therefore it is unlikely that DCC-initiated transport in this system would be observed even if conversion of precursors to active compound was very high.

## 3.6 Conclusions

It has been demonstrated in this work that it is possible to use dynamic covalent chemistry to form an active transporter molecule *in situ* in the membrane. It is clear that a condensation type reaction can work well in this case, as these reactions seem to be favoured within the membrane.

It has been shown that both a high level of transporter activity and a high rate of reaction are required to elicit a good DCC response, evidence by compounds **78** & **84** which form quickly but are slow transporters, and **77** which has a low $EC_{50}$ its formation kinetics are slow. It is an interesting point to note that in this series, the phenyl substituents that give transport rates (electron donating substituents to raise transporter $pK_b$) are those that would slow formation rate by the same effects.

This may be an inherent weakness in the thiosemicarbazone system, although it appears possible that a good balance can be struck (given the good DCC responses and pre-formed transport rates for the alkyl compounds). It is possible that exploring a system that does not require protonation to carry out transport could be found to mitigate this effect, but the utility of the thiosemicarbazones pH selectivity would be lost.

Although the rate of aldehyde consumption was a useful indicator of DCC reaction rate there is scope to obtain better experimental detail of the kinetics of the reaction. For example using an excess of one reagent can be used to give pseudo-first order conditions and obtain information on the substituent effects of one of the reagents in similar reactions[129]. These experiments are currently underway, using an excess of phenylthiosemicarbazide to determine the pseudo-first order kinetics with respect to the aldehyde in acetonitrile.

Currently work is also underway to better characterise the performance of this thiosemicarbazone series. To ensure that the maximum transport rate possible is being measured and quantified, valinomycin/monensin assays described by Wu et. al.[93] are being carried out to determine the electrogenic/electroneutral character of the transport process.

# 4 Fluorination, Partitioning and Transport Mechanism

Compounds **99**, **102** & **103** were synthesised by Xin Wu, **99** from previously reported work[93] and **102** & **103** from unpublished results. Biological results were obtained by Hongyu Li and David Sheppard at the University of Bristol.

## 4.1 Introduction

Fluorination of therapeutically active compounds is a common strategy in medicinal chemistry to modulate lipophilicity, acidity, conformation and other properties of the molecule, or to affect reactivity[130]. This could be in order to block unwanted side reactions or binding events or to improve pharmacokinetics and bioavailability, for example by better conforming to Lipinski's rule of 5[95, 130].

Clearly, the ability to modulate molecular properties such as lipophilicity with small structural changes is desirable in trans-membrane transport. The effect of fluorination has been explored previously. The structure-activity relationship of fluorination of phenyl-substituted tren-based receptors (**87**- **91**) has previously been investigated, with the increased activity in the fluorinated derivatives attributed to the increase in lipophilicity (measured by Clog P)[91]. Other studies considering fluorination of diureido decalins (**92** - **94**) found a similar enhancement of transport activity with the introduction of fluorinated substituents on the aryl ring. In this case however, the effect was attributed to increased binding strength due to increased electron deficiency of the ring, and hence increased acidity of the urea N-H[61].

The approach of fluorinating simple anionophores has been applied successfully to the synthesis of **95**, a highly active transporter with an $EC_{50}$ for bicarbonate that is lower (hence more active) than prodigiosin (**1**)[131]. In all of these cases however, fluorination has occurred on aromatic positions directly coupled to the anion binding site. It is therefore difficult to decouple the electronic effects of fluorinating these compounds, with the effect on the compound's partitioning within the bilayer.

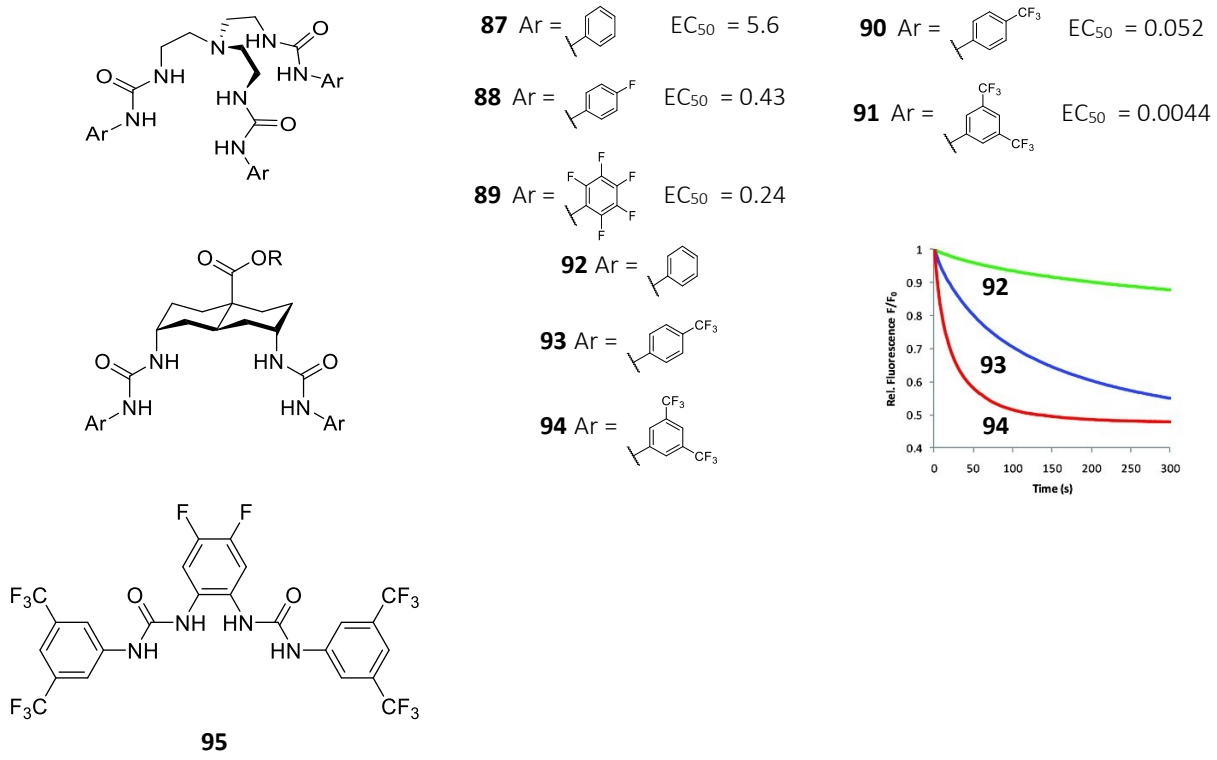


**Figure 4.1** Selected structures of previously studied fluorinated transporter series[61, 91, 131] and their relative $Cl^-$ transport activity. $EC_{50}$s are for $Cl^-/NO_3^-$ exchange after 270 s (in mol %). Fluorescence trace reproduced from[61] showing quenching of lucigenin fluorescence by influx of $Cl^-$ into 7:3 POPC:CHOL vesicles containing $NO_3^-$ facilitated by **92** - **94**.

Fluorine is the most electronegative of all the elements and the strong C-F bond is very polarised[132]. The electrons however are held very tightly and perfluorinated compounds are thus highly non-polarizable[133]. Therefore poly-fluorinated compounds exhibit some interesting intermolecular interactions and unique properties, for example their insolubility in both polar and organic solvents has been exploited in separation of complex organic reaction mixtures[134].

Both hydrocarbon and fluorocarbon chains show a strong hydrophobic effect, with similar contributions from the enthalpy and entropy gains from the release of unfavourably bonded or restricted solvent molecules[135]. In contrast to hydrocarbon chains however, fluorocarbons form much weaker van der Waals interactions between molecules due to their much lower polarisability[136]. Studies using molecular torsion balances to elucidate the energy contributions to the self-association of alkyl and perfluoroalkyl chains found that, despite similar contributions from solvophobic effects for both systems, van der Waals contributions dominated in apolar and fluorous solvents[137]. In this case, fluorous-fluorous interactions were favourable over fluorous-solvent interactions in apolar solvent and vice versa.

Recent research and advances in the conduction of transport experiments has allowed deeper insight into the mechanism anion transporters operate by, notably the distinction between

electrogenic and electroneutral components of the transport process and selectivity for $Cl^-$ transport over other processes such as $H^+/OH^-$ transport[93]. With these tools available, it was interesting to revisit fluorination to determine the origins of its effect on the transport process. Additionally, exploring the effect of fluorination of alkyl as opposed to aryl substituents would help to explore the physical effects on the compound's partitioning into the membrane (distinguished from electronic effects in aryl systems) to better understand the relationship between structure and transport mechanism.

## 4.2 Fluorinated Tren Series

To explore how fluorination can be used to modulate the partitioning of anion transporters, a series of tren-based tripodal thioureas was designed containing alkyl substituents with varying degrees of fluorination (Figure 4.2). The alkyl substituent used was such that a methylene spacer was always present between the thiourea N-H and the fluorinated section of the alkyl tail. This was to minimise any inductive electronic effects on the binding group from the electronegative fluorines.

The series was based on four simple alkyl-substituted trens **96** - **99** with $C_2$-$C_5$ chains and their fluorinated analogues **100** - **103** (note the methylene spacer in each case (Figure 4.2)). Two additional analogues of the $C_3$ and $C_4$ analogues with just a terminal $CF_3$ group **104** & **105** were also synthesised to probe whether the number of fluorines mediate any observed effects.

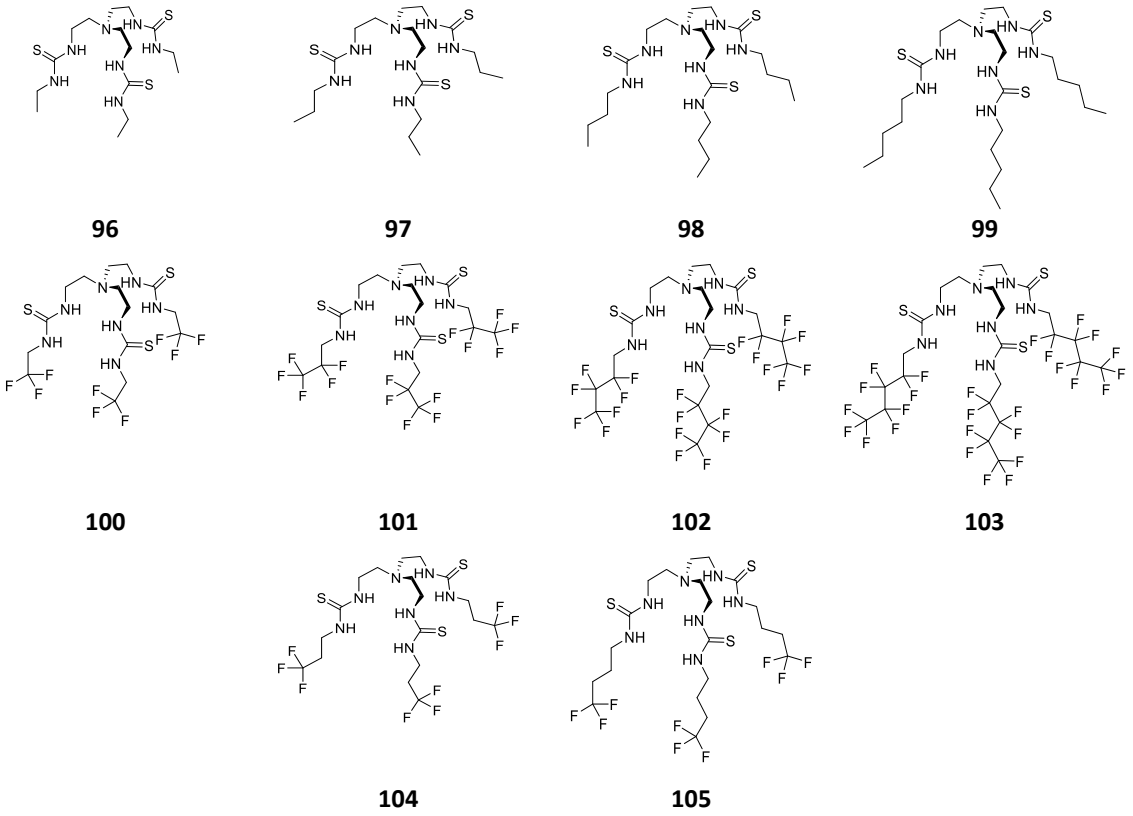


**Figure 4.2** Structure of the fluorinated tren series.

Compounds **98** & **99** were previously reported[63, 93]. Compounds **96** - **99** were synthesised in one step from tris-(2-aminoethyl)amine and the appropriate alkyl isothiocyanate and **100** - **105** were prepared from the reaction of the appropriate fluorinated amine and tris-(2-isothiocyanatoethyl)amine (**106**) prepared by the method of Young et. al.[138]. Full synthetic and characterisation details are appended (Appendix I.1).

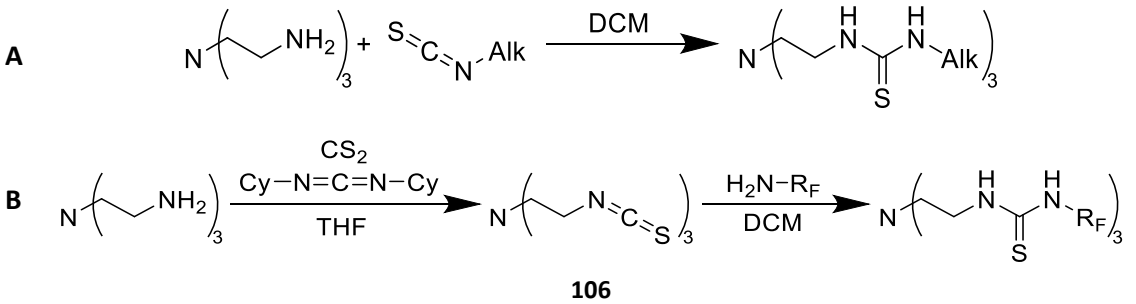


**Scheme 4.1** Synthesis of the fluorinated tren series, **A**: compounds **96** - **99**, **B**: compounds **100** - **105** from **106**. Reaction conditions and work ups varied, full details are appended (Appendix I).

## 4.3 Lipophilicity

To quantify the lipophilic effects of the fluorinated substituents, log P was again calculated using various available methods, from common programs such as Chemdraw and ACD/Labs, and also online tools such as VCCLab[105, 107].

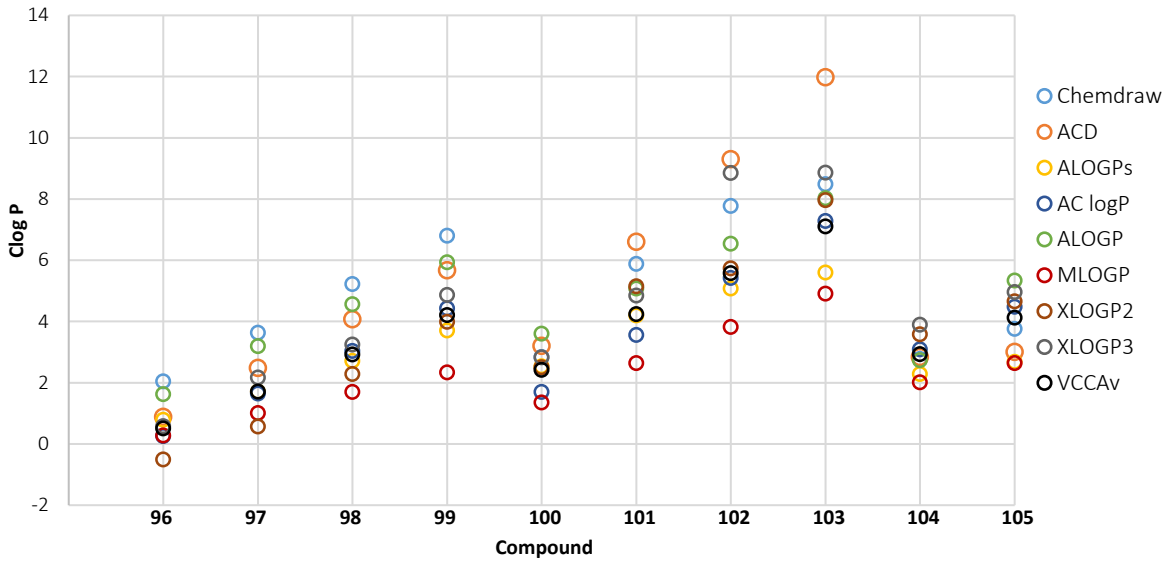


**Figure 4.3** Plot of the calculated log P values for **96** - **105** using various calculation methods. Legend contains the usual names for each calculation method, VCCAv = the average value returned by methods calculated from the Virtual Computational Chemistry Laboratory site[107].

The results from the calculations were generally unsatisfactory for the purposes of this work. The values for some compounds varied by as much as 7 log P units for some compounds, while there seemed to be no agreed order of lipophilicity between the models used.

To obtain experimental values for comparison, the compounds' retention time (RT) on a C18 RP-HPLC column was measured using isocratic elution with 30 % acetonitrile/water. The retention times were converted to retention factors (k') using the same method as used previously (section 2.3) the log of which is directly proportional to log P[108]. The column dead time ($t_0$) was determined from the retention time of thiourea[108], which is un-retained. Retention times were measured in triplicate and the average taken.

| Compound | RT 1 /min | RT 2 /min | RT 3 /min | Average RT /min | k' | Log (k') |
|---|---|---|---|---|---|---|
| **96** | 0.22 | 0.22 | 0.23 | 0.22 | 0.0152 | -1.82 |
| **97** | 0.25 | 0.26 | 0.24 | 0.25 | 0.1364 | -0.87 |
| **98** | 0.38 | 0.38 | 0.38 | 0.38 | 0.7273 | -0.14 |
| **99** | 0.85 | 0.85 | 0.82 | 0.84 | 2.8106 | 0.45 |
| **100** | 0.30 | 0.30 | 0.30 | 0.30 | 0.3636 | -0.44 |
| **101** | 0.63 | 0.63 | 0.62 | 0.63 | 1.8485 | 0.27 |
| **102** | 2.05 | 2.06 | 2.05 | 2.05 | 8.3333 | 0.92 |
| **103** | 7.61 | 7.59 | 7.65 | 7.62 | 33.6212 | 1.53 |
| **104** | 0.34 | 0.34 | 0.33 | 0.34 | 0.5303 | -0.28 |
| **105** | 0.42 | 0.42 | 0.43 | 0.42 | 0.9242 | -0.03 |

**Table 4.1** Tabulated values for measured retention times (RT) and calculated retention factors (k') for compounds **96** - **105** from RP-HPLC experiments. Log (k') is proportional to log P.

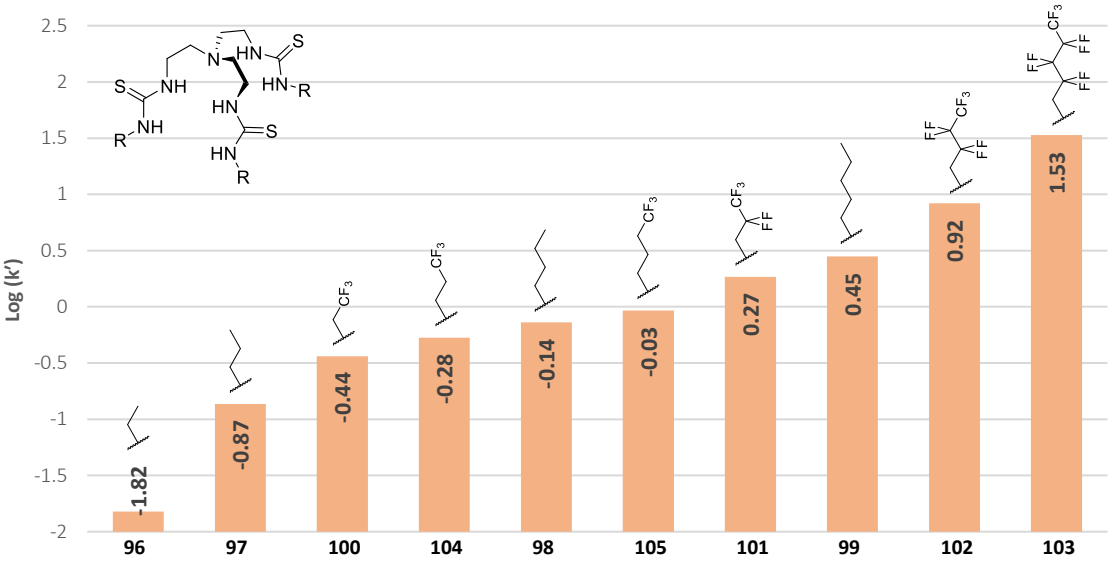


**Figure 4.4** Comparison of the relative lipophilicities of compounds **96** - **105**, using Log (k') values from isocratic RP-HPLC experiments.

The measured values show an expected increase in lipophilicity with the length of side chain. Full fluorination of the alkyl chains yields a very sizeable increase in the lipophilicity of the compounds. For compounds **104** & **105** the increase in lipophilicity with the introduction of a single $CF_3$ group was only modest, which should not be unexpected due to the relative polarity of this group[133], indeed there are examples where trifluoromethylation decreases log P overall[130].

As this method was more successful in obtaining the relative order of lipophilicity of the compounds than the calculated methods, the values of log (k') were used for comparison in the following studies. It should be noted that the C18 chains on the stationary phase in the RP-HPLC column may act as a good model for the long carbon chains in the tail region of the lipid bilayer, hence these measured values may give the most accurate insight into the compounds relative affinity for the membrane.

## 4.4 Anion Binding

Chloride binding constants were obtained by NMR titration with TBA Cl in DMSO-$d_6$/0.5 % $H_2O$. Constants were obtained by a global fitting of both thiourea N-H protons using BindFit v0.5[124, 125]. No other protons were observed to shift. Full experimental details are appended (Appendix II.2.1). A sample stack plot and fitting curve is given in Figure 4.5.

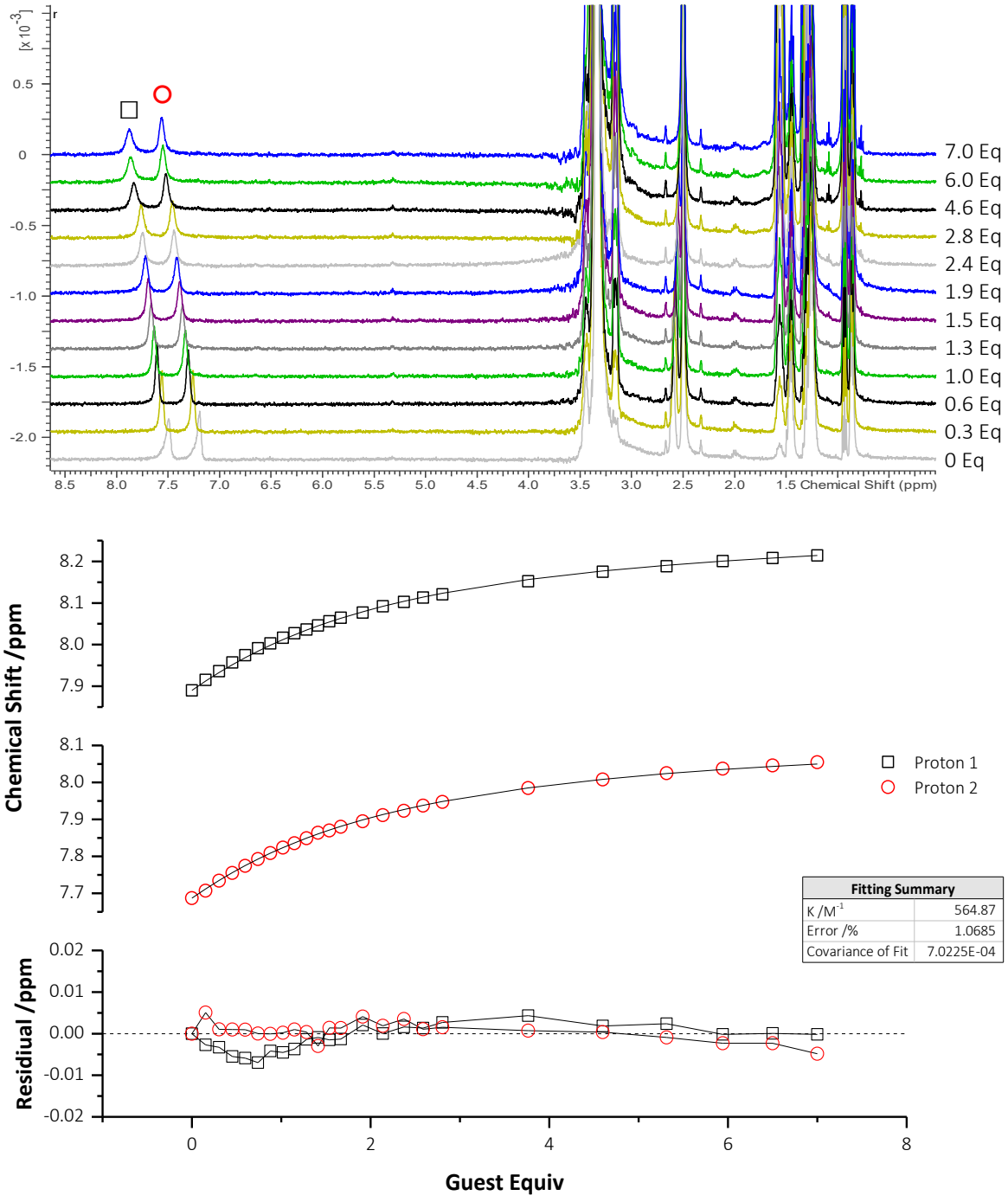


**Figure 4.5** Stack plot for the NMR titration of compound **100**, showing shifting of N-H protons at 7.88 and 7.69 ppm, and fitted curves and calculated values from global fitting by BindFit v0.5[124, 125].

| Compound | $K_a$ ($M^{-1}$) | | Compound | $K_a$ ($M^{-1}$) | | Compound | $K_a$ ($M^{-1}$) |
|---|---|---|---|---|---|---|---|
| **96** | 557 | | **100** | 470 | | | |
| **97** | 677 | | **101** | 565 | | **104** | 466 |
| **98** | 596 | | **102** | 733 | | **105** | 575 |
| **99** | 648 | | **103** | 669 | | | |

**Table 4.2** Association constants ($K_a$) for the compounds **96** - **105** from NMR titrations with TBACl in DMSO-$d_6$, calculated with BindFit v0.5[124, 125], calculated asymptotic errors 3 % or less.

Table 4.2 shows the calculated binding constants for the series. As expected compared to previously published tren-based receptors[63, 91], all are strong chloride binders. The constants do not vary by more than an order of magnitude, suggesting that the degree of fluorination is not having a profound effect on the binding group acidity, as desired. Binding does not seem to be directly correlated to number of fluorine substitutions.

For the ethyl and propyl tren compounds, fluorination of the chain appears to decrease the binding strength (**96** → **100**, $K_a$ decreases by ~90 $M^{-1}$; for **97** → **101** the decrease is ~110 $M^{-1}$, decreasing by another ~100 $M^{-1}$ for **104**). This could well be because the $CF_3$ group, although sterically bulkier, is quite polar[133] and in these short-chained compounds would be in close proximity to a bound chloride, destabilising the complex. This is not seen in the longer chain compounds, particularly **105** where presumably the n-butyl chain is long enough to move the $CF_3$ far enough away from the binding site to affect the binding event.

## 4.5 Chloride Transport Assays

The chloride transport ability of the tren series was tested using a pH-driven HPTS assay. This assay is easily adapted to probe the nature of the transport mechanism (see below)[93]. POPC vesicles containing 8-hydroxypyrene-1,3,6-trisulphonic acid (HPTS) dye were suspended in a buffered solution of NMDG-Cl (pH 7.0). After addition of the transporter as a solution of DMSO, the experiment was initiated with an external spike of NMDG to lower the external pH to 8.0.

The generated pH gradient was the driving force for the transport process. The anionophore is able to dissipate the gradient by either electroneutral efflux of HCl or $Cl^-/OH^-$ exchange. The change in internal pH is monitored by the fluorescence ratio between the absorbance bands of the acidic and basic forms of HPTS, at 403 and 460 nm respectively. The experiment was calibrated to 100 % dissipation by addition of a detergent to lyse the vesicles.

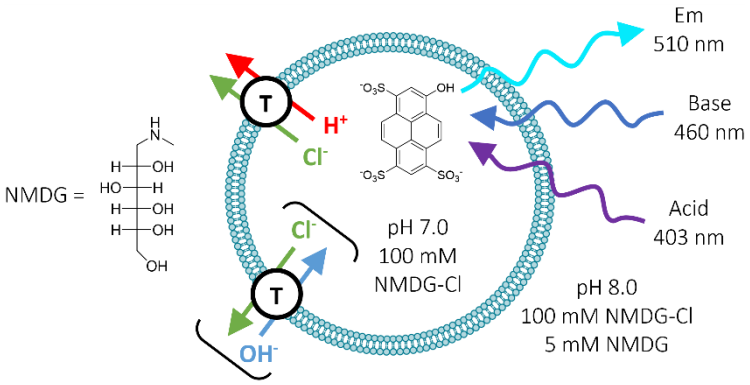


**Figure 4.6** Schematic showing the HPTS assay, T = the anionophore being tested.

The fluorescence trace was fitted to an exponential growth function, which allowed the quantification of the initial rate of transport (Figure 4.7A). The values of the transport rate are given in Figure 4.7B and plotted in Figure 4.7C.

**A**

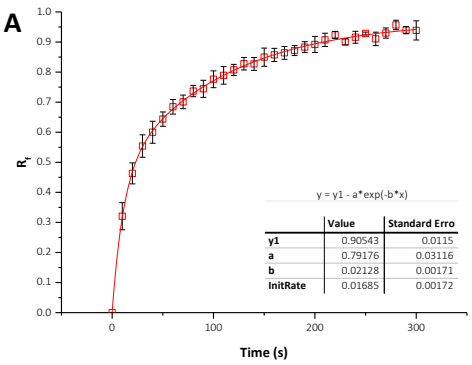


**B**

| Compound | InitRate |
|---|---|
| **96** | 0.00117 |
| **97** | 0.00135 |
| **98** | 0.00135 |
| **99** | 0.00163 |
| **100** | 0.0357 |
| **101** | 0.203 |
| **102** | 0.0455 |
| **103** | 0.0028 |
| **104** | 0.0172 |
| **105** | 0.00796 |

**C**

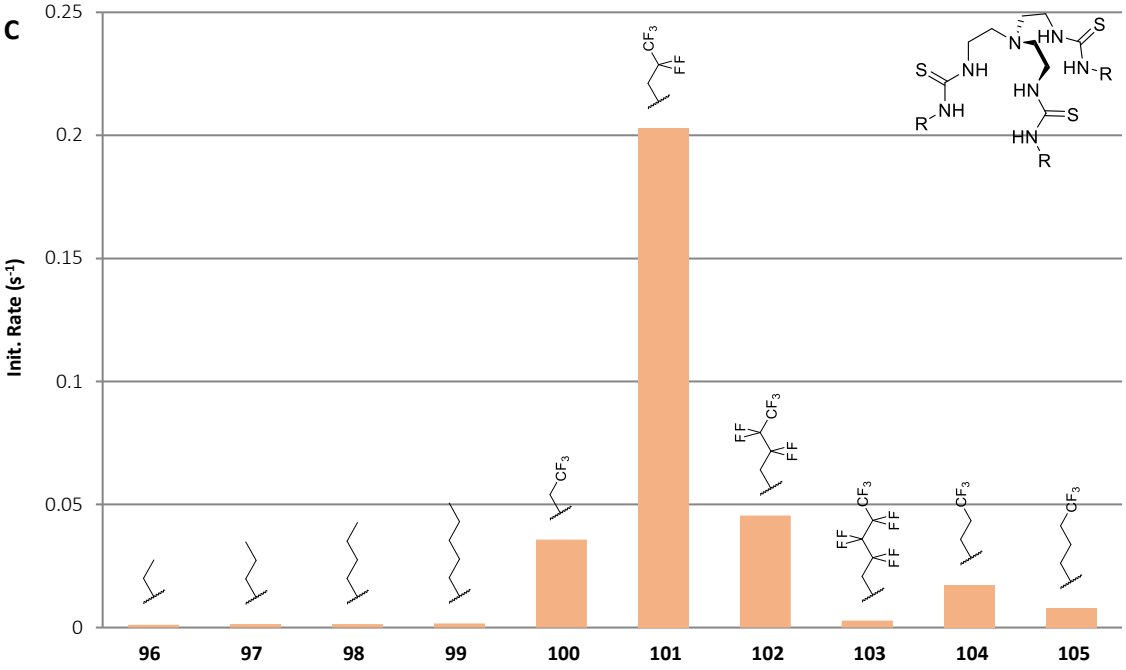


**Figure 4.7** **A**: Example single exponential fitting for compound **102**. **B**: Table of initial rate values for compounds **96** - **105** in the HPTS assay at 0.01 % loading. **C**: Plot showing of initial rate values for compounds **96** - **105** at 0.01 % loading.

Alkyl-substituted trens **96** - **99** are significantly slower transporters than their fluorinated equivalents, following the trend of increasing rate with increasing length of alkyl tail (hence better shielding of the negative charge and a more lipophilic $Cl^-$ complex). Fluorinated ethyl and butyl compounds **100** & **102** demonstrate an enhancement in transport rate of at least an order of magnitude over their alkyl counterparts, whilst for propyl compound **101** this effect is more than 2 orders of magnitude. The effect is less pronounced for pentyl compound **103**, which shows an enhancement over **99**, but only a less than two-fold increase.

Unlike previous series of compounds, it appears that there is not a simple relationship between lipophilicity or anion binding and observed transport rate. Plots of these values against transport rate are shown in Figure 4.8. There is clearly limited correlation between anion binding strength and transport rate. Likewise, there is little evidence of the expected bell-shaped curve for

lipophilicity[85, 106, 139], with a clear ideal zone in the middle. Indeed, the two compounds closest to the fastest compound **101** in terms of lipophilicity, **99** & **105**, are among the slowest transporters.

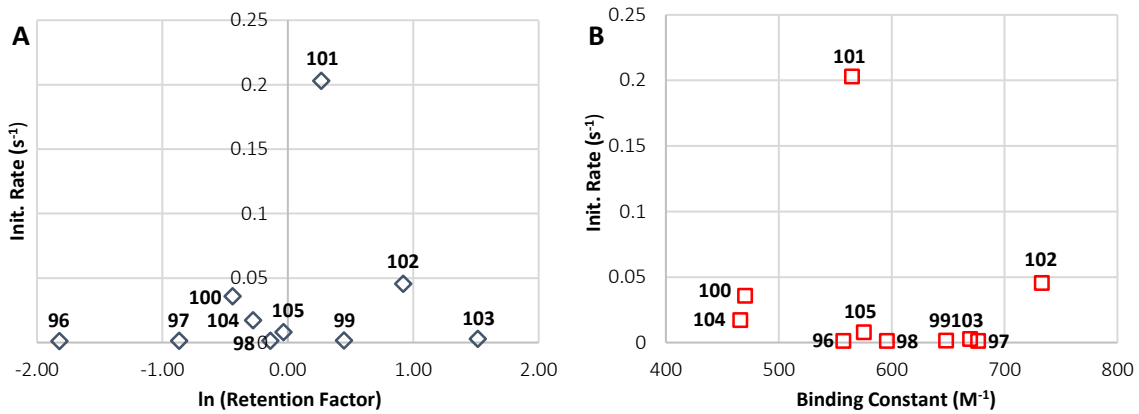


**Figure 4.8** Plots showing the lipophilicity (**A**) and $Cl^-$ binding strength (**B**) of the compounds against initial rate from HPTS assays.

To obtain some information on the origin of the enhancement of transport with fluorination, the $Cl^-$ complexes of compounds **97**, **101** & **104** were modelled with density functional theory (DFT) calculations using Spartan '14 for Windows[140, 141]. The geometry of the complexes was minimised by the M06 model using the 6-31G* basis set in a vacuum. A frequency calculation was performed to check that the geometries had reached a local minimum.

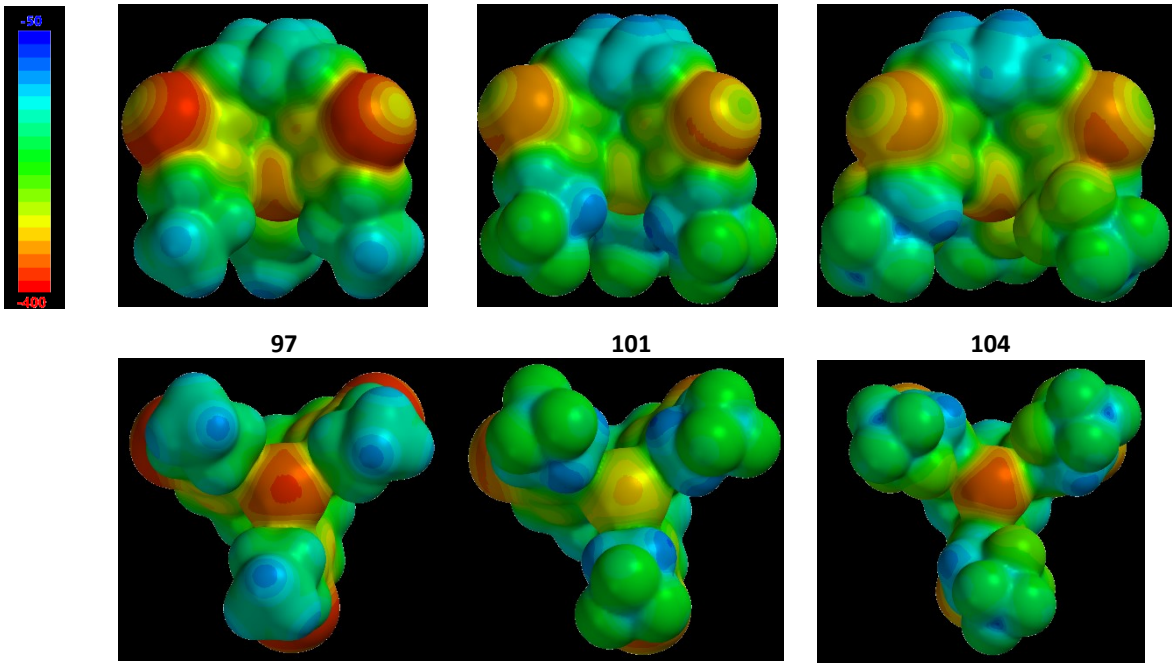


**Figure 4.9** Electrostatic potential maps of **97**, **101** & **104**, red colouring shows areas of higher density of negative charge, blue colours are more neutral. Scale bar shows the scale of electrostatic potential in kJ mol$^{-1}$.

| Compound | Volume /Å$^3$ | Area /Å$^2$ | Acc. Area /Å$^2$ | Min /Max El. Pot. /kJ mol$^{-1}$ | Polarisability |
|---|---|---|---|---|---|
| **97** | 487.8 | 451.9 | 310.0 | -382.4 / -112.4 | 79.47 |
| **101** | 582.4 | 511.0 | 312.0 | -354.2 / -100.8 | 82.77 |
| **104** | 556.0 | 548.6 | 320.6 | -364.0 / -100.0 | 85.01 |

**Table 4.3** Selected molecular properties from DFT simulations of compounds of **97**, **101** & **104**. Acc. Area = solvent accessible area. El. Pot. = electrostatic potential.

For alkyl compound **97**, the polarisation of the thiourea group by hydrogen bonding to the chloride ion can clearly be seen. The red colour on the sulphur atom shows a concentration of negative charge on this group. This effect is much diminished in the models of **101** & **104**, and there is clearly a more even spread of charge over the complexes, indicated by the more prevalent green and blue colours. This is likely due to assistance in spreading the charge by the electronegative fluorine atoms.

It is interesting also to note that with increasing level of fluorination, the area and volume of the complexes increases (488 Å$^3$ for **97**, cf. 556 Å$^3$ for **104**), as to be expected with sterically larger F atoms[133]. In contrast, the calculated solvent accessible areas of these molecules is actually quite similar (310 Å$^2$ for **97**, cf. 320 Å$^2$ for **104**), hence the charge is spread over a larger complex whilst the polar surface exposed to the tail region of the membrane will be more charge diffuse. This is also reflected in the increasing values of the polarisability of the complex. Thus the fluorinated complexes should have a decreased energy barrier to the crossing of the bilayer tail region compared to the alkyl variants.

Given that it is known that some tripodal thioureas possess $Cl^-$ over $H^+/OH^-$ selectivity in transport[93], the HPTS assay was modified to test the relative selectivities of the fluorinated trens. Gramicidin-A (Gr) was added to the membrane at 0.5 % loading before addition of the anionophore. Gr is a bacterial channel that conducts protons through the membrane via formation of a water wire[142]. Should $H^+/OH^-$ transport be rate-limiting, and thus the anionophore be capable of a component of electrogenic $Cl^-$ transport, then the overall transport rate will be enhanced in the presence of Gr due to the fast proton efflux through the channel (Figure 4.10A).

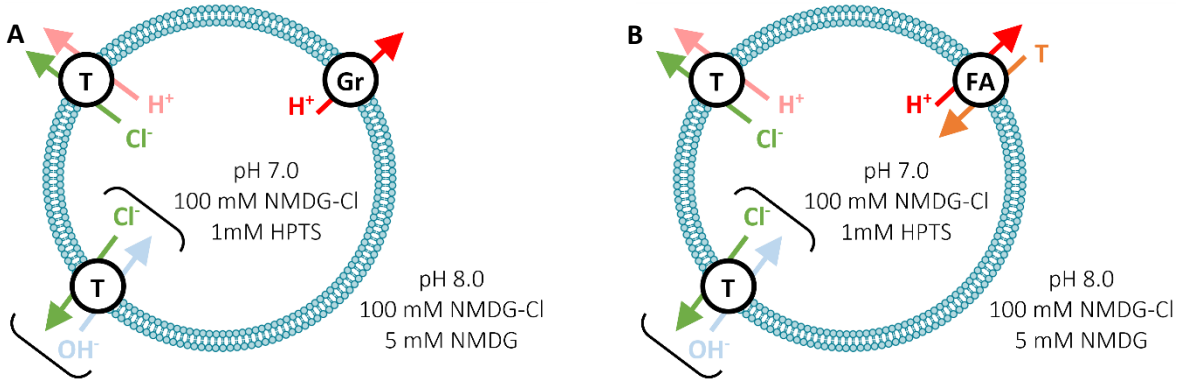


**Figure 4.10** Schematics of the modified HPTS assays. **A**: The gramicidin (Gr) assay with the addition of 0.5 mol % gramicidin-A. **B**: The fatty acid assay (FA) with addition of 2 mol % oleic acid.

Example fluorescence curves are given in Figure 4.11. The alkyl substituted compounds showed significant rate enhancement in the presence of Gr (Figure 4.11A). The fluorinated compounds however showed no significant change (Figure 4.11B), whilst for $CF_3$ compounds **104** & **105** the enhancement was only modest (Figure 4.11C). The $Cl^-$ over $H^+/OH^-$ selectivity was quantified by fitting of the curves to an exponential function as before, and dividing the initial rate in the presence of Gr by the rate without. These results are plotted in Figure 4.12. All experiments were carried out at 0.01 % loading, except for compound **101**, which due to its extremely fast transport ability necessitated running at 0.001 % loading to obtain accurate fitted curves.

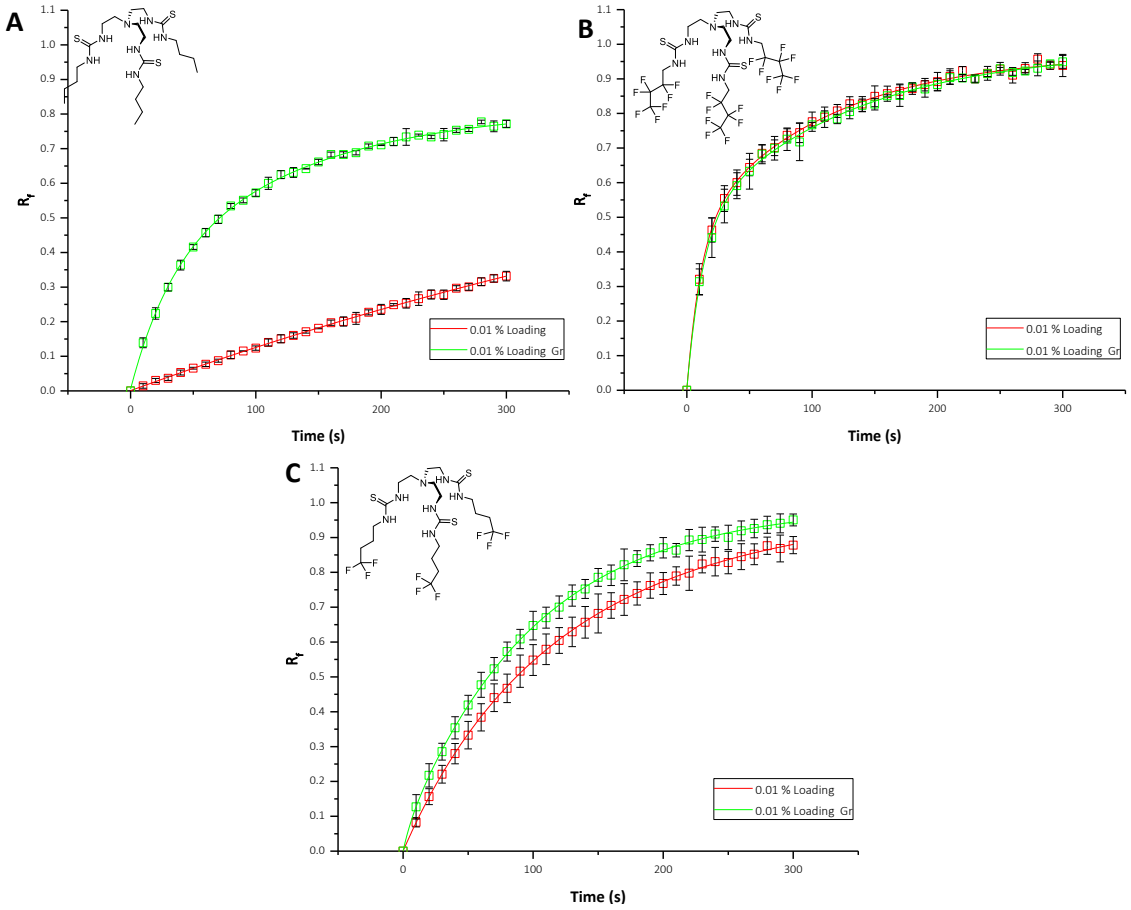


**Figure 4.11** Example comparison plots of fluorescence ratio traces from HPTS assays at 0.01 % loading with (green lines) and without (red lines) 0.5 mol % Gramicidin-A for compounds **98** (**A**), **102** (**B**) & **105** (**C**).

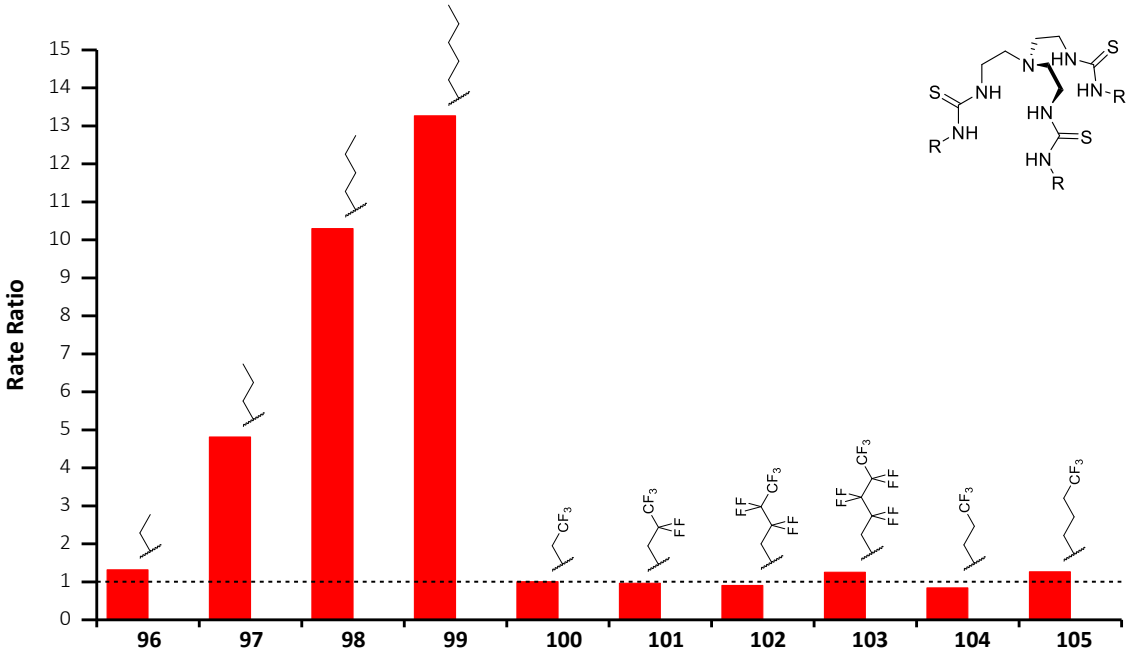


**Figure 4.12** Initial rate ratios between Gr/non-Gr assays for compounds **96** - **105** at 0.01 % loading (compound **101** at 0.001 % loading).

Figure 4.12 clearly shows the difference in behaviour between the alkyl-substituted and fluorinated compounds. The alkyl compounds **96** - **99** show an expected increase in selectivity with increasing tail length, from just over 1.3 times for ethyl-substituted **96** up to more than 13 times for **99**, most likely due to the increasing encapsulation of the $Cl^-$ ion[93].

For the fluorinated analogues however, the selectivity observed for their alkyl equivalents is almost completely switched off, with the selectivity ratios of or close to 1. Even for compound **105** which shows very mild selectivity, the value is much lower than that for its alkyl counterpart **98** which has a selectivity greater than 10. Were selectivity a direct result of encapsulation of the anion, it is not immediately logical that switching H for F on the side chains would remove this effect.

The $Cl^-$ over $H^+$/OH selectivity was further assayed by an alternative method of achieving proton efflux using fatty acids (FA). The HPTS experiments were repeated again, this time with the addition of 2 mol % oleic acid before the addition of anionophore (Figure 4.10B). Oleic acid is the precursor to the unsaturated tail of POPC and free fatty acids such as these are found naturally in biological membranes.

Sample fluorescence traces are given in Figure 4.13. The alkyl compounds are again enhanced by the presence of the protonophore, although not to the same degree as with Gr (Figure 4.13A, blue curve). Enhancement was this time also observed for the fluorinated compounds (Figure 4.13B), whilst the enhancement seen for mono-$CF_3$ compounds was much greater than that seen with Gr (Figure 4.13C). Rate ratios were again calculated and are displayed in Figure 4.14 (blue bars).

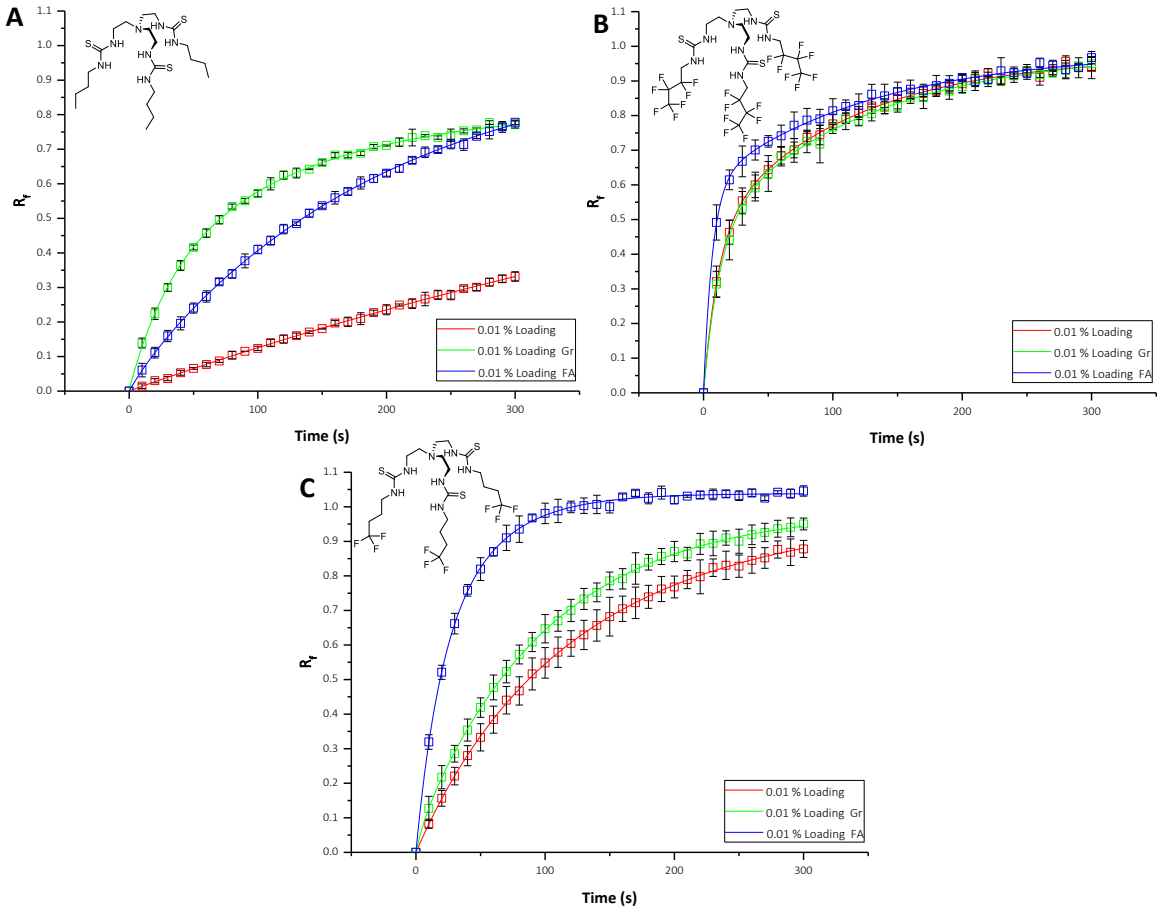


**Figure 4.13** Example comparison plots of fluorescence ratio traces from HPTS assays at 0.01 % loading with 2 mol % oleic acid (blue lines), 0.5 mol % Gramicidin-A (green lines) and without accompanying protonophore (red lines) for compounds **98** (**A**), **102** (**B**) & **105** (**C**).

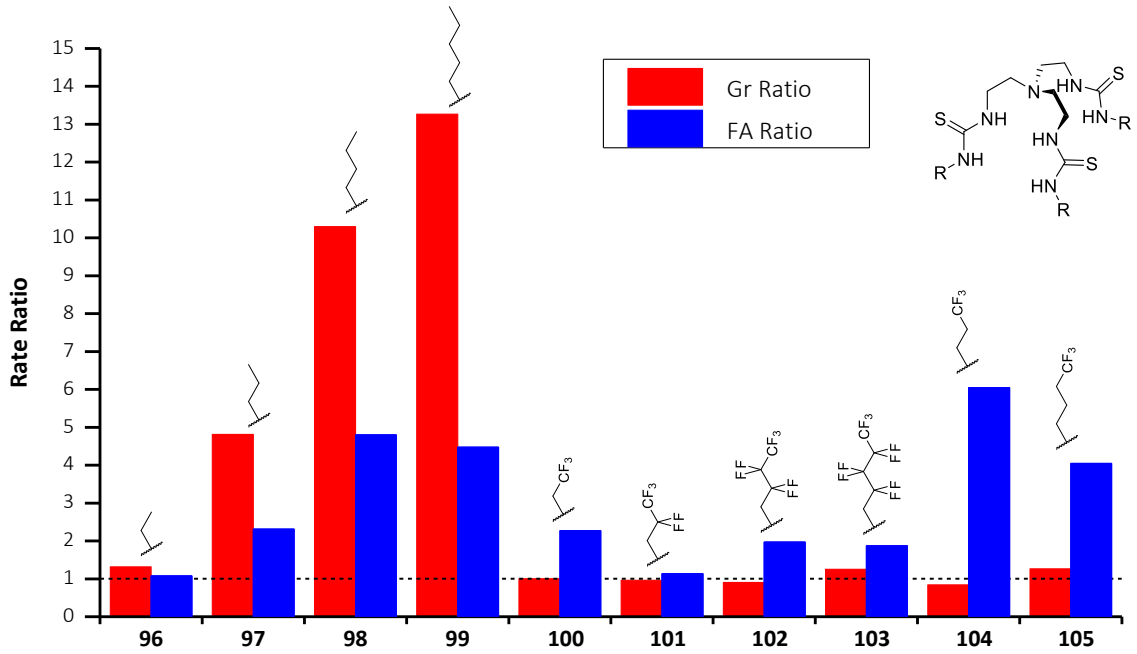


**Figure 4.14** Initial rate ratios between Gr/non-Gr (red bars) and FA/non-FA (blue bars) assays for compounds **96** - **105** at 0.01 % loading (compound **101** at 0.001 % loading).

Figure 4.14 clearly shows the recovery of the expected $Cl^-$ over $H^+/OH^-$ selectivity for the fluorinated compounds. The mono-$CF_3$ compounds also show improved enhancement compared to that for Gr, with up to a 6-fold increase for compound **104**. For all the alkyl compounds the selectivity is much diminished, for example for **99** the selectivity is reduced from 13 times to 4.5 times from Gr to FA.

This difference in enhancement can be rationalised by considering the transport pathways available to the compounds. With the presence of gramicidin, the compound must be capable electrogenic $Cl^-$ transport to couple to the fast proton efflux. To complete the transport cycle, the free neutral transporter must diffuse across the bilayer (Figure 4.15).

For the fluorinated compounds, this step is rate limiting. When a molecule diffuses across the tail group region of the bilayer, van der Waals interactions between the fatty acid chains will be broken[104]. Both the alkyl and fluorinated compounds will have a similar solvophobic driving force for association with the membrane, however the fluorinated compounds will be less able to form favourable van der Waals (vdW) interactions with the lipid tails[135-137]. As they are less able to replace the lipid-lipid vdW interactions, this will give the fluorinated compounds a higher energy barrier to diffusion across the tail region. Hence no enhancement with Gr is observed and $H^+/OH^-$ transport remains the fastest method for the compound to complete the transport cycle.

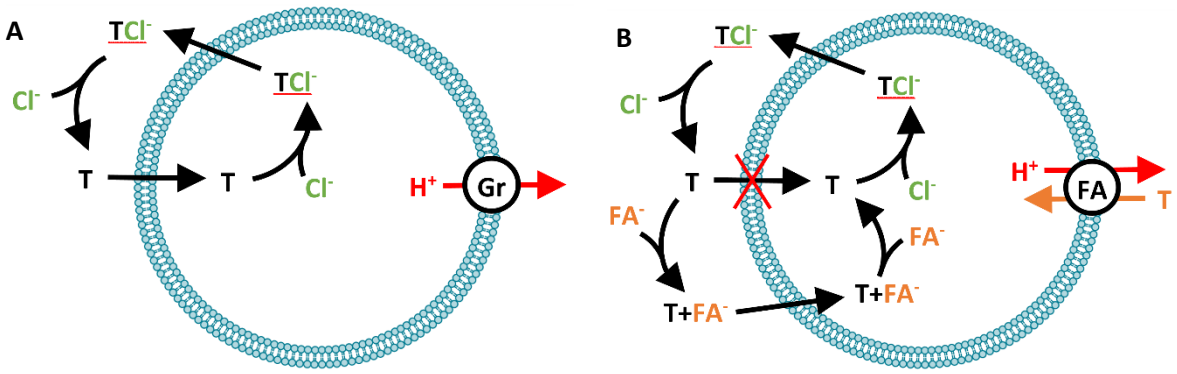


**Figure 4.15** Rationalising the effect of electrogenic transport coupling to Gr and FA for fluorinated tren compounds. **A**: Transporter enhanced by proton efflux by Gr, note T must diffuse back into the vesicle to complete the cycle. **B**: Possible route for enhancement of fluorinated transporters by FA. FA provides additional route for diffusion of T back into the vesicle to complete the cycle.

In the presence of fatty acid transport coupling, the anionophores are able to bind the deprotonated form of the acid and assist its flip-flop across the bilayer[143] (Figure 4.16). It is known that fatty acids can spontaneously flip-flop across the membrane to dissipate a pH gradient[144]; the flip-flop of the deprotonated form is much slower than the protonated transport step however. In nature, this process is accelerated by bilayer proteins[145]. Synthetic anionophores have also been

shown to be capable of assisting flip-flop of phospholipids[71, 146-148] and recent data has shown this activity with fatty acids[149].

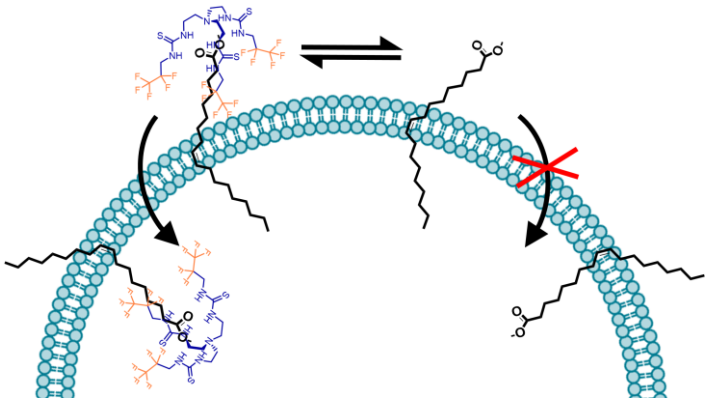

**Figure 4.16** Schematic showing flip-flop of fatty acids across the bilayer, assisted by anionophore binding.

Thus, the coupling to fatty acids as a protonophore in the membrane is mutually enhancing for the fluorinated tren compounds. Assisting the flip-flop of the fatty acids increases the rate of proton efflux from the vesicle whilst simultaneously giving the anionophores a faster route to completing the transport cycle (Figure 4.15). This would otherwise be limited by the compounds' $H^+/OH^-$ transport capability, or diffusion of the free host in the presence of Gr. This also demonstrates why the enhancement of the alkyl trens does not reach the same level as with Gr, as the proton efflux does not become truly kinetically fast, and is still limited by the rate of fatty acid flip-flop, thus their true fastest potential rate as electrogenic $Cl^-$ transporters is not realised.

## 4.6 Cell Testing

To quantify the series' activity in cells, the compounds were sent for testing in cell epithelia by collaborators at the University of Bristol using a previously reported FRT-YFP assay[92]. Fischer rat thyroid (FRT) cells expressing a halide sensitive yellow fluorescent protein (YFP) are grown in epithelia. FRT cells do not contain natural $Cl^-$ channels such as CFTR and hence can be used to quantify the $Cl^-$ transport effected by a synthetic anionophore added to the membrane.

The transporter is added to the extracellular PBS buffer solution as a solution in DMSO. The extracellular solution is perfused with $I^-$ which initiates $Cl^-/I^-$ exchange by the anionophore. Influx of $I^-$ causes quenching of YFP fluorescence which is quantified by fluorescence microscopy. The rate of fluorescence quenching gives a rate for anion transport, which is plotted in Figure 4.17.

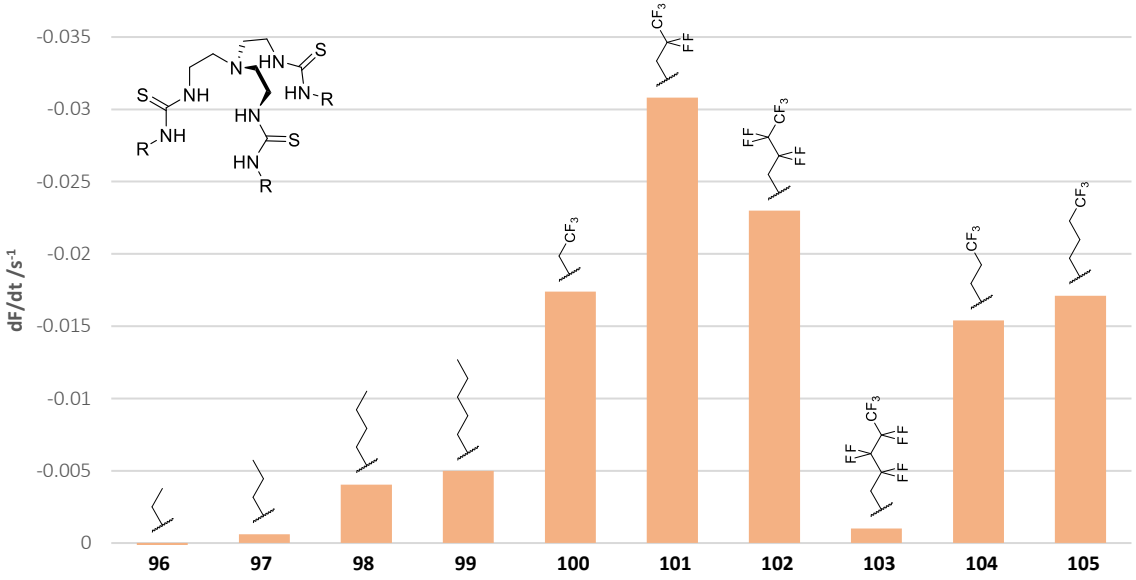


**Figure 4.17** Initial rate of fluorescence decay for compounds **96** - **105** in FRT-YFP cell $Cl^-$ transport assays.

A similar trend in activity is observed in the cell testing as in the vesicle assays, with the majority of fluorinated compounds showing a significant enhancement over the alkyl equivalents. Again the $CF_3$ compounds **104** & **105** show an enhancement over their alkyl parent, but not to the same degree as the fully fluorinated analogues. It is particularly interesting to note that fluorinated pentyl compound **103** is less effective in the cell assays than the alkyl **99**, the opposite order as reported in the HPTS assay.

Figure 4.18 shows a comparison plot of the transport rate observed in FRT-YFP cell assays and the rate from initial HPTS transport assays (with no assisting ionophore, blue squares). It is clear that these vesicle data are significantly underestimating the potential transport rate in cells, note particularly that many compounds are clustered close to the x-axis.

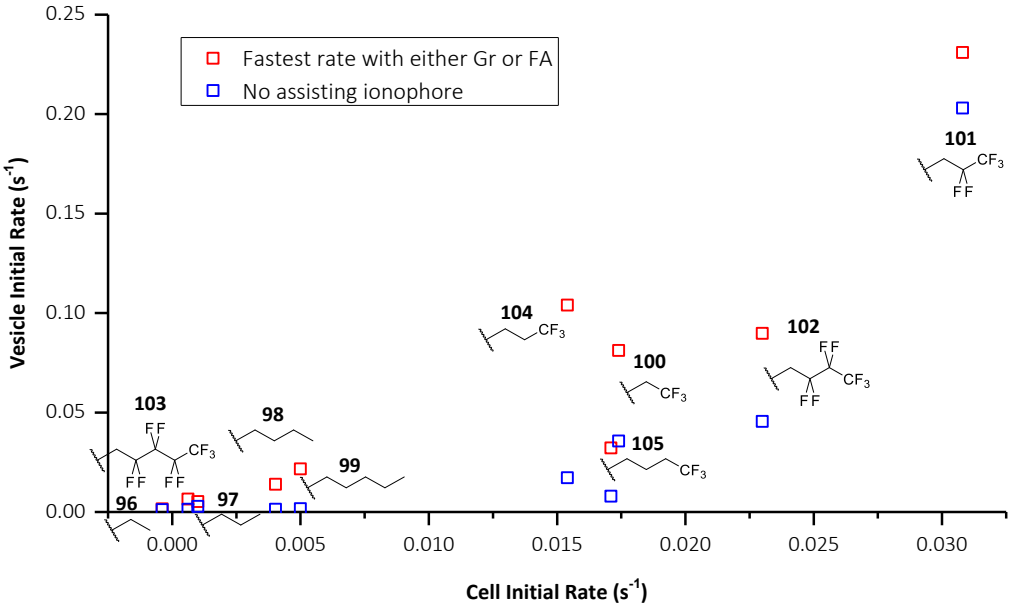


**Figure 4.18** Comparison of transport rates from FRT-YFP cell assays with initial rate data from HPTS assays with no assisting protonophore (blue squares) and the fastest achieved rate in any HPTS assay (red squares).

It is interesting to consider the fastest measured rate obtained by each compound in any of the transport assays described above, either without assisting anionophore, or with Gr or FA assistance. These maximum rate values are also plotted against the rate in FRT-YFP assays in Figure 4.18 (red squares). It is clear that these values achieve a plot closer to linearity than those from the HPTS assay alone. Note that in this plot, the rate of compound **99** is vesicle data is now in agreement with the cell data in showing its higher activity over **103**.

This is an important point to note for future transport studies. Natural cell membranes are going to contain natural proton/cationophores or fatty acids as they are vastly more complex mixtures. Therefore there will be many different processes available to assist synthetic anionophores in their transport. It is therefore important to fully characterise a transporter's mechanism and check for enhancement with naturally occurring pathways to ensure the anionophores true potential in cell membranes is understood.

## 4.7 Conclusions

These experiments show that alkyl compounds **96** - **99** are capable of electrogenic $Cl^-$ transport, and without an accompanying protonophore will be rate-limited by their ability to act as $H^+/OH^-$ transporters. In contrast, fluorinated compounds **100** - **105** are limited in their ability to carry out electrogenic transport by their energy barrier to crossing the membrane as the free host, due to their diminished ability to form favourable van der Waals interactions between the lipid tails and their non-polarisable fluorinated substituents.

Fluorination of the alkyl tails generally increased the rate of transport over the plain alkyl variants. DFT calculations suggested this was from the electronegative fluorines reducing the dipole on the thiourea sulphur, and providing a larger surface area for the charge to be distributed over.

FRT-YFP assays demonstrated a similar level of activity in cell epithelia to that measured in the vesicle assays. Considering the maximum rate achieved by the compounds in any of the experiments with or without assisting ionophores greatly improved the correlation with the cell data. This suggests that fully characterising a synthetic anionophore's mechanism and considering all pathways available for the transport process in cells is key to avoiding the potential underreporting of potential transporter efficacy.

# 5 Conclusions & Further Work

In this thesis, it has been shown that the ideal range of transporter lipophilicity does not change in a range of lipid environments tested. The relative order of efficacy within the series of compounds is retained, which is an important point to note when considering how previously published compound classes might behave in natural systems. It appears that specific interactions between the carriers and the membrane determine the rate determining step of the transport process. Lipophilicity remains an important molecular property to be tuned for optimum transporter efficacy.

It has also been shown that dynamic covalent chemistry can be used to form active transport scaffolds *in situ* in the membrane, which appears to assist the DCC reaction. For the thiosemicarbazone series, a balance has to be struck between transport activity and rate of DCC reaction, but this can be achieved with alkyl substituents on the imine moiety. This work demonstrates that it might be possible to use dynamic reactions such as these to overcome issues in transporter delivery or develop combinatorial libraries for transporter synthesis. In future this may mean that dynamic systems could be used to solubilise inherently lipophilic compounds, by forming active anionophores in the membrane from more water-soluble constituents, or perhaps by mimicking prodrugs and appending solubilising groups to anionophores via dynamic covalent linkages.

Finally, it has been demonstrated that the fluorination of alkyl substituents in anion carriers not only modulates the relative activity of the anionophores, it can also change the mechanism of the transport process. The increased energy barrier to diffusion of the free host, due to unfavourable fluorous-alkyl interactions in the tail region, limits the fluorinated compounds ability to facilitate electrogenic chloride transport. Comparison of the transport activity of the series in the presence and absence of naturally occurring protonophores, with transport data from FRT-YFP cell assays, showed that accounting for all possible coupled transport pathways in laboratory tests is necessary to avoid underestimating a compound's transport performance in cell epithelia.

It is now clear that the specific interactions between transporters and the lipid membrane govern the rate determining steps of the transport process and many observed effects can be rationalised in this way. Further useful detail could be obtained either with the use of NMR experiments such as NOESY to determine how different classes of compounds preferentially sit within the bilayer. Titration work could also shed light on whether different binding motifs have different binding interactions with phospholipid head groups. This information would help complete the picture of what structural features determine which part of the transport process limits observed rate.

As a more complete picture of the factors governing how synthetic anion carriers operate emerges, the development of synthetic anionophores can proceed in a more rational way. It is now possible to elucidate the rate determining step of the transport process for different compounds, thus informed and deliberate modifications can be made to maximise the transport activity of subsequent generations of new carrier scaffolds. A more rational approach such as this, mirroring stages of drug design, will allow more effective prediction of transporter activity *in vivo*. This should prove to be a crucial step to maximising the potential of these compounds as future therapeutics.

# 6 References


1. A. P. Davis, D. N. Sheppard and B. D. Smith, *Chem. Soc. Rev.*, 2007, **36**, 348-357.
2. L. D. Shrode, H. Tapper and S. Grinstein, *J. Bioenerg. Biomembr.*, 1997, **29**, 393-399.
3. K. Strange, F. Emma and P. S. Jackson, *Am. J. Physiol. Cell Physiol.*, 1996, **270**, 711-730.
4. P. D. Bell, J.-Y. Lapointe, R. Sabirov, S. Hayashi, J. Peti-Peterdi, K.-i. Manabe, G. Kovacs and Y. Okada, *Proc. Natl. Acad. Sci, USA*, 2003, **100**, 4322-4327.
5. D. E. Vance and J. E. Vance, *Biochemistry of Lipids, Lipoproteins and Membranes*, Elsevier, 2008.
6. N. Busschaert and P. A. Gale, *Angew. Chem. Int. Ed.*, 2013, **52**, 1374-1382.
7. F. M. Ashcroft, *Ion Channels and Disease*, Academic Press, 2000.
8. S. M. Rowe, S. Miller and E. J. Sorscher, *New Engl. J. Med.*, 2005, **352**, 1992-2001.
9. A. W. R. Serohijos, T. Hegedűs, A. A. Aleksandrov, L. He, L. Cui, N. V. Dokholyan and J. R. Riordan, *Proc. Natl. Acad. Sci, USA*, 2008, **105**, 3256-3261.
10. J. C. Davies, C. E. Wainwright, G. J. Canny, M. A. Chilvers, M. S. Howenstine, A. Munck, J. G. Mainz, S. Rodriguez, H. Li, K. Yen, C. L. Ordoñez and R. Ahrens, *Am. J. Respir. Crit. Care Med.*, 2013, **187**, 1219-1225.
11. D. Cohen and J. Raftery, *BMJ*, 2014, **348**.
12. J. M. Tomich, U. Bukovnik, J. Layman and B. D. Schultz, *Channel Replacement Therapy for Cystic Fibrosis - Cystic Fibrosis - Renewed Hopes Through Research*, InTech, 2012.
13. A. Furstner, *Angew. Chem. Int. Ed.*, 2003, **42**, 3582-3603.
14. J. L. Seganish and J. T. Davis, *Chem. Commun. (Camb.)*, 2005, 5781-5783.
15. T. Kataoka, M. Muroi, S. Ohkuma, T. Waritani, J. Magae, A. Takatsuki, S. Kondo, M. Yamasaki and K. Nagai, *FEBS Lett.*, 1995, **359**, 53-59.
16. S. Ohkuma, T. Sato, M. Okamoto, H. Matsuya, K. Arai, T. Kataoka, K. Nagai and H. H. Wasserman, *Biochem. J*, 1998, **334**, 731-741.
17. R. Pérez-Tomás, B. Montaner, E. Llagostera and V. Soto-Cerrato, *Biochem. Pharmacol.*, 2003, **66**, 1447-1452.
18. J. L. Sessler, L. R. Eller, W. S. Cho, S. Nicolaou, A. Aguilar, J. T. Lee, V. M. Lynch and D. J. Magda, *Angew. Chem. Int. Ed.*, 2005, **44**, 5989-5992.
19. D. F. Shriver and M. J. Biallas, *J. Am. Chem. Soc.*, 1967, **89**, 1078-1081.
20. C. H. Park and H. E. Simmons, *J. Am. Chem. Soc.*, 1968, **90**, 2431-2432.
21. R. A. Bell, G. G. Christoph, F. R. Fronczek and R. E. Marsh, *Science*, 1975, **190**, 151-152.
22. P. D. Beer and P. A. Gale, *Angew. Chem. Int. Ed.*, 2001, **40**, 486-516.
23. F. P. Schmidtchen and G. Müller, *J. Chem. Soc., Chem. Commun.*, 1984, 1115-1116.
24. K. Worm and F. P. Schmidtchen, *Angew. Chem. Int. Ed.*, 1995, **34**, 65-66.
25. E. Graf and J. M. Lehn, *J. Am. Chem. Soc.*, 1976, **98**, 6403-6405.
26. J. M. Lehn, E. Sonveaux and A. K. Willard, *J. Am. Chem. Soc.*, 1978, **100**, 4914-4916.
27. R. A. Pascal Jr., J. Spergel and D. Van Engen, *Tetrahedron Lett.*, 1986, **27**, 4099–4102.
28. S. Valiyaveettil, J. F. J. Engbersen, W. Verboom and D. N. Reinhoudt, *Angew. Chem. Int. Ed.*, 1993, **32**, 900-901.
29. T. R. Kelly and M. H. Kim, *J. Am. Chem. Soc.*, 1994, **116**, 7072-7080.
30. P. Bühlmann, S. Nishizawa, K. P. Xiao and Y. Umezawa, *Tetrahedron*, 1997, **53**, 1647–1654.
31. R. Prohens, S. Tomàs, J. Morey, P. M. Deyà, P. Ballester and A. Costa, *Tetrahedron Lett.*, 1998, **39**, 1063–1066.
32. N. H. Evans and P. D. Beer, *Angew. Chem. Int. Ed.*, 2014, **53**, 11716-11754.
33. A. Baeyer, *Eur. J. Inorg. Chem.*, 1886, **19**, 2184-2185.
34. P. A. Gale, J. L. Sessler, V. Král and V. Lynch, *J. Am. Chem. Soc.*, 1996, **118**, 5140-5141.
35. K. J. Winstanley, A. M. Sayer and D. K. Smith, *Org. Biomol. Chem,*, 2006, **4**, 1760-1767.
36. Y. Li and A. H. Flood, *Angew. Chem. Int. Ed.*, 2008, **47**, 2649-2652.
37. A. Brown and P. D. Beer, *Chem. Commun.*, 2016, **52**, 8645-8658.
38. A. Mele, P. Metrangolo, H. Neukirch, T. Pilati and G. Resnati, *J. Am. Chem. Soc.*, 2005, **127**, 14972-14973.

39. M. G. Sarwar, B. Dragisic, S. Sagoo and M. S. Taylor, *Angew. Chem. Int. Ed.*, 2010, **49**, 1674-1677.
40. Y. Inoue, T. Hakushi, Y. Liu, L. Tong, B. Shen and D. Jin, *J. Am. Chem. Soc.*, 1993, **115**, 475-481.
41. M. Newcomb, A. M. Madonik, M. T. Blanda and J. K. Judice, *J. Am. Chem. Soc.*, 1987, **6**, 145-150.
42. N. Busschaert, C. Caltagirone, W. V. Rossom and P. A. Gale, *Chem. Rev.*, 2015, **115**, 8038-8155.
43. J. M. Engle, C. N. Carroll, D. W. Johnson and M. M. Haley, *Chem. Sci.*, 2012, **3**, 1105-1110.
44. K. P. McDonald, B. Qiao, E. B. Twum, S. Lee, P. J. Gamache, C.-H. Chen, Y. Yi and A. H. Flood, *Chem. Commun.*, 2014, **50**, 13285-13288.
45. M. Yamanaka, T. Nakamura, T. Nakagawa and H. Itagaki, *Tetrahedron Lett.*, 2007, **48**, 8990–8993.
46. B. Hasenknopf, J. M. Lehn, B. O. Kneisel, G. Baum and D. Fenske, *Angew. Chem. Int. Ed.*, 1996, **35**, 1838-1840.
47. B. Hasenknop, J.-M. Lehn, N. Boumediene, A. Dupont-Gervais, A. V. Dorsselaer, B. Kneisel and D. Fenske, *J. Am. Chem. Soc.*, 1997, **119**, 10956-10962.
48. J. A. Wisner, P. D. Beer, M. G. B. Drew and M. R. Sambrook, *J. Am. Chem. Soc.*, 2002, **124**, 12469-12476.
49. R. C. MacDonald, R. I. MacDonald, B. P. M. Menco, K. Takeshita, N. K. Subbarao and L. Hu, *Biochim. Biophys. Acta*, 1991, **1061**, 297–303.
50. P. H. Schlesinger, R. Ferdani, J. Liu, J. Pajewska, R. Pajewski, M. Saito, H. Shabany and G. W. Gokel, *J. Am. Chem. Soc.*, 2002, **124**, 1848-1849.
51. B. A. McNally, A. V. Koulov, B. D. Smith, J. B. Joos and A. P. Davis, *Chem. Commun. (Camb.)*, 2005, 1087-1089.
52. A. V. Hill, *Biochem. J*, 1913, **7**, 471-480.
53. S. Bhosale and S. Matile, *Chirality*, 2006, **18**, 849-856.
54. S. Goutelle, M. Maurin, F. Rougier, X. Barbaut, L. Bourguignon, M. Ducher and P. Maire, *Fundam. & Clin. Pharmacol.*, 2008, **22**, 633-648.
55. L. A. Weiss, N. Sakai, B. Ghebremariam, C. Ni and S. Matile, *J. Am. Chem. Soc.*, 1997, **119**, 12142-12149.
56. B. A. McNally, E. J. O'Neil, A. Nguyen and B. D. Smith, *J. Am. Chem. Soc.*, 2008, **130**, 17274-17275.
57. N. Sakai and S. Matile, *Langmuir*, 2013, **29**, 9031-9040.
58. P. A. Gale, M. E. Light, B. McNally, K. Navakhun, K. E. Sliwinski and B. D. Smith, *Chem. Commun. (Camb.)*, 2005, 3773-3775.
59. P. Iglesias Hernandez, D. Moreno, A. A. Javier, T. Torroba, R. Perez-Tomas and R. Quesada, *Chem. Commun. (Camb.)*, 2012, **48**, 1556-1558.
60. A. V. Koulov, T. N. Lambert, R. Shukla, M. Jain, J. M. Boon, B. D. Smith, H. Li, D. N. Sheppard, J. B. Joos, J. P. Clare and A. P. Davis, *Angew. Chem. Int. Ed.*, 2003, **42**, 4931-4933.
61. S. Hussain, P. R. Brotherhood, L. W. Judd and A. P. Davis, *J. Am. Chem. Soc.*, 2011, **133**, 1614-1317.
62. J. A. Cooper, S. T. G. Street and A. P. Davis, *Angew. Chem. Int. Ed.*, 2014, **53**, 5609-5613.
63. N. Busschaert, P. A. Gale, C. J. E. Haynes, M. E. Light, S. J. Moore, C. C. Tong, J. T. Davis and J. William A. Harrell, *Chem. Commun.*, 2010, **46**, 6252-6254.
64. N. J. Andrews, C. J. E. Haynes, M. E. Light, S. J. Moore, C. C. Tong, J. T. Davis, W. A. H. Jr. and P. A. Gale, *Chem. Sci.*, 2011, **2**, 256-260.
65. N. Busschaert, I. L. Kirby, S. Young, S. J. Coles, P. N. Horton, M. E. Light and P. A. Gale, *Angew. Chem. Int. Ed.*, 2012, **51**, 4426-4430.
66. C. C. Tong, R. Quesada, J. L. Sessler and P. A. Gale, *Chem. Commun.*, 2008, 6321-6323.
67. Y. Marcus, *J. Am. Chem. Soc., Faraday Trans.*, 1991, **87**, 2995-2999.
68. N. Busschaert, L. E. Karagiannidis, M. Wenzel, C. J. E. Haynes, N. J. Wells, P. G. Young, D. Makuc, J. Plavec, K. A. Jolliffe and P. A. Gale, *Chem. Sci.*, 2014, **5**, 1118-1127.

69. S. J. Moore, C. J. E. Haynes, J. González, J. L. Sutton, S. J. Brooks, M. E. Light, J. Herniman, G. J. Langley, V. Soto-Cerrato, R. Pérez-Tomás, I. Marques, P. J. Costa, V. Félix and P. A. Gale, *Chem. Sci.*, 2013, **4**, 103-117.
70. C. J. E. Haynes, S. N. Berry, J. Garric, J. Herniman, J. R. Hiscock, I. L. Kirby, M. E. Light, G. Perkes and P. A. Gale, *Chem. Commun.*, 2012, **49**, 246-248.
71. J. M. Boon and B. D. Smith, *J. Am. Chem. Soc.*, 1999, **121**, 11924-11925.
72. J. M. Boon, T. N. Lambert, B. D. Smith, A. M. Beatty, V. Ugrinova and S. N. Brown, *J. Org. Chem.*, 2002, **67**, 2168-2174.
73. T. N. Lambert, J. M. Boon, B. D. Smith, M. N. Pérez-Payán and A. P. Davis, *J. Chem. Soc.*, 2002, **124**, 5276-5277.
74. A. V. Jentzsch, D. Emery, J. Mareda, S. K. Nayak, P. Metrangolo, G. Resnati, N. Sakai and S. Matile, *Nature Communications*, 2012, **3**, 905.
75. D. Milano, B. Benedetti, M. Boccalon, A. Brugnara, E. Iengo and P. Tecilla, *Chem. Commun.*, 2014, **50**, 9157-9160.
76. P. V. Santacroce, J. T. Davis, M. E. Light, P. A. Gale, J. C. Iglesias-Sánchez, P. Prados and R. Quesada, *J. Am. Chem. Soc.*, 2007, **129**, 1886-1887.
77. C. J. E. Haynes, N. Busschaert, I. L. Kirby, J. Herniman, M. E. Light, N. J. Wells, I. Marques, V. Félix and P. A. Gale, *Org. Biomol. Chem,*, 2014, **12**, 62-72.
78. B. A. McNally, A. V. Koulov, T. N. Lambert, B. D. Smith, J. B. Joos, A. L. Sisson, J. P. Clare, V. Sgarlata, L. W. Judd, G. Magro and A. P. Davis, *Chem. Eur. J.*, 2008, **14**, 9599-9606.
79. L. W. Judd and A. P. Davis, *Chem. Commun. (Camb.)*, 2010, **46**, 2227-2229.
80. M. G. Fisher, P. A. Gale, J. R. Hiscock, M. B. Hursthouse, M. E. Light, F. P. Schmidtchen and C. C. Tong, *Chem. Commun.*, 2009, 3017-3019.
81. P. A. Gale, C. C. Tong, C. J. Haynes, O. Adeosun, D. E. Gross, E. Karnas, E. M. Sedenberg, R. Quesada and J. L. Sessler, *J. Am. Chem. Soc.*, 2010, **132**, 3240-3241.
82. N. Busschaert, S. J. Bradberry, M. Wenzel, C. J. E. Haynes, J. R. Hiscock, I. L. Kirby, L. E. Karagiannidis, S. J. Moore, N. J. Wells, J. Herniman, G. J. Langley, P. N. Horton, M. E. Light, I. Marques, P. J. Costa, V. Félix, J. G. Frey and P. A. Gale, *Chem. Sci.*, 2013, **4**, 3036-3045.
83. C. Hansch, A. Leo and R. W. Taft, *Chem. Rev.*, 1991, **91**, 165-195.
84. H. Valkenier, C. J. E. Haynes, J. Herniman, P. A. Gale and A. P. Davis, *Chem. Sci.*, 2014, **5**, 1128-1134.
85. N. J. Knight, E. Hernando, C. J. E. Haynes, N. Busschaert, H. J. Clarke, K. Takimoto, M. García-Valverde, J. G. Frey, R. Quesada and P. A. Gale, *Chem. Sci.*, 2016, **7**, 1600-1608.
86. S. N. Berry, V. Soto-Cerrato, E. N. W. Howe, H. J. Clarke, I. Mistry, A. Tavassoli, Y.-T. Chang, R. Pérez-Tomás and P. A. Gale, *Chem. Sci.*, 2016, **7**, 5069-5077.
87. X. Wu, N. Busschaert, N. J. Wells, Y.-B. Jiang and P. A. Gale, *J. Am. Chem. Soc.*, 2015, **137**, 1476-1484.
88. N. Busschaert, R. B. P. Elmes, D. D. Czech, X. Wu, I. L. Kirby, E. M. Peck, K. D. Hendzel, S. K. Shaw, B. Chan, B. D. Smith, K. A. Jolliffe and P. A. Gale, *Chem. Sci.*, 2014, **5**, 3617-3626.
89. E. N. W. Howe, N. Busschaert, X. Wu, S. N. Berry, J. Ho, M. E. Light, D. D. Czech, H. A. Klein, J. A. Kitchen and P. A. Gale, *J. Am. Chem. Soc.*, 2016, **138**, 8301-8308.
90. E. Hernando, V. Soto-Cerrato, S. Cortés-Arroyo, R. Pérez-Tomás and R. Quesada, *Org. Biomol. Chem,*, 2014, **12**, 1771-1778.
91. N. Busschaert, M. Wenzel, M. E. Light, P. Iglesias-Hernández, R. Pérez-Tomás and P. A. Gale, *J. Am. Chem. Soc.*, 2011, **133**, 14136-14148.
92. H. Li, H. Valkenier, L. W. Judd, P. R. Brotherhood, S. Hussain, J. A. Cooper, O. Jurček, H. A. Sparkes, D. N. Sheppard and A. P. Davis, *Nat. Chem.*, 2016, **8**, 24-32.
93. X. Wu, L. W. Judd, E. N. W. Howe, A. M. Withecombe, V. Soto-Cerrato, H. Li, N. Busschaert, H. Valkenier, R. Pérez-Tomás, D. N. Sheppard, Y.-B. Jiang, A. P. Davis and P. A. Gale, *Chem*, 2016, **1**, 127-146.
94. G. van Meer, D. R. Voelker and G. W. Feigenson, *Nat. Rev. Mol. Cell Biol.*, 2008, **9**, 112-124.
95. C. A. Lipinski, F. Lombardo, B. W. Dominy and P. J. Feeney, *Adv. Drug Del. Rev.*, 1997, **23**, 3–25.

96. R. M. Epand, *Biochim. Biophys. Acta, Rev. Biomembr.*, 1998, **1376**, 353–368.
97. S. M. Bezrukov, *Curr. Opin. Colloid Interface Sci.*, 2000, **5**, 237–243.
98. M. Bogdanov and W. Dowhan, *J. Biol. Chem.*, 1999, **274**, 36827-36830.
99. G. D. Paolo and P. D. Camilli, *Nature*, 2006, **443**, 651-657.
100. T. Róg, M. Pasenkiewicz-Gierula, I. Vattulainena and M. Karttunen, *Biochim. Biophys. Acta*, 2009, **1788**, 97–121.
101. P. A. Gale, *Acc. Chem. Res.*, 2011, **44**, 216-226.
102. C. J. E. Haynes, S. J. Moore, J. R. Hiscock, I. Marques, P. J. Costa, V. Félix and P. A. Gale, *Chem. Sci.*, 2012, **3**, 1436-1444.
103. S.-J. Marrink and H. J. C. Berendsen, *J. Phys. Chem.*, 1994, **98**, 4155-4168.
104. C. L. Wennberg, D. v. d. Spoel and J. S. Hub, *J. Am. Chem. Soc.*, 2012, **134**, 5351-5361.
105. I. V. Tetko, J. Gasteiger, R. Todeschini, A. Mauri, D. Livingstone, P. Ertl, V. A. Palyulin, E. V. Radchenko, N. S. Zefirov, A. S. Makarenko, V. Y. Tanchuk and V. V. Prokopenko, *J. Comput. Aided Mol. Des.*, 2005, **19**, 453-463.
106. V. Saggiomo, S. Otto, I. Marque, V. Félix, T. Torroba and R. Quesada, *Chem. Commun.*, 2012, **48**, 5274-5276.
107. VCCLAB, Virtual Computational Chemistry Laboratory, http://www.vcclab.org.
108. OECD, *OECD Guidelines for the Testing of Chemicals, Section 1*, 2004.
109. A. Berthod and S. Carda-Broch, *J. Chromatogr.*, 2004, **1037**, 3-14.
110. M. J. Hynes, *J. Chem. Soc., Dalton Trans.*, 1993, 311-312.
111. W. F. D. Bennett, J. L. MacCallum and D. P. Tieleman, *J. Am. Chem. Soc.*, 2009, **131**, 1972-1978.
112. F. d. Meyer and B. Smit, *Proc. Natl. Acad. Sci.*, 2009, **106**, 3654-3658.
113. T. T. Mills, E. S. T. Gilman, T.-N. Stephanie, M. S. Detlef, W. F. Gerald and F. N. John, *Biophys. J.*, 2008, **95**, 669-681.
114. J. Pan, T. M. Thalia, T.-N. Stephanie and F. N. John, *Phys. Rev. Lett.*, 2008, **100**, 198103.
115. C. J. E. Haynes, N. Busschaert, I. L. Kirby, J. Herniman, M. E. Light, N. J. Wells, I. Marques, V. Félix and P. A. Gale, *Org. Biomol. Chem,*, 2013.
116. V. J. Stella and K. W. Nti-Addae, *Adv. Drug Del. Rev.*, 2007, **59**, 677–694.
117. R. Marinov and E. J. Dufourc, *Eur. Biophys. J.*, 1996, **24**, 423-431.
118. Avanti Polar Lipids - Phase Transition Temperatures for Glycerophospholipids, http://avantilipids.com/index.php?option=com_content&view=article&id=1700&Itemid=419, Accessed Jan 2014, 2014.
119. D. Larson, in *Dynamic Combinatorial Chemistry and Organocatalysis with Thiosemicarbazones and Organocatalysts for Hydrazone and Oxime Bioconjugations*, University of Copenhagen, Danish National Research Database, 2015.
120. S. J. Rowan, S. J. Cantrill, G. R. L. Cousins, J. K. M. Sanders and J. F. Stoddart, *Angew. Chem. Int. Ed.*, 2002, **41**, 898-952.
121. J. M. Lehn, *Chem. Eur. J.*, 1999, **5**, 2455-2463.
122. V. Soto-Cerrato, P. Manuel-Manresa, E. Hernando, S. Calabuig-Fariñas, A. Martínez-Romero, V. Fernández-Dueñas, K. Sahlholm, T. Knöpfel, M. García-Valverde, A. M. Rodilla, E. Jantus-Lewintre, R. Farràs, F. Ciruela, R. Pérez-Tomás and R. Quesada, *J. Am. Chem. Soc.*, 2015, **137**, 15892-15898.
123. JChem Calculator Plugins for Marvin JS 16.4.18, 2016, ChemAxon (http://www.chemaxon.com), https://epoch.uky.edu/ace/public/pKa.jsp, Accessed June, 2016.
124. P. Thordarson, *Chem. Soc. Rev.*, 2011, **40**, 1305-1323.
125. BindFit v0.5, http://app.supramolecular.org/bindfit/, Accessed May 2016.
126. A. Vargas Jentzsch, A. Hennig, J. Mareda and S. Matile, *Acc. Chem. Res.*, 2013, **46**, 2791-2800.
127. *accumet® Chloride Combination Ion Selective Electrodes: Instructions*, Fisher Scientific, 2008.

128. H. Valkenier, L. W. Judd, H. Li, S. Hussain, D. N. Sheppard and A. P. Davis, *J. Am. Chem. Soc.*, 2014, **136**, 12507-12512.
129. S. T. Keaveney, R. S. Haines and J. B. Harper, *Org. Biomol. Chem,*, 2015, **13**, 8925-8936.
130. S. Purser, P. R. Moore, S. Swallow and V. Gouverneur, *Chem. Soc. Rev.*, 2008, **27**, 320-330.
131. L. E. Karagiannidis, C. J. E. Haynes, K. J. Holder, I. L. Kirby, S. J. Moore, N. J. Wells and P. A. Gale, *Chem. Commun.*, 2014, **50**, 12050-12053.
132. D. O'Hagan, *Chem. Soc. Rev.*, 2008, **37**, 308-319.
133. B. E. Smart, *J. Fluorine Chem.*, 2001, **109**, 3–11.
134. Z. Luo, Q. Zhang, Y. Oderaotoshi and D. P. Curran, *Science*, 2001, **291**, 1766-1769.
135. J. Mecinović, P. W. Snyder, K. A. Mirica, S. Bai, E. T. Mack, R. L. Kwant, D. T. Moustakas, A. Héroux and G. M. Whitesides, *J. Am. Chem. Soc.*, 2011, **133**, 14017-14026.
136. C. A. Hunter, *Chem. Sci.*, 2013, **4**, 834-848.
137. C. Adam, L. Yang and S. L. Cockroft, *Angew. Chem. Int. Ed.*, 2015, **54**, 1164-1167.
138. P. G. Young, J. K. Clegg, M. Bhadbhade and K. A. Jolliffe, *Chem. Commun.*, 2011, **47**, 463-465.
139. M. J. Spooner and P. A. Gale, *Chem. Commun.*, 2015, **51**, 4883-4886.
140. *Spartan '14*, Wavefunction Inc.,Irvine, CA.
141. Y. Shao, L. F. Molnar, Y. Jung, J. Kussmann, C. Ochsenfeld, S. T. Brown, A. T. B. Gilbert, L. V. Slipchenko, S. V. Levchenko, D. P. O'Neill, R. A. D. Jr, R. C. Lochan, T. Wang, G. J. O. Beran, N. A. Besley, J. M. Herbert, C. Y. Lin, T. V. Voorhis, S. H. Chien, A. Sodt, R. P. Steele, V. A. Rassolov, P. E. Maslen, P. P. Korambath, R. D. Adamson, B. Austin, J. Baker, E. F. C. Byrd, H. Dachsel, R. J. Doerksen, A. Dreuw, B. D. Dunietz, A. D. Dutoi, T. R. Furlani, S. R. Gwaltney, A. Heyden, S. Hirata, C.-P. Hsu, G. Kedziora, R. Z. Khalliulin, P. Klunzinger, A. M. Lee, M. S. Lee, W. Liang, I. Lotan, N. Nair, B. Peters, E. I. Proynov, P. A. Pieniazek, Y. M. Rhee, J. Ritchie, E. Rosta, C. D. Sherrill, A. C. Simmonett, J. E. Subotnik, H. L. W. III, W. Zhang, A. T. Bell, A. K. Chakraborty, D. M. Chipman, F. J. Keil, A. Warshel, W. J. Hehre, H. F. S. III, J. Kong, A. I. Krylov, P. M. W. Gill and M. Head-Gordon, *PCCP*, 2006, **8**, 3172-3191.
142. D. Bonhenry, S. Kraszewski, F. Picaud, C. Ramseyer, S. Balme, J.-M. Janot and F. Henn, *Soft Matter*, 2011, **7**, 10651-10659.
143. X. Wu and P. A. Gale, *Manuscript submitted*, 2016.
144. F. Kamp and J. A. Hamilton, *Proc. Natl. Acad. Sci, USA*, 1992, **89**, 11367-11370.
145. A. Fedorenko, P. V. Lishko and Y. Kirichok, *Cell*, 2012, **151**, 400-413.
146. B. D. Smith and T. N. Lambert, *Chem. Commun.*, 2003, 2261-2268.
147. Y. Sasaki, R. Shukla and B. D. Smith, *Org Biomol Chem*, 2004, **2**, 214-219.
148. K. M. DiVittorio, F. T. Hofmann, J. R. Johnson, L. Abu-Esba and B. D. Smith, *Bioorg. Med. Chem.*, 2009, **17**, 141-148.
149. X. Wu and P. A. Gale, *J. Am. Chem. Soc.*, 2016, DOI: 10.1021/jacs.1026b10615.
150. W. Weith, *Berichte der deutschen chemischen Gesellschaft*, 1875, **8**, 1523-1530.
151. A. Yahyazadeh and Z. Ghasemi, *Eur. Chem. Bull.*, 2013, **2**, 573-575.

# Appendix I Synthesis

## I.1 Synthetic Procedures

NMR spectra were recorded on Bruker AVII400 or Bruker AVIIIHD400 FT-NMR spectrometers in the indicated solvent at 298 K. Chemical shifts for proton and carbon spectra are reported on the delta scale in ppm and were referenced to residual solvent references or internal TMS reference. High resolution mass spectra were recorded using positive/negative ion electrospray ionisation and analysed using a MaXis (Bruker Daltonics, Bremen, Germany) mass spectrometer equipped with a Time of Flight (TOF) analyser. Samples were introduced to the mass spectrometer via a Dionex Ultimate 3000 autosampler and uHPLC pump. Gradient 20% acetonitrile (0.2% formic acid) to 100% acetonitrile (0.2% formic acid ) in five minutes at 0.6 mL min. Column, Acquity UPLC BEH C18 (Waters) 1.7 micron 50 x 2.1mm. Starting materials were used as provided by suppliers. Dichloromethane was distilled over sodium hydroxide under nitrogen before use. Other solvents were used without further purification.

### I.1.1 1-Phenyl-3-ethylthiourea **56**

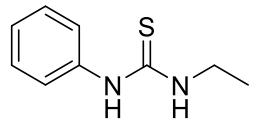

This compound had been previously reported[150].

Aniline (2.5 mmol) was dissolved in pyridine (10 ml) under a nitrogen atmosphere. Ethyl isothiocyanate (2.5 mmol) was added and the pale yellow solution stirred at 80°C under nitrogen overnight. The volatiles were removed under reduced pressure yielding a yellow oil.

The oil was dissolved in methanol and purified on an Isolute® SCX-2 cation-exchange column. The methanol phase was collected and the solvent removed, yielding a colourless oil. The oil was purified by flash chromatography (ethyl acetate eluent) yielding a waxy white solid. The solid was further purified by crystallisation from chloroform/hexane, yielding white crystals.

Yield: 43 %. HRMS ESI$^+$ = $[C_9H_{13}N_2S]^+$: 181.0794 (calc), 181.0796 (found), -1.4 ppm (err); $[C_9H_{12}N_2SNa]^+$: 203.0613 (calc), 203.0616 (found), -1.5 ppm (err). $^1$H NMR (400 MHz, DMSO-$d_6$) δ = 9.43 (br s, 1H), 7.72 (br s, 1H), 7.39 (br d, *J*=8.1 Hz, 2H), 7.36 - 7.26 (m, 2H), 7.10 (t, *J*=7.3 Hz, 1H), 3.56 - 3.41 (m, 2H), 1.12 (t, *J*=7.2 Hz, 3H). $^{13}$C NMR (101MHz, DMSO-$d_6$) δ = 180.5, 139.7, 129.1, 124.5, 123.6, 39.2, 14.7. Melting point: 99.6 – 100.4°C.

### I.1.2 1-(p-Tolyl)-3-ethylthiourea **57**

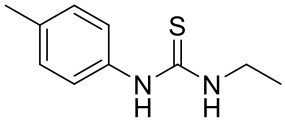

This compound had been previously reported[150].

p-Toluidine (2.5 mmol) was dissolved in pyridine (10 ml) under a nitrogen atmosphere. Ethyl isothiocyanate (2.5 mmol) was added and the orange solution stirred at 80°C under nitrogen overnight. The volatiles were removed under reduced pressure yielding a brown oil.

The oil was dissolved in methanol and purified on an Isolute® SCX-2 cation-exchange column. The methanol phase was collected and the solvent removed, yielding an off-white solid. The solid was purified by flash chromatography (3:1 Ethyl Acetate:Hexane eluent) yielding a waxy white solid. The solid was further purified by crystallisation from chloroform/hexane, yielding white, needle-like crystals.

Yield: 21 %. HRMS ESI$^+$ = $[C_{10}H_{15}N_2S]^+$: 195.0950 (calc), 195.0949 (found), 0.9 ppm (err); $[C_{10}H_{14}N_2SNa]^+$: 217.0770 (calc), 217.0769 (found), 0.3 ppm (err). $^1$H NMR (400 MHz, DMSO-$d_6$) δ = 9.32 (br s, 1H), 7.59 (br s, 1H), 7.23 (d, *J*=8.3 Hz, 2H), 7.13 (d, *J*=8.3 Hz, 2H), 3.52 - 3.41 (m, 2H), 2.27 (s, 3H), 1.10 (t, *J*=7.2 Hz, 3H). $^{13}$C NMR (101MHz, DMSO-$d_6$) δ = 180.6, 137.0, 133.9, 129.6, 124.1, 39.2, 21.0, 14.7. Melting point: 99.9 – 100.8°C.

### I.1.3 1-(4-Ethylphenyl)-3-ethylthiourea **58**

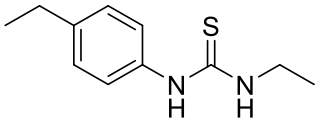

This compound had been previously reported[151].

4-Ethylaniline (2.5 mmol) was dissolved in pyridine (10 ml) under a nitrogen atmosphere. Ethyl isothiocyanate (2.5 mmol) was added and the orange solution stirred at 80°C under nitrogen overnight. The volatiles were removed under reduced pressure yielding a brown oil.

The oil was dissolved in methanol and purified on an Isolute® SCX-2 cation-exchange column. The methanol phase was collected and the solvent removed, yielding a waxy yellow solid. The solid was purified by flash chromatography (3:1 Ethyl Acetate:Hexane eluent) yielding a waxy off-white solid. The solid was further purified by crystallisation from chloroform/hexane, yielding white crystals.

Yield: 42 %. HRMS ESI$^+$ = $[C_{11}H_{17}N_2S]^+$: 209.1107 (calc), 209.1106 (found), 0.6 ppm (err); $[C_{11}H_{16}N_2SNa]^+$: 231.0926 (calc), 231.0928 (found), -0.7 ppm (err) ; $[C_{22}H_{32}N_4S_2Na]^+$: 439.1961 (calc), 439.1965 (found), -0.9 ppm (err). $^1$H NMR (400 MHz, DMSO-$d_6$) δ = 9.33 (br s, 1H), 7.61 (br s, 1H), 7.25 (d, *J*=8.2 Hz, 2H), 7.16 (br d, *J*=8.2 Hz, 2H), 3.51 - 3.39 (m, 2H), 2.58 (q, *J*=7.6 Hz, 2H), 1.18 (t, *J*=7.6 Hz, 3H), 1.10 (t, *J*=7.1 Hz, 3H). $^{13}$C NMR (101MHz, DMSO-$d_6$) δ = 180.5, 140.2, 137.2, 128.4, 124.0, 39.2, 28.1, 16.1, 14.7. Melting point: 89.9 – 90.5°C.

### I.1.4 1-(4-Ethylphenyl)-3-propylthiourea **59**

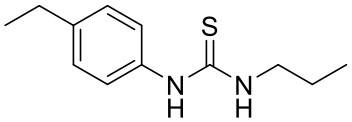

4-Ethylaniline (2.5 mmol) was dissolved in dry DCM (6 ml) under a nitrogen atmosphere. Propyl isothiocyanate (2.5 mmol) was added and the orange solution stirred under nitrogen overnight. The volatiles were removed under reduced pressure yielding a yellow solid.

The solid was dissolved in methanol and purified on an Isolute® SCX-2 cation-exchange column. The methanol phase was collected and the solvent removed, yielding a waxy yellow solid. The solid was purified by flash chromatography (diethyl ether eluent) yielding a waxy white solid.

Yield: 11 %. HRMS ESI$^+$ = $[C_{12}H_{19}N_2S]^+$: 223.1263 (calc), 223.1266 (found), -1.3 ppm (err). $^1$H NMR (400 MHz, DMSO-$d_6$) δ = 9.39 (br s, 1H), 7.69 (br s, 1H), 7.32 (d, *J*=8.3 Hz, 2H), 7.21 (d, *J*=8.3 Hz, 2H), 3.52 - 3.42 (m, *J*=5.6 Hz, 2H), 2.63 (q, *J*=7.7 Hz, 2H), 1.60 (qt, *J*=7.3, 7.3 Hz, 2H), 1.23 (t, *J*=7.6 Hz, 3H), 0.93 (t, *J*=7.4 Hz, 3H). $^{13}$C NMR (101MHz, DMSO-$d_6$) δ = 180.8, 140.2, 137.3, 128.4, 123.9, 46.1, 28.1, 22.3, 16.1, 11.9. Melting point: 71.7 – 71.8°C.

### I.1.5 1-(4-Propylphenyl)-3-propylthiourea **60**

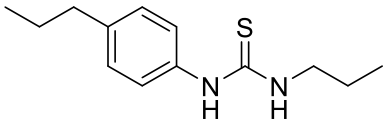

4-Propylaniline (2.5 mmol) was dissolved in pyridine (10 ml) under a nitrogen atmosphere. Propyl isothiocyanate (2.5 mmol) was added and the solution stirred at 80°C under nitrogen overnight. The volatiles were removed under reduced pressure yielding a brown oil.

The oil was dissolved in methanol and purified on an Isolute® SCX-2 cation-exchange column. The methanol phase was collected and the solvent removed, yielding a colourless oil. The oil was

purified by flash chromatography (1st elution DMC, second diethyl ether) yielding a waxy off-white solid. The solid was further purified by crystallisation from methanol/water, yielding a white solid.

Yield: 30 %. HRMS ESI$^+$ = $[C_{13}H_{21}N_2S]^+$: 237.1420 (calc), 237.1419 (found), 0.5 ppm (err); $[C_{13}H_{20}N_2SNa]^+$: 259.1239 (calc), 259.1240 (found), -0.1 ppm (err). $^1$H NMR (400 MHz, DMSO-$d_6$) δ = 9.34 (br s, 1H), 7.64 (br s, 1H), 7.27 (d, *J*=8.3 Hz, 2H), 7.13 (d, *J*=8.3 Hz, 2H), 3.47 - 3.37 (m, 2H), 2.54 - 2.48 (m, obsc., 2H), 1.63 - 1.50 (m, 4H), 0.95 - 0.83 (m, 6H). $^{13}$C NMR (101MHz, DMSO-$d_6$) δ = 180.8, 138.6, 137.3, 128.9, 123.7, 46.1, 37.2, 24.6, 22.3, 14.2, 11.9. Melting point: 71.1 – 71.8°C.

### I.1.6 1-(4-Propylphenyl)-3-butylthiourea **61**

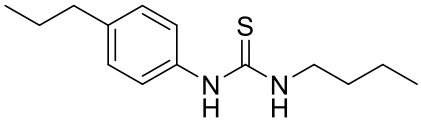


4-Propylaniline (2.5 mmol) was dissolved in dry DCM (6 ml) under a nitrogen atmosphere. n-Butyl isothiocyanate (2.5 mmol) was added and the yellow solution stirred under nitrogen overnight. The volatiles were removed under reduced pressure yielding a cloudy oil.

The oil was dissolved in methanol and purified on an Isolute® SCX-2 cation-exchange column. The methanol phase was collected and the solvent removed, yielding colourless oil. The oil was purified by flash chromatography (1:1 diethyl ether:hexane eluent) yielding a waxy white solid.

Yield: 19 %. HRMS ESI$^+$ = $[C_{14}H_{23}N_2S]^+$: 251.1576 (calc), 251.1582 (found), -2.1 ppm (err). $^1$H NMR (400 MHz, DMSO-$d_6$) δ = 9.32 (br s, 1H), 7.61 (br s, 1H), 7.27 (d, *J*=8.4 Hz, 2H), 7.13 (d, *J*=8.3 Hz, 2H), 3.52 - 3.37 (m, 2H), 2.56 - 2.53 (m, obsc., 2H), 1.63 - 1.47 (m, 4H), 1.31 (qt, *J*=7.4, 7.4 Hz, 2H), 0.90 (t, *J*=7.2 Hz, 6H). $^{13}$C NMR (101MHz, DMSO-$d_6$) δ = 180.7, 128.9, 123.7, 44.0, 37.2, 31.1, 24.6, 20.1, 14.2, 14.2. Melting point: 54.9 – 55.7°C.

### I.1.7 1-(4-Butylphenyl)-3-butylthiourea **62**

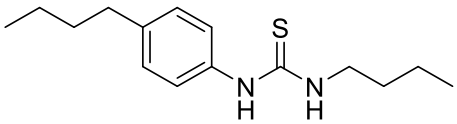


4-Butylaniline (2.5 mmol) was dissolved in pyridine (10 ml) under a nitrogen atmosphere. n-Butyl isothiocyanate (2.5 mmol) was added and the brown solution stirred at 80°C under nitrogen overnight. The volatiles were removed under reduced pressure yielding a brown oil.

The oil was dissolved in methanol and purified on an Isolute® SCX-2 cation-exchange column. The methanol phase was collected and the solvent removed, yielding a colourless oil. The oil was

purified by flash chromatography (1st elution DCM, second diethyl ether) yielding a waxy off-white solid. The solid was further purified by crystallisation from methanol/water, yielding a white solid.

Yield: 28 %. HRMS ESI$^+$ = $[C_{15}H_{25}N_2S]^+$: 265.1733 (calc), 265.1728 (found), 1.7 ppm (err); $[C_{15}H_{24}N_2SNa]^+$: 287.1552 (calc), 287.1547 (found), 1.8 ppm (err). $^1$H NMR (400 MHz, DMSO-$d_6$) δ = 9.33 (br s, 1H), 7.62 (br s, 1H), 7.26 (d, *J*=8.2 Hz, 2H), 7.13 (d, *J*=8.3 Hz, 2H), 3.58 - 3.38 (m, 2H), 2.54 (t, *J*=7.8 Hz, 2H), 1.59 - 1.46 (m, 4H), 1.31 (qt, *J*=7.4, 7.4 Hz, 4H), 0.90 (t, *J*=7.3 Hz, 6H). $^{13}$C NMR (101MHz, DMSO-$d_6$) δ = 180.7, 138.7, 137.3, 128.8, 123.7, 44.0, 34.7, 33.6, 31.1, 22.2, 20.1, 14.3, 14.2. Melting point: 57.8 – 58.2°C.

### I.1.8 1-(4-Butylphenyl)-3-pentylthiourea **63**

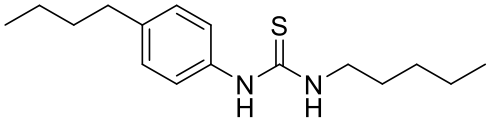


4-Butylaniline (2.5 mmol) was dissolved in dry DCM (6 ml) under a nitrogen atmosphere. n-Pentyl isothiocyanate (2.5 mmol) was added and the orange solution stirred under nitrogen overnight. The volatiles were removed under reduced pressure yielding an orange oil.

The oil was dissolved in methanol and purified on an Isolute® SCX-2 cation-exchange column. The methanol phase was collected and the solvent removed, yielding a yellow solid. The solid was purified by flash chromatography (2:1 diethyl ether:hexane eluent) yielding a waxy white solid.

Yield: 24 %. HRMS ESI$^+$ = $[C_{16}H_{27}N_2S]^+$: 279.1889 (calc), 279.1892 (found), -1.0 ppm (err). $^1$H NMR (400 MHz, DMSO-$d_6$) δ = 9.32 (br s, 1H), 7.61 (br s, 1H), 7.27 (d, *J*=8.3 Hz, 2H), 7.13 (d, *J*=8.3 Hz, 2H), 3.50 - 3.38 (m, 2H), 2.54 (br t, *J*=7.6 Hz, 2H), 1.60 - 1.47 (m, 4H), 1.38 - 1.22 (m, 6H), 0.96 - 0.83 (m, 6H). $^{13}$C NMR (101MHz, DMSO-$d_6$) δ = 180.7, 138.7, 137.3, 128.9, 123.7, 44.3, 34.8, 33.6, 29.1, 28.7, 22.4, 22.2, 14.4, 14.3. Melting point: 53.9 – 54.4°C.

### I.1.9 1-(4-Pentylphenyl)-3-pentylthiourea **64**

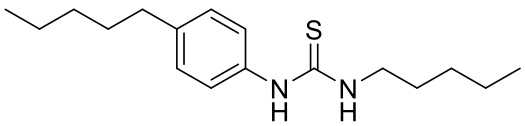


4-Pentylaniline (2.5 mmol) was dissolved in dry DCM (6 ml) under a nitrogen atmosphere. n-Pentyl isothiocyanate (2.5 mmol) was added and the pale yellow solution stirred under nitrogen overnight. The volatiles were removed under reduced pressure yielding an off-white solid.

The solid was dissolved in methanol and purified on an Isolute® SCX-2 cation-exchange column. The methanol phase was collected and the solvent removed, yielding an off-white solid. The solid was purified by flash chromatography (2:1 diethyl ether:hexane eluent) yielding a waxy white solid.

Yield: 18 %. HRMS ESI$^+$ = $[C_{17}H_{29}N_2S]^+$: 293.2046 (calc), 293.2048 (found), -0.8 ppm (err). $^1$H NMR (400 MHz, DMSO-$d_6$) δ = 9.33 (br s, 1H), 7.61 (br s, 1H), 7.26 (d, *J*=8.4 Hz, 2H), 7.13 (d, *J*=8.4 Hz, 2H), 3.51 - 3.38 (m, 2H), 2.56 - 2.54 (m, 2H), 1.62 - 1.47 (m, 4H), 1.37 - 1.21 (m, 8H), 0.94 - 0.82 (m, 6H). $^{13}$C NMR (101MHz, DMSO-$d_6$) δ = 180.7, 138.8, 137.3, 128.9, 123.7, 44.3, 35.0, 31.4, 31.1, 29.1, 28.7, 22.4, 22.4, 14.4 (br s). Melting point: 55.6 – 56.6°C.

### I.1.10 1-(4-Pentylphenyl)-3-hexylthiourea **65**

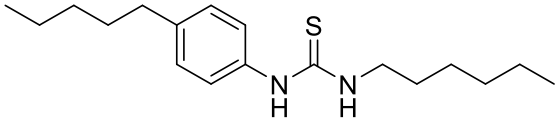


This compound had been previously reported[82].

4-Pentylaniline (2.5 mmol) was dissolved in dry DCM (6 ml) under a nitrogen atmosphere. n-Hexyl isothiocyanate (2.5 mmol) was added and the pale yellow solution stirred under nitrogen overnight. The volatiles were removed under reduced pressure yielding a yellow oil.

The oil was dissolved in methanol and purified on an Isolute® SCX-2 cation-exchange column. The methanol phase was collected and the solvent removed, yielding a yellow solid. The solid was purified by flash chromatography (2:1 diethyl ether:hexane eluent) yielding a waxy white solid.

Yield: 22 %. HRMS ESI$^+$ = $[C_{18}H_{31}N_2S]^+$: 307.2202 (calc), 307.2203 (found), -0.3 ppm (err). $^1$H NMR (400 MHz, DMSO-$d_6$) δ = 9.33 (br s, 1H), 7.60 (br s, 1H), 7.26 (d, *J*=8.3 Hz, 2H), 7.13 (d, *J*=8.4 Hz, 2H), 3.50 - 3.38 (m, 2H), 2.56 - 2.52 (m, 2H), 1.62 - 1.46 (m, 4H), 1.35 - 1.23 (m, 10H), 0.93 - 0.82 (m, 6H). $^{13}$C NMR (101MHz, DMSO-$d_6$) δ = 180.7, 138.7, 137.3, 128.9, 123.7, 44.3, 35.0, 31.5, 31.4, 31.2, 29.0, 26.6, 22.6, 22.4, 14.4 (br s). Melting point: 53.8 – 54.7°C.

### I.1.11 1-(4-Hexylphenyl)-3-hexylthiourea **66**

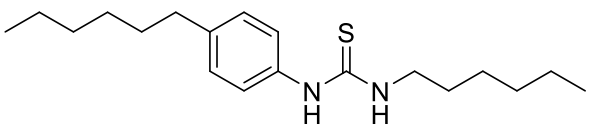


4-Hexylaniline (2.5 mmol) was dissolved in pyridine (10 ml) under a nitrogen atmosphere. n-Hexyl isothiocyanate (2.5 mmol) was added and the red solution stirred at 80°C under nitrogen overnight. The volatiles were removed under reduced pressure yielding an orange oil.

The oil was dissolved in methanol and purified on an Isolute® SCX-2 cation-exchange column. The methanol phase was collected and the solvent removed, yielding a yellow solid. The solid was purified by flash chromatography (2:1 hexane:ethyl acetate) yielding a waxy yellow solid. The solid was further purified by crystallisation from methanol/water, yielding a white solid.

Yield: 67 %. HRMS ESI$^+$ = $[C_{19}H_{33}N_2S]^+$: 321.2359 (calc), 321.2363 (found), -1.3 ppm (err). $^1$H NMR (400 MHz, DMSO-$d_6$) δ = 9.31 (br s, 1H), 7.59 (br s, 1H), 7.26 (d, *J*=8.4 Hz, 2H), 7.12 (d, *J*=8.3 Hz, 2H), 3.49 - 3.40 (m, 2H), 2.57 - 2.52 (m, 2H), 1.59 - 1.46 (m, 4H), 1.34 - 1.22 (m, 12H), 0.91 - 0.82 (m, 6H). $^{13}$C NMR (101MHz, DMSO-$d_6$) δ = 180.7, 138.8, 137.2, 128.8, 123.7, 44.3, 35.1, 31.6, 31.5, 31.4, 28.9, 28.8, 26.6, 22.5 (br s), 14.4, 14.4. Melting point: 45.9 – 47.4°C.

### I.1.12 1-(4-Hexylphenyl)-3-heptylthiourea **67**

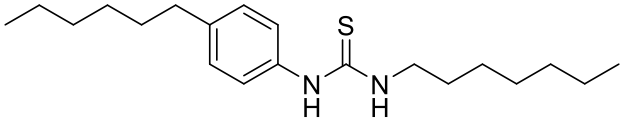


4-Hexylaniline (2.5 mmol) was dissolved in pyridine (10 ml) under a nitrogen atmosphere. n-Heptyl isothiocyanate (2.5 mmol) was added and the red solution stirred at 80°C under nitrogen overnight. The volatiles were removed under reduced pressure yielding an orange oil.

The oil was dissolved in methanol and purified on an Isolute® SCX-2 cation-exchange column. The methanol phase was collected and the solvent removed, yielding a yellow solid. The solid was purified by flash chromatography (2:1 hexane:ethyl acetate) yielding a waxy white solid on drying. The solid was further purified by crystallisation from methanol/water, yielding white crystals.

Yield: 90 %. HRMS ESI$^+$ = $[C_{20}H_{35}N_2S]^+$: 335.2515 (calc), 335.2524 (found), -2.4 ppm (err). $^1$H NMR (400 MHz, DMSO-$d_6$) δ = 9.31 (br s, 1H), 7.58 (br s, 1H), 7.25 (br d, *J*=7.7 Hz, 2H), 7.12 (br d, *J*=8.2 Hz, 2H), 2.56 - 2.52 (m, 2H), 1.58 - 1.42 (m, 4H), 1.33 - 1.20 (m, 14H), 0.91 - 0.79 (m, 6H). $^{13}$C NMR (101MHz, DMSO-$d_6$) δ = 180.7, 138.8, 137.2, 128.9, 123.8, 44.3, 35.1, 31.7, 31.6, 31.4, 29.0, 28.9, 28.8, 26.8, 22.5, 22.5, 14.4 (br s). Melting point: 49.0 – 50.0°C.

### I.1.13 1-(4-Heptylphenyl)-3-heptylthiourea **68**

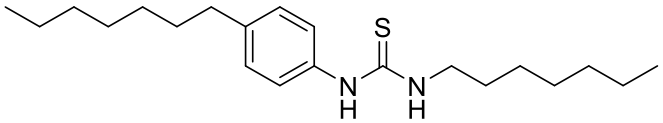

4-Heptylaniline (2.5 mmol) was dissolved in pyridine (10 ml) under a nitrogen atmosphere. n-Heptyl isothiocyanate (2.5 mmol) was added and the orange solution stirred at 80°C under nitrogen overnight. The volatiles were removed under reduced pressure yielding an orange oil.

The oil was dissolved in methanol and purified on an Isolute® SCX-2 cation-exchange column. The methanol phase was collected and the solvent removed, yielding an off-white solid. The solid was purified by flash chromatography (2:1 hexane:ethyl acetate) yielding a waxy white solid on drying. The solid was further purified by crystallisation from methanol/water, yielding white crystals.

Yield: 35 %. HRMS ESI$^+$ = $[C_{21}H_{37}N_2S]^+$: 349.2672 (calc), 349.2676 (found), -1.2 ppm (err). $^1$H NMR (400 MHz, DMSO-$d_6$) δ = 9.32 (br s, 1H), 7.59 (br s, 1H), 7.26 (d, *J*=8.3 Hz, 2H), 7.12 (d, *J*=8.4 Hz, 2H), 3.49 - 3.38 (m, 2H), 2.58 - 2.52 (m, obsc., 2H), 1.60 - 1.47 (m, 4H), 1.37 - 1.17 (m, 16H), 0.92 - 0.81 (m, 6H). $^{13}$C NMR (101MHz, DMSO-$d_6$) δ = 180.7, 138.8, 137.3, 128.8, 123.7, 44.3, 35.1, 31.7, 31.7, 31.5, 29.1, 29.0, 29.0, 28.9, 26.9, 22.6, 22.5, 14.4 (br s). Melting point: 47.2 – 47.8°C.

### I.1.14 1-(4-Heptylphenyl)-3-octylthiourea **69**

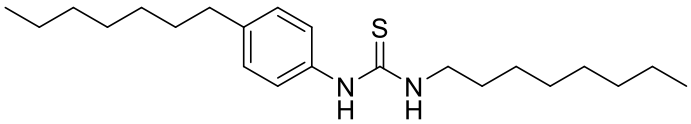


4-Heptylaniline (2.5 mmol) was dissolved in dry DCM (6 ml) under a nitrogen atmosphere. n-Octyl isothiocyanate (2.5 mmol) was added and the orange solution stirred under nitrogen overnight. The volatiles were removed under reduced pressure yielding an orange oil.

The oil was dissolved in methanol and purified on an Isolute® SCX-2 cation-exchange column. The methanol phase was collected and the solvent removed, yielding yellow oil. The oil was purified by flash chromatography (1:1 diethyl ether:hexane eluent) yielding a waxy white solid.

Yield: 9 %. HRMS ESI$^+$ = $[C_{22}H_{39}N_2S]^+$: 363.2828 (calc), 363.2836 (found), -2.0 ppm (err). $^1$H NMR (400 MHz, DMSO-$d_6$) δ = 9.34 (br s, 1H), 7.61 (br s, 1H), 7.26 (d, *J*=8.3 Hz, 2H), 7.13 (d, *J*=8.3 Hz, 2H), 3.43 (br s, 2H), 2.55 (s, 2H), 1.64 - 1.40 (m, 4H), 1.34 - 1.20 (m, 18H), 0.92 - 0.81 (m, 6H). $^{13}$C NMR (101MHz, DMSO-$d_6$) δ = 180.7, 138.8, 128.8, 123.9, 123.7, 44.3, 40.9, 35.1, 31.7, 31.7, 31.5, 29.2, 29.1, 29.1, 29.0, 29.0, 26.9, 22.6, 14.4 (br s). Melting point: 48.8 – 49.9°C.

### I.1.15 1-(4-Octylphenyl)-3-octylthiourea **70**

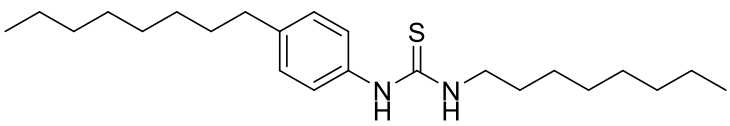

4-Octylaniline (2.5 mmol) was dissolved in pyridine (10 ml) under a nitrogen atmosphere. n-Octyl isothiocyanate (2.5 mmol) was added and the pale yellow solution stirred at 80°C under nitrogen overnight. The volatiles were removed under reduced pressure yielding brown oil.

The oil was dissolved in 3:1 methanol/chloroform and purified on an Isolute® SCX-2 cation-exchange column. The methanol phase was collected and the solvent removed, yielding an off-white solid. The solid was purified by flash chromatography (diethyl ether eluent) yielding a waxy white solid on drying. The solid was further purified by crystallisation from methanol/DCM, yielding a white solid.

Yield: 29 %. HRMS ESI$^+$ = $[C_{23}H_{41}N_2S]^+$: 377.2985 (calc), 377.2984 (found), 0.3 ppm (err); $[C_{23}H_{40}N_2SNa]^+$: 399.2804 (calc), 399.2806 (found), -0.4 ppm (err). $^1$H NMR (400 MHz, DMSO-$d_6$) δ = 9.32 (br s, 1H), 7.59 (br s, 1H), 7.26 (d, *J*=8.3 Hz, 2H), 7.12 (d, *J*=8.3 Hz, 2H), 3.50 - 3.36 (m, 2H), 1.59 - 1.46 (m, 4H), 1.34 - 1.20 (m, 20H), 0.92 - 0.81 (m, 6H). $^{13}$C NMR (101MHz, DMSO-$d_6$) δ = 180.7, 138.7, 128.8, 128.6, 124.2, 44.3, 35.1, 31.8, 31.7, 31.5, 29.3, 29.2, 29.2 (br s), 29.0, 26.9, 22.6 (br s), 14.4 (br s). Melting point: 58.3 – 59.4°C.

### I.1.16 Tris(2-isothiocyanatoethyl)amine **106**

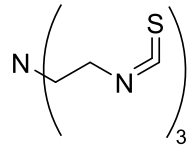


This compound was synthesised by an adapted literature procedure[138].

Tris-(2-aminoethyl)amine (10 mmol) was dissolved in THF (150 ml) under $N_2$ atmosphere. Carbon disulphide (200 mmol) was added yielding a cloudy solution. N,N-dicyclohexylcarbodiimide (31 mmol) was added and the reaction stirred overnight.

The yellow suspension was filtered 3 times to remove white/yellow solid precipitate. The solvent was removed from the filtrate under reduced pressure and the residue purified by flash chromatography (eluent: DCM) yielding pale yellow solid which was immediately carried forward for subsequent reactions without further isolation.

Yield: 32 %.

### I.1.17 1,1',1''-(Nitrilotris(ethane-2,1-diyl))tris(3-ethylthiourea) **96**

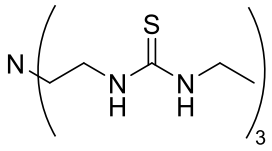

Tris(2-aminoethyl)amine (1 mmol) was dissolved in DCM (10 ml). Ethyl isothiocyanate (3 mmol) was added and the solution stirred at room temperature overnight. The solvent was removed under reduced pressure and the residue recrystallised from ethylacetate/hexane yielding white crystals.

Yield: 32 %. HRMS ESI$^+$ = $[C_{15}H_{34}N_7S_3]^+$: 408.2032 (calc), 408.22040 (found), -2.0 ppm (err). $^1$H NMR (400 MHz, DMSO-$d_6$) δ = 7.49 (br s, 1H), 7.19 (br s, 1H), 3.44 (br s, 2H), 3.33 (m, obsc.), 2.61 (t, *J*=6.2 Hz, 2H), 1.05 (t, *J*=7.2 Hz, 3H) $^{13}$C NMR (101MHz, DMSO-$d_6$) δ = 182.0, 53.1, 42.0, 38.7, 14.9. Melting point: 122.4 – 123.6°C.

### I.1.18 1,1',1''-(Nitrilotris(ethane-2,1-diyl))tris(3-propylthiourea) **97**

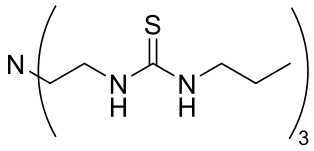

Tris(2-aminoethyl)amine (1 mmol) was dissolved in DCM (10 ml). Propyl isothiocyanate (3 mmol) was added and the solution stirred at room temperature overnight. The solvent was removed under reduced pressure yielding a yellow oil.

The oil was purified by flash chromatography (eluent: ethyl acetate) yielding a colourless oil. Appropriate phases were combined and solvent removed under reduced pressure. The residue was dried under vacuum yielding an amorphous white solid.

Yield: 62 %. HRMS ESI$^+$ = $[C_{18}H_{40}N_7S_3]^+$: 450.2502 (calc), 450.2498 (found), 0.8 ppm (err). $^1$H NMR (400 MHz, DMSO-$d_6$) δ = 7.52 (br s, 1H), 7.21 (br s, 1H), 3.46 (br s, 2H), 3.29 (br s, 2H), 2.62 (t, *J*=6.4 Hz, 2H), 1.48 (sxt, *J*=7.3 Hz, 2H), 0.85 (t, *J*=7.4 Hz, 3H). $^{13}$C NMR (101MHz, DMSO-$d_6$) δ = 182.4, 53.1, 45.8, 42.0, 22.5, 11.8 Melting point: 109.7 – 110.3°C.

### I.1.19 1,1',1''-(Nitrilotris(ethane-2,1-diyl))tris(3-butylthiourea) **98**

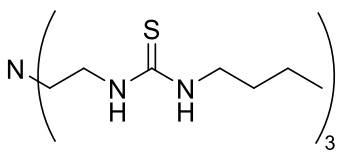

This compound had been previously reported[63].

Tris(2-aminoethyl)amine (1 mmol) was dissolved in DCM (10 ml). Butyl isothiocyanate (3 mmol) was added and the solution stirred at room temperature overnight. The solvent was removed under reduced pressure yielding a yellow oil.

Oil was purified by flash chromatography (eluent: ethyl acetate) yielding a colourless oil. Appropriate phases were combined and solvent removed under reduced pressure. The residue was dried under vacuum yielding an amorphous white solid.

Yield: 64 %. HRMS ESI$^+$ = $[C_{21}H_{46}N_7S_3]^+$: 492.2971 (calc), 492.2978 (found), -1.4 ppm (err). $^1$H NMR (400 MHz, DMSO-$d_6$) δ = 7.48 (br s, 1H), 7.19 (br s, 1H), 3.45 (br s, 2H), 3.3 (m, obsc.) 2.61 (t, *J*=6.4 Hz, 2H), 1.44 (quin, *J*=7.3 Hz, 2H), 1.28 (tq, *J*=7.3, 7.5 Hz, 2H), 0.87 (t, *J*=7.3 Hz, 3H). $^{13}$C NMR (101MHz, DMSO-$d_6$) δ = 182.4, 53.1, 43.7, 42.0, 31.3, 20.1, 14.2. Melting point 83.5 – 85.1°C.

### I.1.20 1,1',1''-(Nitrilotris(ethane-2,1-diyl))tris(3-pentylthiourea) **99**

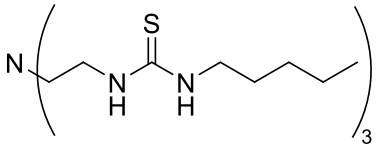

This compound was synthesised by Xin Wu and had been previously reported[93].

$^1$H NMR (400 MHz, DMSO-$d_6$) δ = 7.49 (br s, 1H), 7.20 (br s, 1H), 3.45 (br s, 2H), 3.31 (br s, obsc.), 2.70 - 2.53 (m, 2H), 1.47 (quin, *J*=7.1 Hz, 2H), 1.34 - 1.20 (m, 4H), 0.87 (t, *J*=7.0 Hz, 3H). $^{13}$C NMR (101MHz, DMSO-$d_6$) δ = 53.1, 52.2, 43.9, 42.0, 29.1, 29.2, 28.9, 28.8, 22.4, 22.3, 14.4. Melting point 80.7 – 82.8°C.

### I.1.21 1,1',1''-(Nitrilotris(ethane-2,1-diyl))tris(3-(2,2,2-trifluoroethyl)thiourea) **100**

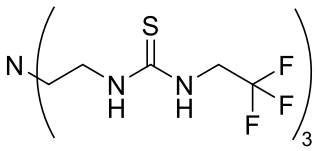

Tris(2-isothiocyanatoethyl)amine (**106**, I.1.16) (1 mmol) was dissolved in DCM (10 ml). 2,2,2-trifluoroethylamine (3 mmol) was added and the solution stirred at room temperature for 24 hours. The solvent was removed under reduced pressure and the residue was recrystallized from DCM/Hexane yielding a white powder.

Yield: 66 %. HRMS ESI$^+$ = $[C_{15}H_{25}F_9N_7S_3]^+$: 570.1184 (calc), 570.1170 (found), 2.5 ppm (err). $^1$H NMR (400 MHz, DMSO-$d_6$) δ ppm 2.65 (br t, *J*=6.85 Hz, 3 H) 3.53 (br s, 2 H) 4.29 - 4.47 (m, 3 H) 7.66 (br s, 1 H) 7.97 (br s, 1 H). $^{13}$C NMR (101 MHz, DMSO-$d_6$) δ ppm 42.6484 (br s, 1 C) 44.6061 (br q, *J*=35.40 Hz, 1 C) 52.6228 (br s, 1 C) 125.3424 (q, *J*=279.50 Hz, 1 C) 184.3689 (br s, 1 C). $^{19}$F NMR (376 MHz, DMSO-$d_6$) δ ppm -70.6143 (br s, 1 F). Melting point: 142.0 – 142.8°C.

### I.1.22 1,1',1''-(Nitrilotris(ethane-2,1-diyl))tris(3-(2,2,3,3,3-pentafluoropropyl)thiourea) **101**

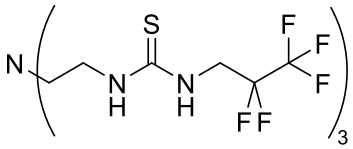

Tris(2-isothiocyanatoethyl)amine (**106**, I.1.16) (1 mmol) was dissolved in DCM (10 ml). 2,2,3,3,3-pentafluoropropylamine (3 mmol) was added and the solution stirred at room temperature for 24 hours.

The solvent was removed under reduced pressure and the residue purified by flash chromatography on an Isolute Si-II column. The residue was loaded with diethyl ether and eluted with ethyl acetate. The ethyl acetate phase was evaporated yielding a colourless oil. The oil was further purified by recrystallization from DCM/hexane yielding a white solid.

Yield: 18 %. HRMS ESI$^+$ = $[C_{18}H_{25}F_{15}N_7S_3]^+$: 720.1089 (calc), 720.1094 (found), -0.7 ppm (err). $^1$H NMR (400 MHz, DMSO-$d_6$) δ = 7.91 (br s, 1H), 7.70 (br s, 1H), 4.50 (dt, *J*=5.7, 16.1 Hz, 2H), 3.54 (br s, 2H), 2.66 (br t, *J*=6.8 Hz, 2H). $^{13}$C NMR (101MHz, DMSO-$d_6$) δ = 184.6, 117.4 (tq, *J*=34.5, 286.8 Hz), 113.9 (qt, *J*=36.0, 253.1 Hz), 52.6, 43.0, 42.7. $^{19}$F NMR (376MHz, DMSO-$d_6$) δ = -83.58 (br s), -120.44 (br t, *J*=15.6 Hz). Melting point: 130.9 – 131.5°C.

### I.1.23 1,1',1''-(Nitrilotris(ethane-2,1-diyl))tris(3-(2,2,3,3,4,4,4-heptafluorobutyl)thiourea) **102**

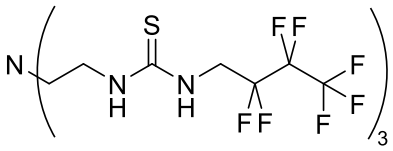

This compound was synthesised by Xin Wu in currently unpublished results.

A suspension of 1H,1H-perfluorobutylamine (0.49 g, 2.5 mmol) and tris(2-isothiocyanatoethyl)amine (**106**, I.1.16) (0.22 g, 0.81 mmol) in DCM (8 ml) was left to stand for 6 days. The white crystals formed were collected and washed with DCM to give pure product.

Yield: 58 %. $^{1}$H NMR (400 MHz, DMSO-$d_6$) δ = 7.91 (br s, 1H), 7.73 (br s, 1H), 4.54 (dt, *J*=5.7, 16.9 Hz, 2H), 3.33 (s, 1H), 2.67 (br t, *J*=6.8 Hz, 2H). $^{13}$C NMR (101MHz, DMSO-$d_6$) δ = 184.7, 117.8 (qt, *J*=286.8, 33.8 Hz), 115.8 (tt, *J*=254.9, 30.5 Hz), 109.0 (tq, *J*=264.1, 36.7 Hz), 52.6, 43.0 (t, *J*=21.3 Hz), 42.7. $^{19}$F NMR (376MHz, DMSO-$d_6$) δ = -80.43 (br t, *J*=8.7 Hz), -117.35 - -118.13 (m), -127.67 (br s). Melting point 152.5 – 153.2°C.

### I.1.24 1,1',1''-(Nitrilotris(ethane-2,1-diyl))tris(3-(2,2,3,3,4,4,5,5,5-nonafluoropentyl)thiourea) **103**

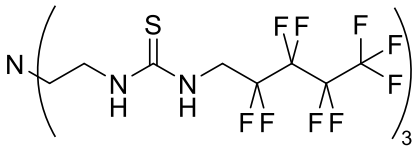

This compound was synthesised by Xin Wu in currently unpublished results.

A solution of 1H,1H-perfluoropentylamine (0.54 g, 2.2 mmol) and tris(2-isothiocyanatoethyl)amine (**106**, I.1.16) (0.19 g, 0.72 mmol) in DCM (4 ml) was left to stand for 6 days. The white crystals formed were collected and washed with DCM to give pure product.

Yield: 72 %. $^{1}$H NMR (400 MHz, DMSO-$d_6$) δ = 7.91 (br s, 1H), 7.72 (br s, 1H), 4.56 (dt, *J*=5.6, 16.8 Hz, 2H), 3.55 (br s, 2H), 2.67 (br t, *J*=6.8 Hz, 2H). $^{19}$F NMR (376MHz, DMSO-$d_6$) δ = -80.67 (br t, *J*=8.7 Hz), -117.16 (br s), -124.34 (br s), -126.01 (br t, *J*=12.1 Hz). Melting point 164.4 – 165.2°C.

### I.1.25 1,1',1''-(Nitrilotris(ethane-2,1-diyl))tris(3-(3,3,3-trifluoropropyl)thiourea) **104**

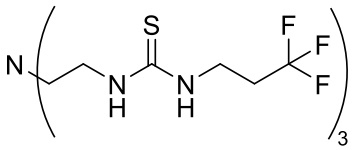

Tris(2-isothiocyanatoethyl)amine (**106**, I.1.16) (1 mmol) was dissolved in DCM (10 ml). 3,3,3-trifluoropropylamine (3 mmol) was added and the solution stirred at room temperature for 24 hours.

The solvent was removed under reduced pressure and the residue purified by flash chromatography on an Isolute Si-II column. The residue was loaded with diethyl ether and eluted with ethyl acetate. The ethyl acetate phase was evaporated yielding a colourless oil which formed an amorphous solid on drying.

Yield: 92 %. HRMS ESI$^{+}$ = $[C_{18}H_{31}F_9N_7S_3]^{+}$: 612.1654 (calc), 612.1668 (found), -2.3 ppm (err). $^{1}$H NMR (400 MHz, DMSO-$d_6$) δ = 7.62 (br s, 1H), 7.47 (br s, 1H), 3.63 (br s, 2H), 3.45 (br s, 2H), 2.63 (t, *J*=6.6

Hz, 2H), 2.53 (m, obsc.). $^{13}$C NMR (101MHz, DMSO-$d_6$) δ = 183.0, 127.3 (q, *J*=276.8 Hz), 52.9, 42.0, 37.3, 33.0. $^{13}$C NMR (101MHz, DMSO-$d_6$) δ = 184.7, 117.4 (qt, *J*=288.3, 34.5 Hz,, 116.3 ((tt, *J*=256.0, 32.3 Hz), 112.33 - 104.25 (m), 52.6, 43.1, 42.7. $^{19}$F NMR (376MHz, DMSO-$d_6$) δ = -63.78 (br t, *J*=12.1 Hz). Melting point: 82.3 – 83.6°C.

### I.1.26 1,1',1''-(Nitrilotris(ethane-2,1-diyl))tris(3-(4,4,4-trifluorobutyl)thiourea) **105**

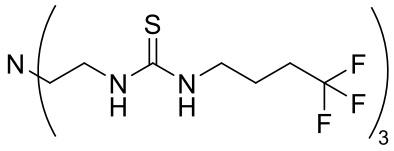

Tris(2-isothiocyanatoethyl)amine (**106**, I.1.16) (1 mmol) was dissolved in DCM (10 ml). 4,4,4-trifluorobutylamine (3 mmol) was added and the solution stirred at room temperature for 24 hours.

The solvent was removed under reduced pressure and the residue purified by flash chromatography on an Isolute Si-II column. The residue was loaded with diethyl ether and eluted with ethyl acetate. The ethyl acetate phase was evaporated yielding a colourless oil which formed an amorphous solid on drying.

Yield: 77 %. HRMS ESI$^+$ = [$C_{21}H_{37}F_9N_7S_3$]$^+$: 654.2123 (calc), 654.2126 (found), -0.4 ppm (err). $^1$H NMR (400 MHz, DMSO-$d_6$) δ = 7.61 (br s, 1H), 7.28 (br s, 1H), 3.43 (br s, 4H), 2.62 (br t, *J*=6.7 Hz, 2H), 2.24 (tq, *J*=8.3, 11.6 Hz, 2H), 1.70 (tt, *J*=7.5 Hz, 2H). $^{13}$C NMR (101MHz, DMSO-$d_6$) δ = 182.7, 128.1 (q, *J*=276.3 Hz), 52.9, 42.6, 42.0, 30.7 (q, *J*=27.9 Hz), 22.1. $^{19}$F NMR (376MHz, DMSO-$d_6$) δ = -64.84 (t, *J*=11.3 Hz). Melting point: 97.6 – 99.9°C.

## I.2 NMR Spectra

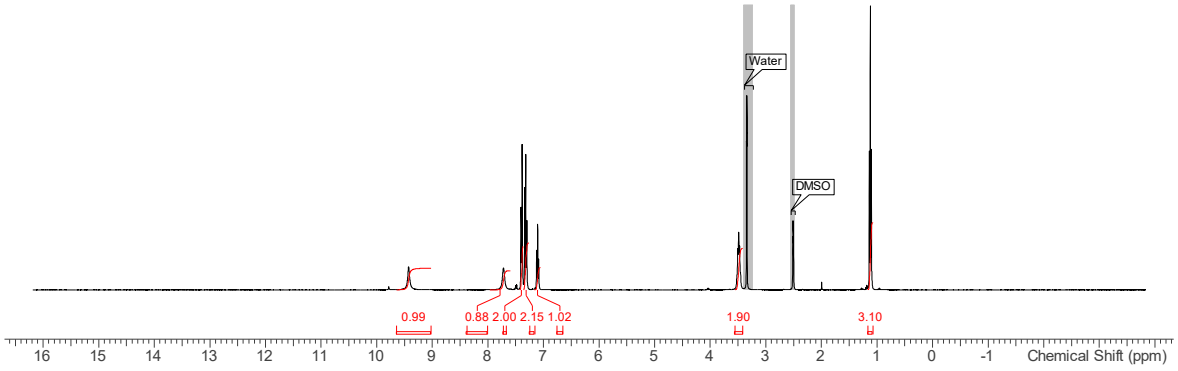


**Figure I.1** $^{1}$H NMR (400 MHz, DMSO-$d_6$) spectrum of 1-phenyl-3-ethylthiourea **56**.

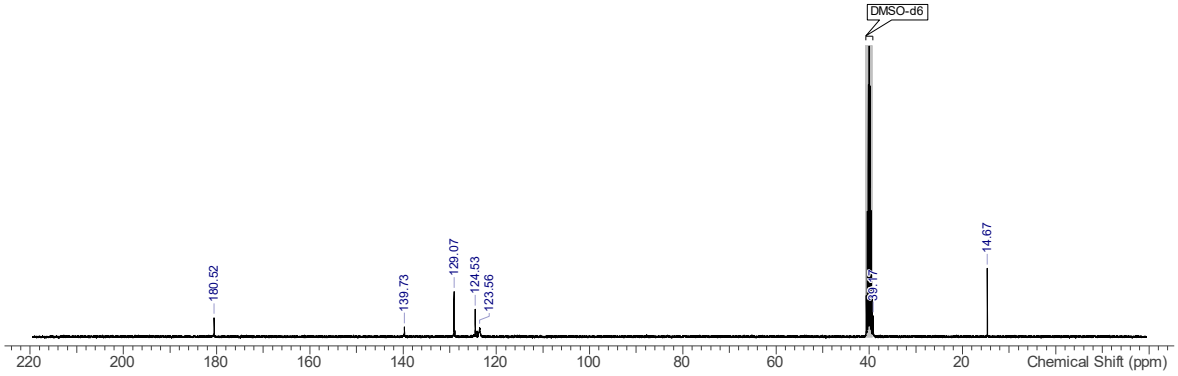


**Figure I.2** $^{13}$C NMR (101 MHz, DMSO-$d_6$) spectrum of 1-phenyl-3-ethylthiourea **56**.

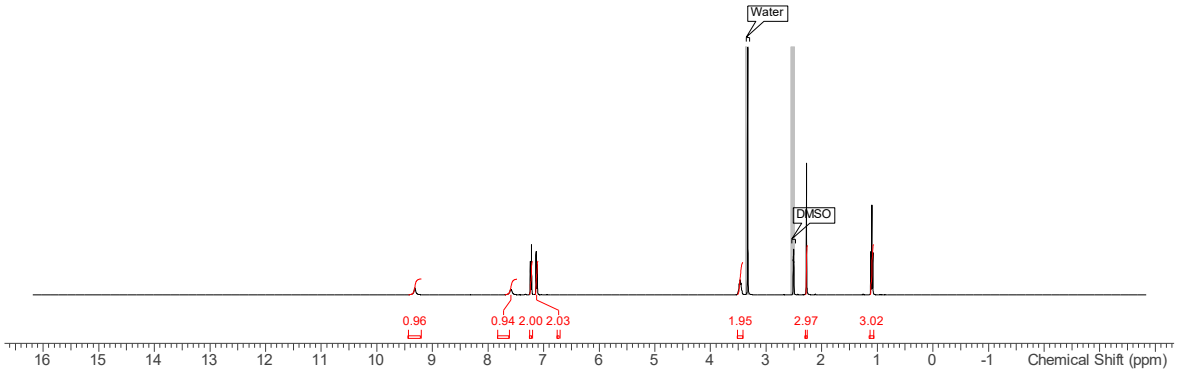


**Figure I.3** $^{1}$H NMR (400 MHz, DMSO-$d_6$) spectrum of 1-(p-tolyl)-3-ethylthiourea **57**.

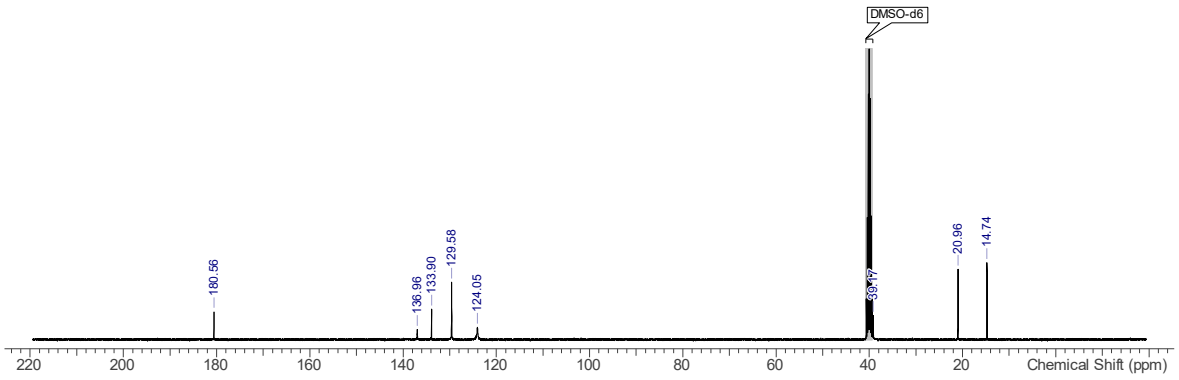


**Figure I.4** $^{13}$C NMR (101 MHz, DMSO-d$_6$) spectrum of 1-(p-tolyl)-3-ethylthiourea **57**.

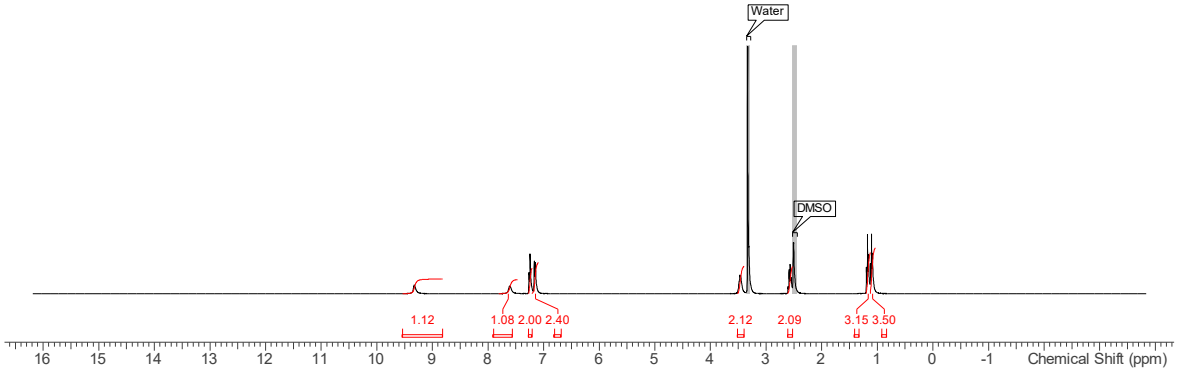


**Figure I.5** $^{1}$H NMR (400 MHz, DMSO-d$_6$) spectrum of 1-(4-ethylphenyl)-3-ethylthiourea **58**.

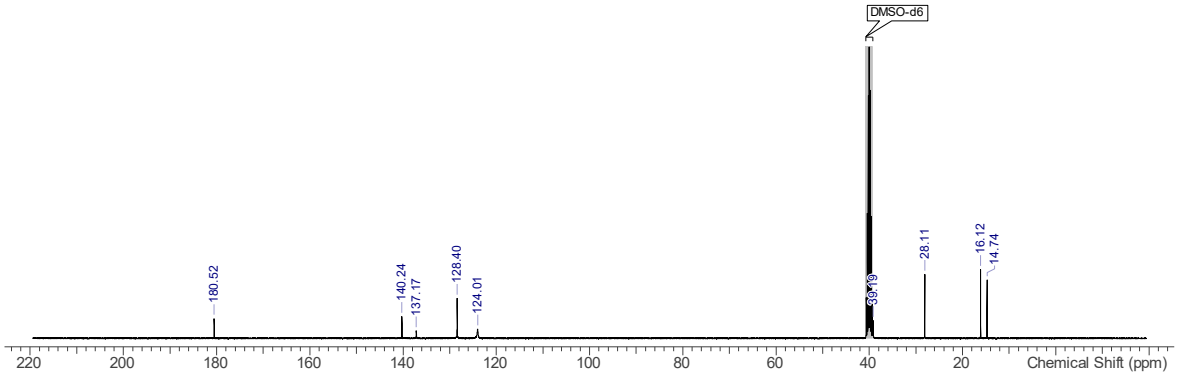


**Figure I.6** $^{13}$C NMR (101 MHz, DMSO-d$_6$) spectrum of 1-(4-ethylphenyl)-3-ethylthiourea **58**.

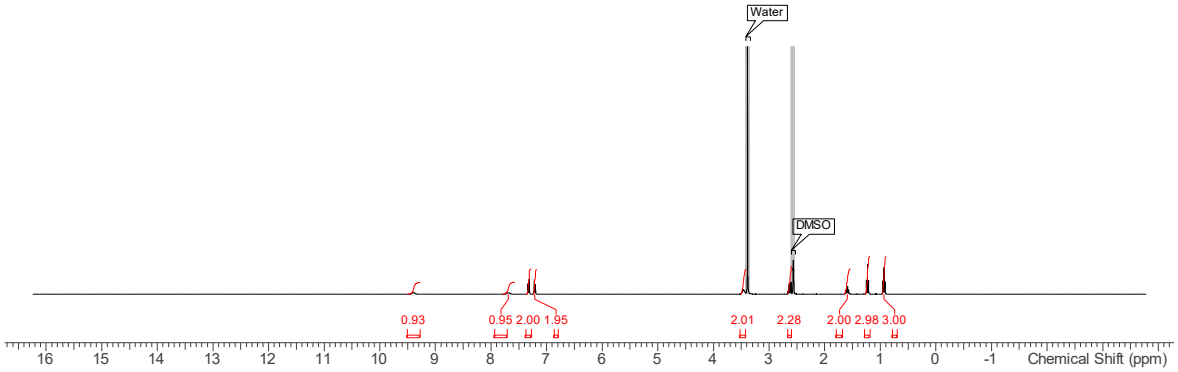


**Figure I.7** $^{1}$H NMR (400 MHz, DMSO-$d_6$) spectrum of 1-(4-ethylphenyl)-3-propylthiourea **59**.

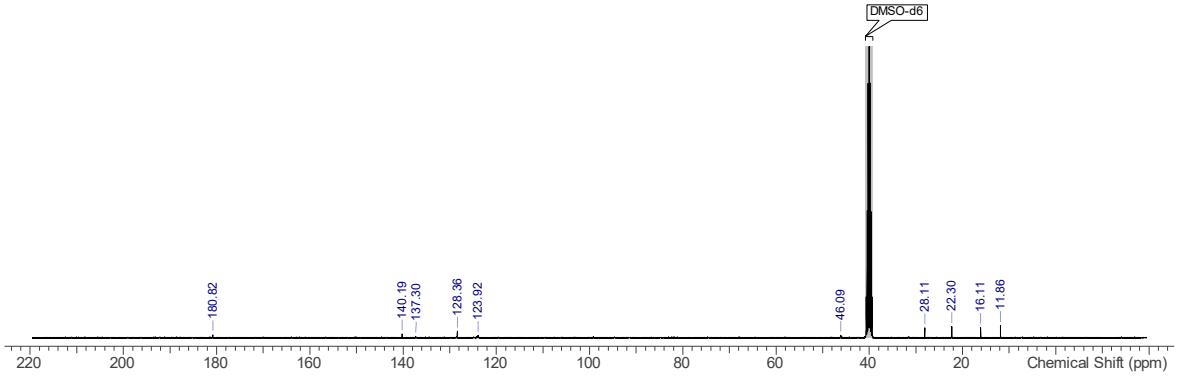


**Figure I.8** $^{13}$C NMR (101 MHz, DMSO-$d_6$) spectrum of 1-(4-ethylphenyl)-3-propylthiourea **59**.

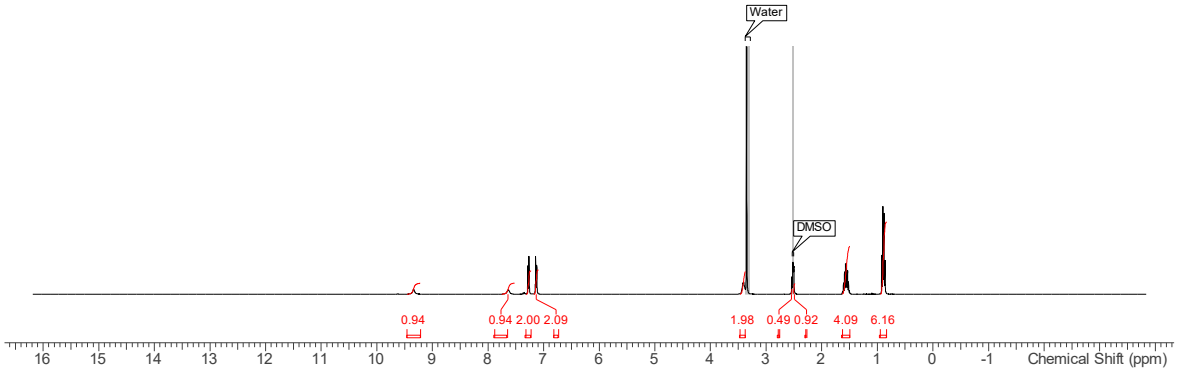


**Figure I.9** $^{1}$H NMR (400 MHz, DMSO-$d_6$) spectrum of 1-(4-propylphenyl)-3-propylthiourea **60**.

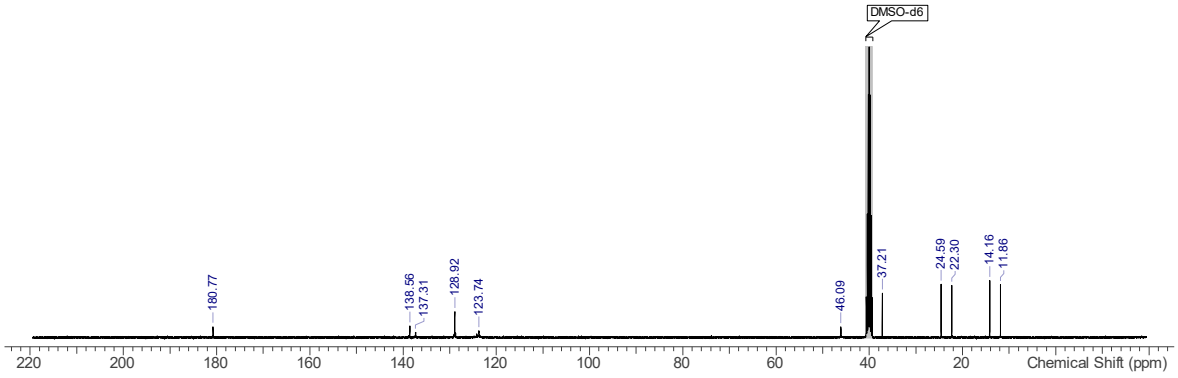


**Figure I.10** $^{13}$C NMR (101 MHz, DMSO-$d_6$) spectrum of 1-(4-propylphenyl)-3-propylthiourea **60**.

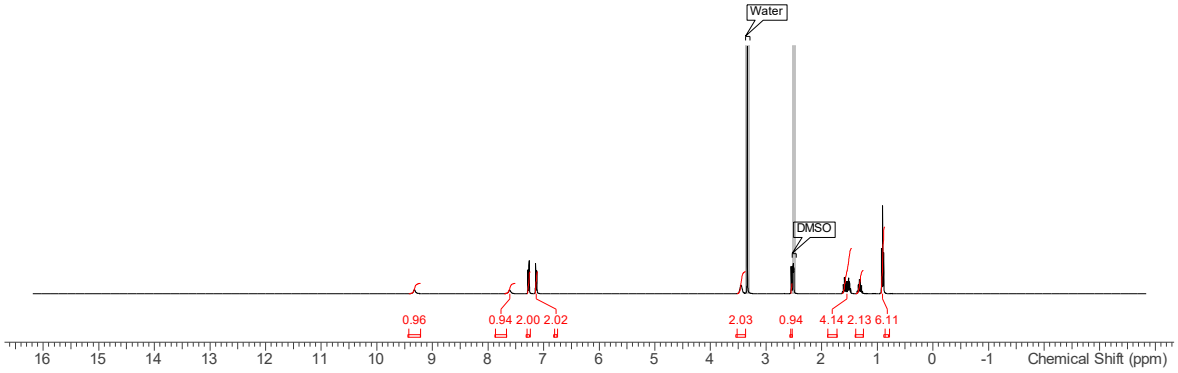


**Figure I.11** $^{1}$H NMR (400 MHz, DMSO-$d_6$) spectrum of 1-(4-propylphenyl)-3-butylthiourea **61**.

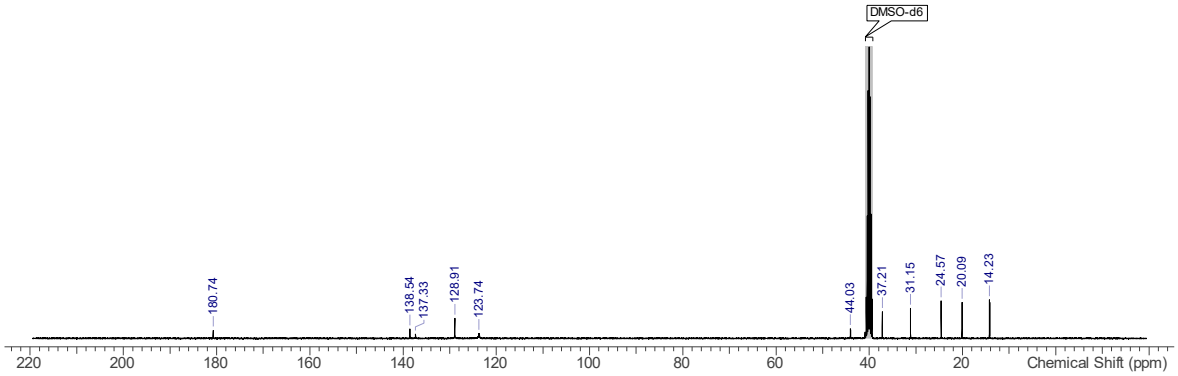


**Figure I.12** $^{13}$C NMR (101 MHz, DMSO-$d_6$) spectrum of 1-(4-propylphenyl)-3-butylthiourea **61**.

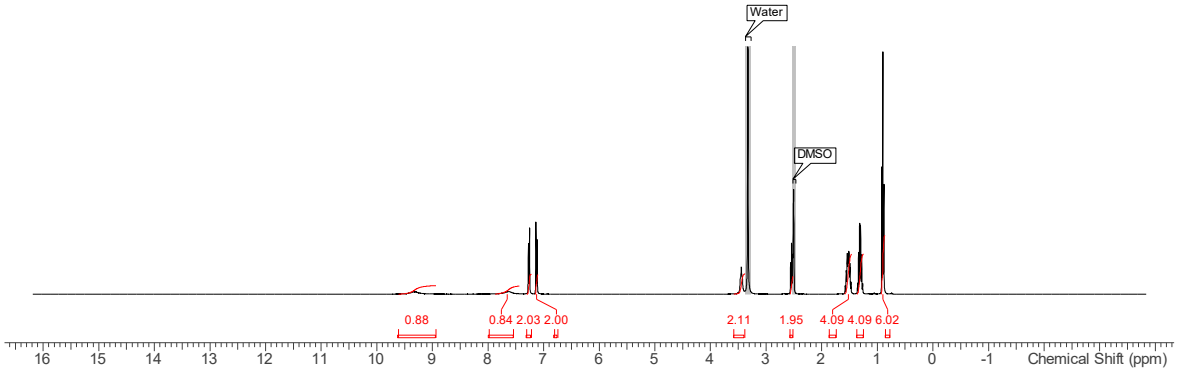


**Figure I.13** $^{1}$H NMR (400 MHz, DMSO-$d_6$) spectrum of 1-(4-butylphenyl)-3-butylthiourea **62**.

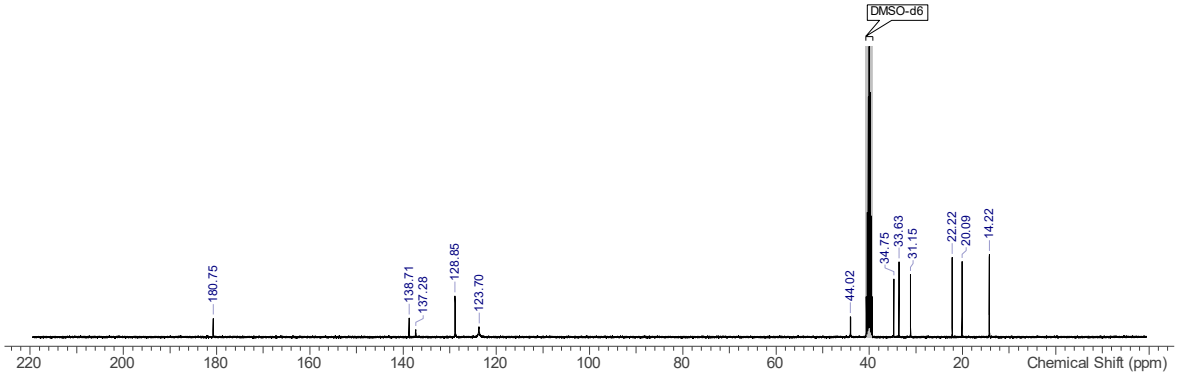


**Figure I.14** $^{13}$C NMR (101 MHz, DMSO-$d_6$) spectrum of 1-(4-butylphenyl)-3-butylthiourea **62**.

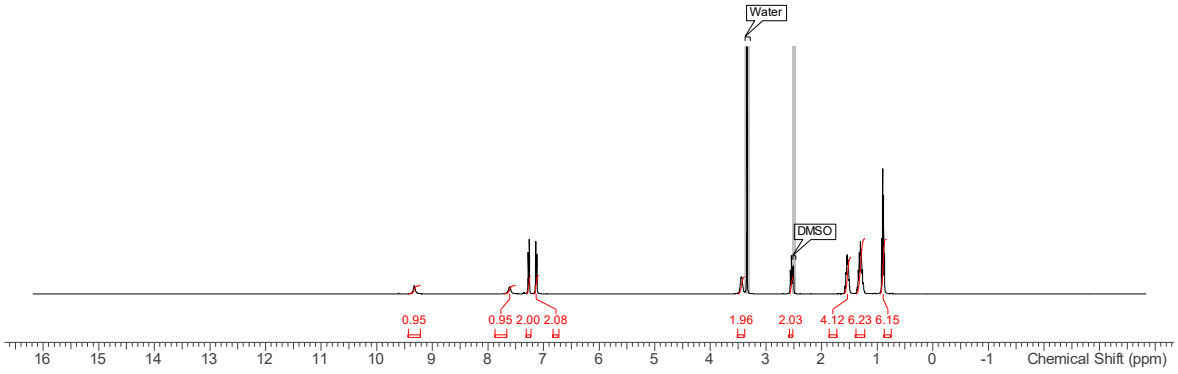


**Figure I.15** $^{1}$H NMR (400 MHz, DMSO-$d_6$) spectrum of 1-(4-butylphenyl)-3-pentylthiourea **63**.

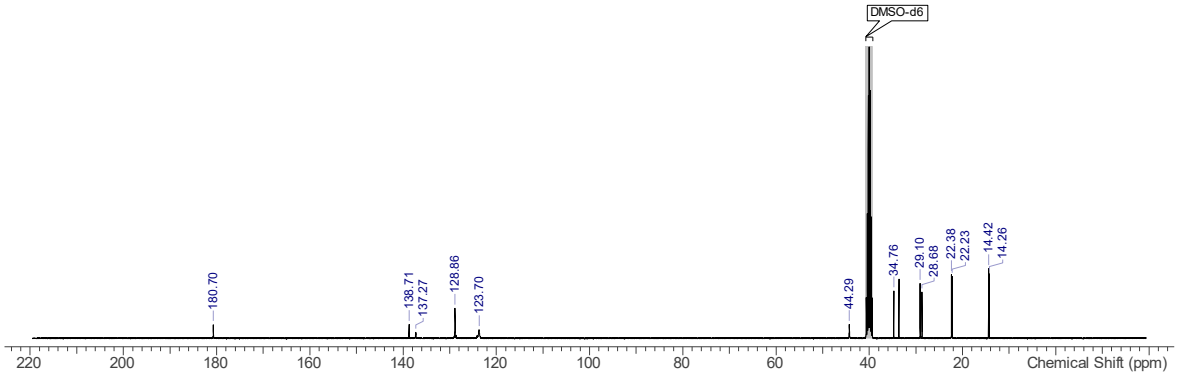


**Figure I.16** $^{13}$C NMR (101 MHz, DMSO-$d_6$) spectrum of 1-(4-butylphenyl)-3-pentylthiourea **63**.

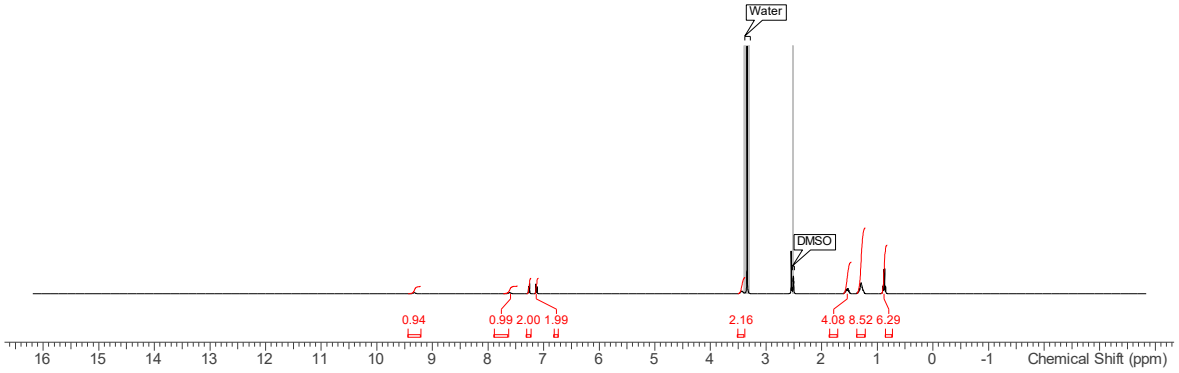


**Figure I.17** $^{1}$H NMR (400 MHz, DMSO-$d_6$) spectrum of 1-(4-pentylphenyl)-3-pentylthiourea **64**.

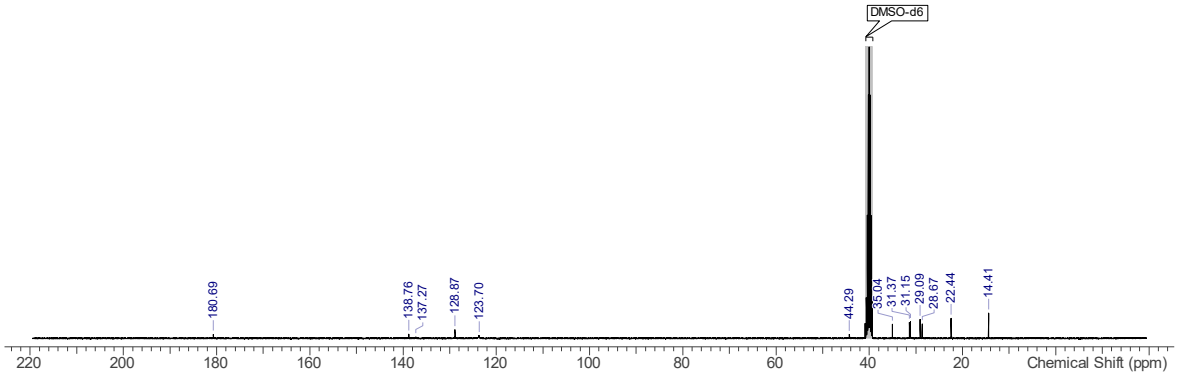


**Figure I.18** $^{13}$C NMR (101 MHz, DMSO-$d_6$) spectrum of 1-(4-pentylphenyl)-3-pentylthiourea **64**.

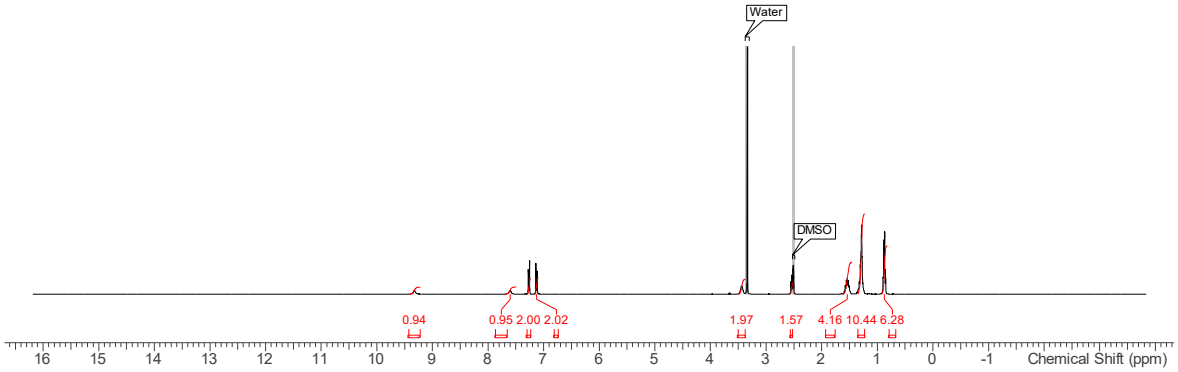


**Figure I.19** $^{1}$H NMR (400 MHz, DMSO-$d_6$) spectrum of 1-(4-pentylphenyl)-3-hexylthiourea **65**.

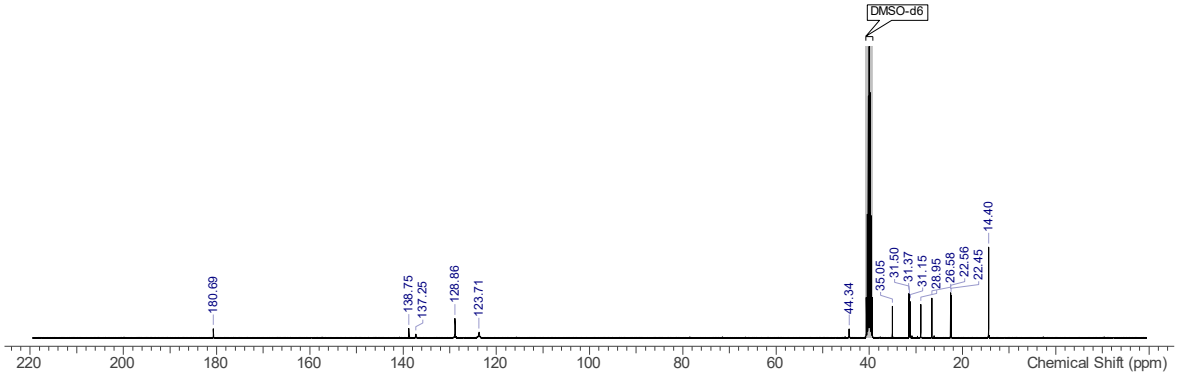


**Figure I.20** $^{13}$C NMR (101 MHz, DMSO-$d_6$) spectrum of 1-(4-pentylphenyl)-3-hexylthiourea **65**.

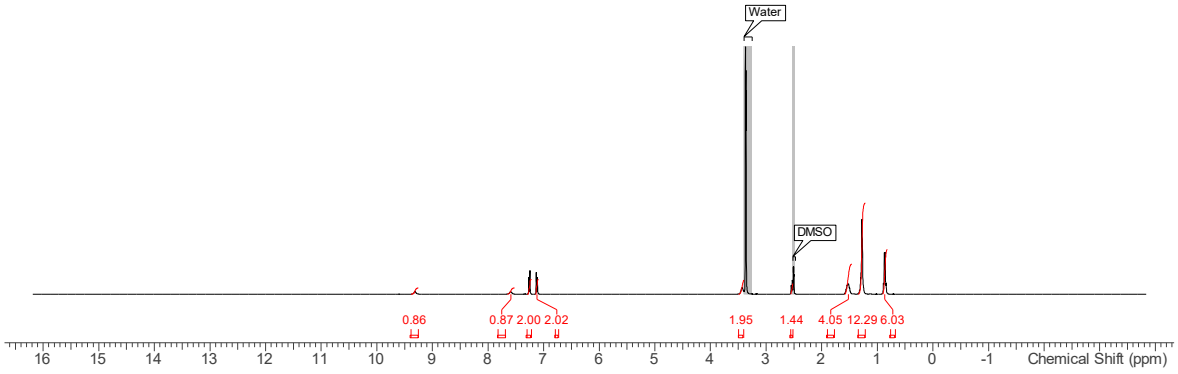


**Figure I.21** $^{1}$H NMR (400 MHz, DMSO-$d_6$) spectrum of 1-(4-hexylphenyl)-3-hexylthiourea **66**.

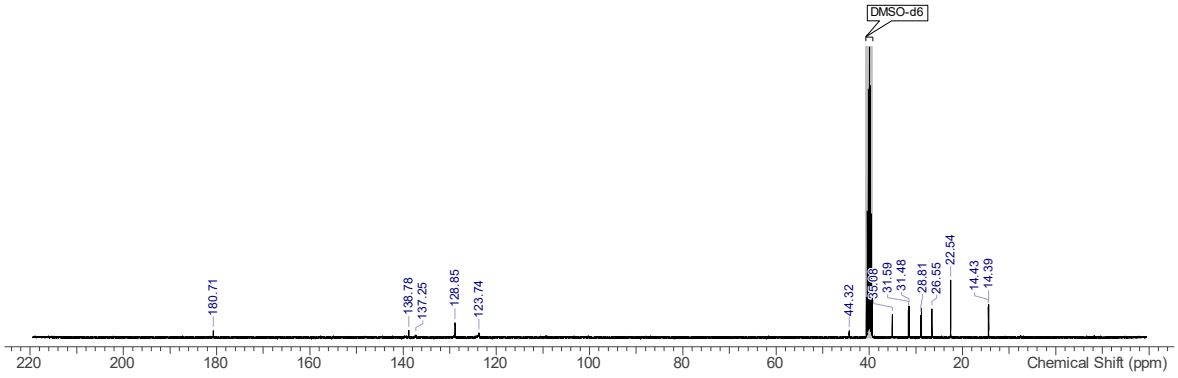


**Figure I.22** $^{13}$C NMR (101 MHz, DMSO-$d_6$) spectrum of 1-(4-hexylphenyl)-3-hexylthiourea **66**.

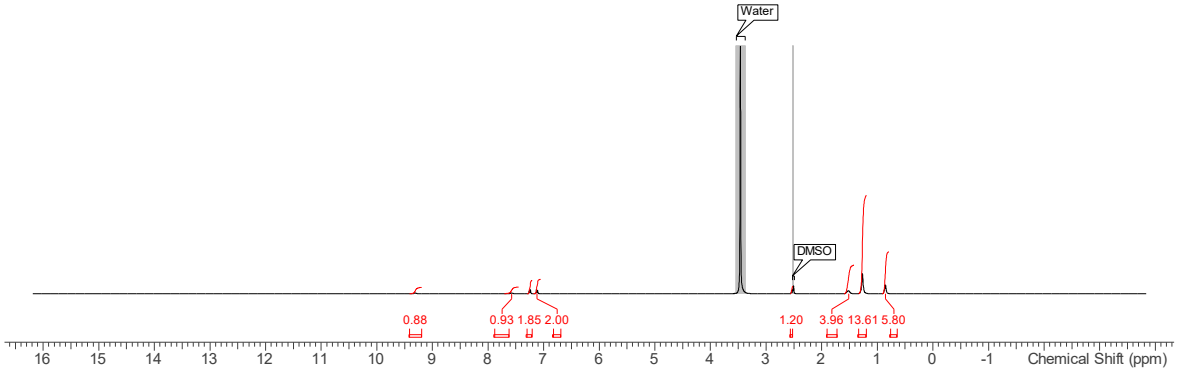


**Figure I.23** $^{1}$H NMR (400 MHz, DMSO-$d_6$) spectrum of 1-(4-hexylphenyl)-3-heptylthiourea **67**.

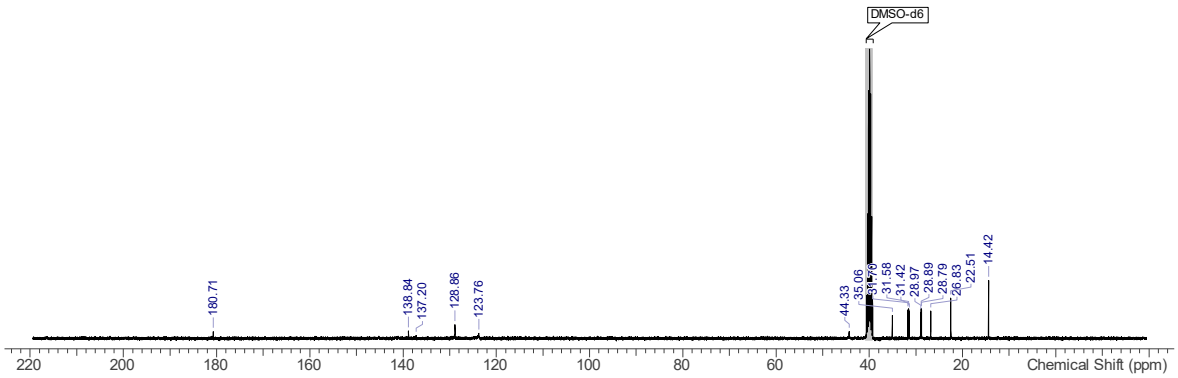


**Figure I.24** $^{13}$C NMR (101 MHz, DMSO-$d_6$) spectrum of 1-(4-hexylphenyl)-3-heptylthiourea **67**.

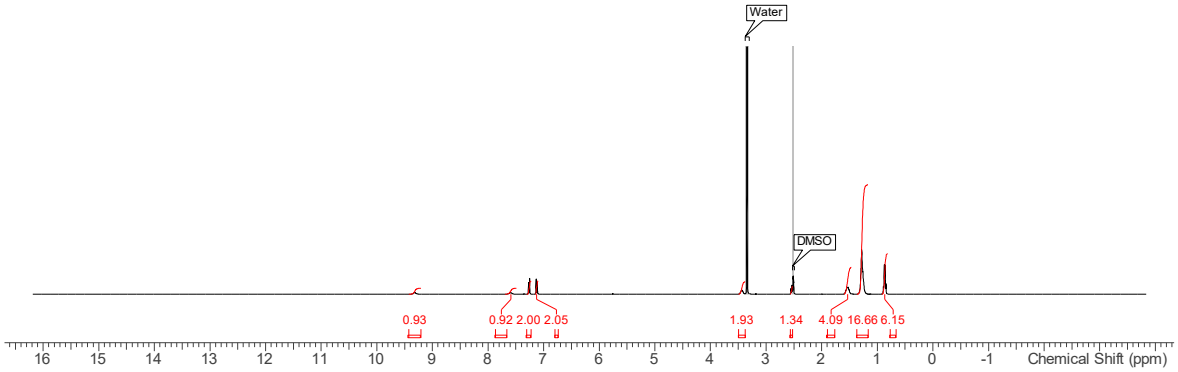


**Figure I.25** $^{1}$H NMR (400 MHz, DMSO-$d_6$) spectrum of 1-(4-heptylphenyl)-3-heptylthiourea **68**.

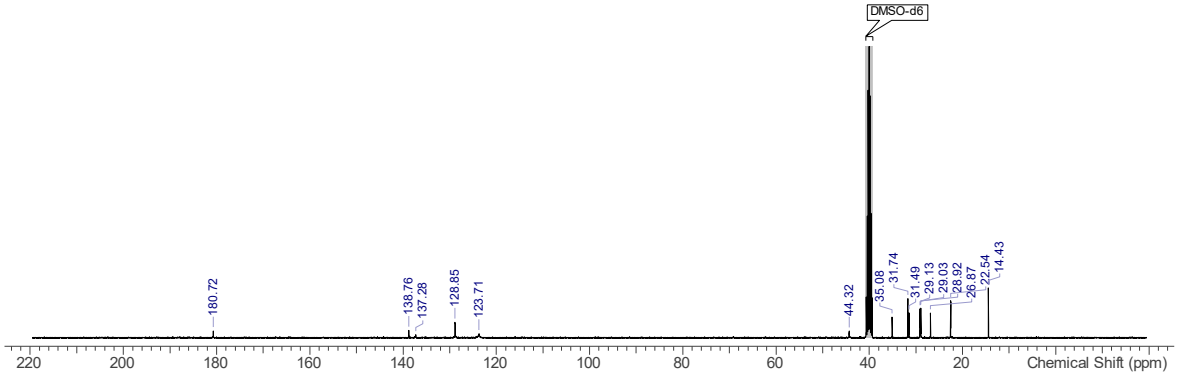


**Figure I.26** $^{13}$C NMR (101 MHz, DMSO-$d_6$) spectrum of 1-(4-heptylphenyl)-3-heptylthioure **68**.

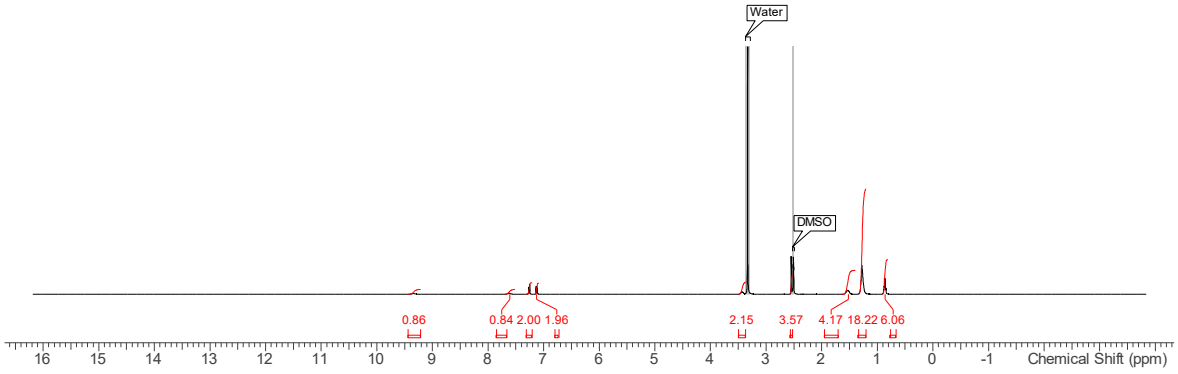


**Figure I.27** $^{1}$H NMR (400 MHz, DMSO-$d_6$) spectrum of 1-(4-heptylphenyl)-3-octylthiourea **69**.

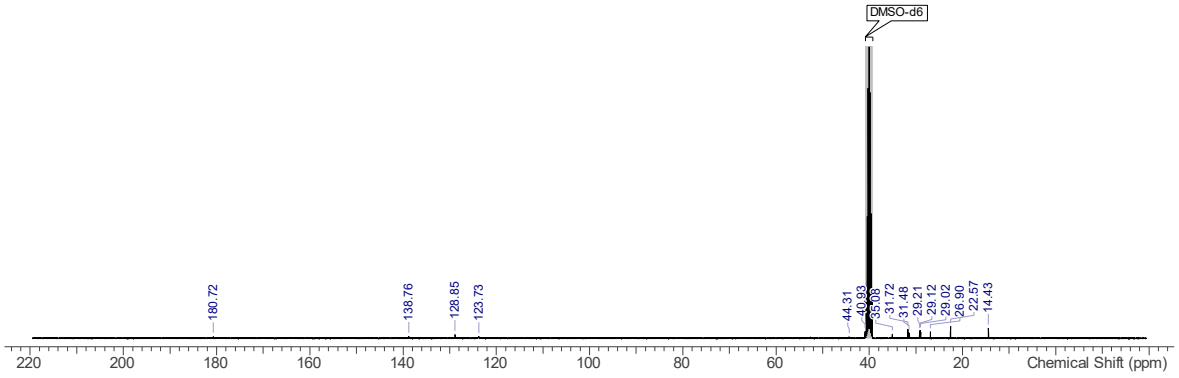


**Figure I.28** $^{13}C$ NMR (101 MHz, DMSO-$d_6$) spectrum of 1-(4-heptylphenyl)-3-octylthiourea **69**.

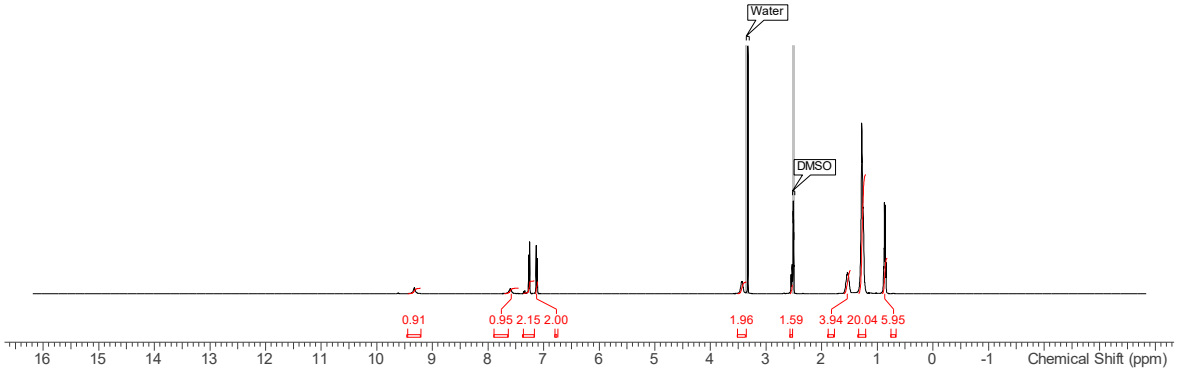


**Figure I.29** $^{1}H$ NMR (400 MHz, DMSO-$d_6$) spectrum of 1-(4-octylphenyl)-3-octylthiourea **70**.

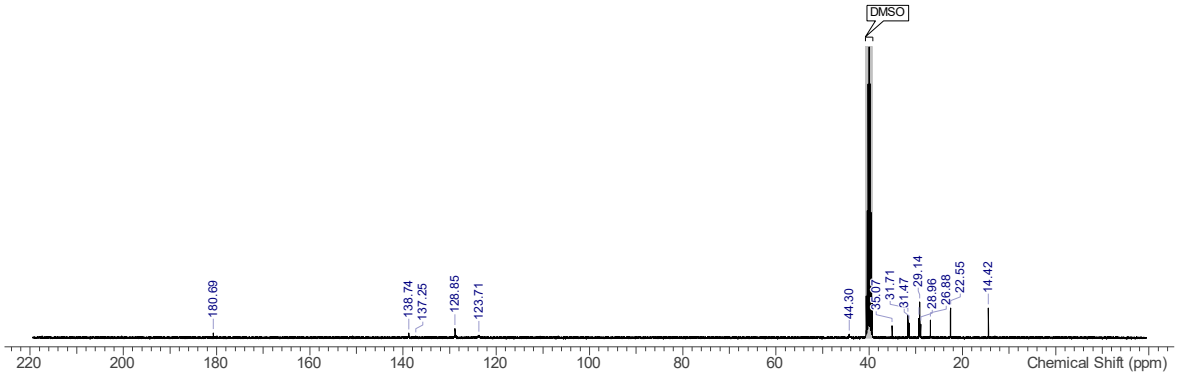


**Figure I.30** $^{13}C$ NMR (101 MHz, DMSO-$d_6$) spectrum of 1-(4-octylphenyl)-3-octylthiourea **70**.

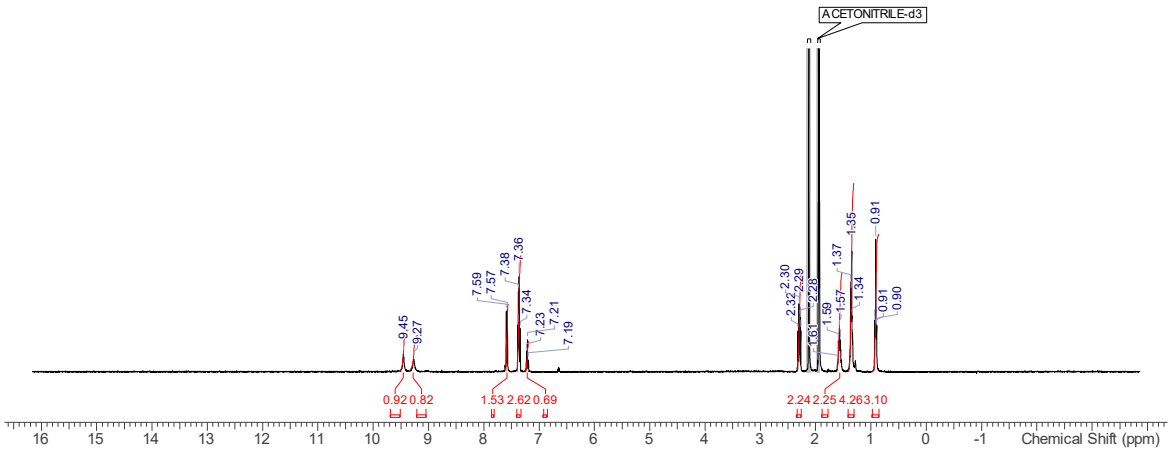


**Figure I.31** $^{1}$H NMR (400 MHz, $CD_3CN$) spectrum of (*E*)-2-hexylidene-*N*-phenylhydrazine-1-carbothioamide **73**. $^{1}$H NMR (400 MHz, $CD_3CN$) δ = 9.45 (br s, 1H), 9.27 (br s, 1H), 7.58 (d, *J*=7.6 Hz, 2H), 7.40 - 7.33 (m, 3H), 7.25 - 7.18 (m, 1H), 2.30 (dt, *J*=5.5, 7.4 Hz, 2H), 1.62 - 1.51 (m, 2H), 1.41 - 1.30 (m, 4H), 0.98 - 0.85 (m, 3H).

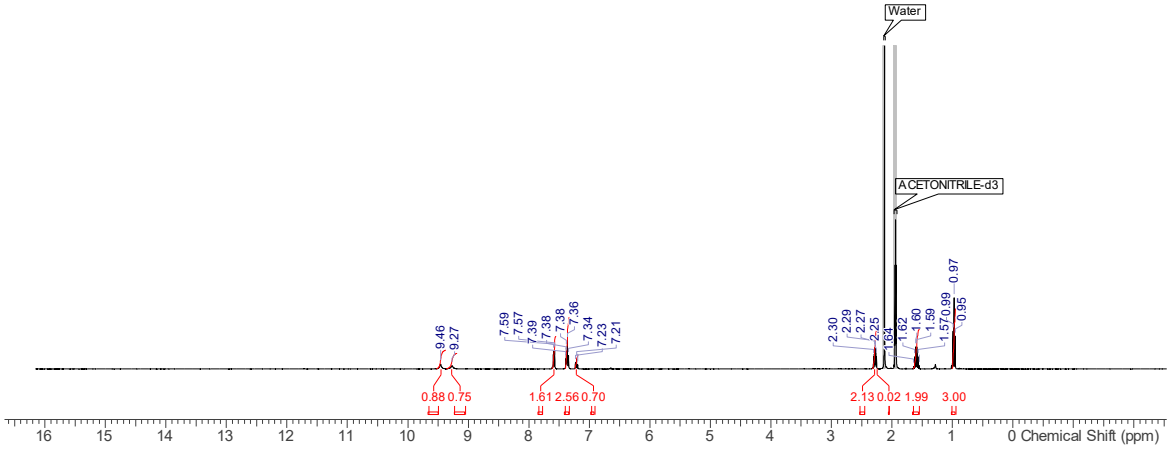


**Figure I.32** $^{1}$H NMR (400 MHz, $CD_3CN$) spectrum of (*E*)-2-butylidene-*N*-phenylhydrazine-1-carbothioamide **74**. $^{1}$H NMR (400 MHz, $CD_3CN$) δ = 9.46 (br s, 1H), 9.37 - 9.19 (m, 1H), 7.58 (d, *J*=7.6 Hz, 2H), 7.40 - 7.33 (m, 3H), 7.24 - 7.19 (m, 1H), 2.28 (dt, *J*=5.5, 7.4 Hz, 2H), 1.64 - 1.55 (m, 2H), 0.97 (t, *J*=7.5 Hz, 3H).

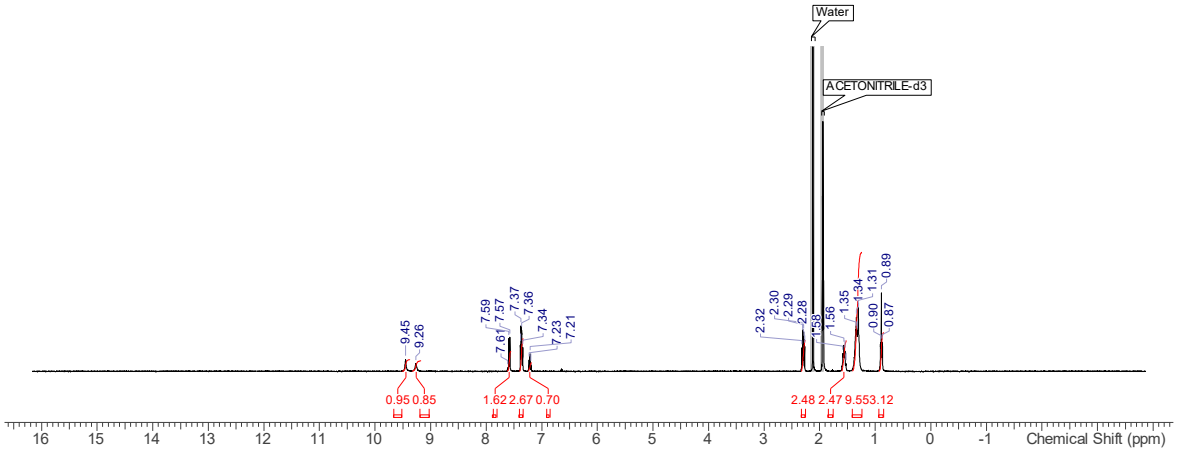


**Figure I.33** $^{1}$H NMR (400 MHz, $CD_3CN$) spectrum of (*E*)-2-octylidene-*N*-phenylhydrazine-1-carbothioamide **75**. $^{1}$H NMR (400 MHz, $CD_3CN$) δ = 9.45 (br s, 1H), 9.26 (br s, 1H), 7.58 (d, *J*=7.6 Hz, 2H), 7.40 - 7.33 (m, 3H), 7.25 - 7.18 (m, 1H), 2.30 (dt, *J*=5.5, 7.4 Hz, 2H), 1.60 - 1.52 (m, 2H), 1.41 - 1.24 (m, 10H), 0.89 (t, *J*=7.1 Hz, 3H).

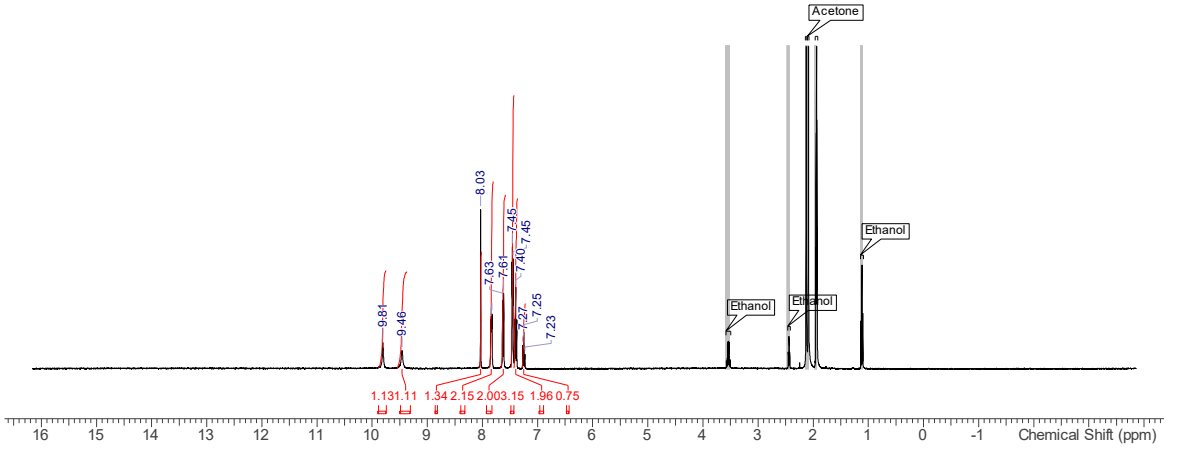


**Figure I.34** $^{1}$H NMR (400 MHz, $CD_3CN$) spectrum of (*E*)-2-benzylidene-*N*-phenylhydrazine-1-carbothioamide **76**. $^{1}$H NMR (400 MHz, $CD_3CN$) δ = 9.81 (br s, 1H), 9.46 (br s, 1H), 8.03 (s, 1H), 7.88 - 7.80 (m, 2H), 7.62 (d, *J*=7.8 Hz, 2H), 7.48 - 7.43 (m, 3H), 7.40 (t, *J*=7.8 Hz, 2H), 7.25 (t, *J*=7.3 Hz, 1H).

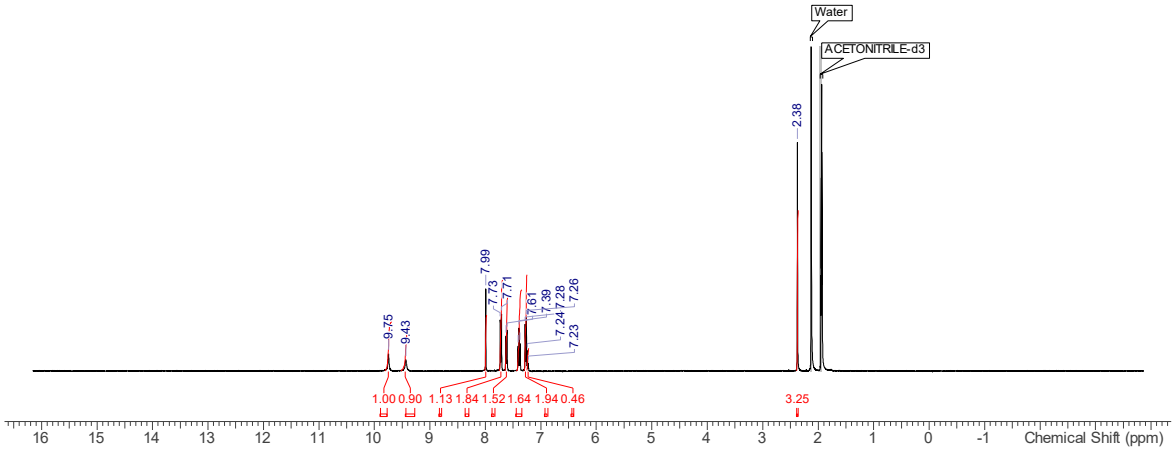


**Figure I.35** $^{1}$H NMR (400 MHz, $CD_3CN$) spectrum of (*E*)-2-(4-methylbenzylidene)-*N*-phenylhydrazine-1-carbothioamide **77**. $^{1}$H NMR (400 MHz, $CD_3CN$) δ = 9.75 (br s, 1H), 9.43 (br s, 1H), 7.99 (s, 1H), 7.72 (d, *J*=8.3 Hz, 2H), 7.62 (d, *J*=7.8 Hz, 2H), 7.39 (t, *J*=7.8 Hz, 2H), 7.27 (d, *J*=8.3 Hz, 2H), 7.25 - 7.21 (m, 1H), 2.38 (s, 3H).

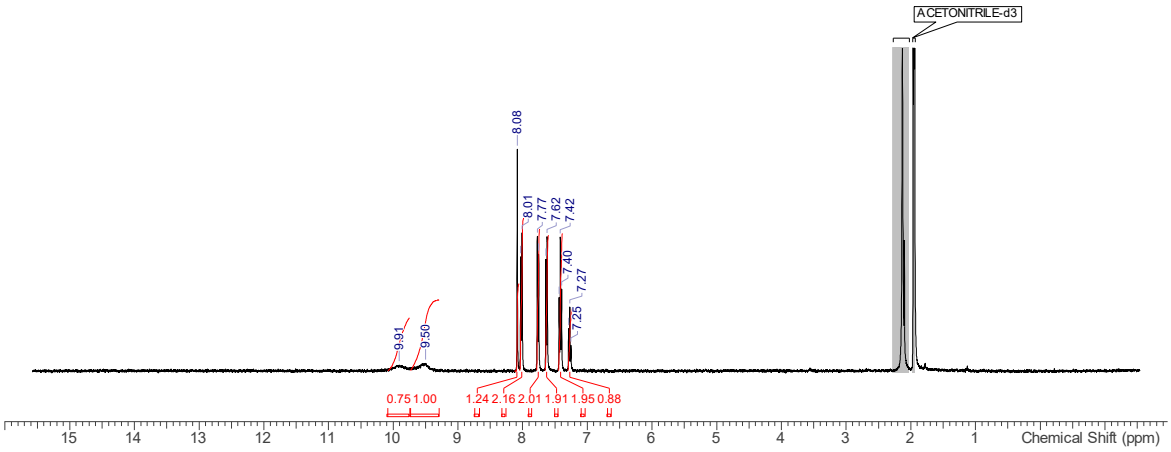


**Figure I.36** $^{1}$H NMR (400 MHz, $CD_3CN$) spectrum of (*E*)-*N*-phenyl-2-(4-(trifluoromethyl)benzylidene) hydrazine-1-carbothioamide **78**. $^{1}$H NMR (400 MHz, $CD_3CN$) δ = 9.91 (br s, 1H), 9.50 (br s, 1H), 8.08 (s, 1H), 8.02 (d, *J*=8.4 Hz, 2H), 7.76 (d, *J*=7.9 Hz, 2H), 7.63 (d, *J*=7.5 Hz, 2H), 7.42 (t, *J*=7.9 Hz, 2H), 7.27 (t, *J*=7.3 Hz, 1H).

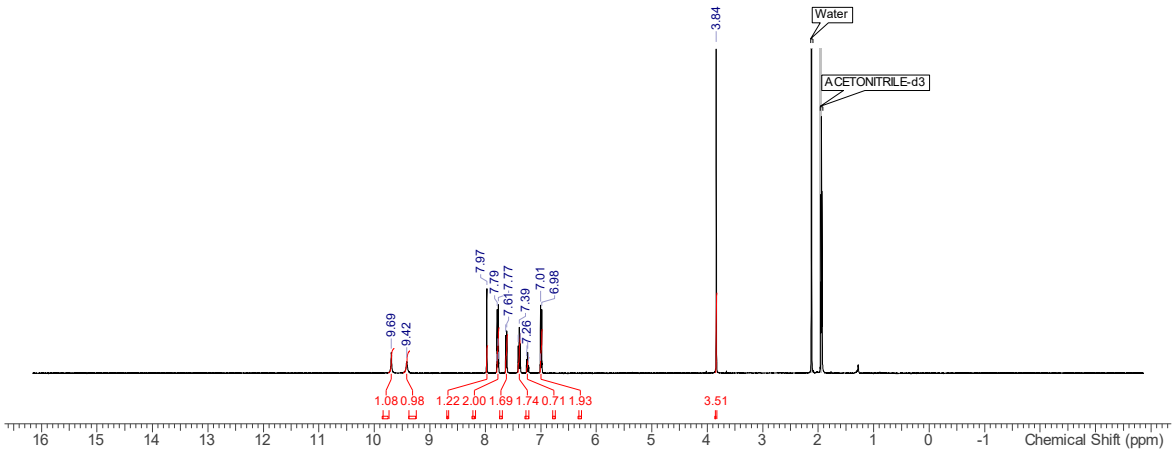


**Figure I.37** $^{1}$H NMR (400 MHz, $CD_3CN$) spectrum of (*E*)-2-(4-methoxybenzylidene)-*N*-phenylhydrazine-1-carbothioamide **79**. $^{1}$H NMR (400 MHz, $CD_3CN$) δ = 9.69 (br s, 1H), 9.42 (br s, 1H), 7.97 (s, 1H), 7.78 (d, *J*=7.9 Hz, 2H), 7.62 (d, *J*=7.6 Hz, 2H), 7.39 (dd, *J*=7.3, 7.6 Hz, 2H), 7.24 (t, *J*=7.3 Hz, 1H), 7.00 (d, *J*=8.0 Hz, 2H), 3.84 (s, 3H).

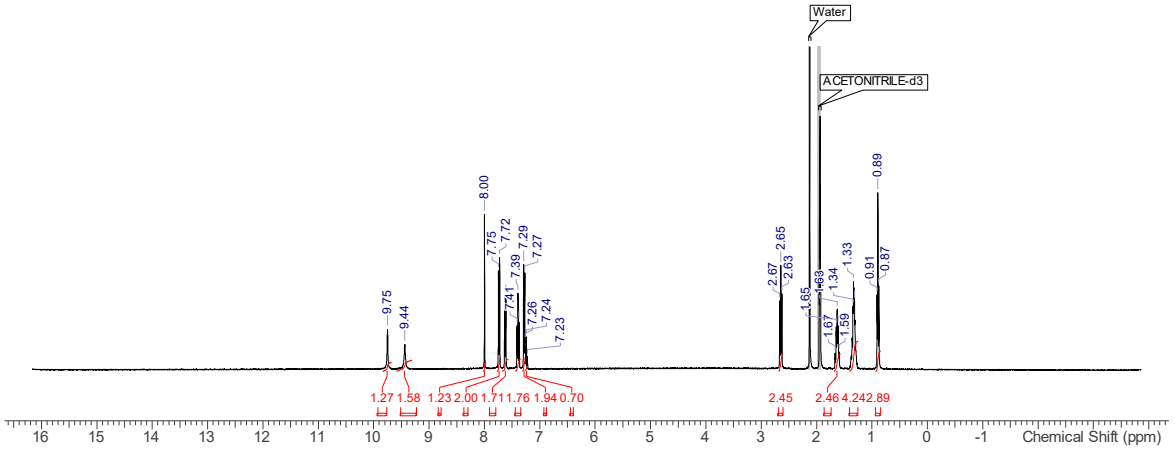


**Figure I.38** $^{1}$H NMR (400 MHz, $CD_3CN$) spectrum of (*E*)-2-(4-pentylbenzylidene)-*N*-phenylhydrazine-1-carbothioamide **80**. $^{1}$H NMR (400 MHz, $CD_3CN$) δ = 9.75 (br s, 1H), 9.44 (br s, 2H), 8.00 (s, 1H), 7.74 (d, *J*=8.3 Hz, 2H), 7.62 (d, *J*=8.3 Hz, 2H), 7.39 (dd, *J*=7.3, 7.8 Hz, 2H), 7.28 (d, *J*=7.8 Hz, 2H), 7.24 (t, *J*=7.3 Hz, 1H), 2.65 (t, *J*=7.8 Hz, 2H), 1.63 (tt, *J*=7.5, 7.8 Hz, 2H), 1.40 - 1.26 (m, 4H), 0.89 (t, *J*=7.1 Hz, 3H).

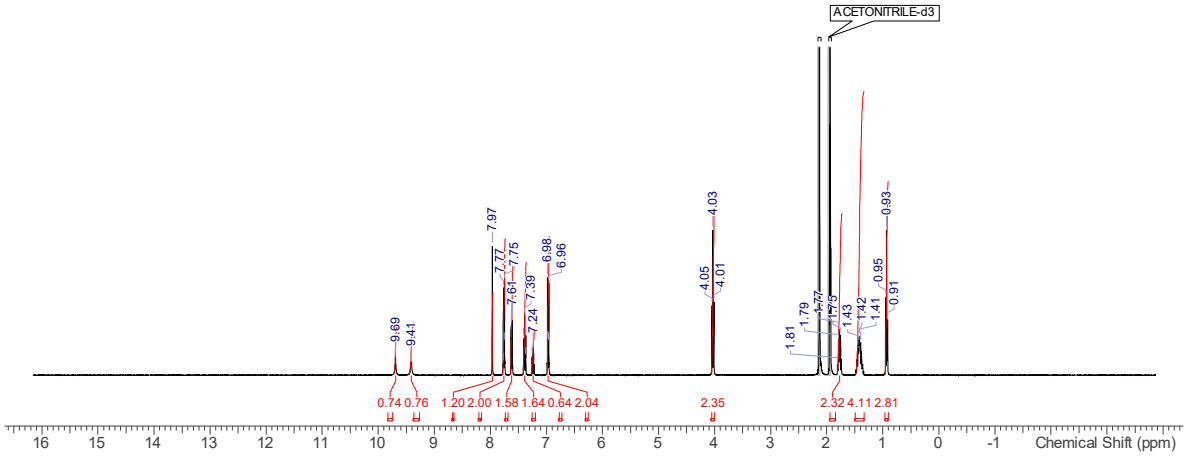


**Figure I.39** $^{1}$H NMR (400 MHz, $CD_3CN$) spectrum of (*E*)-2-(4-(pentyloxy)benzylidene)-*N*-phenylhydrazine-1-carbothioamide **81**. $^{1}$H NMR (400 MHz, $CD_3CN$) δ = 9.69 (br s, 1H), 9.41 (br s, 1H), 7.97 (s, 1H), 7.78 - 7.73 (m, 2H), 7.62 (d, *J*=7.1 Hz, 2H), 7.42 - 7.36 (m, 2H), 7.24 (t, *J*=7.6 Hz, 1H), 6.97 (d, *J*=7.9 Hz, 2H), 4.03 (t, *J*=6.6 Hz, 2H), 1.77 (tt, *J*=6.6, 7.2 Hz, 2H), 1.49 - 1.33 (m, 4H), 0.96 - 0.90 (m, 3H).

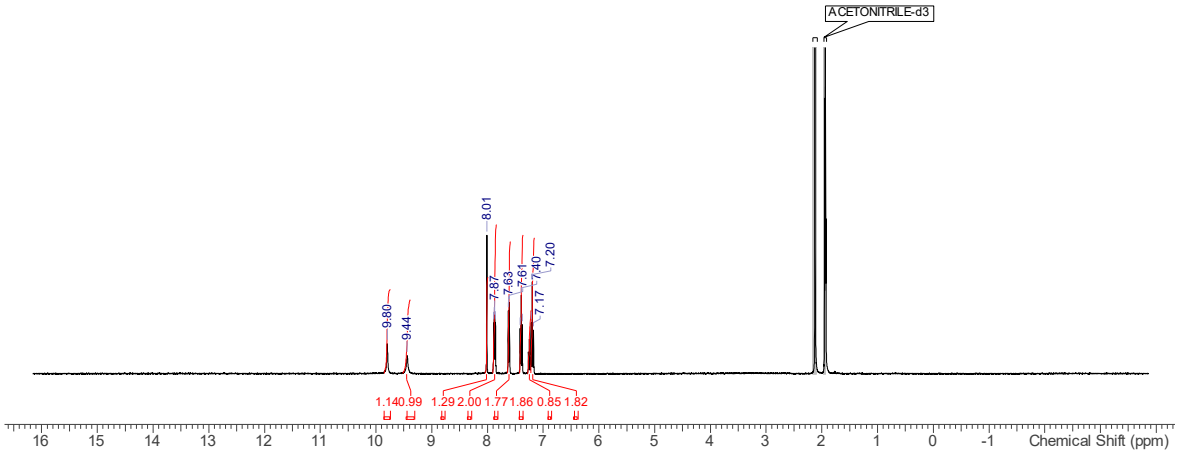


**Figure I.40** $^{1}$H NMR (400 MHz, $CD_3CN$) spectrum of (*E*)-2-(4-fluorobenzylidene)-*N*-phenylhydrazine-1-carbothioamide **82**. $^{1}$H NMR (400 MHz, $CD_3CN$) δ = 9.80 (br s, 1H), 9.44 (br s, 1H), 8.01 (s, 1H), 7.91 - 7.84 (m, *J*=6.0, 7.3 Hz, 2H), 7.62 (d, *J*=7.3 Hz, 2H), 7.39 (t, *J*=7.8 Hz, 2H), 7.25 (t, *J*=7.3 Hz, 1H), 7.22 - 7.15 (m, *J*=7.3 Hz, 2H).

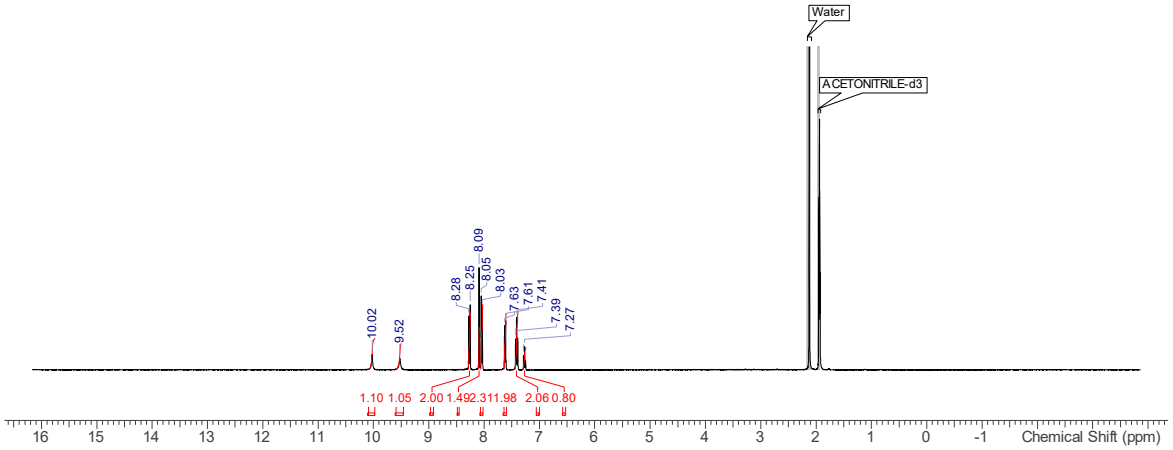


**Figure I.41** $^{1}$H NMR (400 MHz, $CD_3CN$) spectrum of (*E*)-2-(4-nitrobenzylidene)-*N*-phenylhydrazine-1-carbothioamide **83**. $^{1}$H NMR (400 MHz, $CD_3CN$) δ = 10.02 (br s, 1H), 9.52 (br s, 1H), 8.27 (d, *J*=8.8 Hz, 2H), 8.09 (s, 1H), 8.04 (d, *J*=9.3 Hz, 2H), 7.62 (d, *J*=7.3 Hz, 2H), 7.41 (t, *J*=7.3 Hz, 2H), 7.27 (t, *J*=7.3 Hz, 1H).

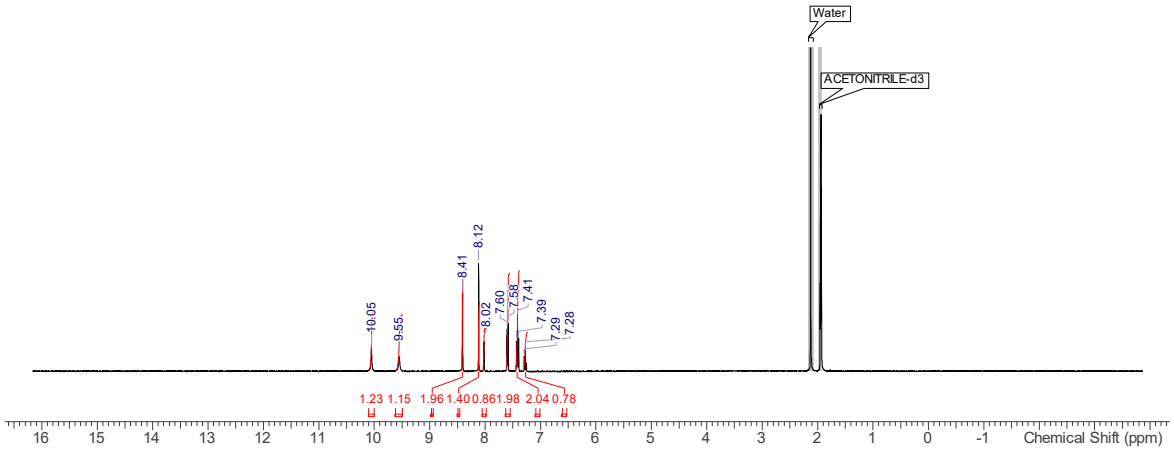


**Figure I.42** $^{1}$H NMR (400 MHz, $CD_3CN$) spectrum of *(E)*-2-(3,5-bis(trifluoromethyl)benzylidene)-*N*-phenylhydrazine-1-carbothioamide **84**. $^{1}$H NMR (400 MHz, $CD_3CN$) δ = 10.05 (br s, 1H), 9.55 (br s, 1H), 8.41 (s, 2H), 8.12 (s, 1H), 8.02 (s, 1H), 7.59 (d, *J*=7.3 Hz, 2H), 7.41 (t, *J*=7.8 Hz, 2H), 7.28 (d, *J*=7.3 Hz, 1H).

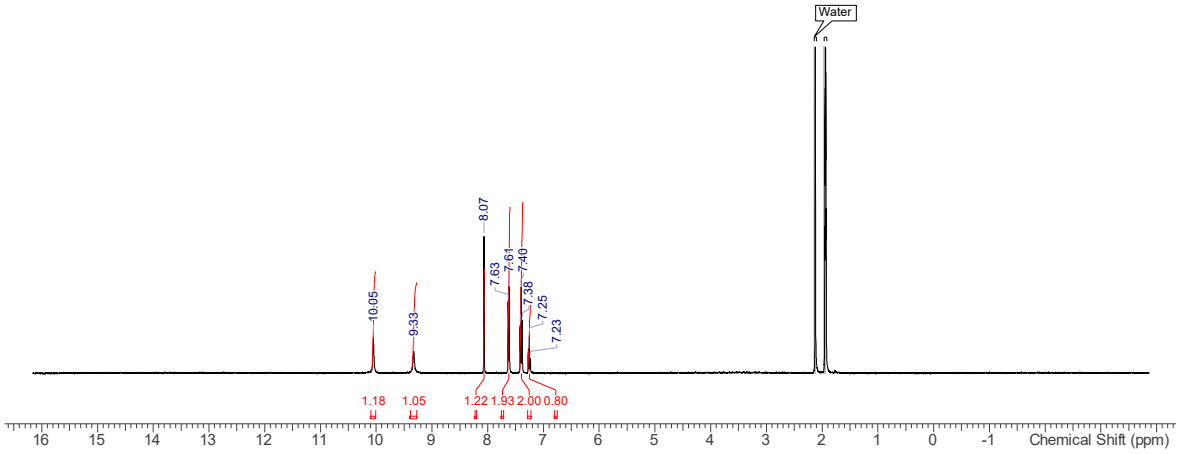


**Figure I.43** $^{1}$H NMR (400 MHz, $CD_3CN$) spectrum of (*E*)-2-((perfluorophenyl)methylene)-*N*-phenylhydrazine-1-carbothioamide **85**. $^{1}$H NMR (400 MHz, $CD_3CN$) δ = 10.05 (br s, 1H), 9.33 (br s, 1H), 8.07 (s, 1H), 7.62 (d, *J*=7.8 Hz, 2H), 7.40 (dd, *J*=7.3, 7.8 Hz, 2H), 7.26 (t, *J*=7.3 Hz, 1H).

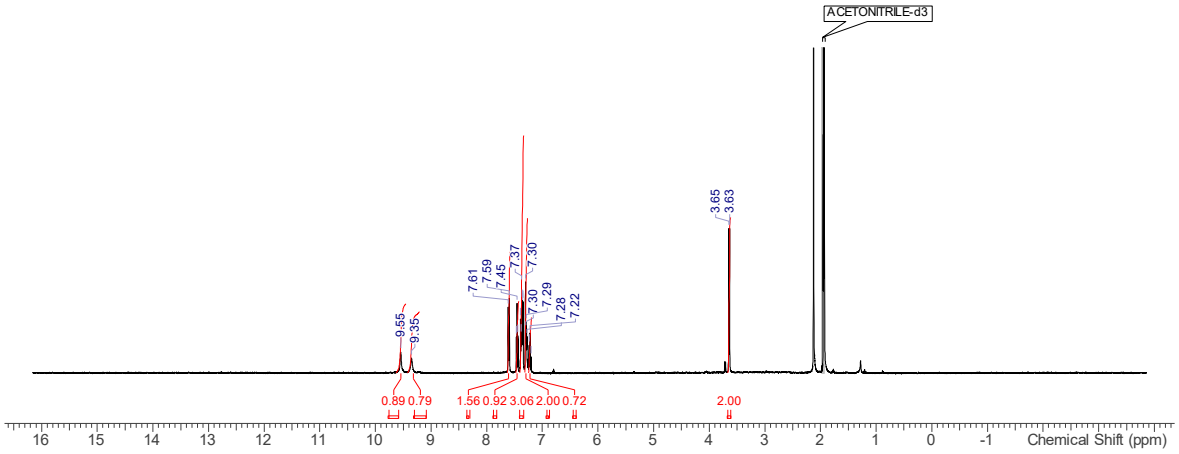


**Figure I.44** $^{1}$H NMR (400 MHz, $CD_3CN$) spectrum of (*E*)-*N*-phenyl-2-(2-phenylethylidene)hydrazine-1-carbothioamide **86**. $^{1}$H NMR (400 MHz, $CD_3CN$) δ = 9.55 (br s, 1H), 9.35 (br s, 1H), 7.63 - 7.58 (m, 2H), 7.45 (t, *J*=5.7 Hz, 1H), 7.41 - 7.33 (m, 3H), 7.32 - 7.27 (m, 2H), 7.22 (tt, *J*=1.2, 7.6 Hz, 1H), 3.64 (d, *J*=5.9 Hz, 2H).

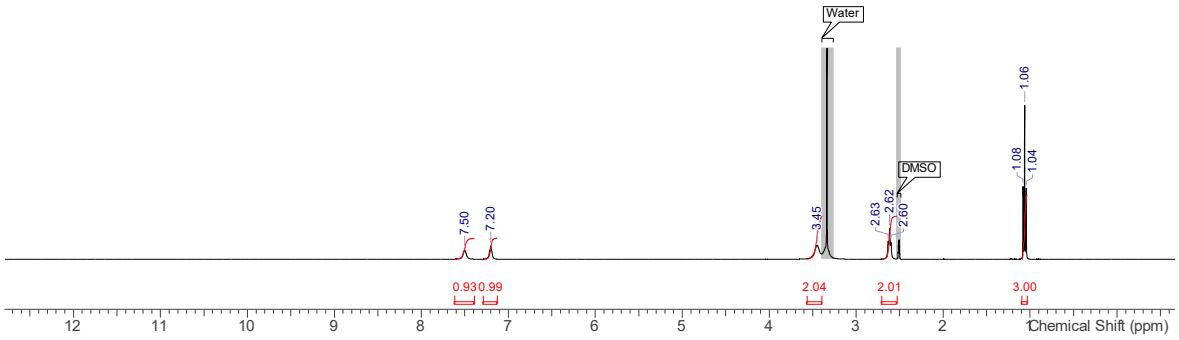


**Figure I.45** $^{1}$H NMR (400 MHz, DMSO-$d_6$) spectrum of 1,1',1''-(nitrilotris(ethane-2,1-diyl))tris(3-ethylthiourea) **96**.

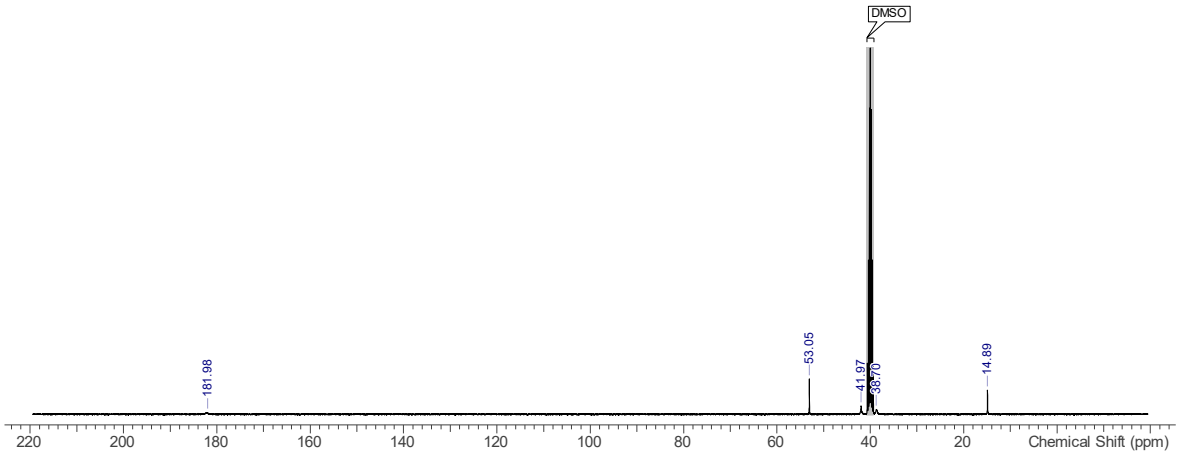


**Figure I.46** $^{13}$C NMR (101 MHz, DMSO-$d_6$) spectrum of 1,1',1''-(nitrilotris(ethane-2,1-diyl))tris(3-ethylthiourea) **96**.

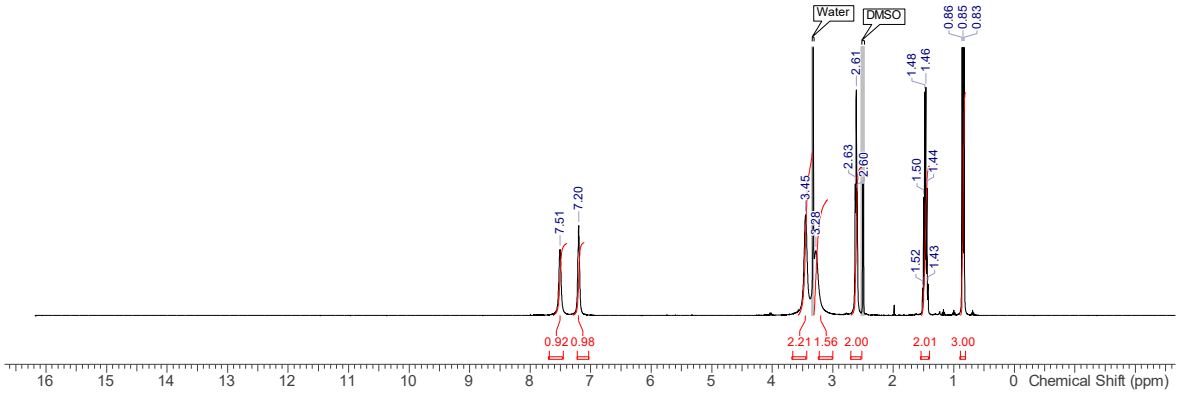


**Figure I.47** $^{1}$H NMR (400 MHz, DMSO-$d_6$) spectrum of 1,1',1''-(nitrilotris(ethane-2,1-diyl))tris(3-propylthiourea) **97**.

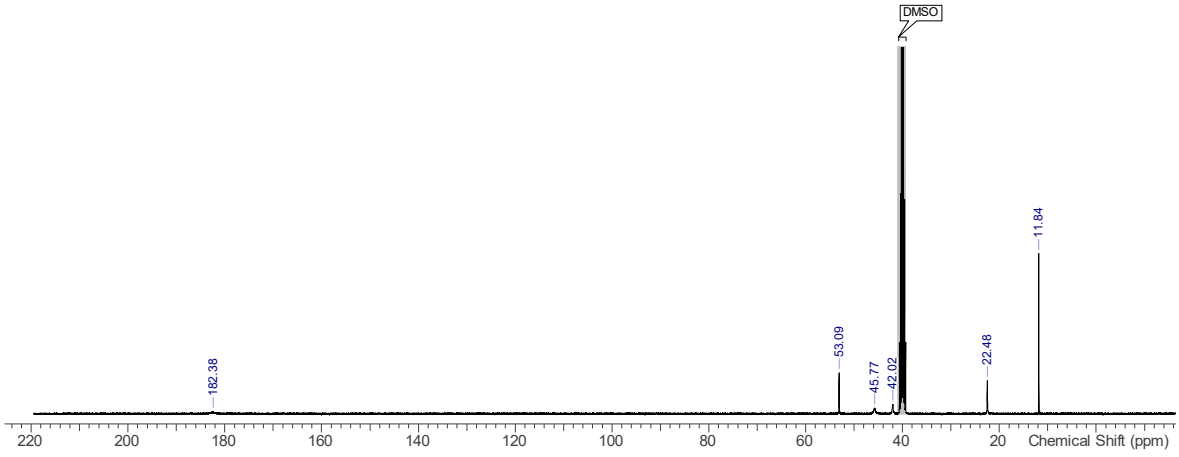


**Figure I.48** $^{13}$C NMR (101 MHz, DMSO-$d_6$) spectrum of 1,1',1''-(nitrilotris(ethane-2,1-diyl))tris(3-propylthiourea) **97**.

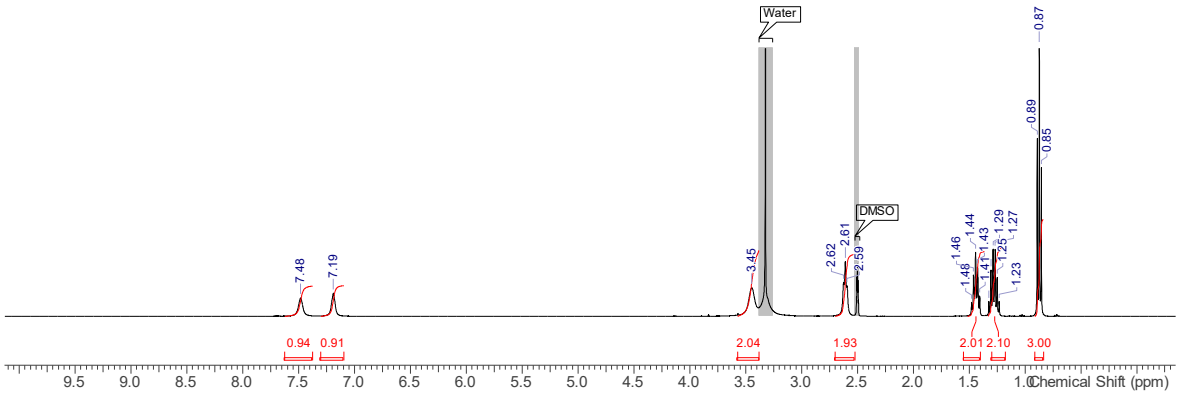


**Figure I.49** $^{1}$H NMR (400 MHz, DMSO-$d_6$) spectrum of 1,1',1''-(nitrilotris(ethane-2,1-diyl))tris(3-butylthiourea) **98**.

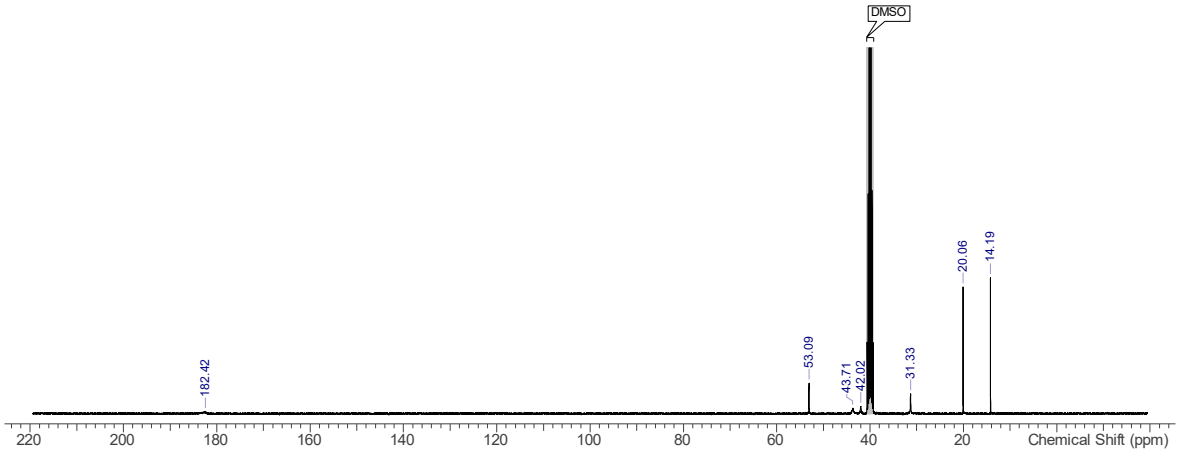


**Figure I.50** $^{13}$C NMR (101 MHz, DMSO-$d_6$) spectrum of 1,1',1''-(nitrilotris(ethane-2,1-diyl))tris(3-butylthiourea) **98**.

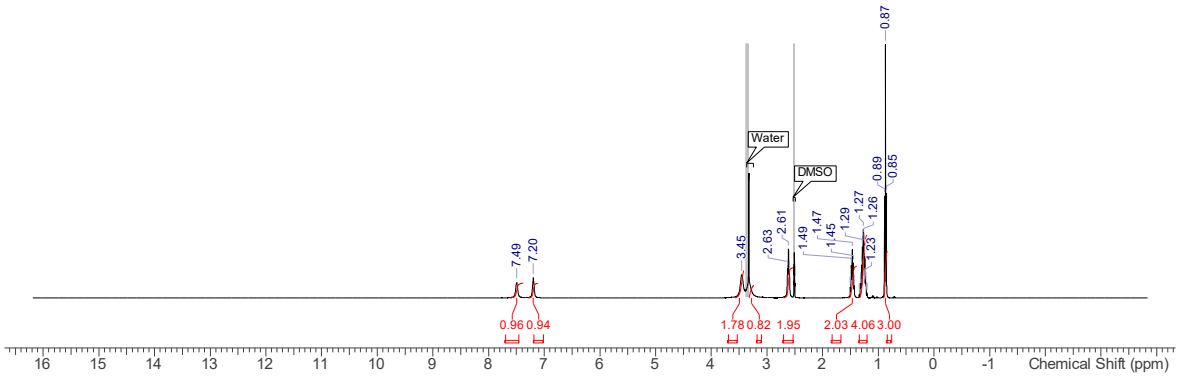


**Figure I.51** $^{1}$H NMR (400 MHz, DMSO-$d_6$) spectrum of 1,1',1''-(nitrilotris(ethane-2,1-diyl))tris(3-pentylthiourea) **99**.

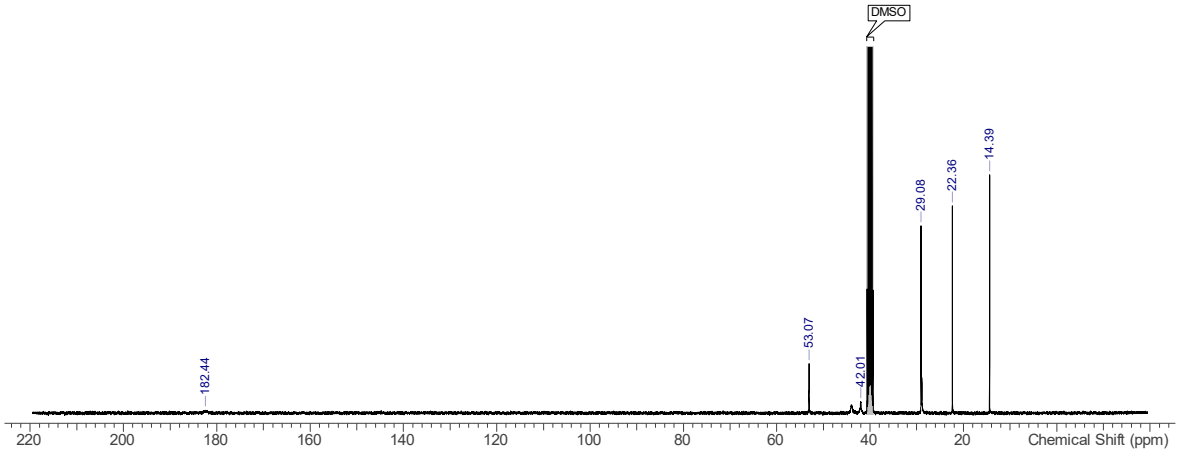


**Figure I.52** $^{13}$C NMR (101 MHz, DMSO-$d_6$) spectrum of 1,1',1''-(nitrilotris(ethane-2,1-diyl))tris(3-pentylthiourea) **99**.

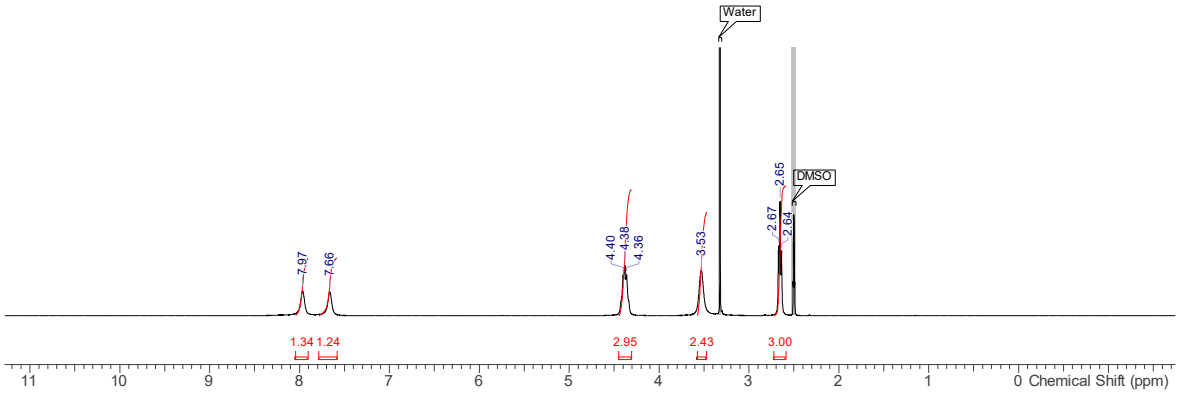


**Figure I.53** $^{1}$H NMR (400 MHz, DMSO-$d_6$) spectrum of 1,1',1''-(nitrilotris(ethane-2,1-diyl))tris(3-(2,2,2-trifluoroethyl)thiourea) **100**.

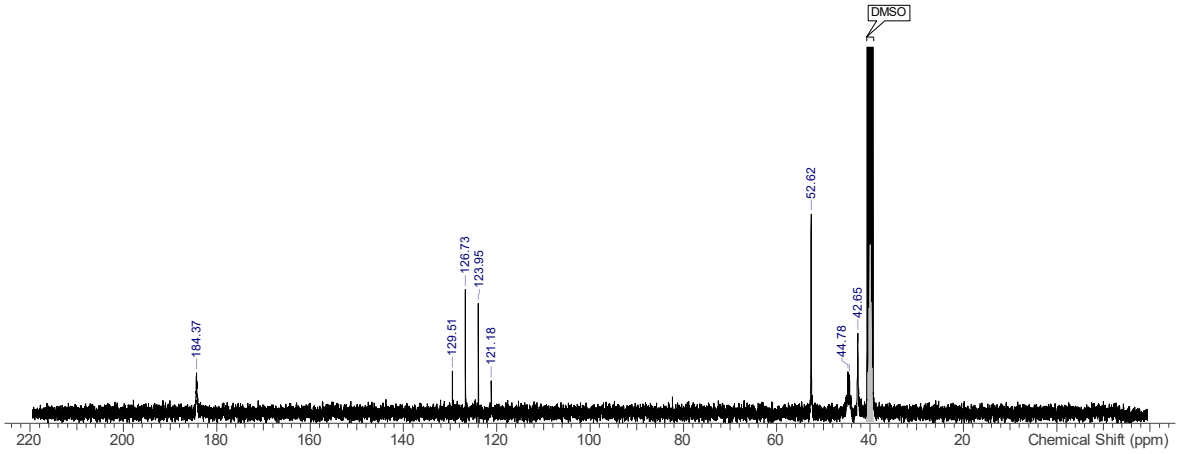


**Figure I.54** $^{13}$C NMR (101 MHz, DMSO-$d_6$) spectrum of 1,1',1''-(nitrilotris(ethane-2,1-diyl))tris(3-(2,2,2-trifluoroethyl)thiourea) **100**.

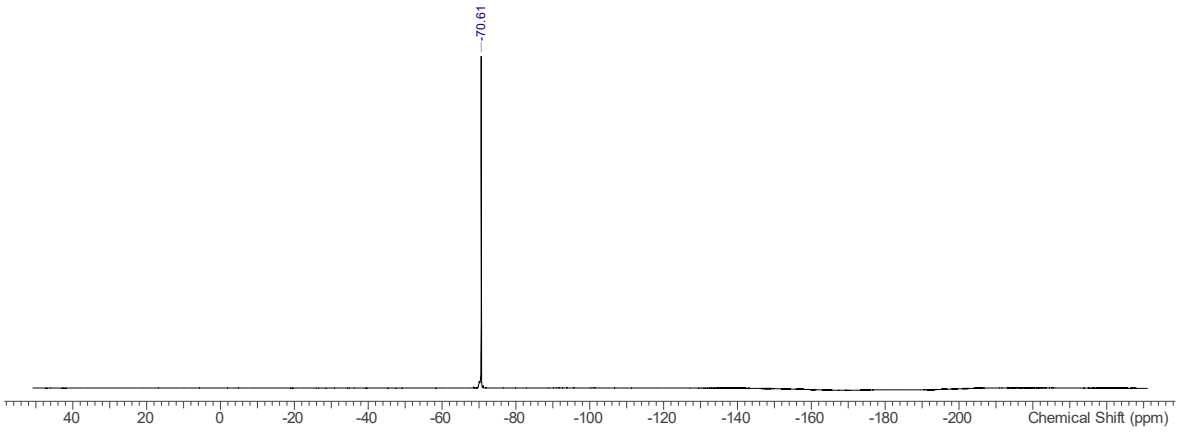


**Figure I.55** $^{19}$F NMR (376 MHz, DMSO-$d_6$) spectrum of 1,1',1''-(nitrilotris(ethane-2,1-diyl))tris(3-(2,2,2-trifluoroethyl)thiourea) **100**.

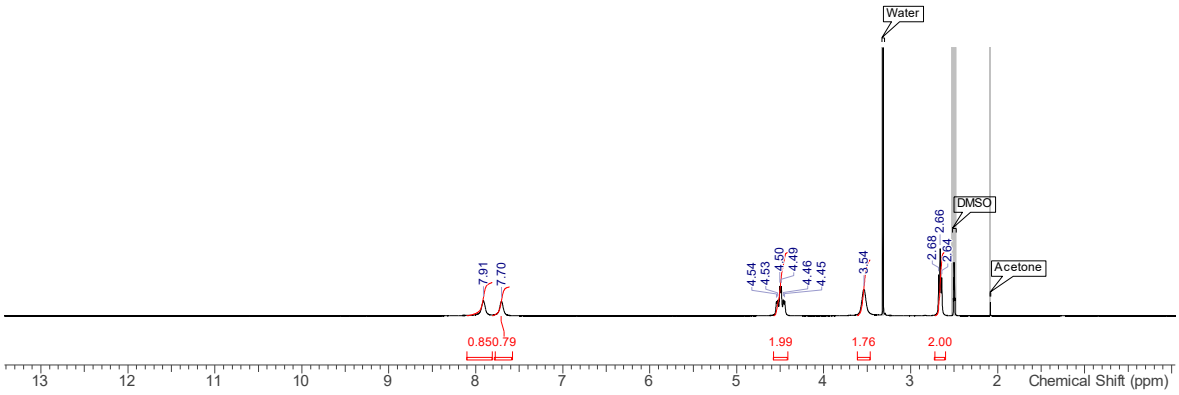


**Figure I.56** $^{1}$H NMR (400 MHz, DMSO-$d_6$) spectrum of 1,1',1''-(nitrilotris(ethane-2,1-diyl))tris(3-(2,2,3,3,3-pentafluoropropyl)thiourea) **101**.

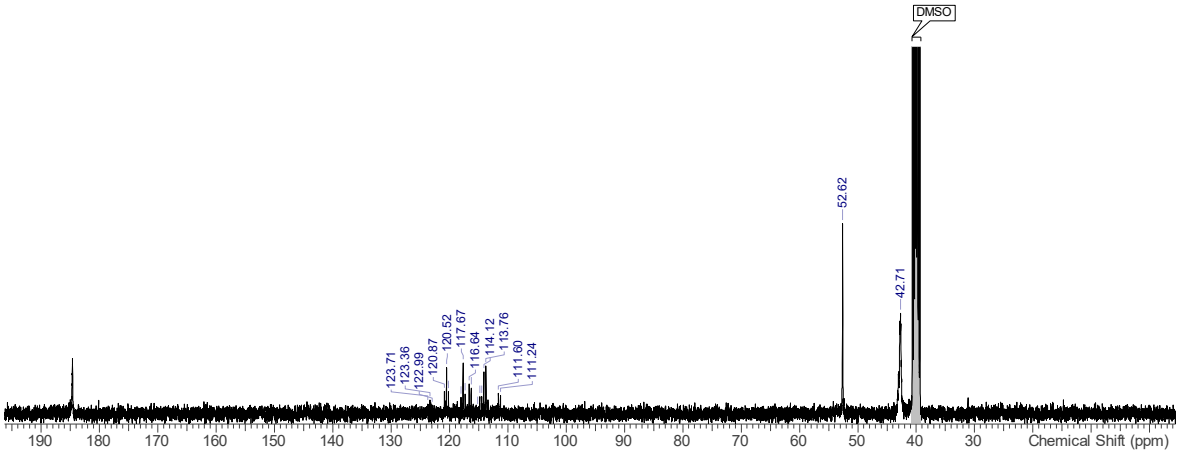


**Figure I.57** $^{13}C$ NMR (101 MHz, DMSO-$d_6$) spectrum of 1,1',1''-(nitrilotris(ethane-2,1-diyl))tris(3-(2,2,3,3,3-pentafluoropropyl)thiourea) **101**.

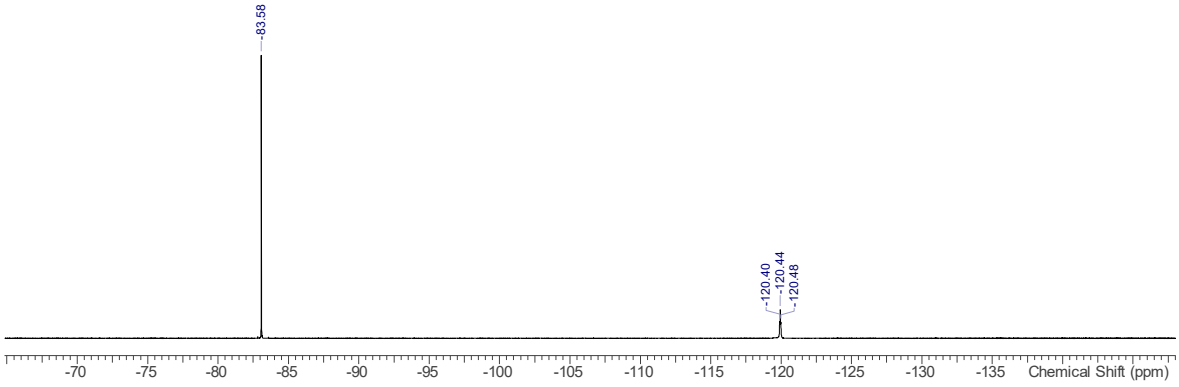


**Figure I.58** $^{19}F$ NMR (376 MHz, DMSO-$d_6$) spectrum of 1,1',1''-(nitrilotris(ethane-2,1-diyl))tris(3-(2,2,3,3,3-pentafluoropropyl)thiourea) **101**.

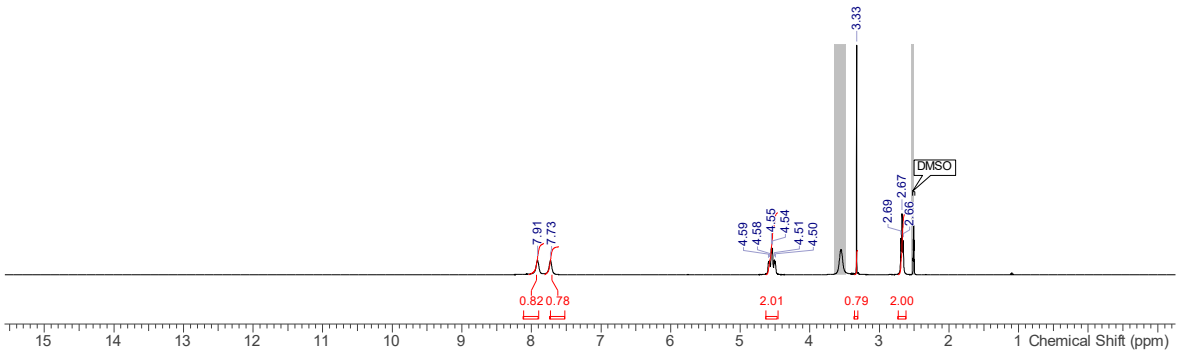


**Figure I.59** $^{1}H$ NMR (400 MHz, DMSO-$d_6$) spectrum of 1,1',1''-(nitrilotris(ethane-2,1-diyl))tris(3-(2,2,3,3,4,4,4- heptafluorobutyl)thiourea) **102**.

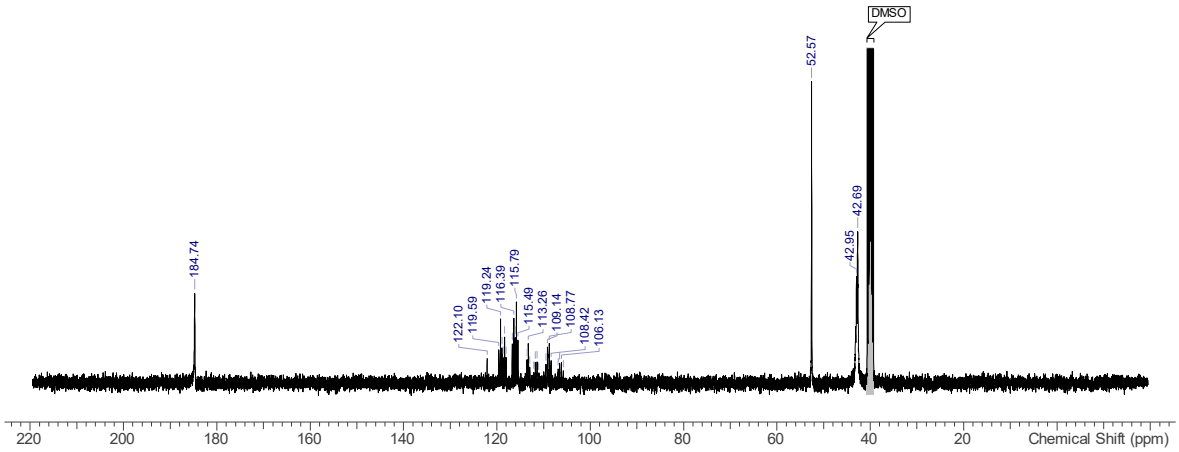


**Figure I.60** $^{13}$C NMR (101 MHz, DMSO-$d_6$) spectrum of 1,1',1''-(nitrilotris(ethane-2,1-diyl))tris(3-(2,2,3,3,4,4,4- heptafluorobutyl)thiourea) **102**.

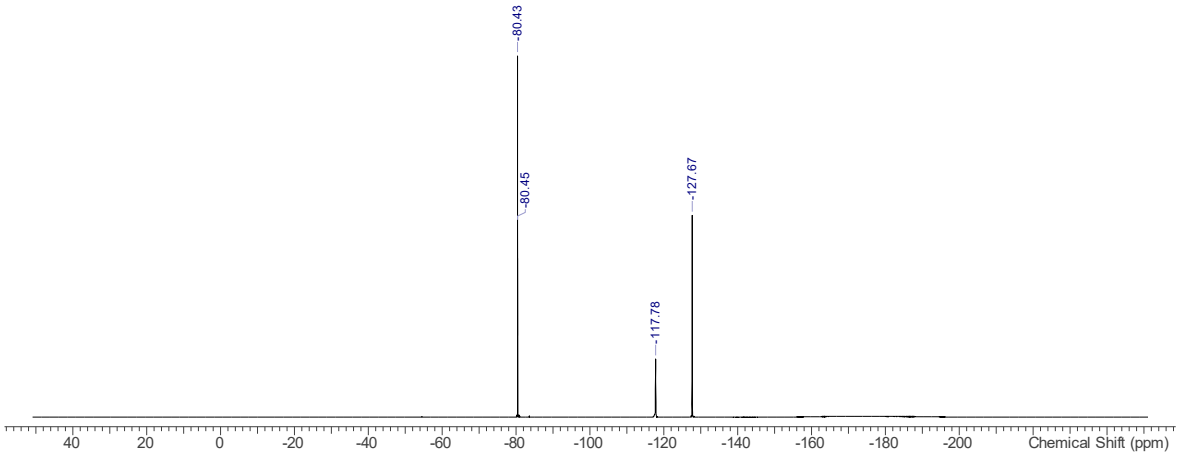


**Figure I.61** $^{19}$F NMR (376 MHz, DMSO-$d_6$) spectrum of 1,1',1''-(nitrilotris(ethane-2,1-diyl))tris(3-(2,2,3,3,4,4,4- heptafluorobutyl)thiourea) **102**.

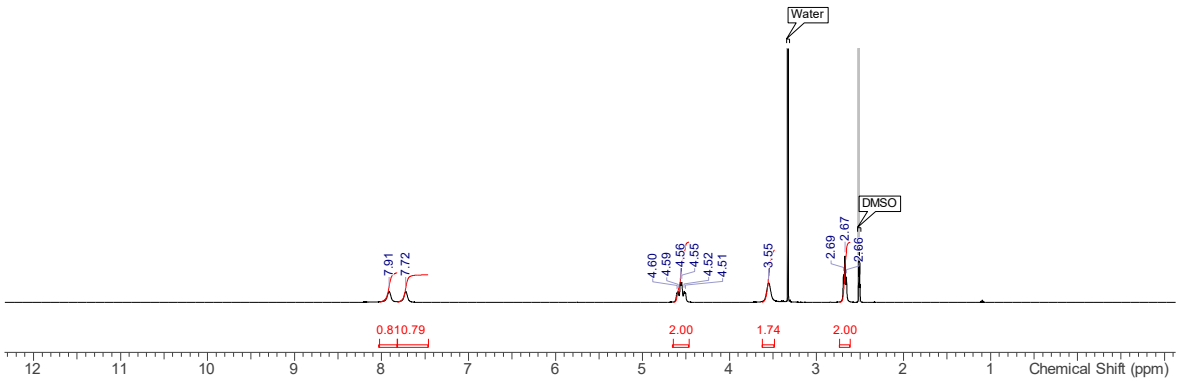


**Figure I.62** $^{1}$H NMR (400 MHz, DMSO-$d_6$) spectrum of 1,1',1''-(nitrilotris(ethane-2,1-diyl))tris(3-(2,2,3,3,4,4,5,5,5-nonafluoropentyl)thiourea) **103**.

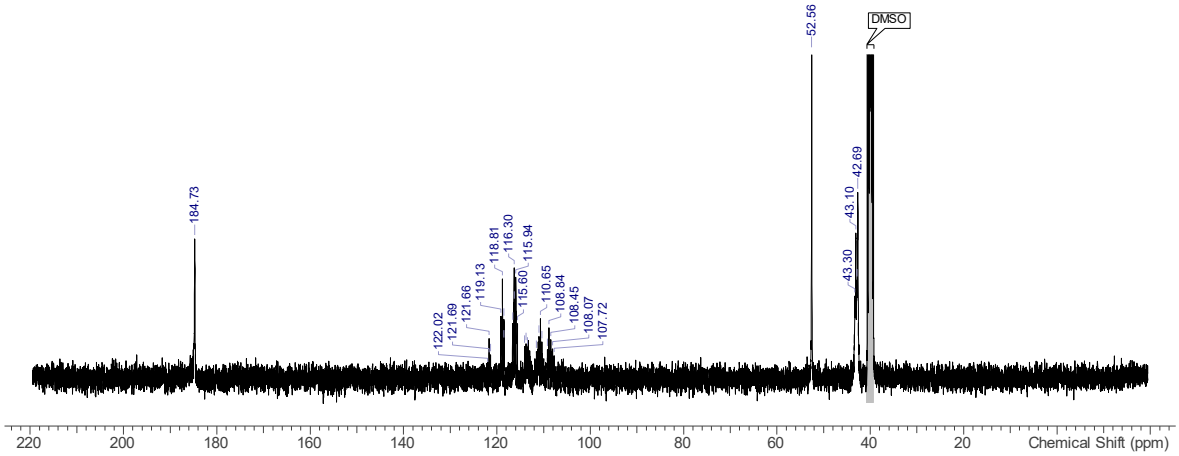


**Figure I.63** $^{13}C$ NMR (101 MHz, DMSO-$d_6$) spectrum of 1,1',1''-(nitrilotris(ethane-2,1-diyl))tris(3-(2,2,3,3,4,4,5,5,5-nonafluoropentyl)thiourea) **103**.

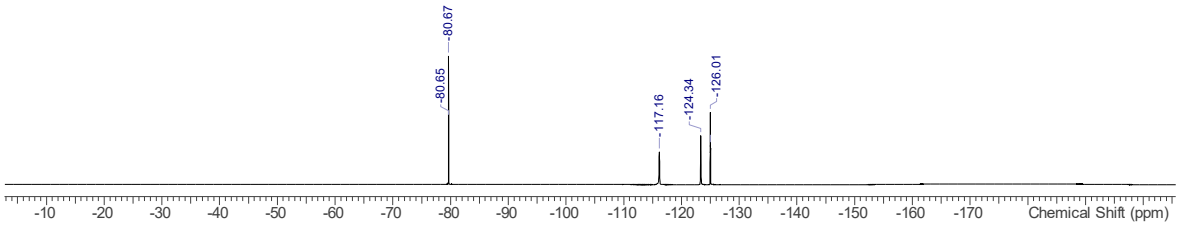


**Figure I.64** $^{19}F$ NMR (376 MHz, DMSO-$d_6$) spectrum of 1,1',1''-(nitrilotris(ethane-2,1-diyl))tris(3-(2,2,3,3,4,4,5,5,5-nonafluoropentyl)thiourea) **103**.

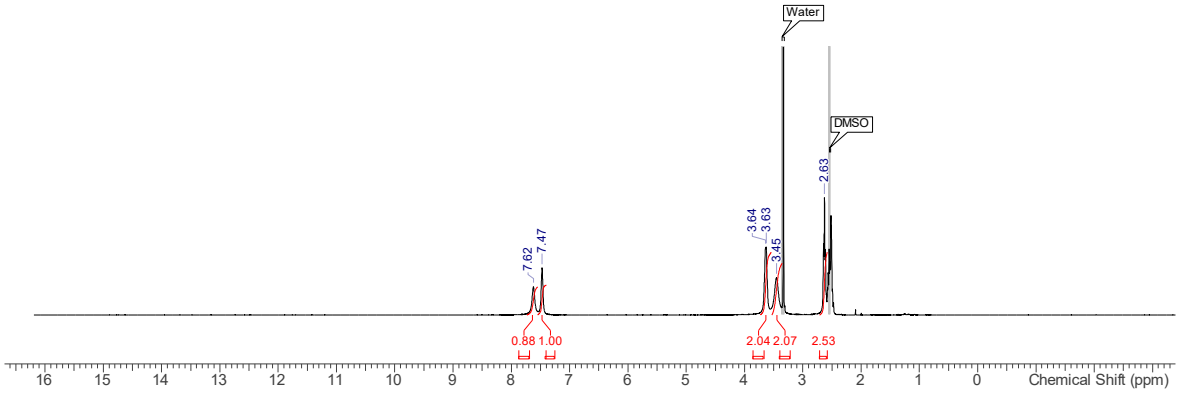


**Figure I.65** $^{1}H$ NMR (400 MHz, DMSO-$d_6$) spectrum of 1,1',1''-(nitrilotris(ethane-2,1-diyl)) tris(3-(3,3,3-trifluoropropyl)thiourea) **104**.

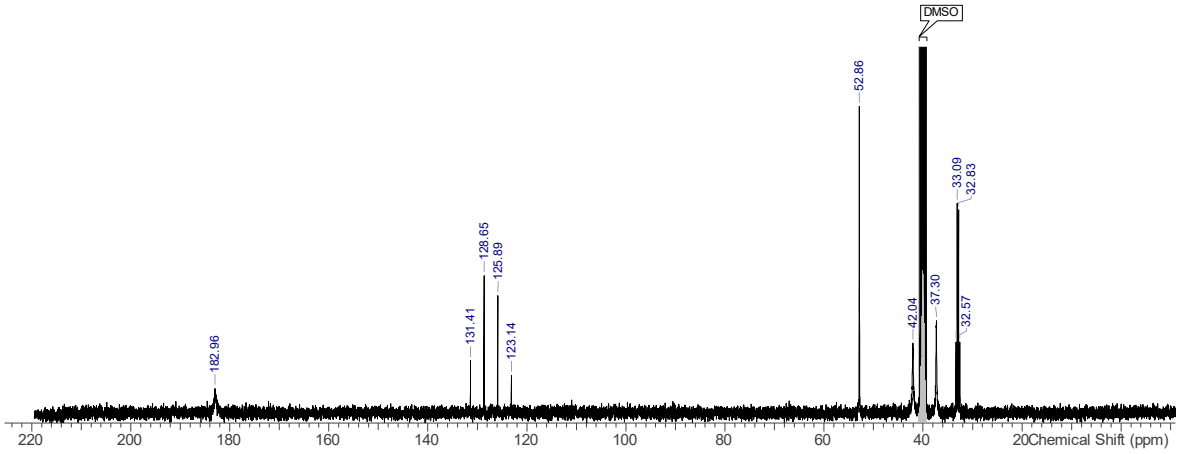


**Figure I.66** $^{13}$C NMR (101 MHz, DMSO-d$_6$) spectrum of 1,1',1''-(nitrilotris(ethane-2,1-diyl)) tris(3-(3,3,3-trifluoropropyl)thiourea) **104**.

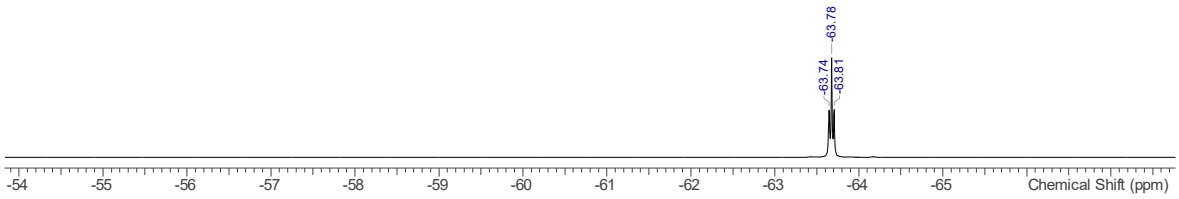


**Figure I.67** $^{19}$F NMR (376 MHz, DMSO-d$_6$) spectrum of 1,1',1''-(nitrilotris(ethane-2,1-diyl)) tris(3-(3,3,3-trifluoropropyl)thiourea) **104**.

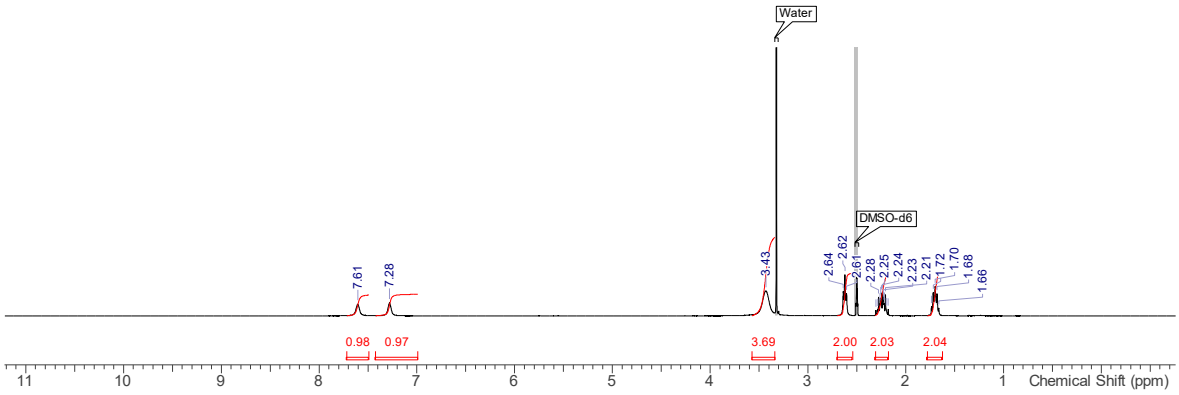


**Figure I.68** $^{1}$H NMR (400 MHz, DMSO-d$_6$) spectrum of 1,1',1''-(nitrilotris(ethane-2,1-diyl))tris(3-(4,4,4-trifluorobutyl)thiourea) **105**.

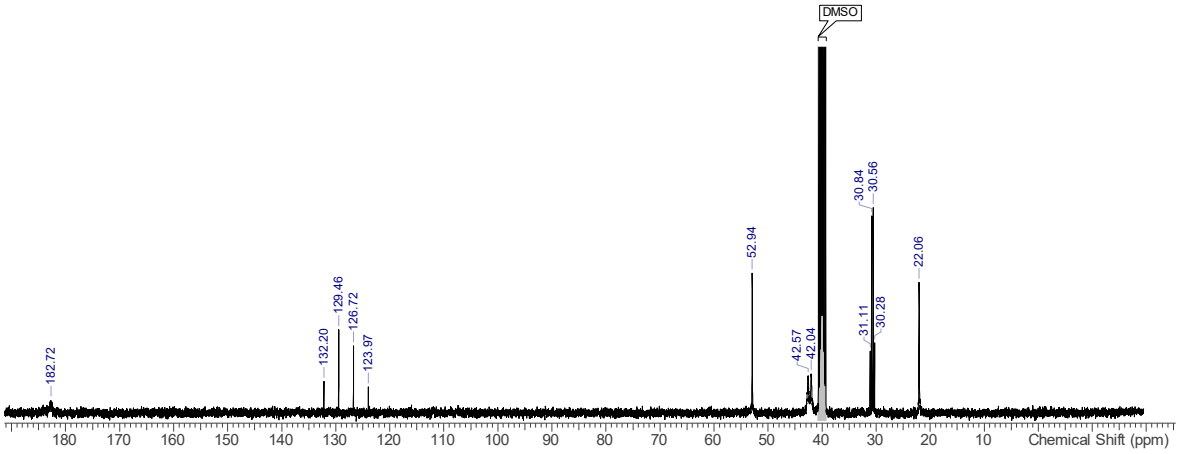


**Figure I.69** $^{13}C$ NMR (101 MHz, DMSO-$d_6$) spectrum of 1,1',1''-(nitrilotris(ethane-2,1-diyl))tris(3-(4,4,4-trifluorobutyl)thiourea) **105**.

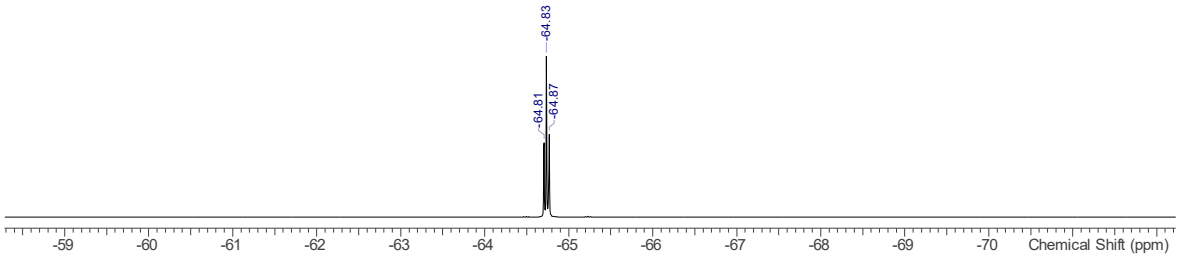


**Figure I.70** $^{19}F$ NMR (376 MHz, DMSO-$d_6$) spectrum of 1,1',1''-(nitrilotris(ethane-2,1-diyl)) tris(3-(3,3,3-trifluoropropyl)thiourea) **105**.

# Appendix II Experimental

## II.1 Transport Studies

### II.1.1 Lipid Vesicle Synthesis

POPG, POPE and DPPC were all purchased from Avanti Polar Lipids, cholesterol from Sigma-Aldrich. POPC was purchased from either Avanti Polar Lipids or Corden Pharma. POPG, POPE and CHOL were used as supplied; POPC was stored as a solution in chloroform (1 g lipid in 35 ml).

For POPC vesicles, POPC solution was added to a 50 ml RBF of known mass and the solvent removed under reduced pressure forming a lipid film. The film was dried *in vacuo* for at least 4 hours and the mass of lipid weighed. Dry lipids were pre-weighed then dissolved in chloroform to produce dry film *in vacuo* as above. For mixed vesicles, the correct mass of the second lipid to achieve the correct molar ratio was then weighed out, dissolved in chloroform and the solution transferred in a quantitative manner to the RBF, the POPC film re-dissolving in this solution. The solvent was again removed under reduced pressure and the film dried for at least 4 hours as before.

The lipid film was re-suspended in a known quantity of internal buffer (INT) containing relevant salts for the experiment and buffered to the required pH. This suspension was subjected to 9 freeze-thaw cycles in liquid nitrogen before being allowed to rest for 30 minutes. The suspension was extruded 25 times through a 200 nm polycarbonate membrane forming monodisperse unilamellar vesicles. Buffer not encased by the vesicles was replaced by the relevant external buffer (EXT) by either dialysis or size-exclusion chromatography, as appropriate for the individual experiment (see below).

### II.1.2 $Cl^-/NO_3^-$ Exchange ISE Assays – Initial Rate

Internal buffer (INT): 489 mM NaCl, 5 mM phosphate buffers, pH 7.2
External buffer (EXT): 489 mM $NaNO_3$, 5 mM phosphate buffers, pH 7.2

Extruded vesicles were dialysed against ~1.8 l of EXT for at least 2 hours. Vesicle suspension was finally diluted to 10 ml in EXT to obtain a solution of known concentration (after adjustment for any losses during extrusion).

For each trial, a 1 mM sample of dialysed vesicles diluted in EXT was equipped with a stirrer bar and Accumet chloride selective electrode. The electrode was connected to a Thermo Scientific Orion Star A321 Portable pH Meter linked to Thermo Star Com data logging software. Transport

assays were initiated by the addition of a 10 mM solution in DMSO of the compound to be tested, such that loading of transporter was 1 % with respect to lipid.

The electrode voltage was recorded every 3 s for 5 minutes before addition of a detergent solution (polyoxyethylene-(8)-lauryl ether, TCI, 1 g in 8 ml 7:1 $H_2O$:DMSO, 50 µl) to lyse the vesicles. A final reading was taken at 7 minutes and the value at this time taken as 100 % efflux. Trials were conducted in triplicate, averaged and the mV readings from the electrode were converted to a % $Cl^-$ efflux after calibration with NaCl solutions of known concentration.

To obtain initial rate values from ISE trials, an approach similar to that used by Quesada et. al.[106] was used. The data points for the first 30 seconds of each run were considered to be approximately linear and the rate taken as the gradient obtained by performing a linear regression on the data. $r^2$ values for the regression analysis were always greater than 0.88, with the majority of values (ie those not at the extremes of lipophilicity) in excess of 0.94.

### II.1.3 $Cl^-/NO_3^-$ Exchange ISE Assays – Low pH Hill Plots

Internal buffer (INT): 486 mM NaCl, 5 mM citrate buffers, pH 4.5
External buffer (EXT): 486 mM $NaNO_3$, 5 mM citrate buffers, pH 4.5

Extruded POPC vesicles were dialysed against ~1.8 l of EXT for at least 2 hours. Vesicle suspension was finally diluted to 10 ml in EXT to obtain a solution of known concentration (after adjustment for any losses during extrusion).

Each trial was obtained by exactly the same method as section II.1.2. Triton x-100 was used as the detergent (Sigma-Aldrich, 1 g in 8 ml 7:1 $H_2O$:DMSO, 50 µl). All trials were obtained in triplicate and averaged. For each compound, at least 6 points were obtained at different % loading, to obtain effluxes at 270 s ranging from ~10 % to ~100 %. This allowed fitting of the Hill Equation[52-54] (6).

$$y = \frac{V_{max}[x]^n}{\mathrm{k^n} + x^n} \tag{6}$$

$$EC_{50} = \sqrt[-n]{\frac{-k^{-n}(50 - V_{max})}{50}} \tag{7}$$

Where $V_{max}$ = maximum transporter response ($y_{max}$), n = Hill coefficient, k = concentration of anionophore were y is half of $V_{max}$, x = concentration of anionophore, y = chloride efflux.

For each compound, the efflux at 270 s was plotted against concentration (% loading wrt. lipid). The points were fitted to equation (6) using Origin 2015. For most compounds, $V_{max}$ could be fixed to 100 % to obtain a good fit, at which point the value of k was equivalent to the $EC_{50}$. For curves

that flattened out before reaching 100 %, $V_{max}$ was allowed to vary, and equation (7) was used to derive the $EC_{50}$ from the fitting results.

### II.1.4 $Cl^-/SO_4^-$, $NO_3^-$ Spike ISE Assays

Internal buffer (INT): 489 mM NaCl, 5 mM phosphate buffers, pH 7.2
External buffer (EXT): 162 mM $Na_2SO_4$, 5 mM phosphate buffers, pH 7.2

Samples set up as per experiment 6II.1.2. Experiment was initiated by addition of a 10mM solution in DMSO of the compound of interest. After 2 minutes, transport was initiated by the addition of a solution of $NaNO_3$ such that the final concentration of nitrate was 40 mM. Detergent was added at 7 minutes and final reading taken at 9 minutes. The initial rate at 120 s was calculated by linear approximation as before.

### II.1.5 Calcein Leakage Assays

Internal buffer (INT): 450 mM NaCl, 20 mM phosphate buffers, 100 mM calcein, pH 7.2
External buffer (EXT): 162 mM $Na_2SO_4$, 20 mM phosphate buffers, pH 7.2

Un-encapsulated calcein was removed from extruded vesicles by size-exclusion chromatography on a Sephadex G-50 column using EXT as the eluent. 1 mM samples of vesicles were suspended in EXT and compound to be tested was added as a DMSO solution (such that final loading was 1% wrt. lipid). The fluorescence emission at 520 nm (after excitation at 490 nm) was monitored for 16 hours using an Agilent Technologies Carey Eclipse Fluorescence Spectrophotometer. At the end of the experiment, the vesicles were lysed with detergent (polyoxyethylene-(8)-lauryl ether, TCI, 1 g in 8 ml 7:1 $H_2O$:DMSO, 50 µl) to calibrate for total calcein release. The fraction calcein release was calculated by equation (1).

$$Fraction\ Calecin\ release = \frac{I_t - I_0}{I_{FINAL} - I_0} \quad (8)$$

### II.1.6 Internal pH HCl Assays

Internal buffer (INT): 489 mM NaCl, 5 mM phosphate buffers, 1 mM HPTS, pH 7.2
External buffer (EXT): 162 mM $Na_2SO_4$, 5 mM phosphate buffers, pH 7.2

Un-encapsulated HPTS was removed from extruded vesicles by size-exclusion chromatography on a Sephadex G-50 column using EXT as the eluent. 10 mM samples of the compound to be tested were added to 1 mM samples of vesicles suspended in EXT (such that final loading was 1% wrt.

lipid), to commence a trial. The fluorescence emission at 510 nm after excitation at 403 and 460 nm was monitored for 5 minutes using an Agilent Technologies Carey Eclipse Fluorescence Spectrophotometer. At the end of the experiment, the vesicles were lysed with detergent (polyoxyethylene-(8)-lauryl ether, TCI, 1 g in 8 ml 7:1 $H_2O$:DMSO, 50 µl). The difference in emission intensity after excitation at 403 nm and 460 nm was converted to the internal pH of the vesicles using equation (9)[63].

$$pH = -\frac{1}{1.796}\ln\left(\frac{4.2055}{\frac{I_{460}}{I_{403}} - 1}\right) \quad (9)$$

### II.1.7 Lucigenin Anion Assays

Internal buffer (INT): 100 mM NaCl, 20 mM phosphate buffers, 2 mM lucigenin, pH 7.2
External buffer (EXT): 100 mM NaCl, 20 mM phosphate buffers, pH 7.2

Un-encapsulated lucigenin was removed from extruded vesicles by size-exclusion chromatography on a Sephadex G-50 column using EXT as the eluent. The fluorescence emission at 520 nm (after excitation at 490 nm) of 1 mM samples of vesicles suspended in EXT was monitored using an Agilent Technologies Carey Eclipse Fluorescence Spectrophotometer. After 30 s, a solution of anion (1 M NaCl / 1 M $NaNO_3$ / 0.5 M $NaSO_4$) was added to the sample to a final concentration of 40mM. At 90 s, a 10 mM solution of the test compound in DMSO was added such that final loading was 1% wrt. lipid. After 390 s, the vesicles were lysed with detergent (polyoxyethylene-(8)-lauryl ether, TCI, 1 g in 8 ml 7:1 $H_2O$:DMSO, 50 µl).

### II.1.8 NMDG/HPTS Assays

Internal buffer (INT): 100 mM NaCl, 10 mM HEPES buffer, 1 mM HPTS, pH 7.2
External buffer (EXT): 100 mM NaCl, 10 mM HEPES buffer, pH 7.2

Un-encapsulated HPTS was removed from extruded vesicles by size-exclusion chromatography on a Sephadex G-50 column using EXT as the eluent. 1 mM samples of vesicles suspended in EXT were loaded into an Agilent Technologies Carey Eclipse Fluorescence Spectrophotometer. The change in internal pH was monitored by recording the ratio between HPTS emission 510 nm after excitation at 460 nm and 405 nm every 10 seconds.

At the start of the experiment any assisting protonophore was added to the sample if required as a 2 µl solution in DMSO (either Gramicidin-A to a final concentration of 0.5 % loading wrt. lipid, or oleic acid to 2% loading). The compound to be tested was then added, again as 2 µl of an

appropriately diluted solution in DMSO to the final concentration required. The experiment was initiated by addition of 20 µl of aqueous NMDG, to raise the external pH to pH 8.

After 300 s, a detergent was added (Triton X-100, Sigma-Aldrich, 1 g in 8 ml 7:1 $H_2O$:DMSO, 20 µl) to lyse the vesicles and calibrate to 100 % pH gradient dissipation. All trials were obtained in triplicate and the curves averaged. Curves were fitted to either a single exponential (10) or a double exponential function (11) using Origin 2015. This allowed the calculation of the initial transport rate at t = 0 as shown.

$$y = \mathrm{y}_1 - \mathrm{a}e^{-bx} \qquad \Longrightarrow Init.Rate = ab \tag{10}$$

$$y = \mathrm{y}_1 - \mathrm{a}e^{-bx} - \mathrm{c}e^{-dx} \qquad \Longrightarrow Init.Rate = ab + cd \tag{11}$$

## II.2 NMR Studies

### II.2.1 NMR Titrations

All salts obtained from Sigma-Aldrich and dried under vacuum overnight prior to use. ~0.01 M solution of the sample receptor produced in 0.5 % $H_2O$/DMSO-$d_6$. 500 µl of initial sample placed in an NMR tube and $^1$H spectrum recorded using Bruker AVII400 FT-NMR spectrometer at 298 K. Aliquots of an ~0.16 M solution of the TBA (tetrabutylammonium) salt of the anionic guest (dissolved in receptor sample solution) were added and $^1$H NMR spectra obtained for each titre. Approx. 20 spectra obtained spanning 0 to 6 equivalents of anion to receptor.

For the simple thiourea series (Chapter 2.4), the chemical shift of the alkyl N-H proton over the course of the titration was plotted against the concentration of the anionic guest and the data fitted assuming a 1:1 binding model using WINEQNMR2[110] to obtain the binding constant K. All errors in the calculated values were < 10%, except for when K < 10 (due to a large errors in fitting with small K, these values are reported as K < 10).

For the fluorinated tren series (Chapter 4.4), the chemical shifts of both NH protons were globally fitted using BindFit v0.5[124, 125]. The data were fitted to a 1:1 binding model giving binding constants with asymptotic errors errors all < 3 %.

### II.2.2 DCC NMR Studies

$CDCl_3$ was dried and de-acidified over $K_2CO_3$ prior to use. For each compound (**73** - **86**) a stock solution of the phenylthiosemicarbazone (20 mM) and the appropriate aldehyde (20 mM) were prepared in $CDCl_3$. A 10 mM sample of the pre-formed compound in $CDCl_3$ was also prepared.

$^{1}$H NMR spectra of the aldehyde and phenylthiosemicarbazone (600 µl sample volumes) were recorded using Bruker AVII400 FT-NMR spectrometer at 298 K for reference. To prepare for the experiment, a 600 µl sample of the pre-formed compound loaded in to the instrument. TD was set to 64k, the number of scans to 8 and dummy scans to 3 which gave a 60 s experiment time to record the spectrum of the pre-formed compound, again for reference.

The shim settings for the preformed compound were retained for the DCC experiment to ensure good resolution for the experiment. An NMR tube was charged with 300 µl of the phenylthiosemicarbazone stock. 300 µl of the aldehyde stock, the tube shaken and immediately loaded onto the instrument. 60 $^{1}$H NMR spectra were recorded using the same settings as before, giving 1 spectrum a minute for a total experiment time of 1 hour.

# Appendix III Additional Data

## III.1 Thiourea Series

### III.1.1 Raw Transport Curves

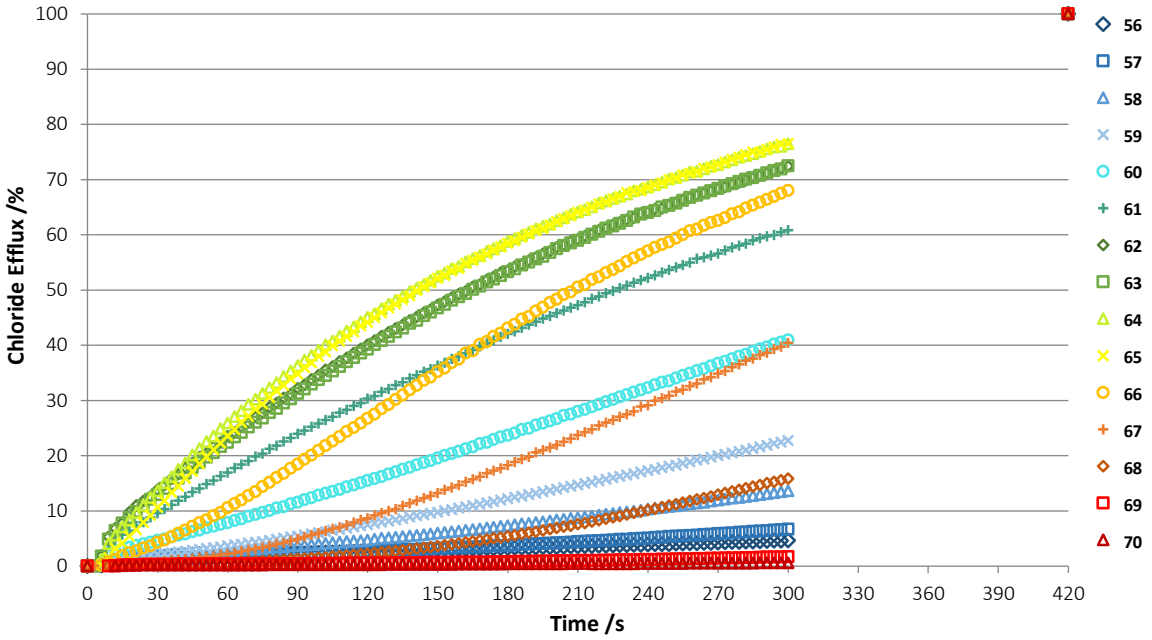


**Figure III.1** Transport curves for **56** - **70** in $Cl^-/NO_3^-$ assays in 100% POPC vesicles. Each curve represents the average of 3 trials.

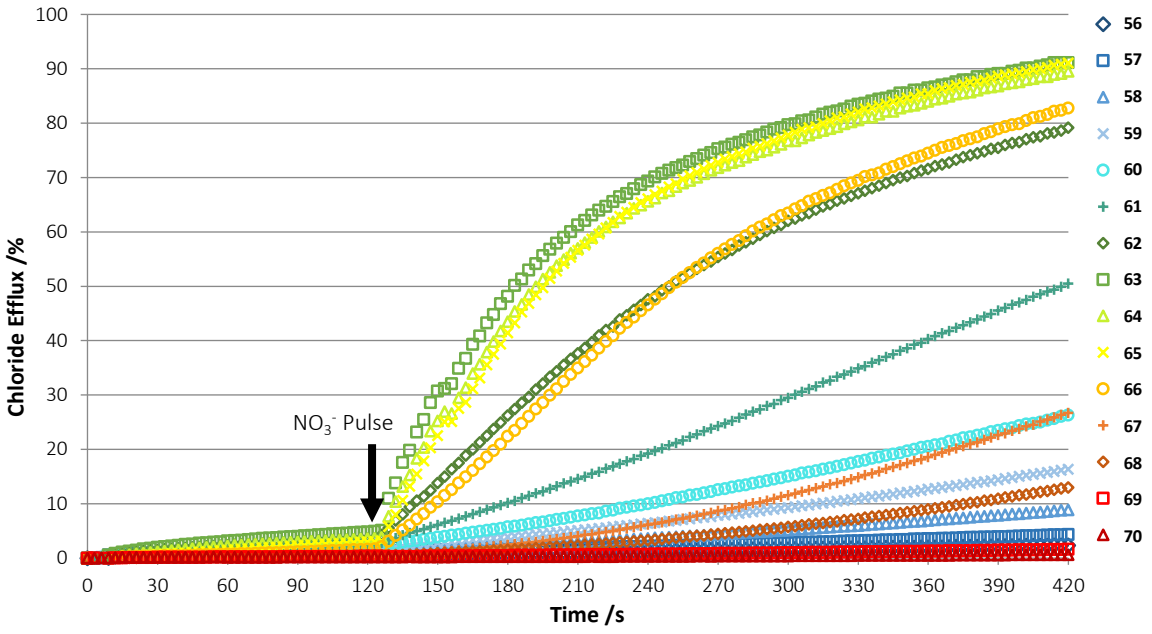


**Figure III.2** Transport curves for compounds **56** - **70** in $SO_4^{2-}$ / $NO_3^-$ spike assays in 100% POPC vesicles. Each curve represents the average of 3 trials.

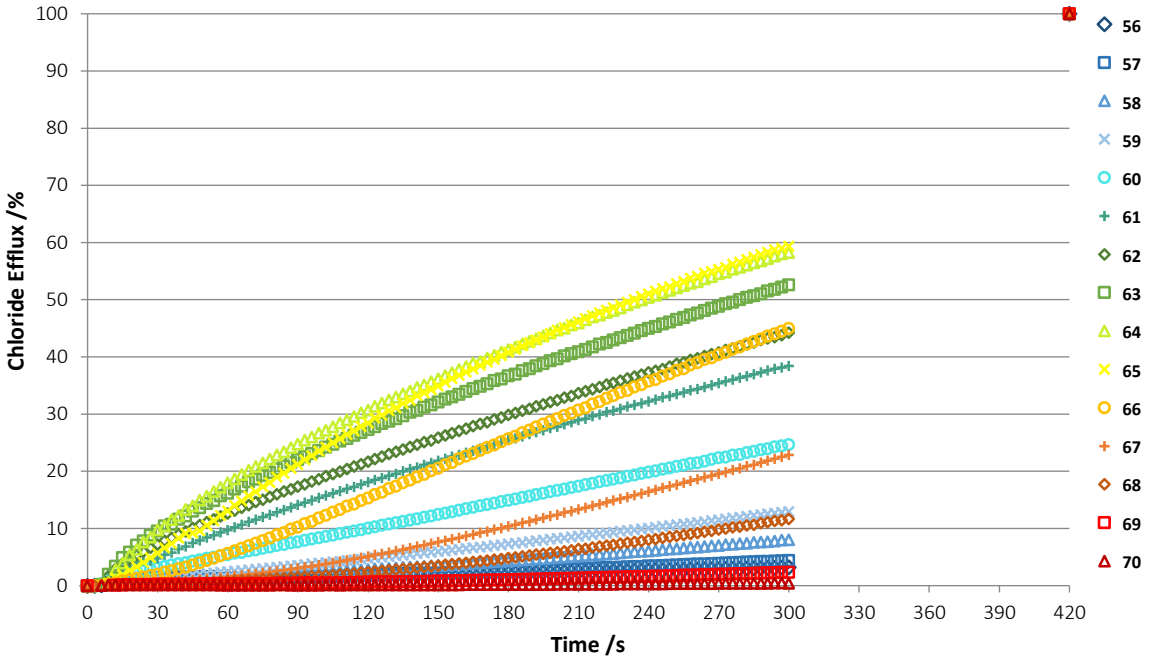


**Figure III.3** Transport curves for compounds **56** - **70** in $Cl^-/NO_3^-$ assays in 100% POPG vesicles. Each curve represents the average of 3 trials.

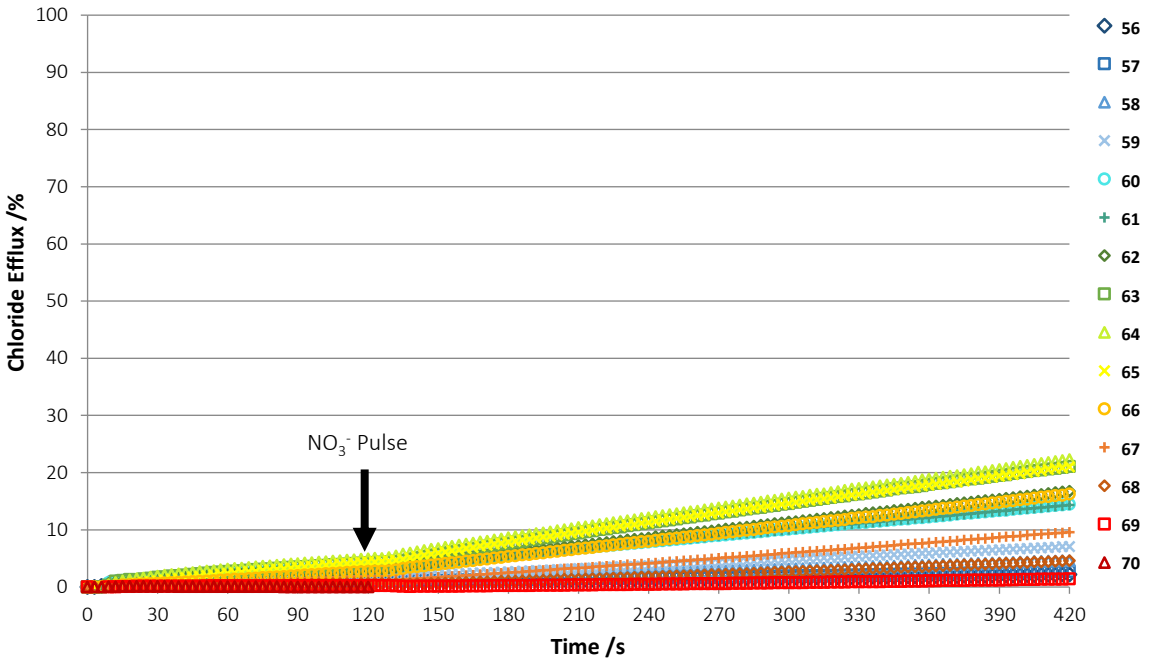


**Figure III.4** Transport curves for compounds **56** - **70** in $SO_4^{2-}$ / $NO_3^-$ spike assays in 100% POPG vesicles. Each curve represents the average of 3 trials.

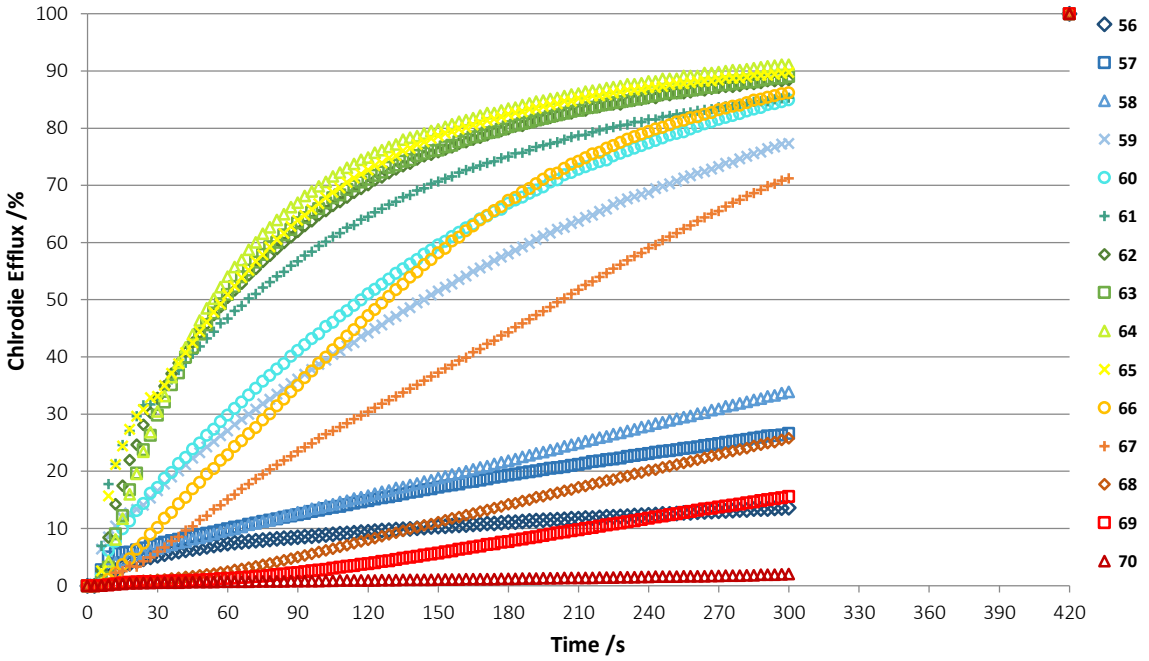


**Figure III.5** Transport curves for compounds **56** - **70** in $Cl^-/NO_3^-$ assays in 3:1 POPE:POPC vesicles. Each curve represents the average of 3 trials.

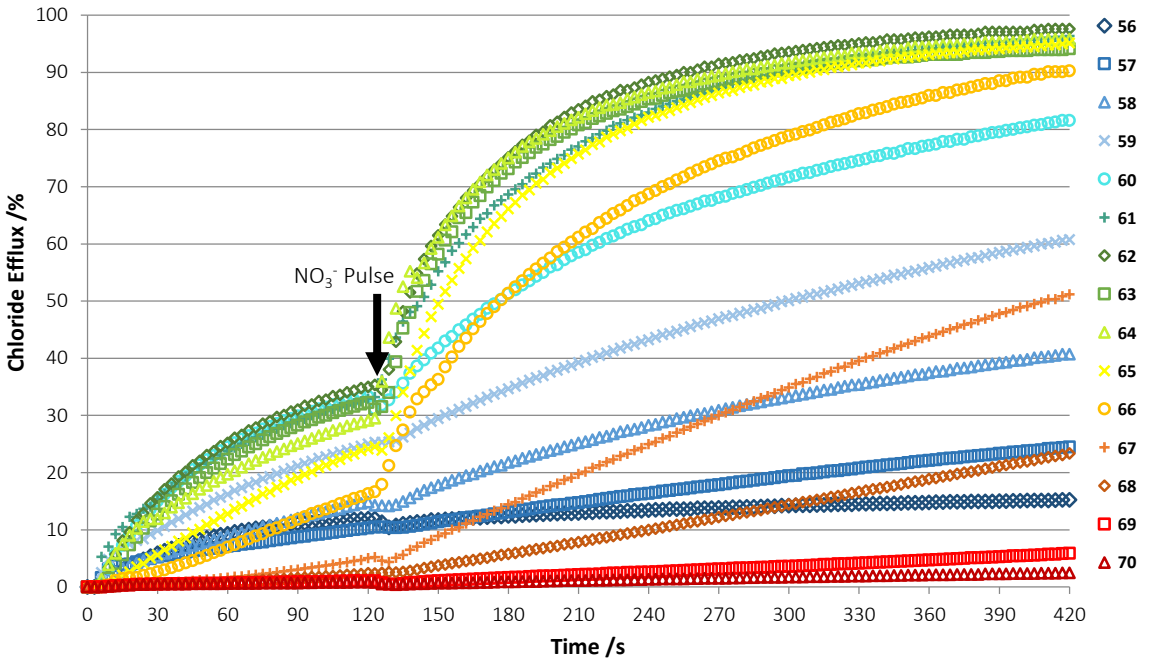


**Figure III.6** Transport curves for compounds **56** - **70** in $SO_4^{2-}$ / $NO_3^-$ spike assays in 3:1 POPE:POPC vesicles. Each curve represents the average of 3 trials. Possible sulphate transport before the addition of nitrate is observed before the addition of nitrate. Mechanisms for this are investigated in Appendix III.1.3.

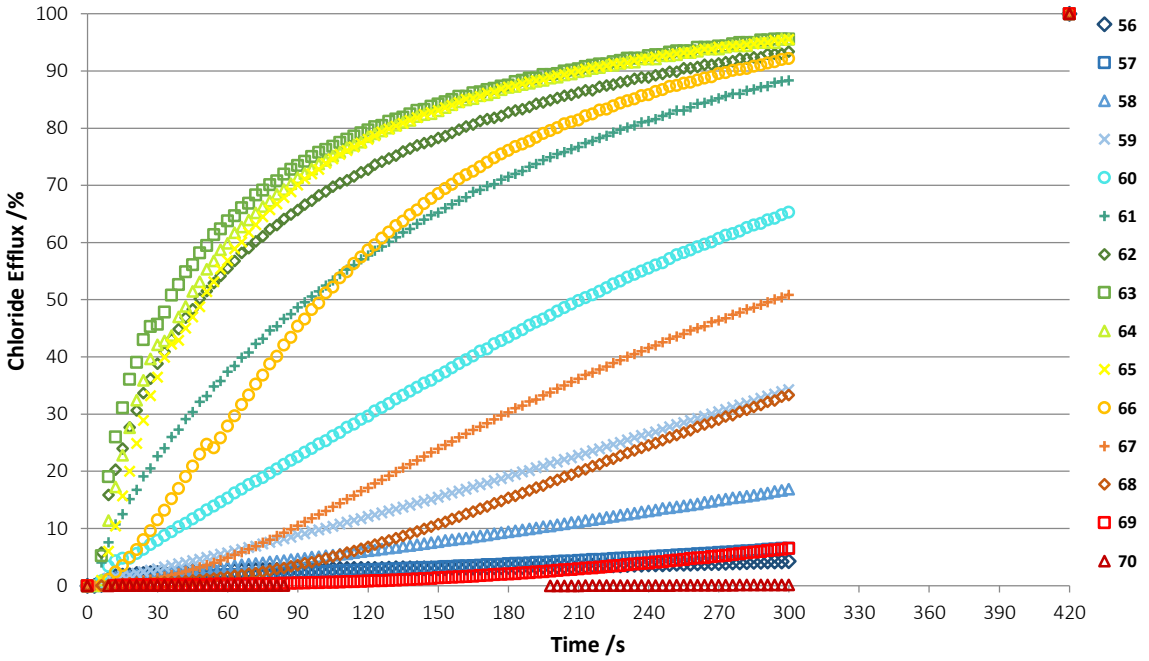


**Figure III.7** Transport curves for compounds **56** - **70** in $Cl^-/NO_3^-$ assays in 7:3 POPC:CHOL vesicles. Each curve represents the average of 3 trials.

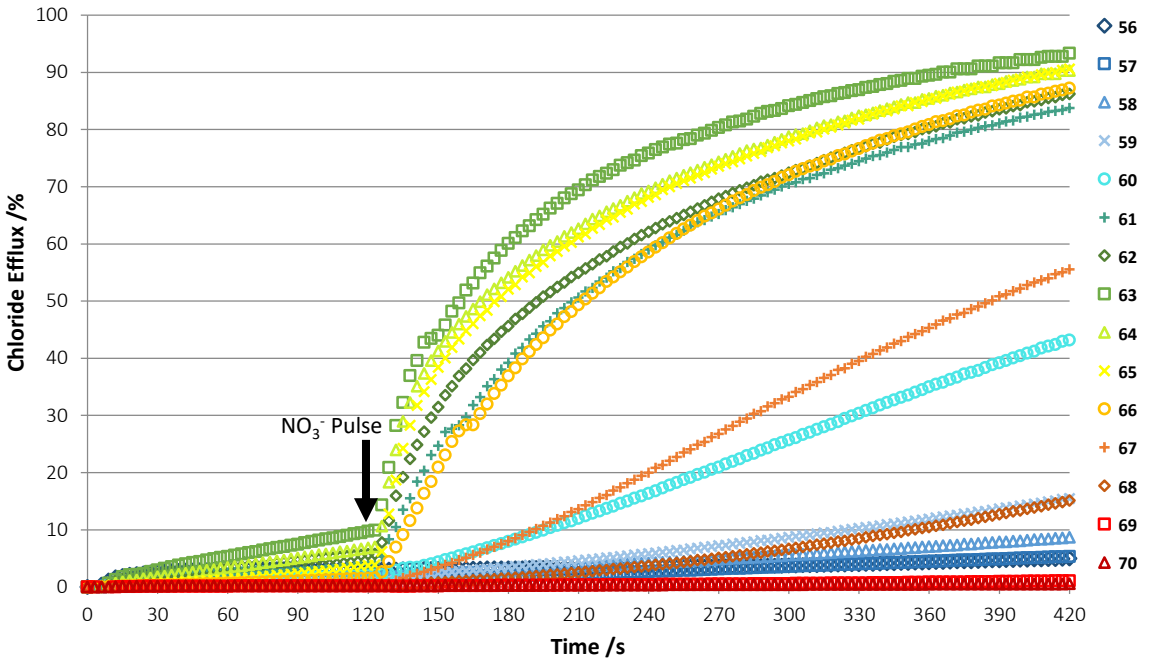


**Figure III.8** Transport curves for compounds **56** - **70** in $SO_4^{2-}$ / $NO_3^-$ spike assays in 7:3 POPC:CHOL vesicles. Each curve represents the average of 3 trials.

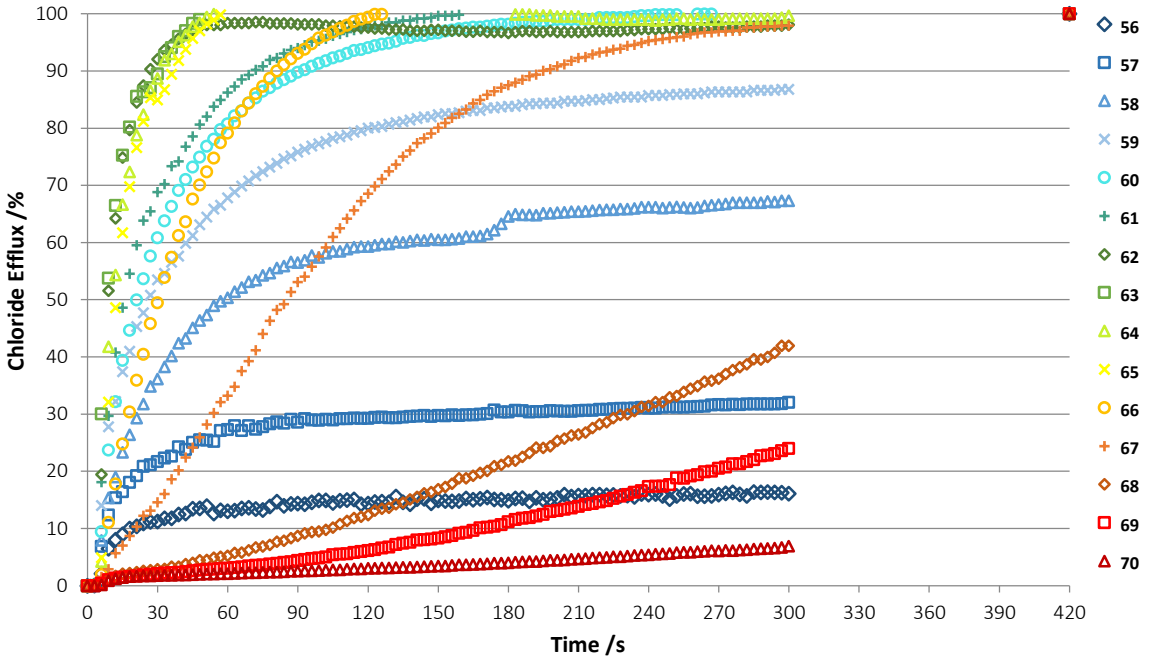


**Figure III.9** Transport curves for compounds **56** - **70** in $Cl^-/NO_3^-$ assays in 100% POPC vesicles at 55°C. Each curve represents the average of 3 trials.

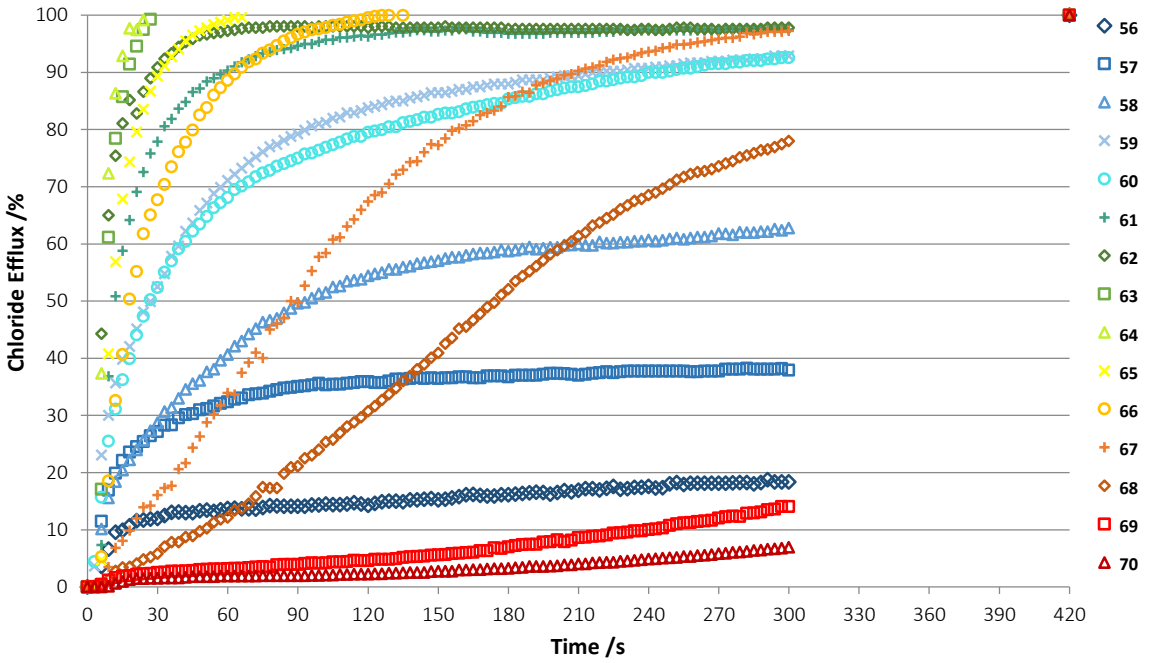


**Figure III.10** Transport curves for compounds **56** - **70** in $Cl^-/NO_3^-$ assays in 100% DPPC vesicles at 55°C. Each curve represents the average of 3 trials.

### III.1.2 NMR Titration Fit Plots

The following fit plots obtained by fitting to a 1:1 binding model using WINEQNMR2[110].

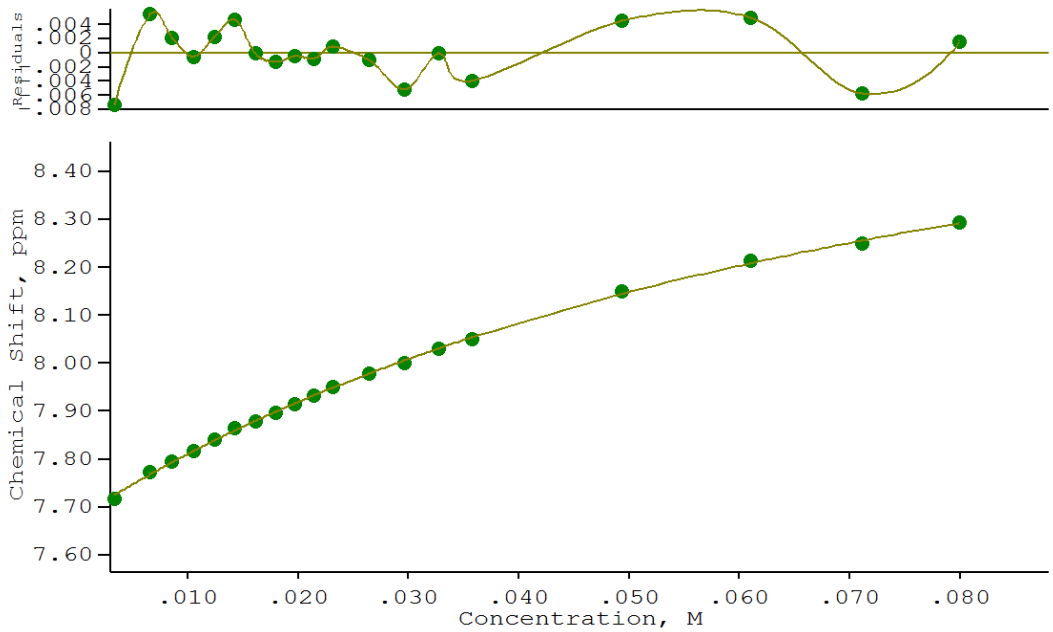


**Figure III.11** Fit plot for $^{1}$H titration of 1-phenyl-3-ethylthiourea **56** with TBA Cl, following the alkyl NH proton (δ = 7.69 ppm). K = 14 $M^{-1}$, error = 4.8 %.

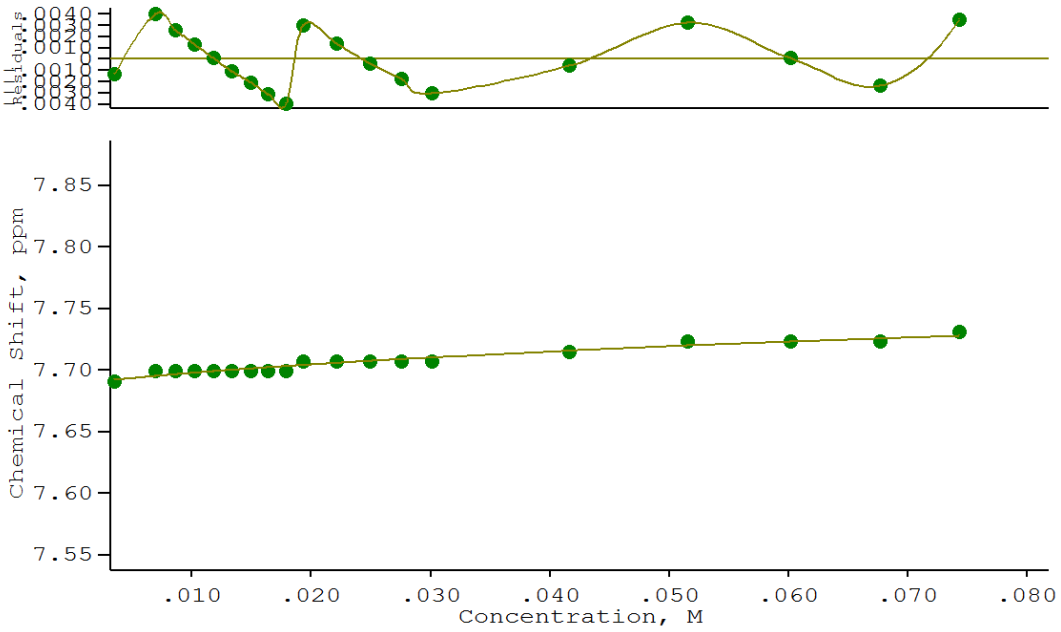


**Figure III.12** Fit plot for $^{1}$H titration of 1-phenyl-3-ethylthiourea **56** with TBA $NO_3$, following the alkyl NH proton (δ = 7.69 ppm) $M^{-1}$. K < 10.

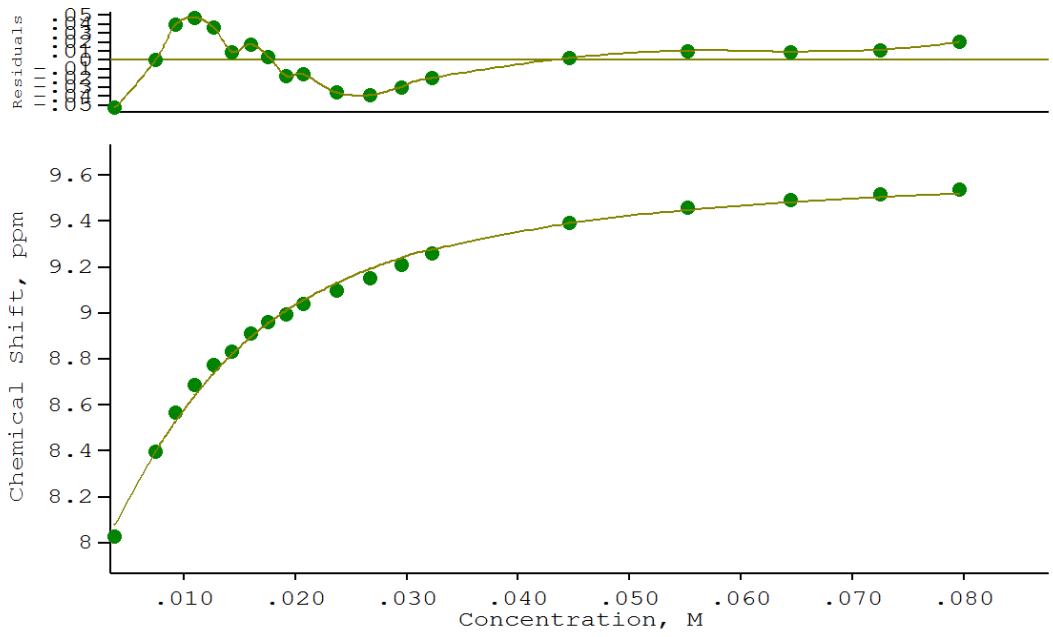


**Figure III.13** Fit plot for $^{1}H$ titration of 1-phenyl-3-ethylthiourea **56** with TBA $H_2PO_4$, following the alkyl NH proton (δ = 7.69 ppm). K = 180 $M^{-1}$, error = 8.5 %.

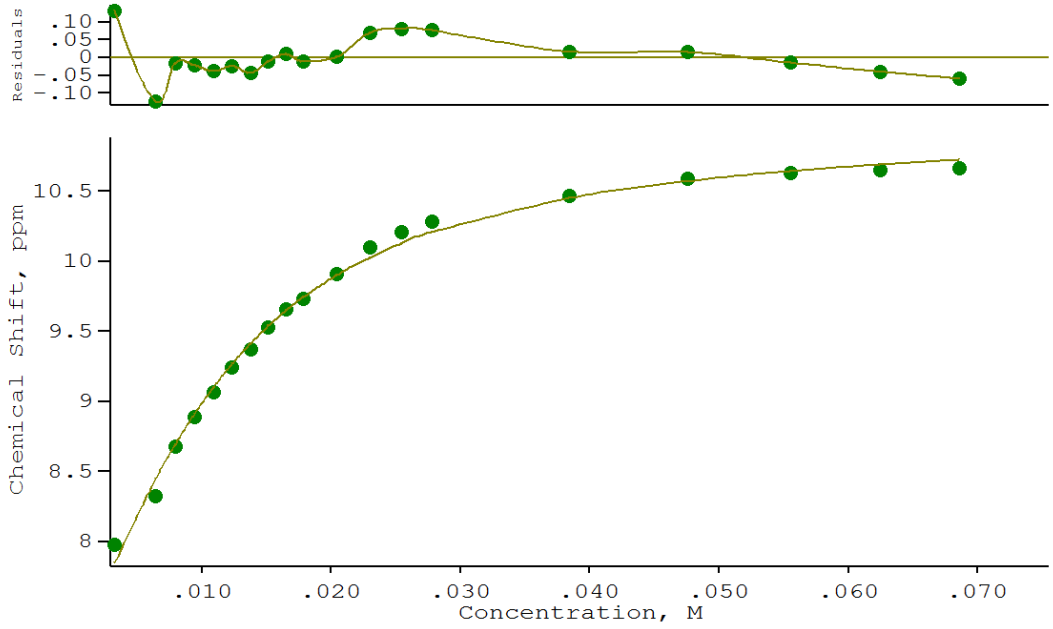


**Figure III.14** Fit plot for $^{1}H$ titration of 1-phenyl-3-ethylthiourea **56** with $TBA_2$ $SO_4$, following the alkyl NH proton (δ = 7.68 ppm). K = 200 $M^{-1}$, error = 9.2 %.

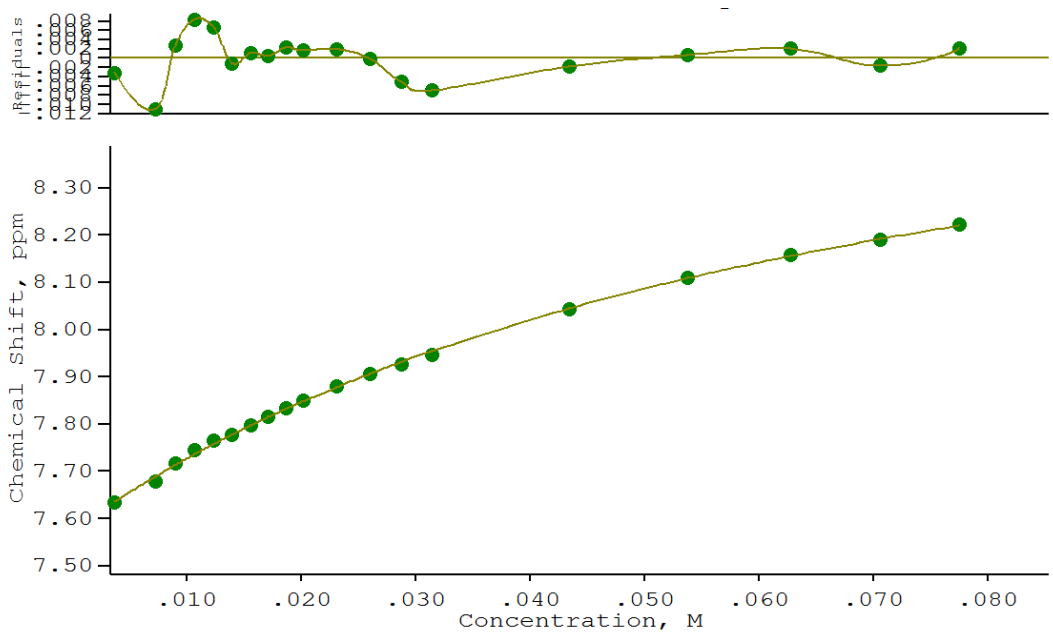


**Figure III.15** Fit plot for $^{1}H$ titration of 1-(4-butylphenyl)-3-butylthiourea **62** with TBA Cl, following the alkyl NH proton (δ = 7.57 ppm). K = 17 $M^{-1}$, error = 5.6 %.

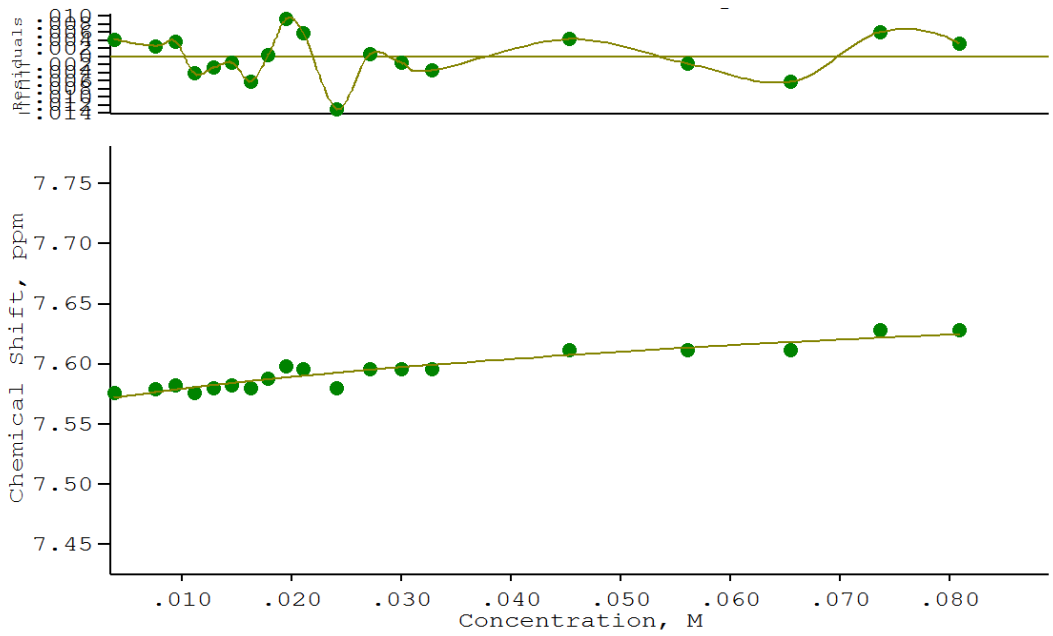


**Figure III.16** Fit plot for $^{1}H$ titration of 1-(4-butylphenyl)-3-butylthiourea **62** with TBA $NO_3$, following the alkyl NH proton (δ = 7.57 ppm). K < 10 $M^{-1}$.

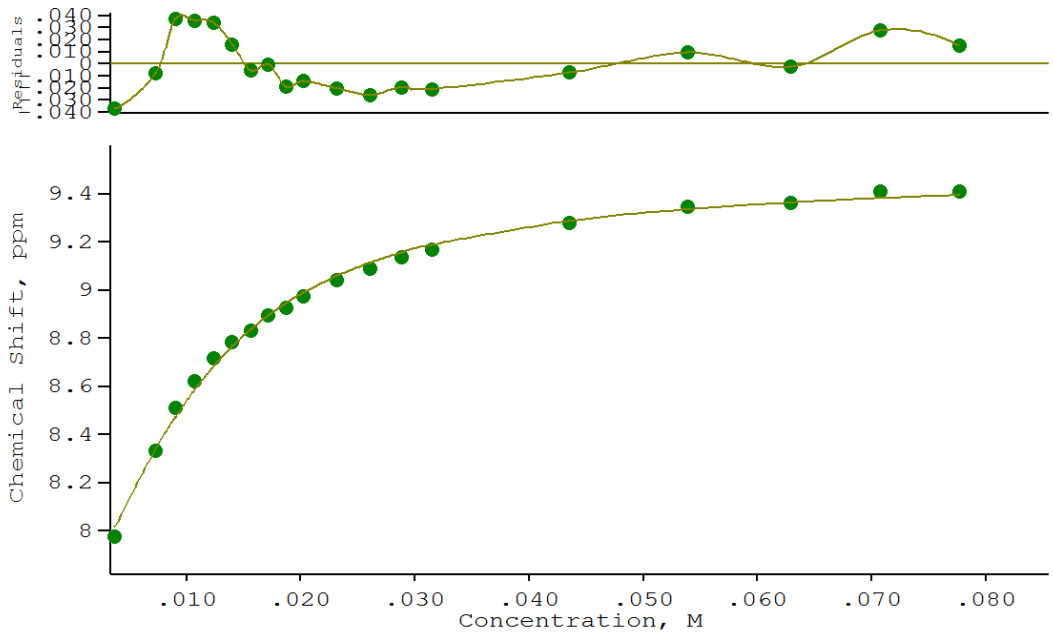


**Figure III.17** Fit plot for $^{1}H$ titration of 1-(4-butylphenyl)-3-butylthiourea **62** with TBA $H_2PO_4$, following the alkyl NH proton (δ = 7.58 ppm). K = 220 $M^{-1}$, error 7.5 %.

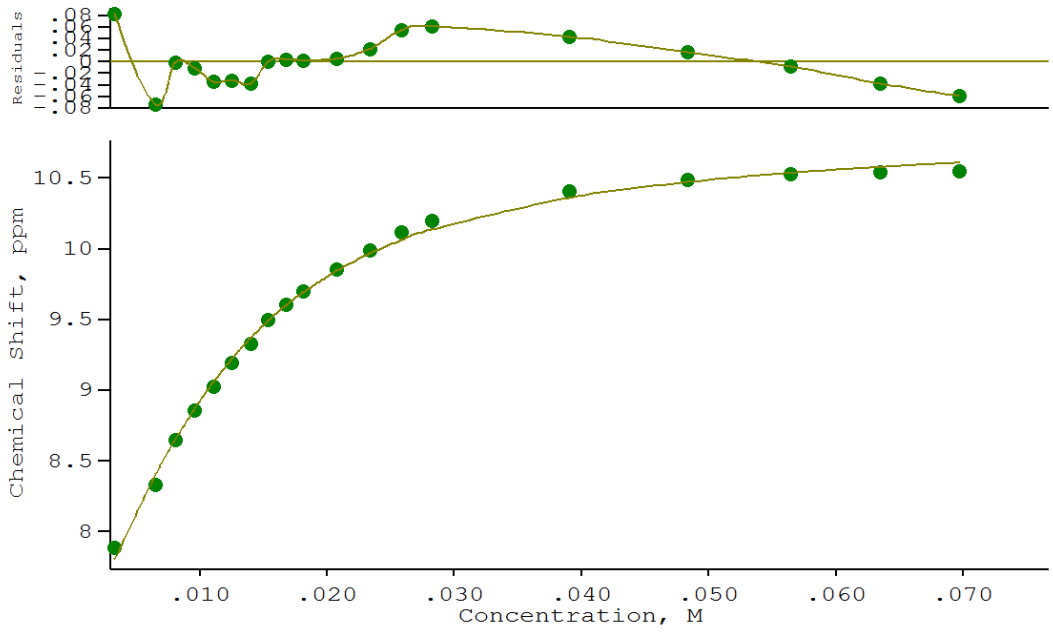


**Figure III.18** Fit plot for $^{1}H$ titration of 1-(4-butylphenyl)-3-butylthiourea **62** with $TBA_2$ $SO_4$, following the alkyl NH proton (δ = 7.57 ppm). K = 220 $M^{-1}$, error = 6.7 %.

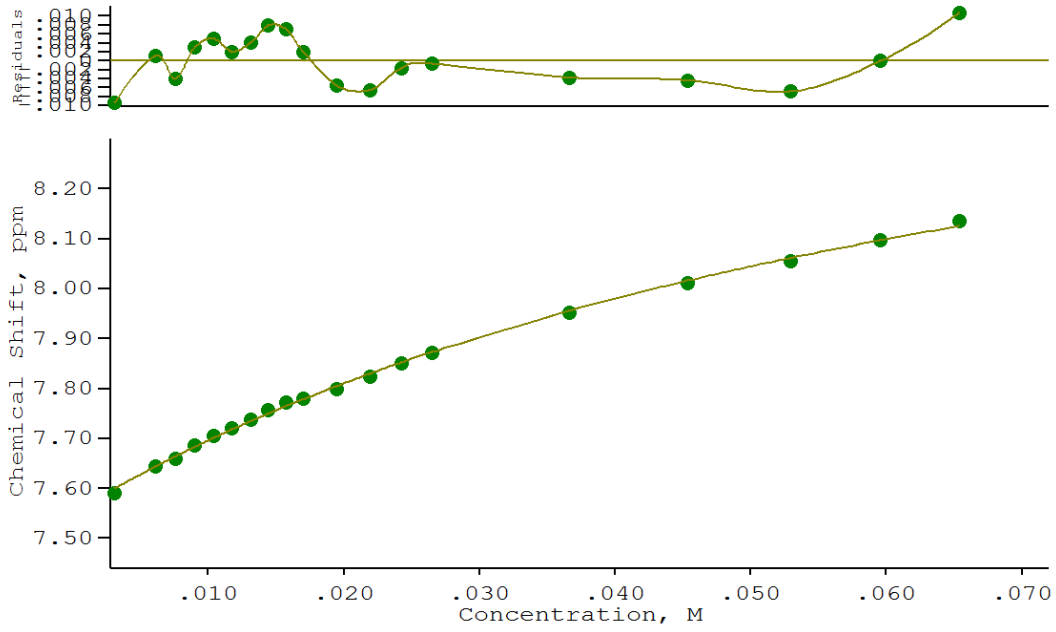


**Figure III.19** Fit plot for $^{1}$H titration of 1-(4-octylphenyl)-3-octylthiourea **70** with TBA Cl, following the alkyl NH proton (δ = 7.55 ppm). K = 16 $M^{-1}$, error = 8.7 %.

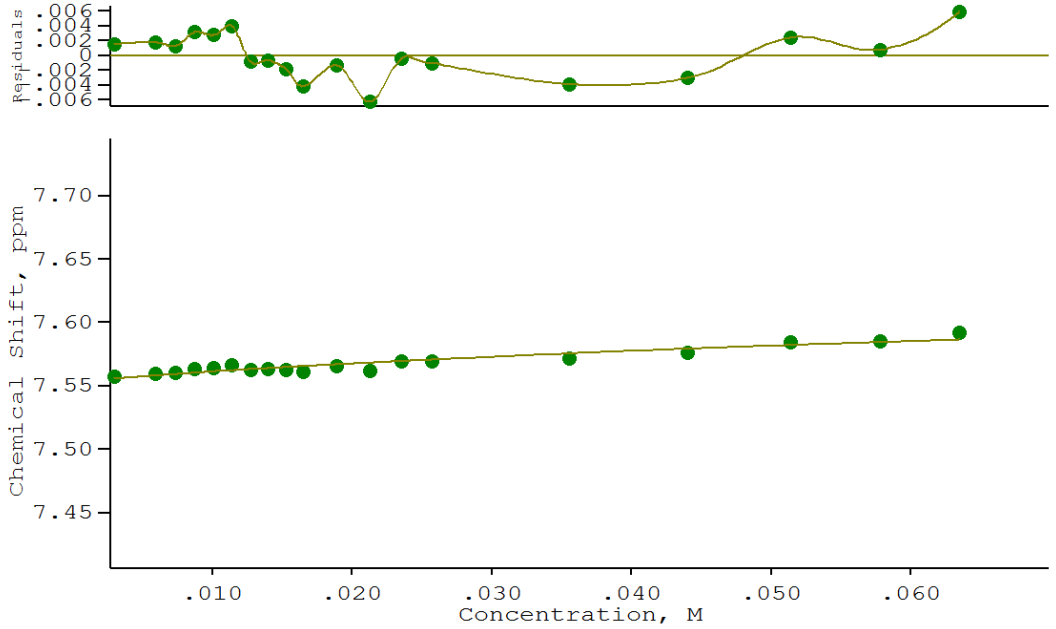


**Figure III.20** Fit plot for $^{1}$H titration of 1-(4-octylphenyl)-3-octylthiourea **70** with TBA $NO_3$, following the alkyl NH proton (δ = 7.55 ppm). K < 10 $M^{-1}$.

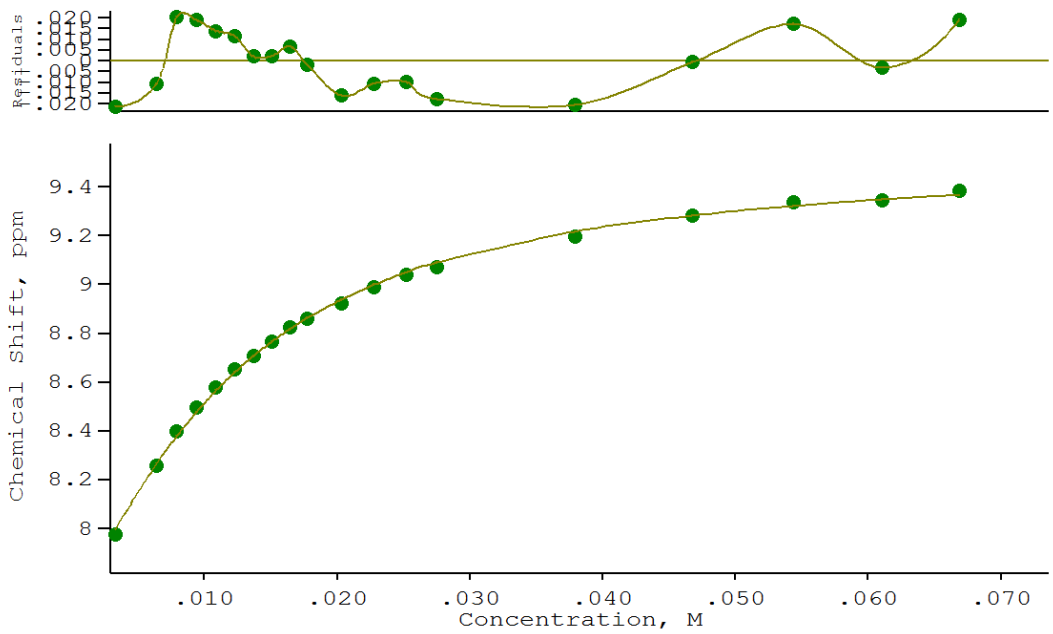


**Figure III.21** Fit plot for $^{1}H$ titration of 1-(4-octylphenyl)-3-octylthiourea **70** with TBA $H_2PO_4$, following the alkyl NH proton (δ = 7.56 ppm). K = 160 $M^{-1}$, error = 4.7 %.

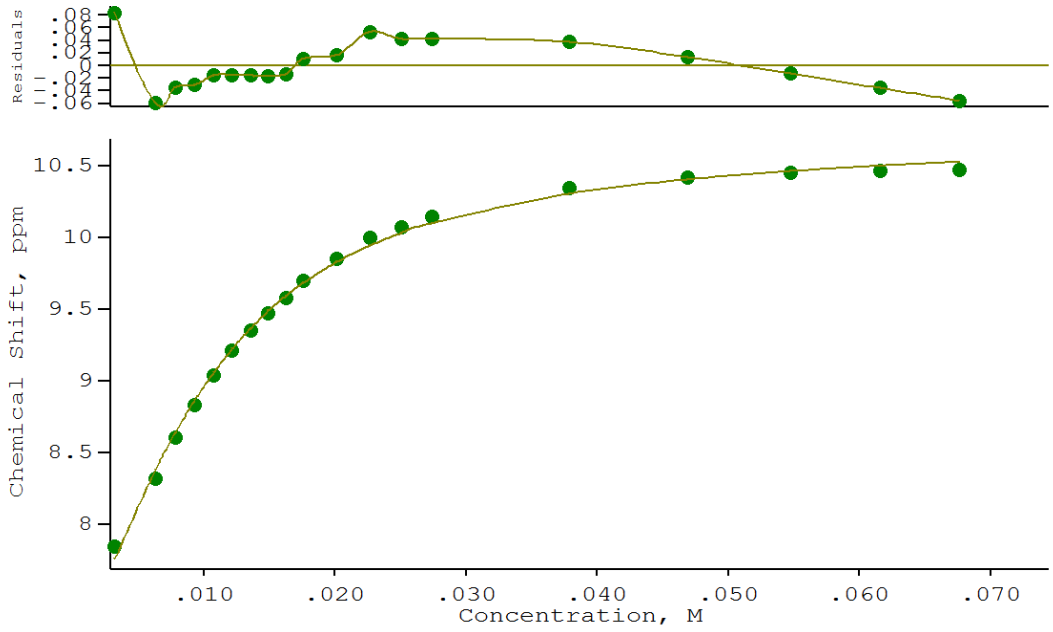


**Figure III.22** Fit plot for $^{1}H$ titration of 1-(4-octylphenyl)-3-octylthiourea **70** with $TBA_2$ $SO_4$, following the alkyl NH proton (δ = 7.56 ppm). K = 250 $M^{-1}$, error = 6.3 %.

### III.1.3 Possible $SO_4^{2-}$ Transport

As much as 30 % chloride efflux was observed for the series before the addition of nitrate in $SO_4^{2-}$/$NO_3^-$ spike assays in the 3:1 POPE:POPC system (Figure III.6). Possible explanations of this include general leakage of the vesicles, $SO_4^{2-}$/$Cl^-$ antiport, HCl co-transport or MCl symport.

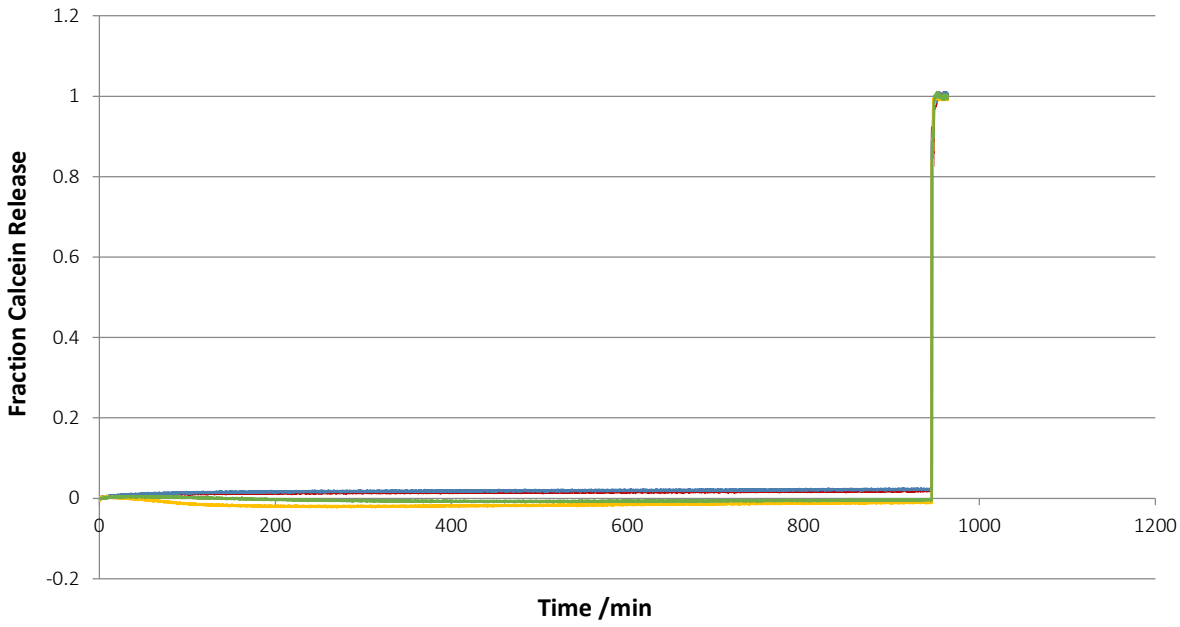


**Figure III.23** Calcein leakage test for compounds **56**, **62** & **70**.

The general leakage of the 3:1 POPE:POPC system was tested by a calcein leakage test. Calcein is a self-quenching fluorophore and an increase in calcein fluorescence is observed with increasing leakage from the vesicles. No significant leakage was observed up to 16 hours after addition of the thioureas.

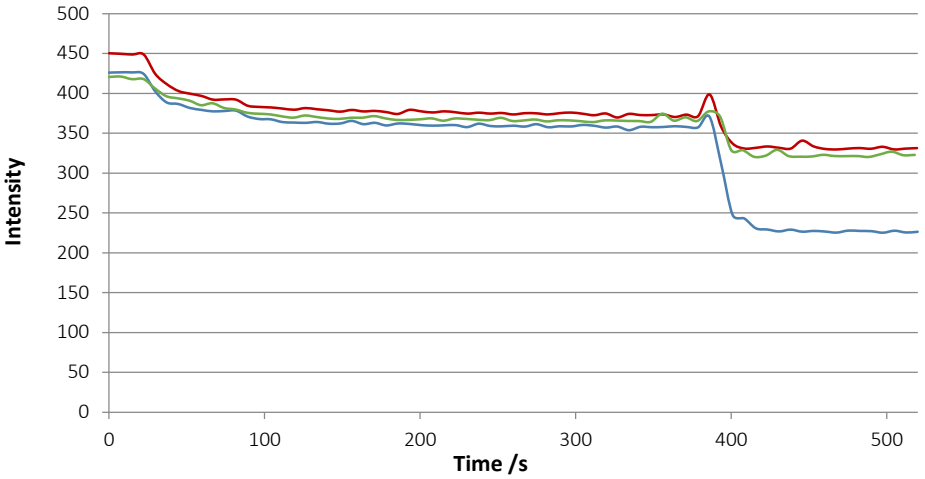


**Figure III.24** Fluorescence trace (Ex. 372 nm, Em. 503 nm) for lucigenin assay for DMSO. External anion added at 30 s, test compound added at 90 s, vesicles lysed at 390 s. Anion added – Blue: $Cl^-$, Green: $NO_3^-$, Red: $SO_4^{2-}$. Each point represents the average of 3 trials.

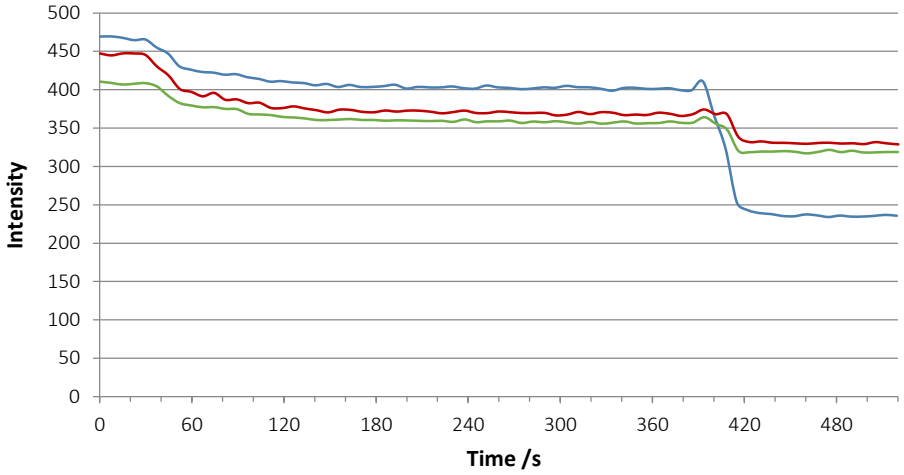


**Figure III.25** Fluorescence trace (Ex. 372 nm, Em. 503 nm) for lucigenin assay for compound **56**. External anion added at 30 s, test compound added at 90 s, vesicles lysed at 390 s. Anion added – Blue: $Cl^-$, Green: $NO_3^-$, Red: $SO_4^{2-}$. Each point represents the average of 3 trials.

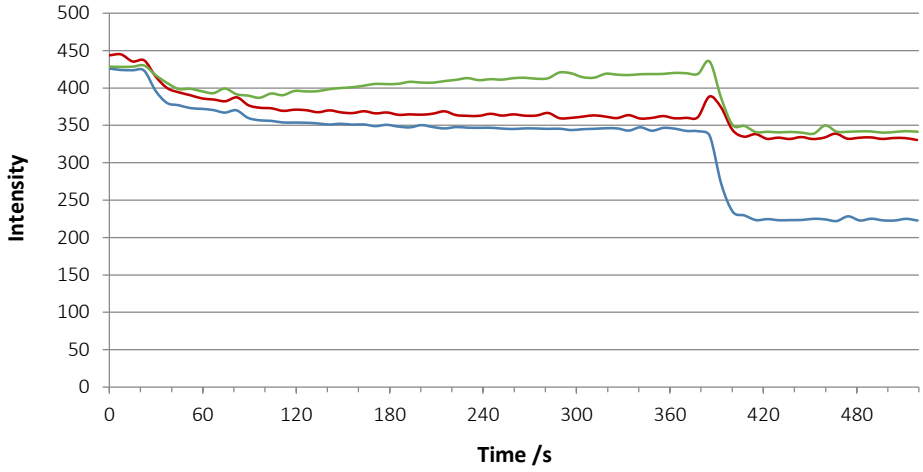


**Figure III.26** Fluorescence trace (Ex. 372 nm, Em. 503 nm) for lucigenin assay for compound **62**. External anion added at 30 s, test compound added at 90 s, vesicles lysed at 390 s. Anion added – Blue: $Cl^-$, Green: $NO_3^-$, Red: $SO_4^{2-}$. Each point represents the average of 3 trials.

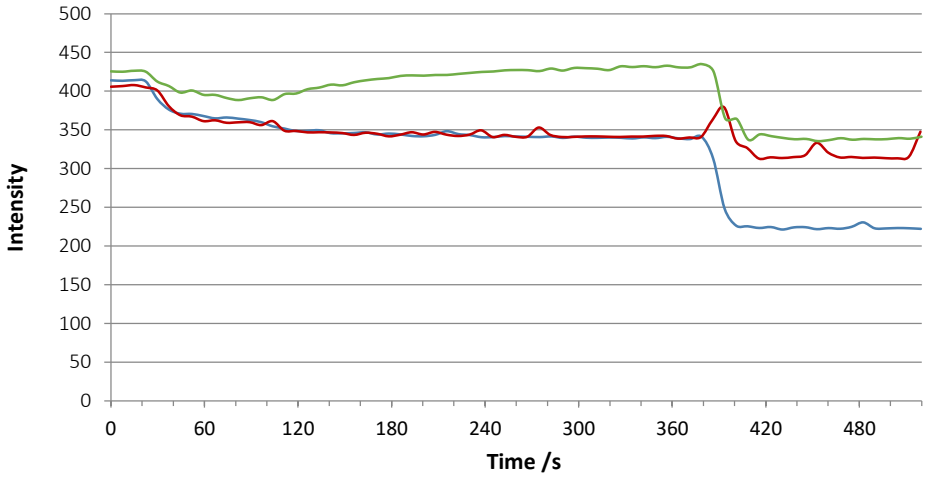


**Figure III.27** Fluorescence trace (Ex. 372 nm, Em. 503 nm) for lucigenin assay for compound **64**. External anion added at 30 s, test compound added at 90 s, vesicles lysed at 390 s. Anion added – Blue: $Cl^-$, Green: $NO_3^-$, Red: $SO_4^{2-}$. Each point represents the average of 3 trials.

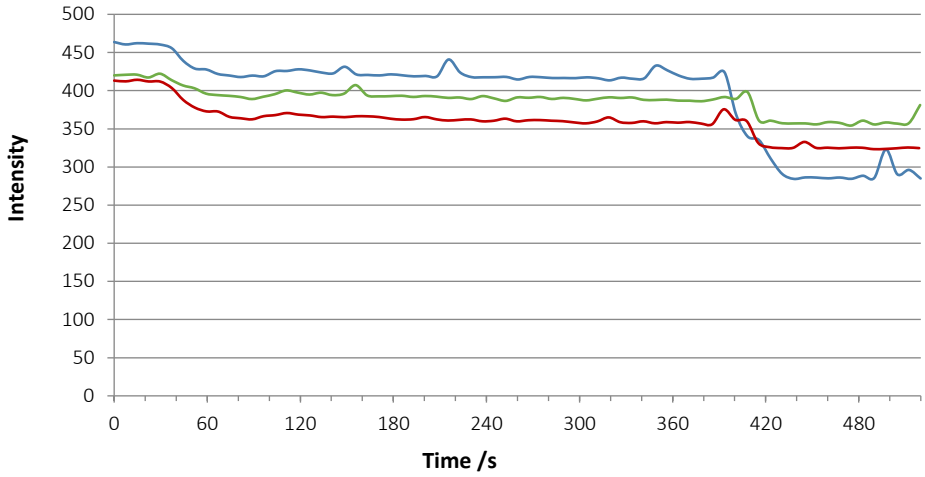


**Figure III.28** Fluorescence trace (Ex. 372 nm, Em. 503 nm) for lucigenin assay for compound **70**. External anion added at 30 s, test compound added at 90 s, vesicles lysed at 390 s. Anion added – Blue: $Cl^-$, Green: $NO_3^-$, Red: $SO_4^{2-}$. Each trace represents the average of 3 trials.

It was attempted to directly observe sulphate transport by a lucigenin assay. Vesicles were prepared containing lucigenin dye and containing $Cl^-$ in both the external and internal medium. During the experiment, a pulse of external anion ($Cl^-$ / $NO_3^-$ / $SO_4^{2-}$) is added, followed 60 s later by the test compound. As lucigenin fluorescence is quenched in the presence of chloride, thus an increase in lucigenin fluorescence after anion addition suggests efflux of chloride from the vesicle, replaced by the added external anion.

In all tests, the change in fluorescence in the presence of external $SO_4^{2-}$ is not significantly different from the $Cl^-$ control. By contrast, the transport of $NO_3^-$ into the vesicle is evident, in line with the relative transport rates observed for each compounds previously. This suggests there is little to no significant sulphate transport in this system.

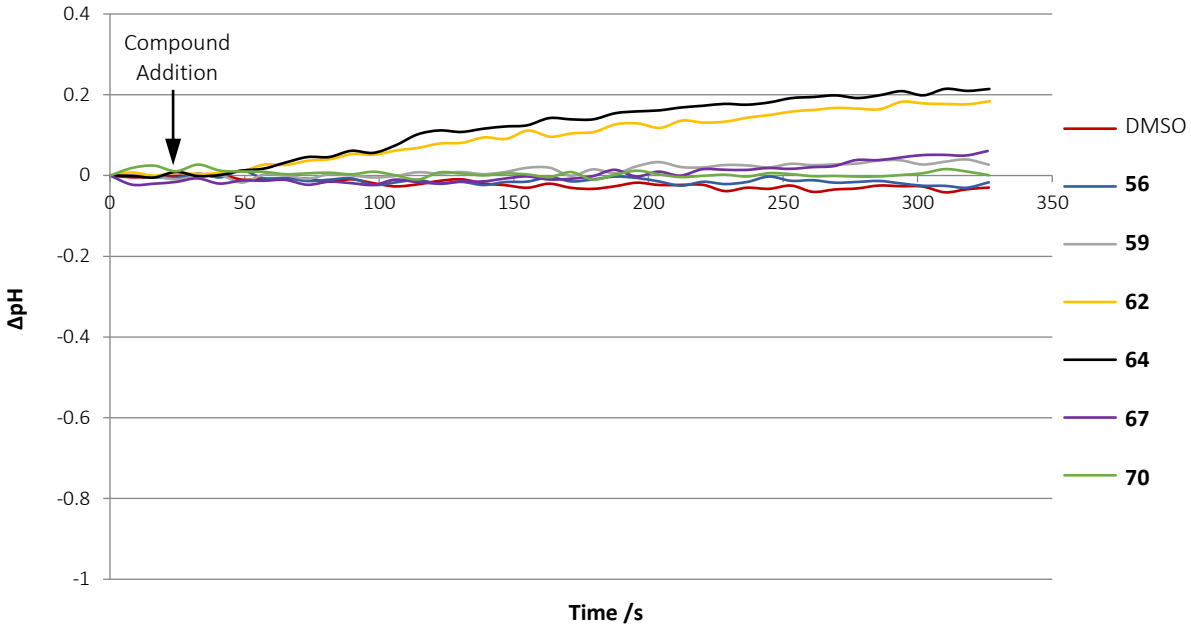


**Figure III.29** Change in intravesicular pH calculated via HPTS assay. Test compound added at 30 s. Each trace represents the average of 3 trials.

The possibility of HCl co-transport (or $Cl^-$ / $OH^-$ antiport) was tested by monitoring the change in the internal pH of the vesicles. An HPTS assay was used, with the ratio of the fluorescence emissions of the protonated and deprotonated forms converted to a pH value as previously reported[63]. The most active compounds showed a small increase in internal pH over the course of the experiment, indicating that some HCl efflux was possible. However, the magnitude of the pH change is not large enough to fully explain the level of chloride efflux observed in Figure III.6.

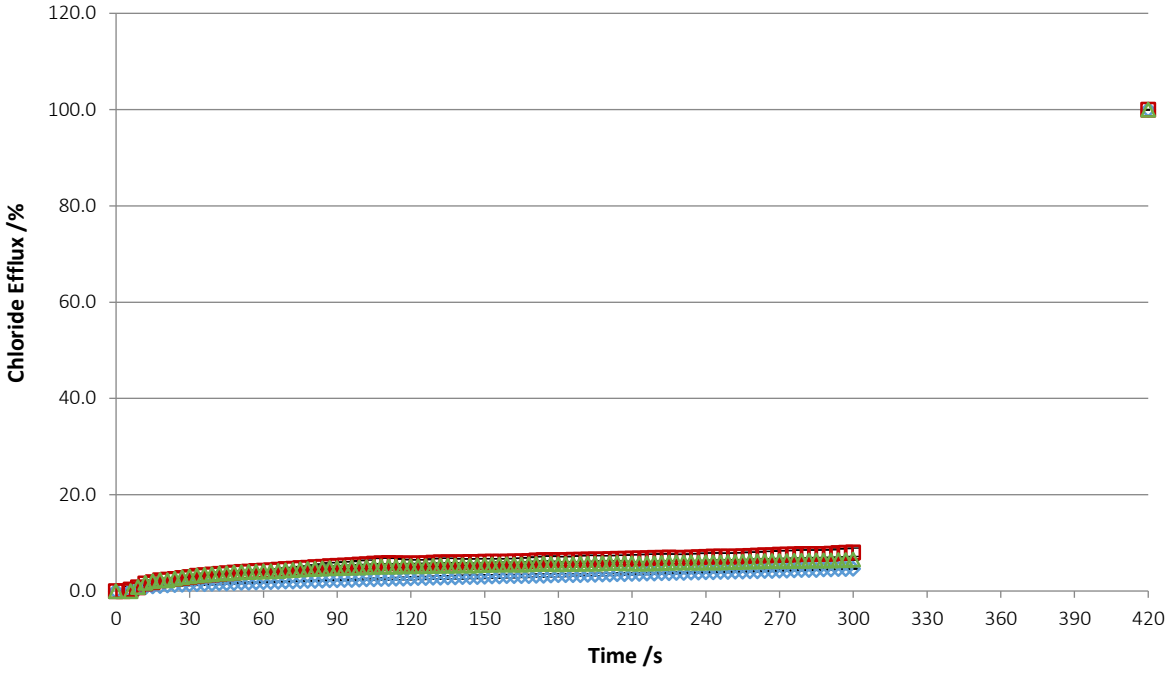


**Figure III.30** Chloride efflux from 3:1 POPE:POPC vesicles in $Cl^-$ / $NO_3^-$ assays by compound **56** in the presence of varying internal cations. Internal cation - blue diamonds: $Na^+$, red squares: $K^+$, green triangles: $Cs^+$. Each point represents the average of 3 trials.

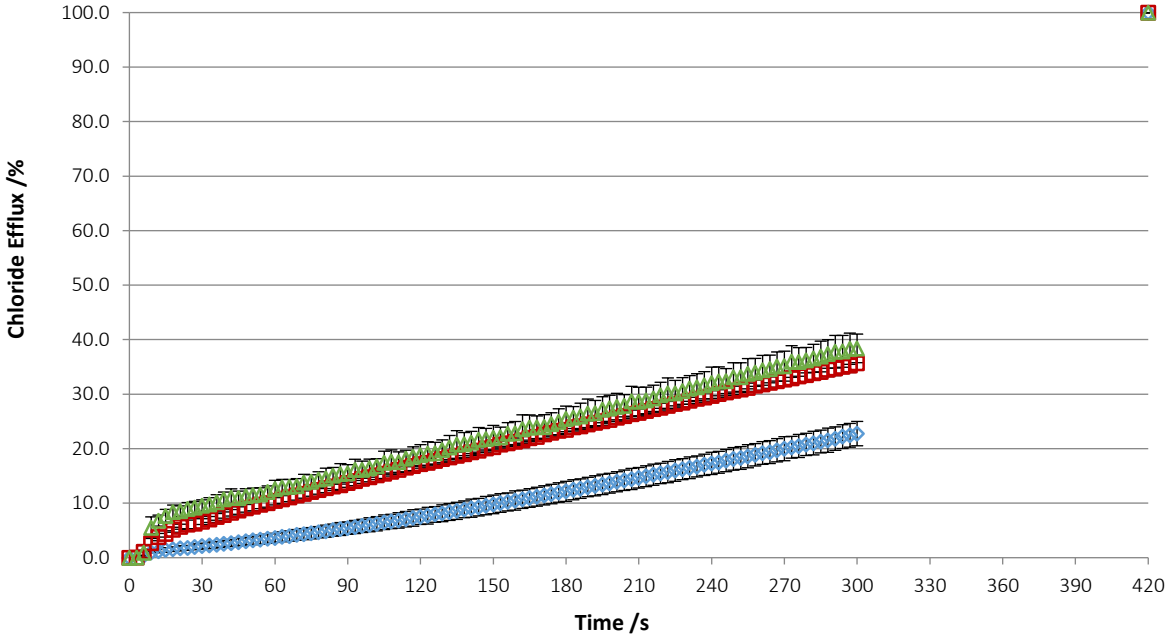


**Figure III.31** Chloride efflux from 3:1 POPE:POPC vesicles in $Cl^-$ / $NO_3^-$ assays by compound **59** in the presence of varying internal cations. Internal cation - blue diamonds: $Na^+$, red squares: $K^+$, green triangles: $Cs^+$. Each point represents the average of 3 trials.

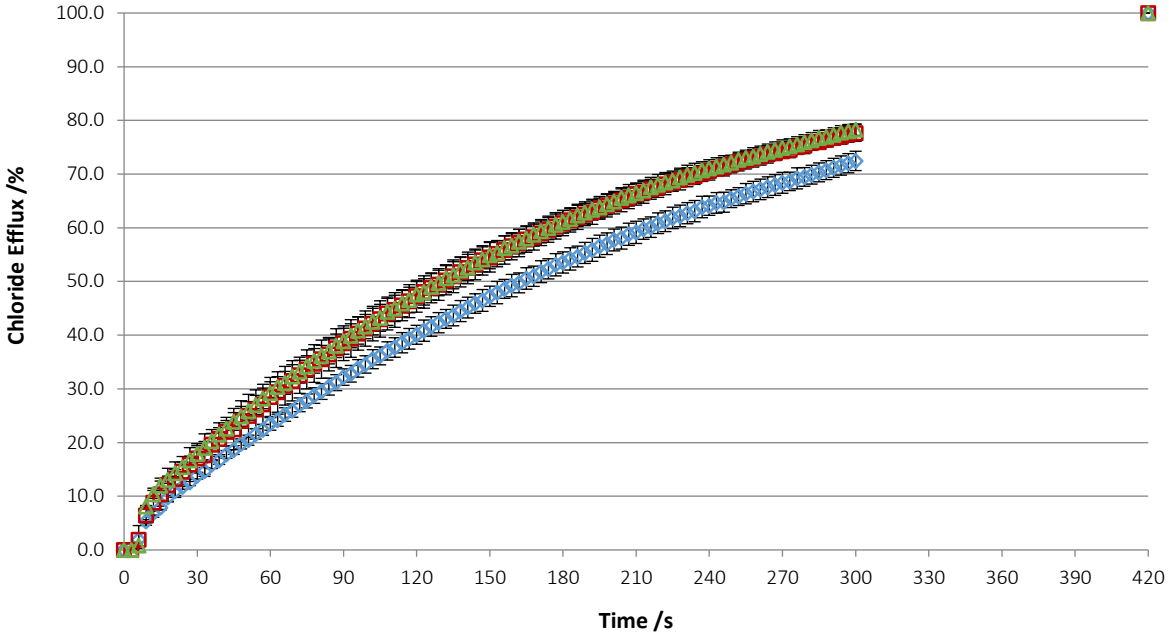


**Figure III.32** Chloride efflux from 3:1 POPE:POPC vesicles in $Cl^-$ / $NO_3^-$ assays by compound **62** in the presence of varying internal cations. Internal cation - blue diamonds: $Na^+$, red squares: $K^+$, green triangles: $Cs^+$. Each point represents the average of 3 trials.

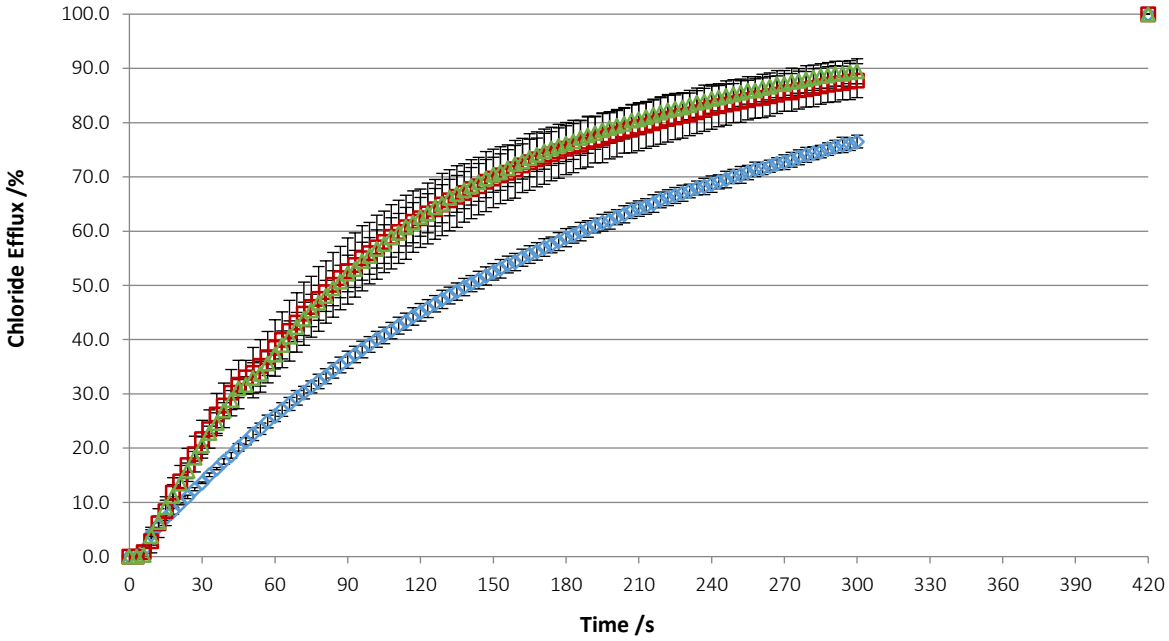


**Figure III.33** Chloride efflux from 3:1 POPE:POPC vesicles in $Cl^-$ / $NO_3^-$ assays by compound **64** in the presence of varying internal cations. Internal cation - blue diamonds: $Na^+$, red squares: $K^+$, green triangles: $Cs^+$. Each point represents the average of 3 trials.

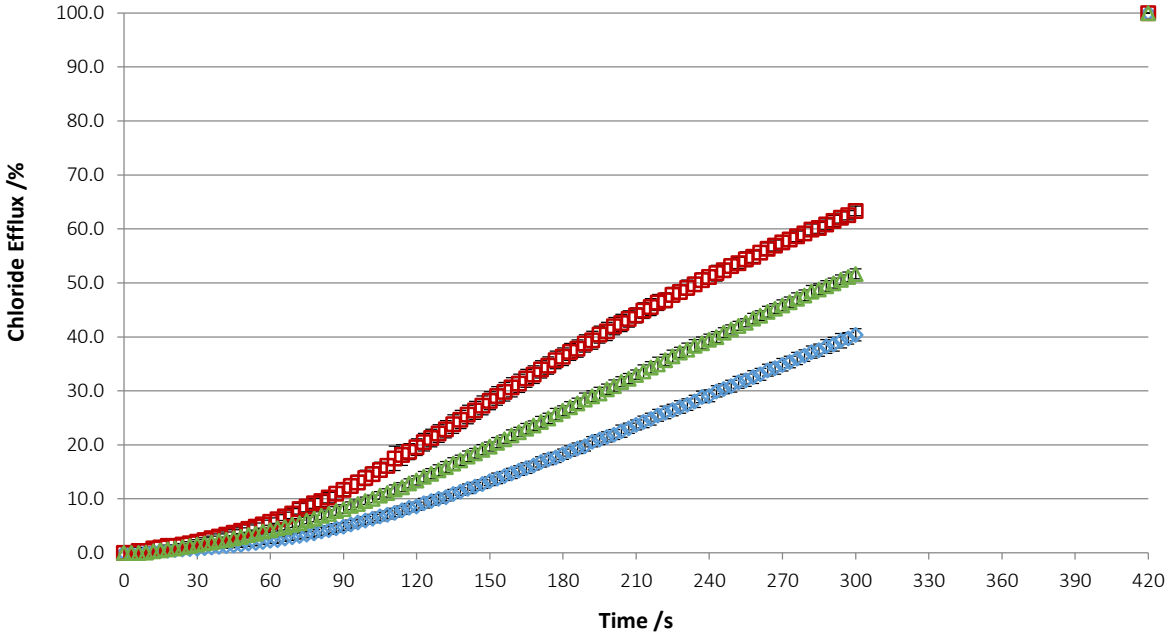


**Figure III.34** Chloride efflux from 3:1 POPE:POPC vesicles in $Cl^-$ / $NO_3^-$ assays by compound **67** in the presence of varying internal cations. Internal cation - blue diamonds: $Na^+$, red squares: $K^+$, green triangles: $Cs^+$. Each point represents the average of 3 trials.

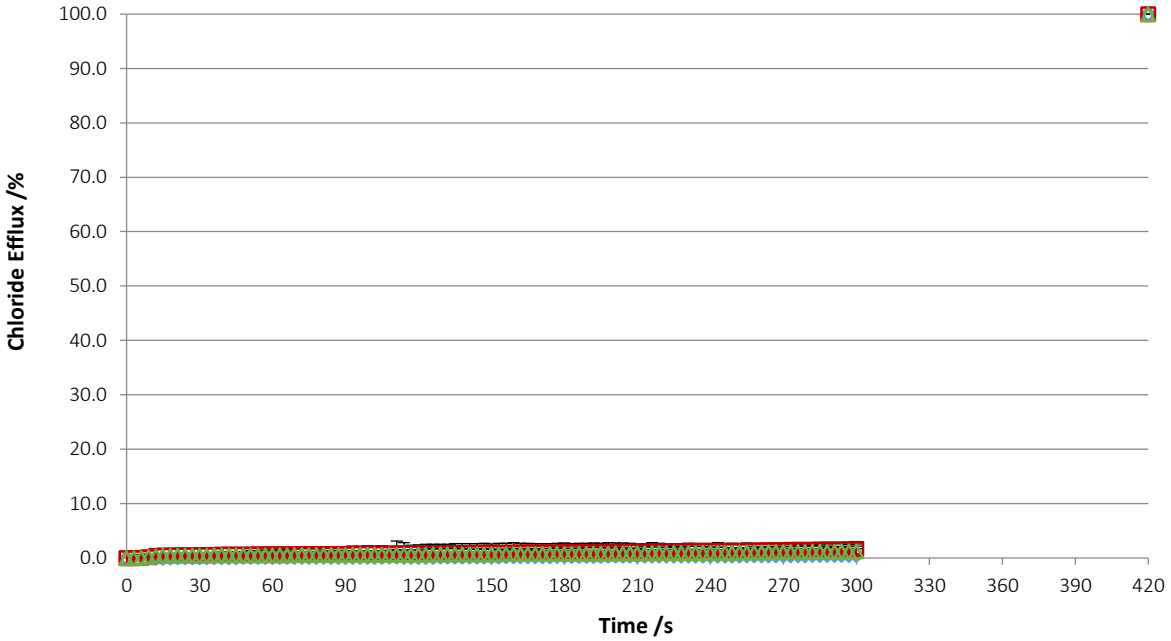


**Figure III.35** Chloride efflux from 3:1 POPE:POPC vesicles in $Cl^-$ / $NO_3^-$ assays by compound **70** in the presence of varying internal cations. Internal cation - blue diamonds: $Na^+$, red squares: $K^+$, green triangles: $Cs^+$. Each point represents the average of 3 trials.

Finally, the dependence on the potential for MCl symport was tested by examining the dependence of transport rate on the internal cation. $Cl^-$ / $NO_3^-$ assays were repeated, replacing the internal salt with KCl and CsCl. It was evident for compounds that were good transporters that the rate of transport was dependent on the cation present. For compounds **62**, **64** & **67** the larger cations appeared to increase the rate of transport, giving up to 15 % more efflux of chloride after 270 s in the case of compound **62**. This suggests that the compounds are capable of some MCl transport, with the larger cations forming stable ion-pair complexes with the chloride-transporter complex. It is noted that the larger cation appear to decrease the rate for compound **59**, we suggest that they are too large to be shielded from unfavourable interactions with the lipid tail groups by the transporter's shorter alkyl chains.

## III.2 Thiosemicarbazone Series

### III.2.1 Hill Fits

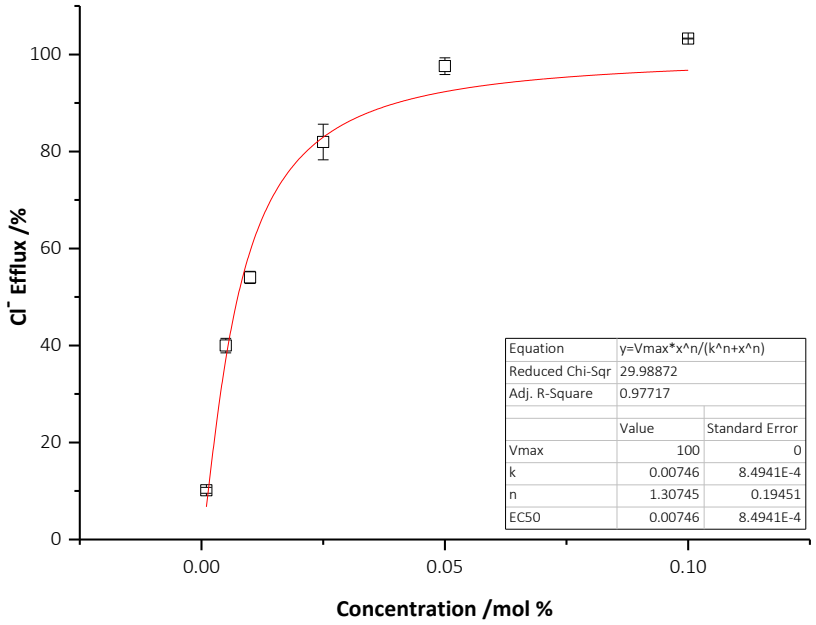


**Figure III.36** Hill plot for compound **73**, showing chloride efflux response after 270 s at each concentration tested (black squares), fitted curve from Hill equation fitting (red line) and assorted output data from the fitting operation (tabulated).

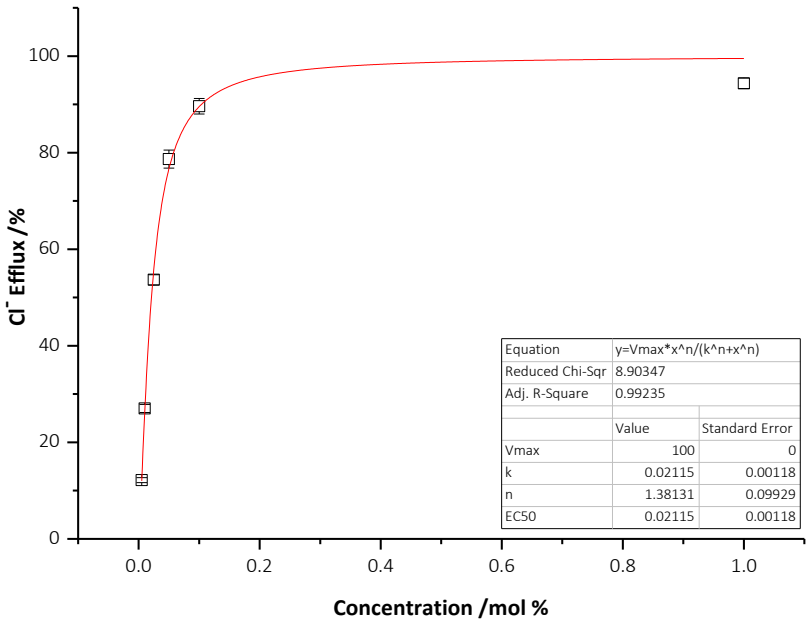


**Figure III.37** Hill plot for compound **74**, showing chloride efflux response after 270 s at each concentration tested (black squares), fitted curve from Hill equation fitting (red line) and assorted output data from the fitting operation (tabulated).

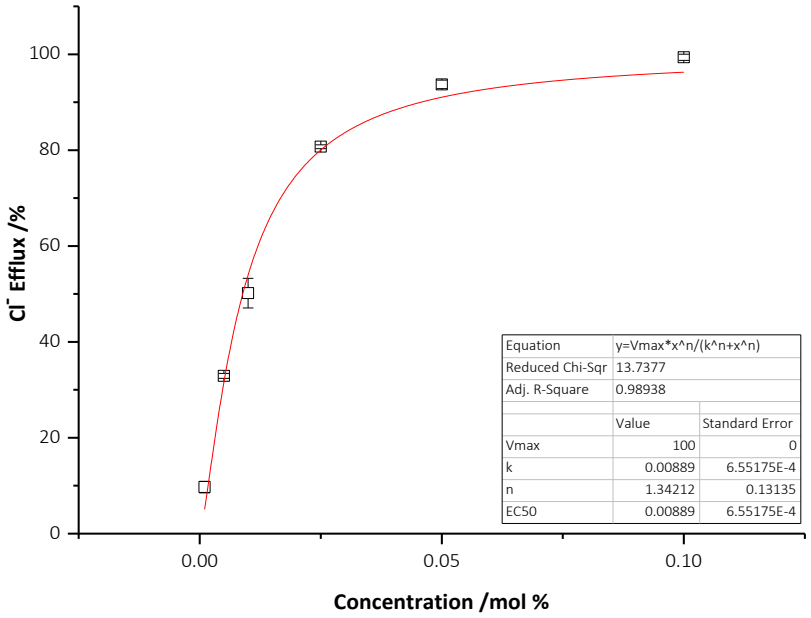


**Figure III.38** Hill plot for compound **75**, showing chloride efflux response after 270 s at each concentration tested (black squares), fitted curve from Hill equation fitting (red line) and assorted output data from the fitting operation (tabulated).

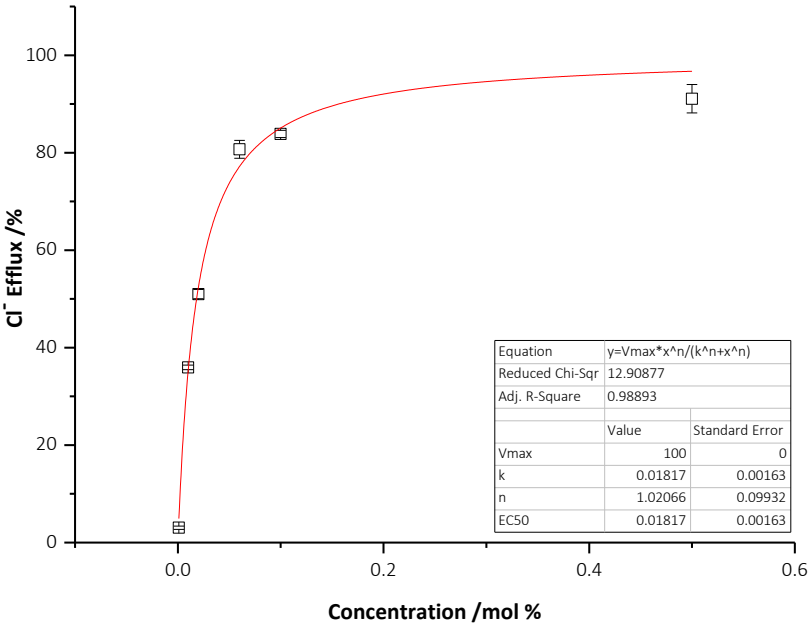


**Figure III.39** Hill plot for compound **76**, showing chloride efflux response after 270 s at each concentration tested (black squares), fitted curve from Hill equation fitting (red line) and assorted output data from the fitting operation (tabulated).

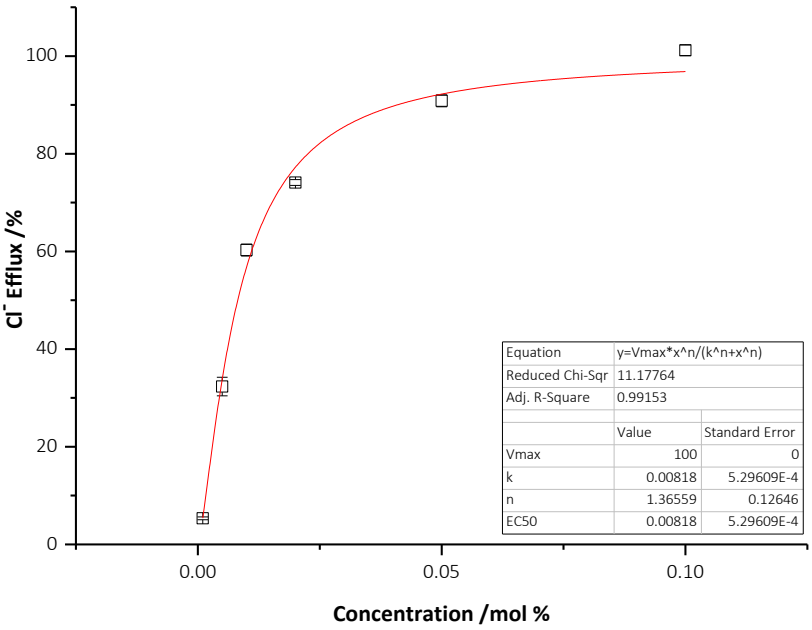


**Figure III.40** Hill plot for compound **77**, showing chloride efflux response after 270 s at each concentration tested (black squares), fitted curve from Hill equation fitting (red line) and assorted output data from the fitting operation (tabulated).

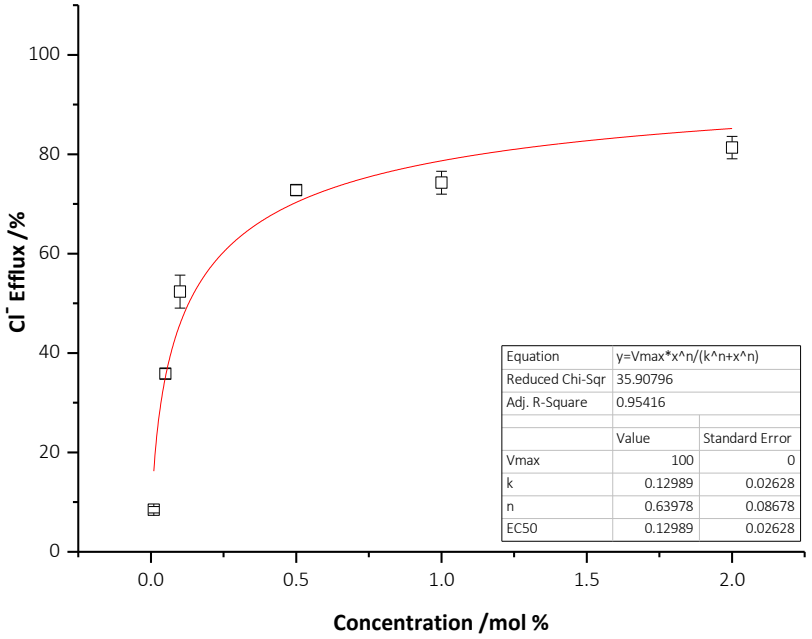


**Figure III.41** Hill plot for compound **78**, showing chloride efflux response after 270 s at each concentration tested (black squares), fitted curve from Hill equation fitting (red line) and assorted output data from the fitting operation (tabulated).

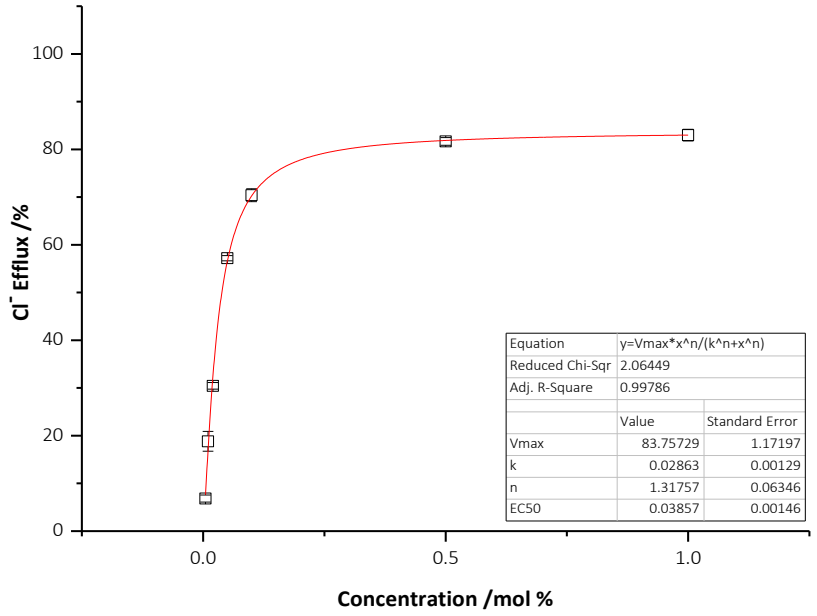


**Figure III.42** Hill plot for compound **79**, showing chloride efflux response after 270 s at each concentration tested (black squares), fitted curve from Hill equation fitting (red line) and assorted output data from the fitting operation (tabulated).

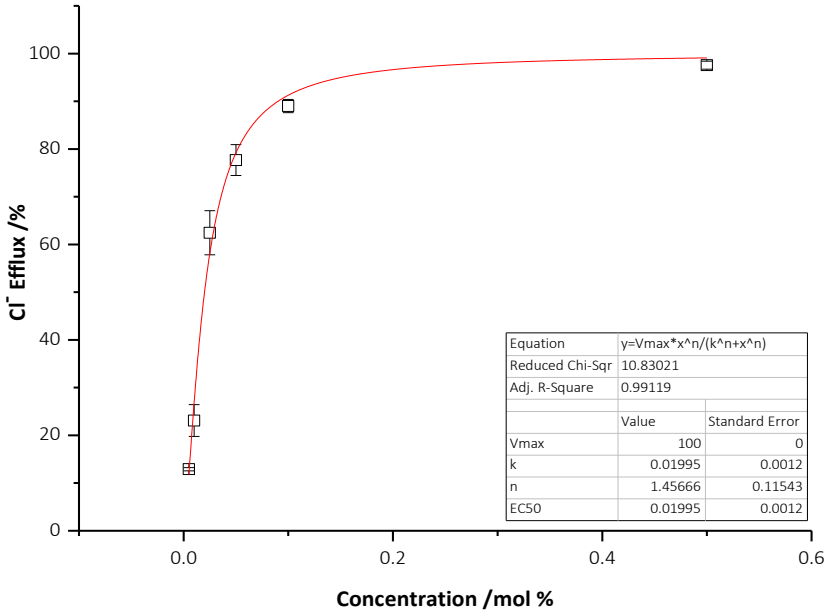


**Figure III.43** Hill plot for compound **80**, showing chloride efflux response after 270 s at each concentration tested (black squares), fitted curve from Hill equation fitting (red line) and assorted output data from the fitting operation (tabulated).

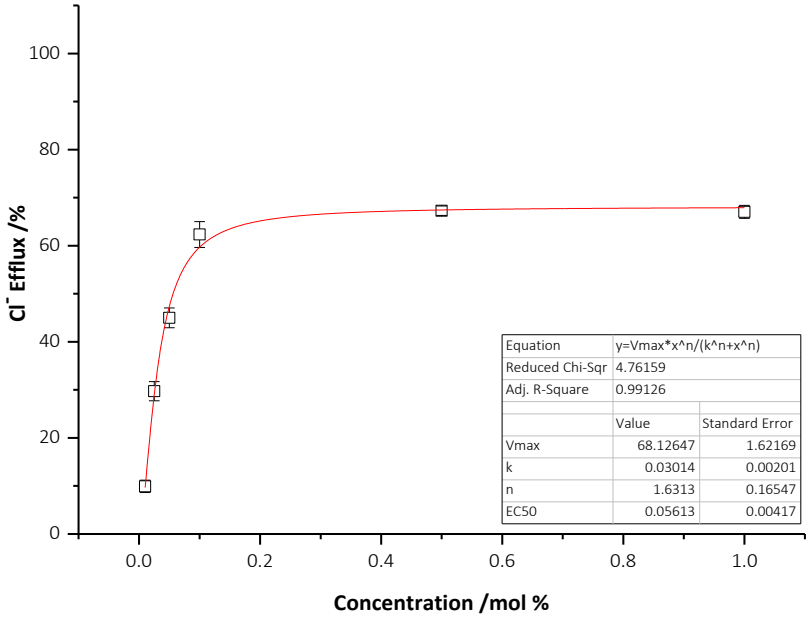


**Figure III.44** Hill plot for compound **81**, showing chloride efflux response after 270 s at each concentration tested (black squares), fitted curve from Hill equation fitting (red line) and assorted output data from the fitting operation (tabulated).

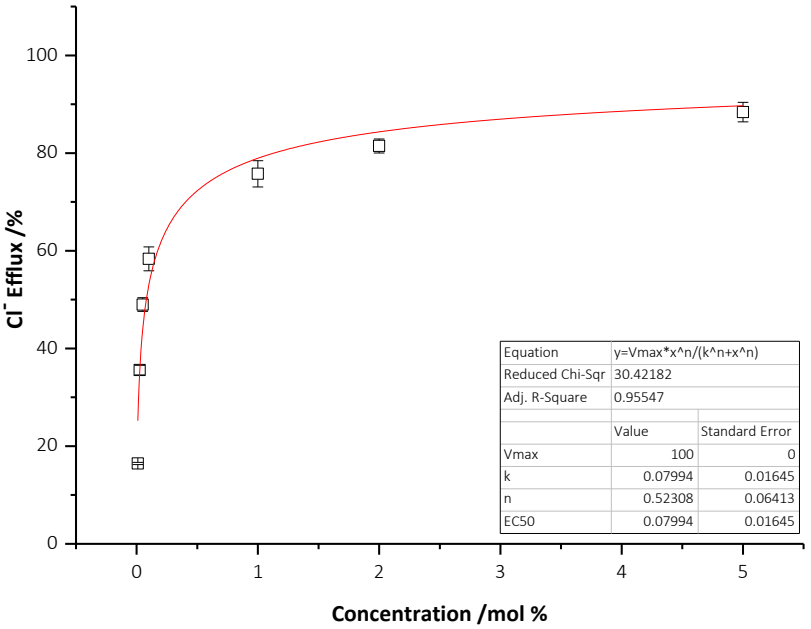


**Figure III.45** Hill plot for compound **82**, showing chloride efflux response after 270 s at each concentration tested (black squares), fitted curve from Hill equation fitting (red line) and assorted output data from the fitting operation (tabulated).

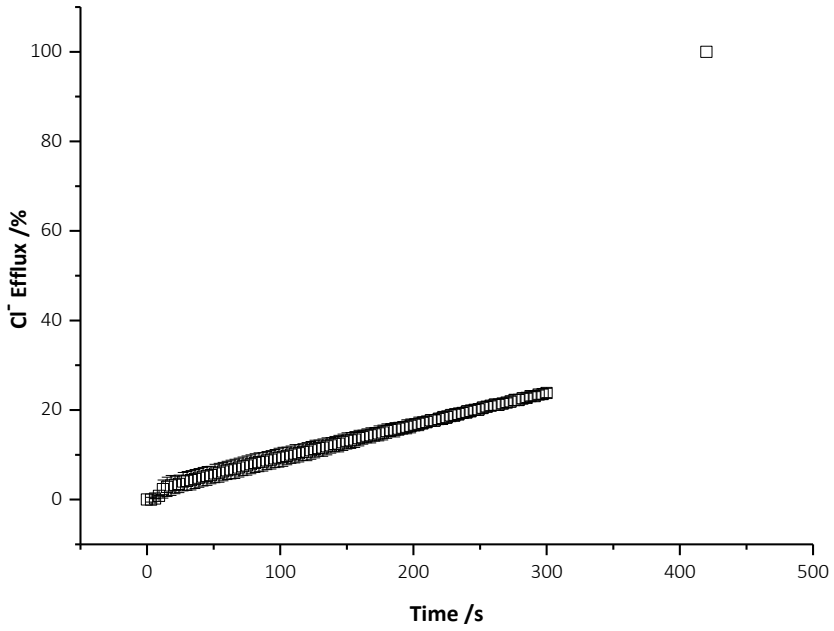


**Figure III.46** Chloride efflux from ISE experiment for $Cl^-/NO_3^-$ exchange assays at pH 4.5 by compound **83** at 10 % loading. No Hill analysis was possible due to low activity.

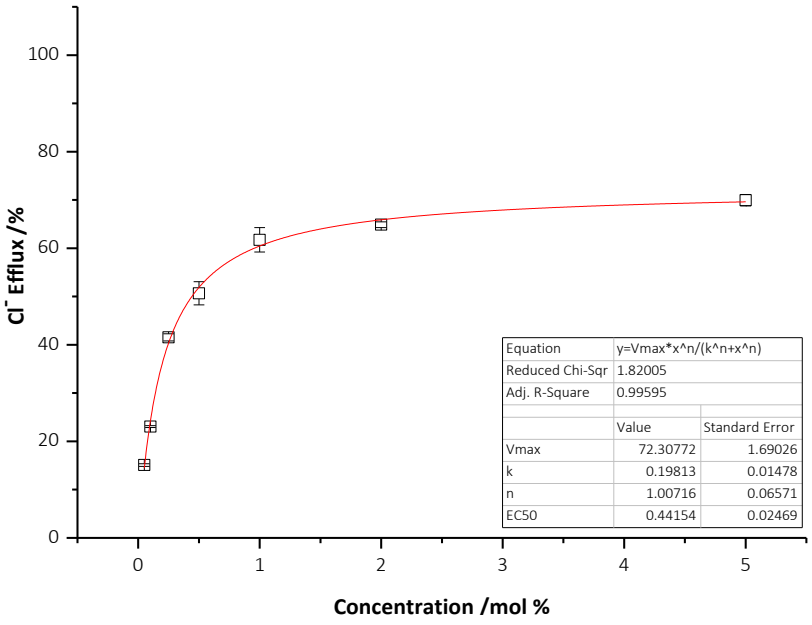


**Figure III.47** Hill plot for compound **84**, showing chloride efflux response after 270 s at each concentration tested (black squares), fitted curve from Hill equation fitting (red line) and assorted output data from the fitting operation (tabulated).

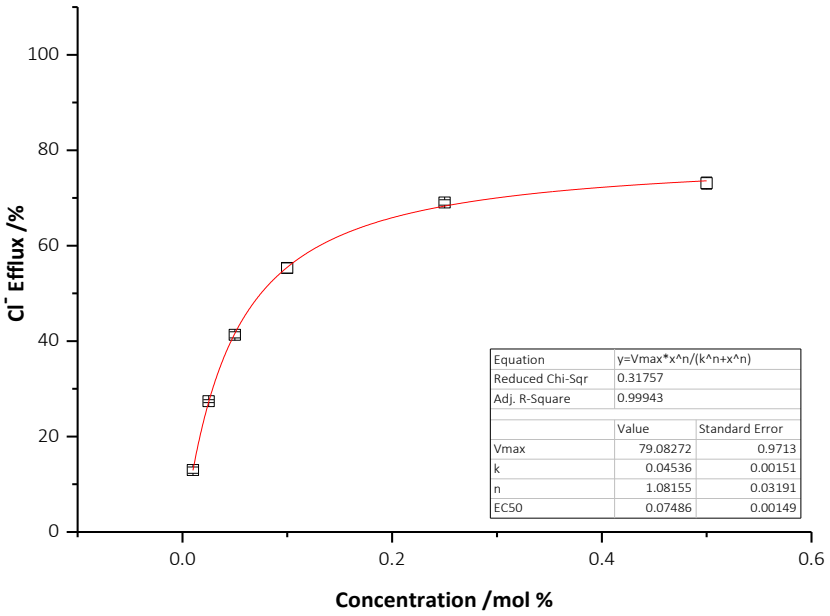


**Figure III.48** Hill plot for compound **85**, showing chloride efflux response after 270 s at each concentration tested (black squares), fitted curve from Hill equation fitting (red line) and assorted output data from the fitting operation (tabulated).

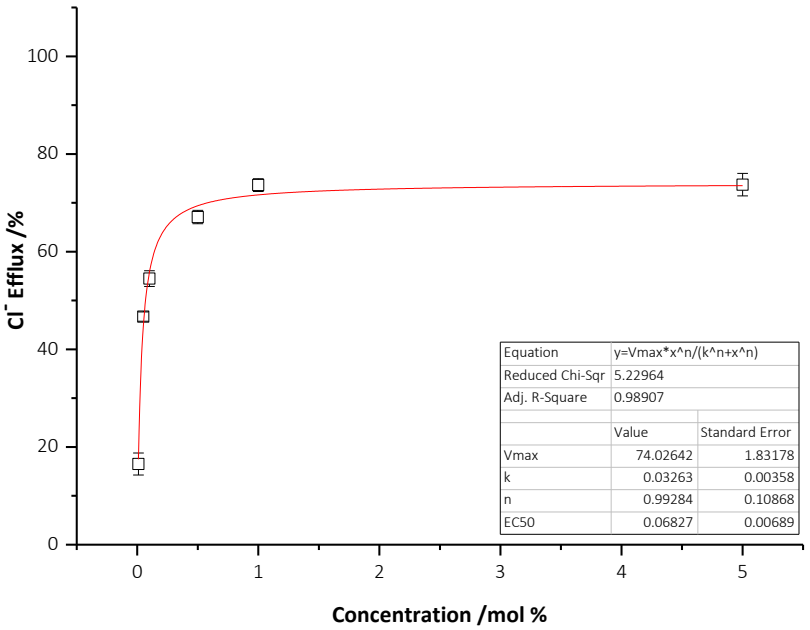


**Figure III.49** Hill plot for compound **86**, showing chloride efflux response after 270 s at each concentration tested (black squares), fitted curve from Hill equation fitting (red line) and assorted output data from the fitting operation (tabulated).

## III.3 Fluorinated Tren Series

### III.3.1 Raw Transport Curves

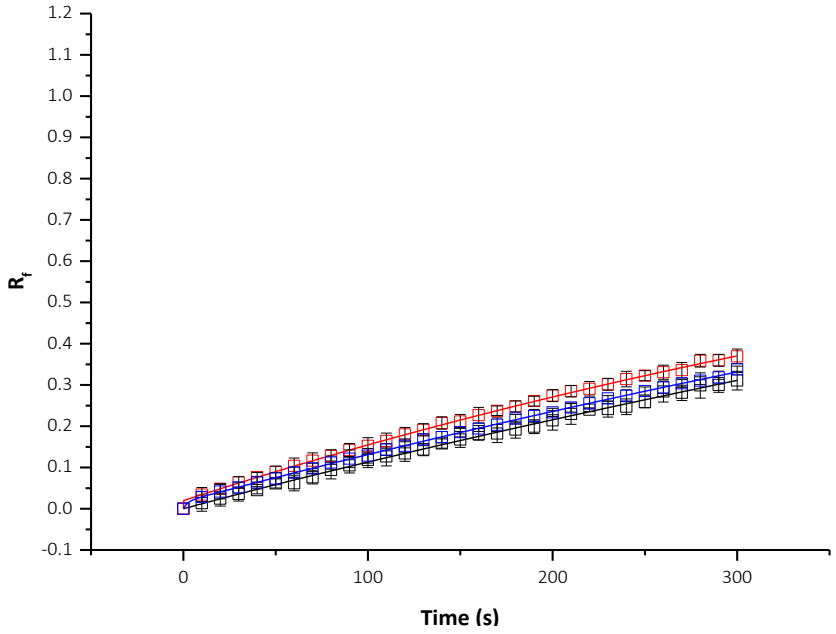


**Figure III.50** Relative fluorescence trace from HPTS assays for compound **96** at 0.01 % loading with fitted exponential function curves. Black squares: no assisting protonophore; red squares: 0.5 mol % Gramicidin-A; blue squares: 2 mol % oleic acid.

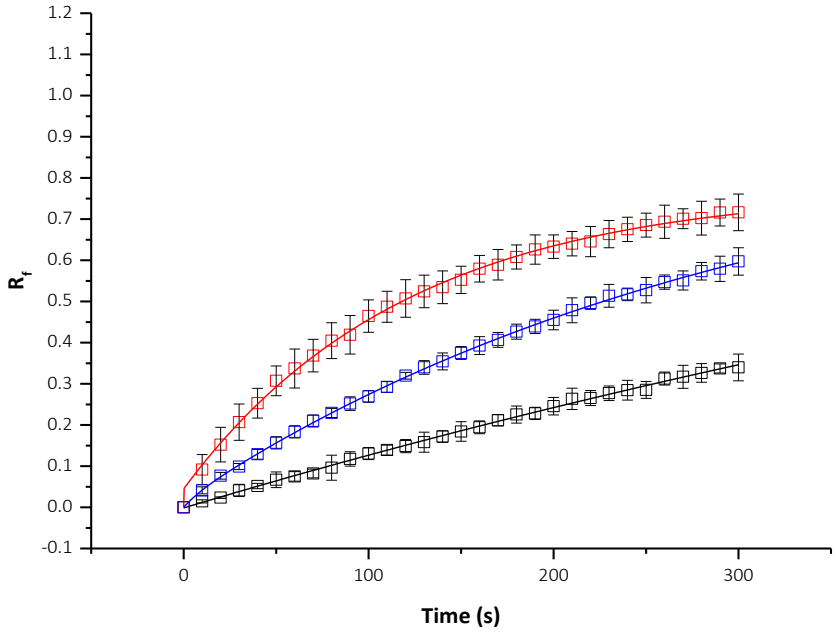


**Figure III.51** Relative fluorescence trace from HPTS assays for compound **97** at 0.01 % loading with fitted exponential function curves. Black squares: no assisting protonophore; red squares: 0.5 mol % Gramicidin-A; blue squares: 2 mol % oleic acid.

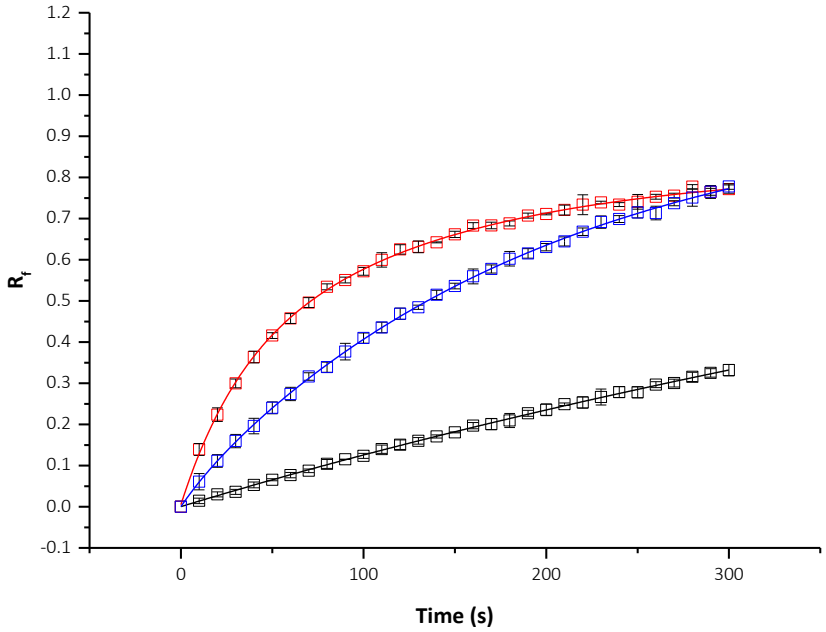


**Figure III.52** Relative fluorescence trace from HPTS assays for compound **98** at 0.01 % loading with fitted exponential function curves. Black squares: no assisting protonophore; red squares: 0.5 mol % Gramicidin-A; blue squares: 2 mol % oleic acid.

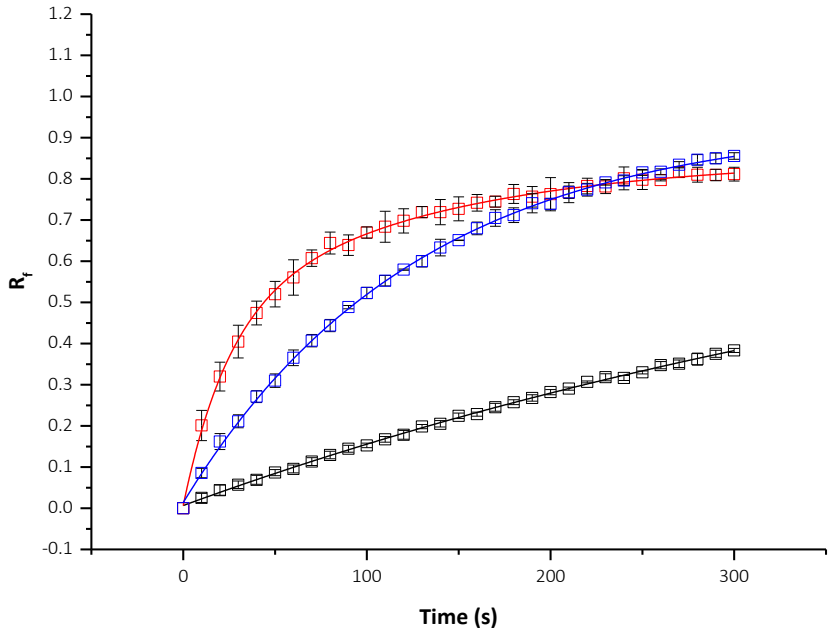


**Figure III.53** Relative fluorescence trace from HPTS assays for compound **99** at 0.01 % loading with fitted exponential function curves. Black squares: no assisting protonophore; red squares: 0.5 mol % Gramicidin-A; blue squares: 2 mol % oleic acid.

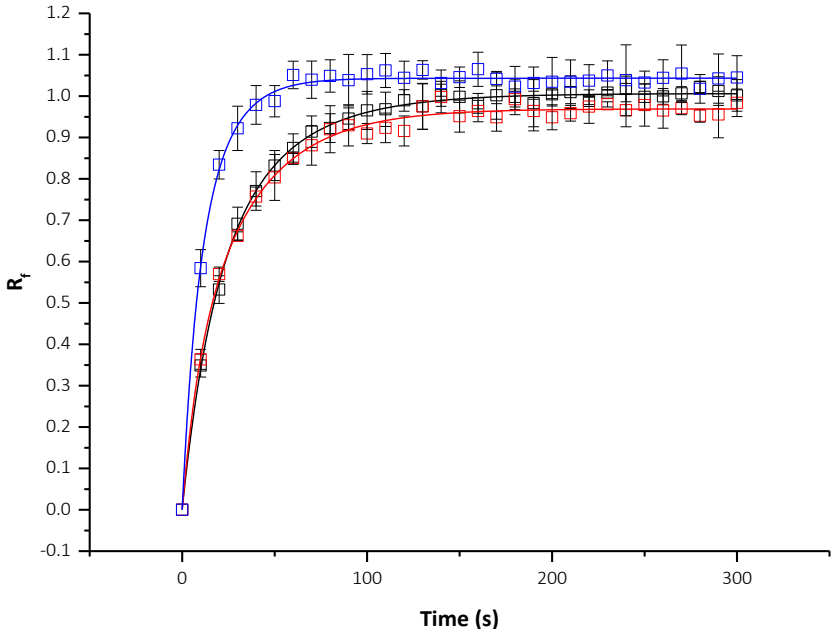


**Figure III.54** Relative fluorescence trace from HPTS assays for compound **100** at 0.01 % loading with fitted exponential function curves. Black squares: no assisting protonophore; red squares: 0.5 mol % Gramicidin-A; blue squares: 2 mol % oleic acid.

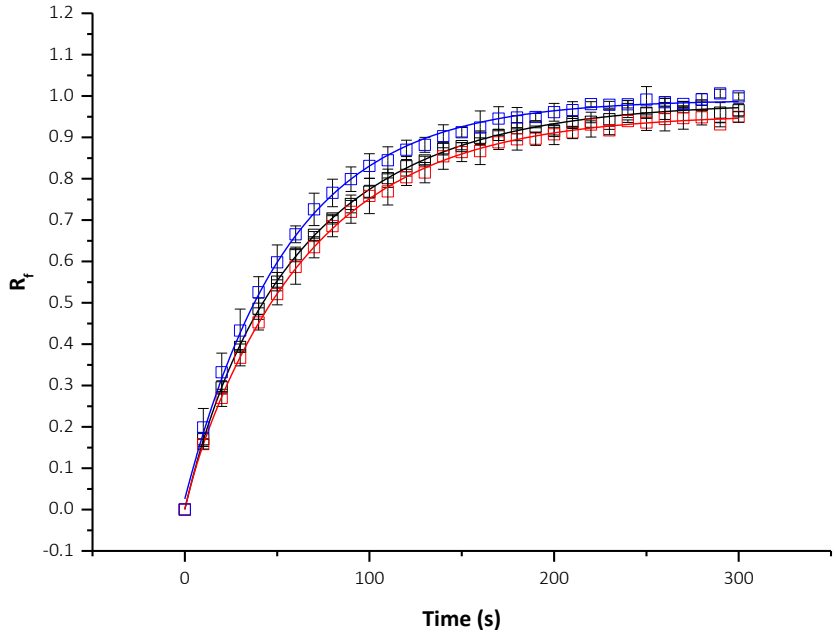


**Figure III.55** Relative fluorescence trace from HPTS assays for compound **101** at 0.001 % loading with fitted exponential function curves. Black squares: no assisting protonophore; red squares: 0.5 mol % Gramicidin-A; blue squares: 2 mol % oleic acid.

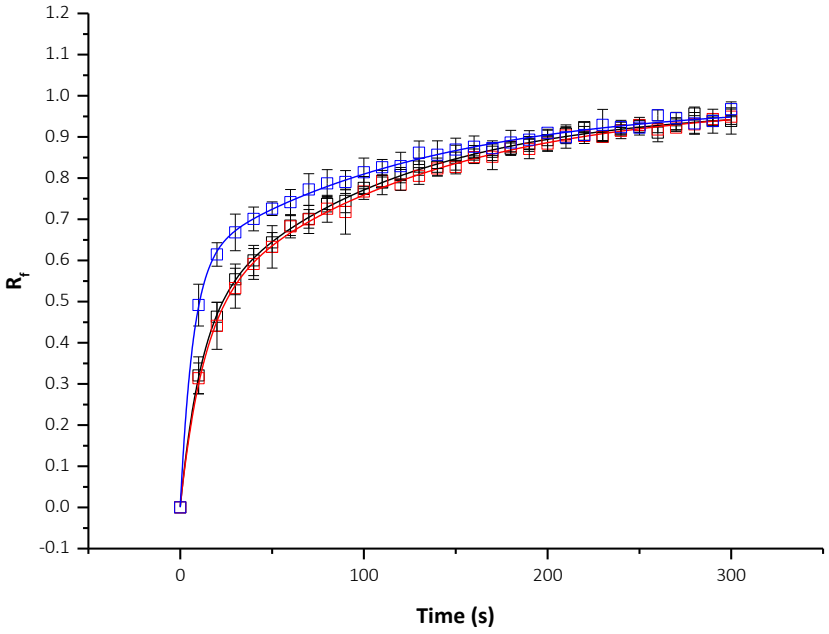


**Figure III.56** Relative fluorescence trace from HPTS assays for compound **102** at 0.01 % loading with fitted exponential function curves. Black squares: no assisting protonophore; red squares: 0.5 mol % Gramicidin-A; blue squares: 2 mol % oleic acid.

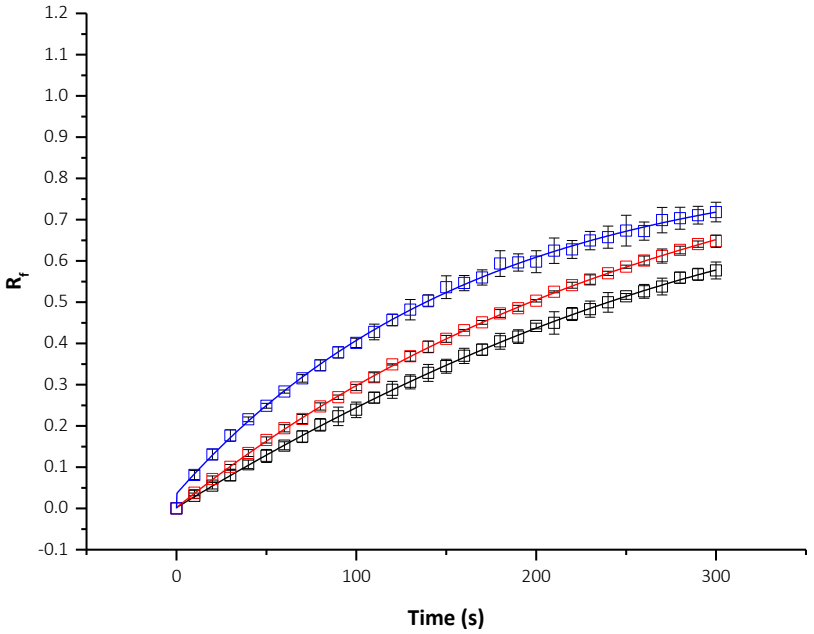


**Figure III.57** Relative fluorescence trace from HPTS assays for compound **103** at 0.01 % loading with fitted exponential function curves. Black squares: no assisting protonophore; red squares: 0.5 mol % Gramicidin-A; blue squares: 2 mol % oleic acid.

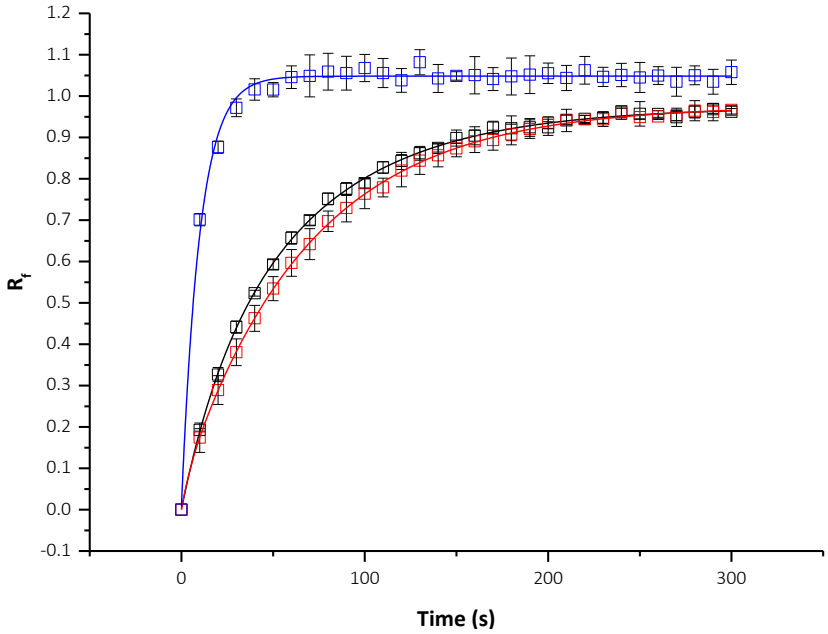


**Figure III.58** Relative fluorescence trace from HPTS assays for compound **104** at 0.01 % loading with fitted exponential function curves. Black squares: no assisting protonophore; red squares: 0.5 mol % Gramicidin-A; blue squares: 2 mol % oleic acid.

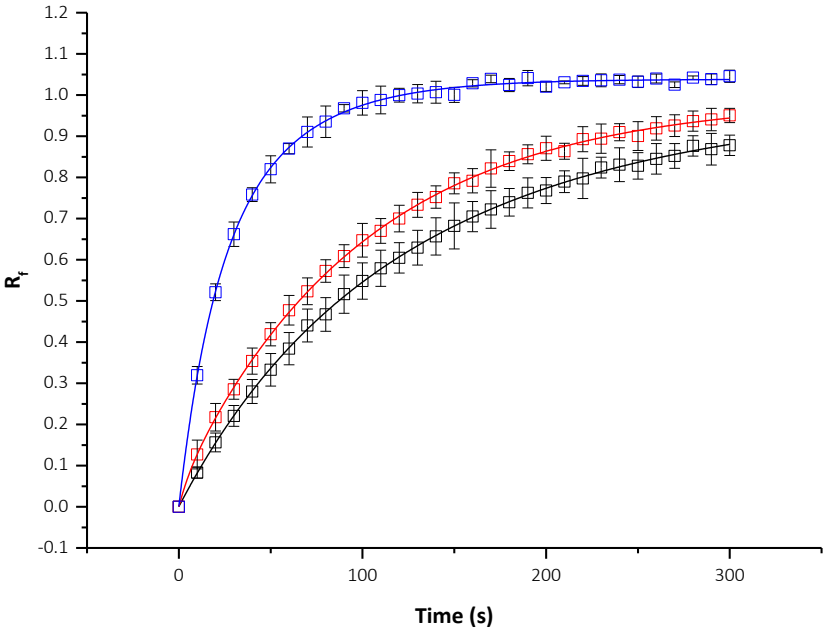


**Figure III.59** Relative fluorescence trace from HPTS assays for compound **105** at 0.01 % loading with fitted exponential function curves. Black squares: no assisting protonophore; red squares: 0.5 mol % Gramicidin-A; blue squares: 2 mol % oleic acid.

### III.3.2 NMR Titration Fit Plots

The following fit plots obtained for the tren series using global fitting with BindFit v0.5[124, 125].

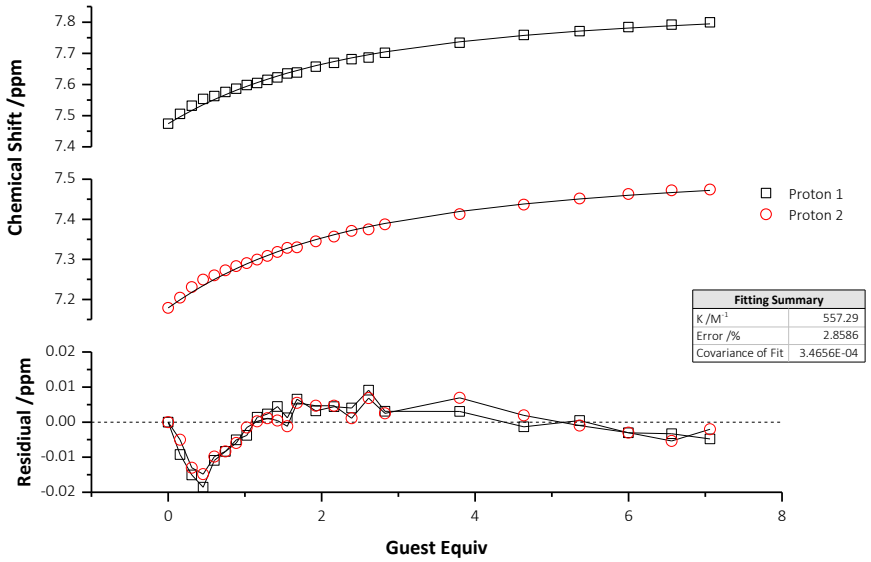


**Figure III.60** Fit plot for 1,1',1''-(nitrilotris(ethane-2,1-diyl))tris(3-ethylthiourea) **96** with TBA Cl, following both NH protons (δ = 7.47, 7.18 ppm). K = 557 $M^{-1}$, error = 2.9 %.

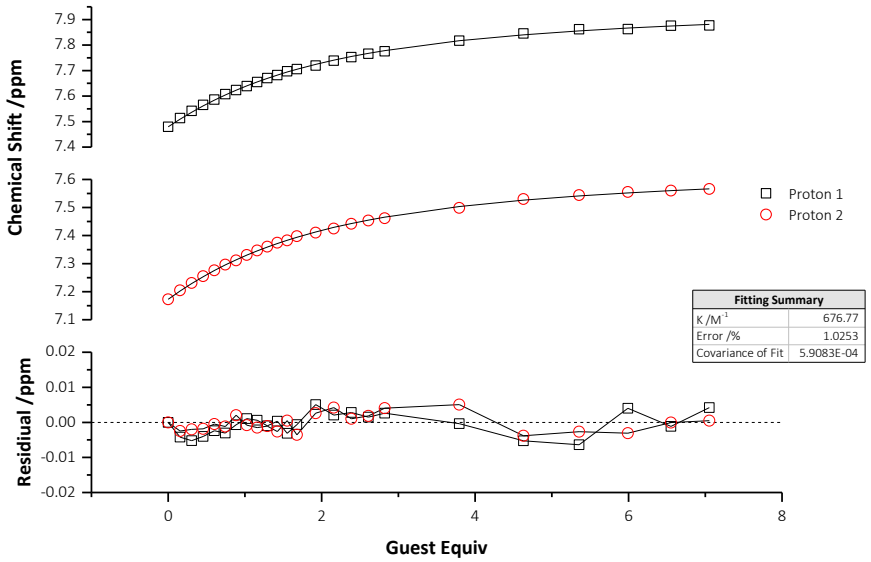


**Figure III.61** Fit plot for 1,1',1''-(nitrilotris(ethane-2,1-diyl))tris(3-propylthiourea) **97** with TBA Cl, following both NH protons (δ = 7.48, 7.17 ppm). K = 677 $M^{-1}$, error = 1.0 %.

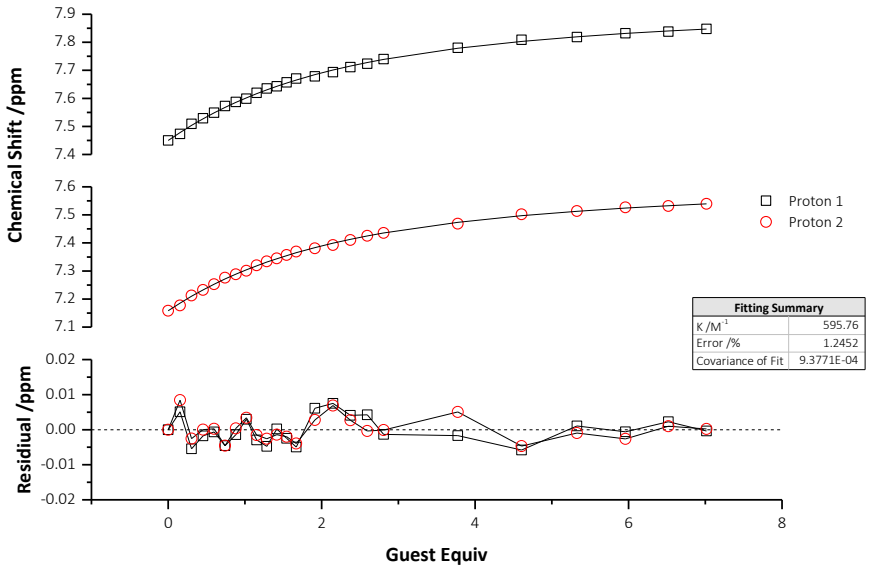


**Figure III.62** Fit plot for 1,1',1''-(nitrilotris(ethane-2,1-diyl))tris(3-butylthiourea) **98** with TBA Cl, following both NH protons (δ = 7.45, 7.16 ppm). K = 596 $M^{-1}$, error = 1.2 %.

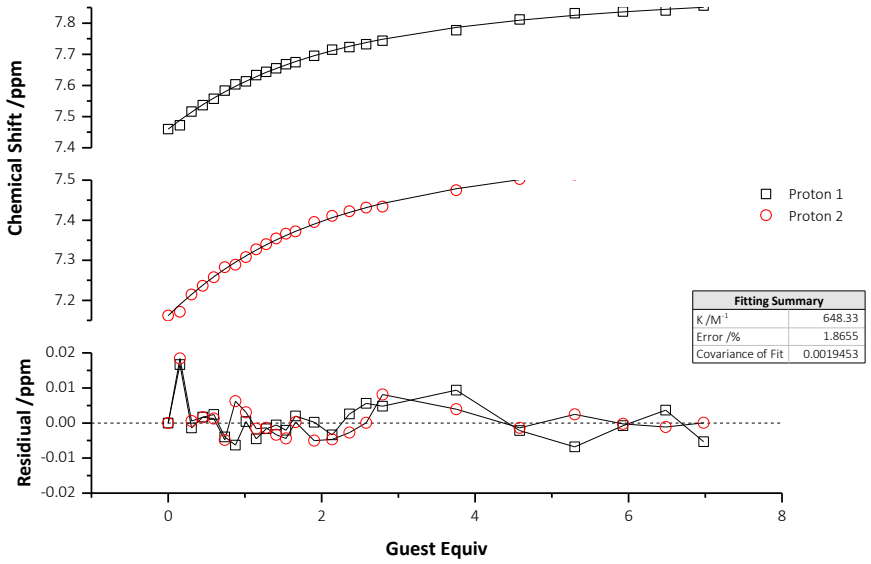


**Figure III.63** Fit plot for 1,1',1''-(nitrilotris(ethane-2,1-diyl))tris(3-pentylthiourea) **99** with TBA Cl, following both NH protons (δ = 7.46, 7.16 ppm). K = 648 $M^{-1}$, error = 1.92 %.

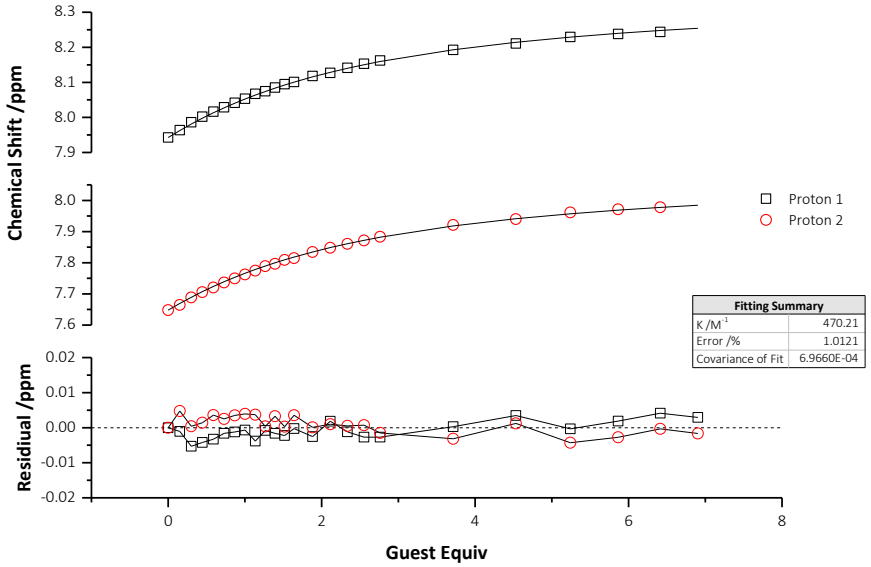


**Figure III.64** Fit plot for 1,1',1''-(nitrilotris(ethane-2,1-diyl))tris(3-(2,2,2-trifluoroethylthiourea) **100** with TBA Cl, following both NH protons (δ = 7.94, 7.65 ppm). K = 470 $M^{-1}$, error = 1.0 %.

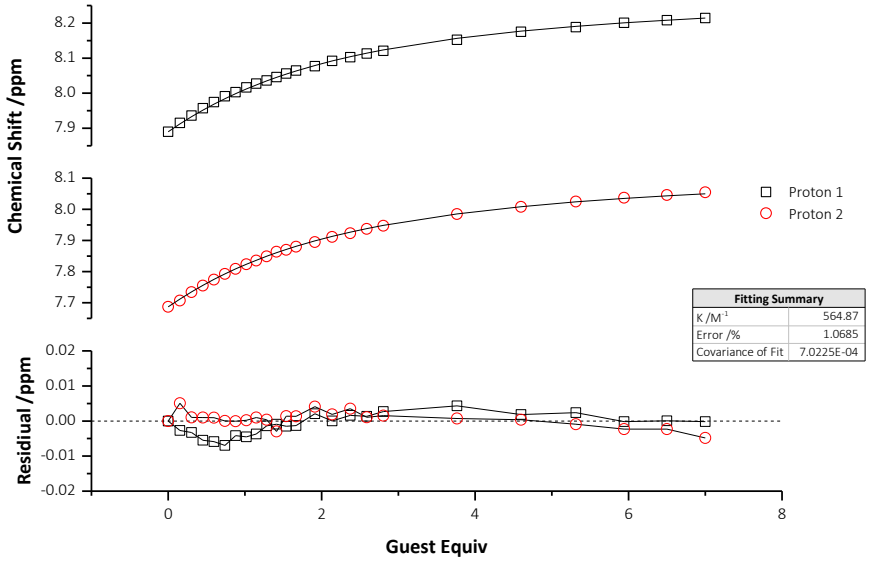


**Figure III.65** Fit plot for 1,1',1''-(nitrilotris(ethane-2,1-diyl))tris(3-(2,2,3,3,3-pentafluoropropylthiourea) **101** with TBA Cl, following both NH protons (δ = 7.89, 7.69 ppm). K = 565 $M^{-1}$, error = 1.1 %.

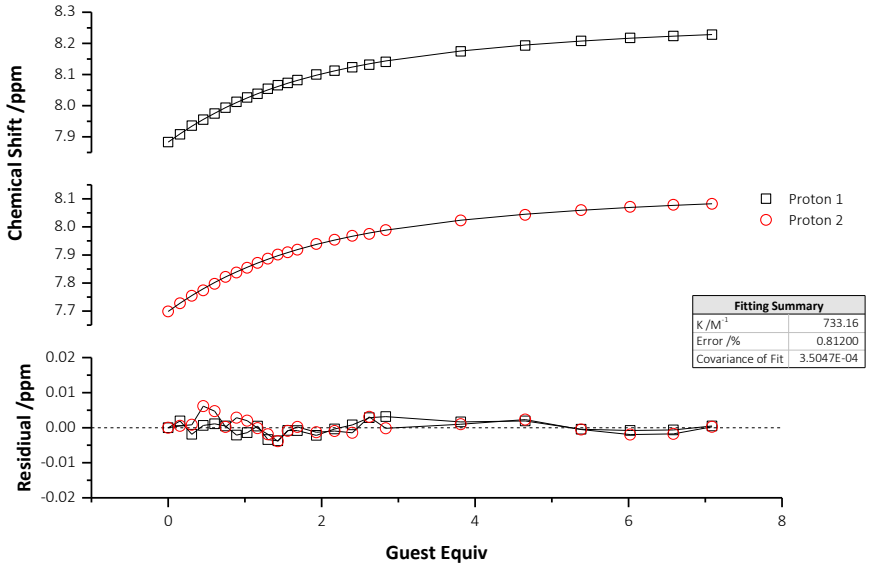


**Figure III.66** Fit plot for 1,1',1''-(nitrilotris(ethane-2,1-diyl))tris(3-(2,2,3,3,4,4,4-heptafluorobutylthiourea) **102** with TBA Cl, following both NH protons (δ = 7.88, 7.70 ppm). K = 733 $M^{-1}$, error = 0.8 %.

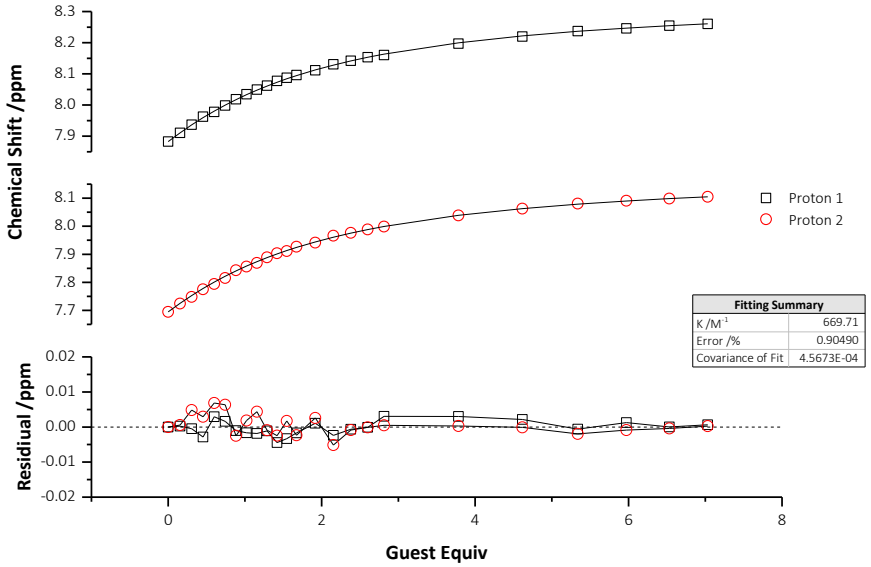


**Figure III.67** Fit plot for 1,1',1''-(nitrilotris(ethane-2,1-diyl))tris(3-(2,2,3,3,4,4,5,5,5-nonafluoropentylthiourea) **103** with TBA Cl, following both NH protons (δ = 7.88, 7.69 ppm). K = 670 $M^{-1}$, error = 0.9 %.

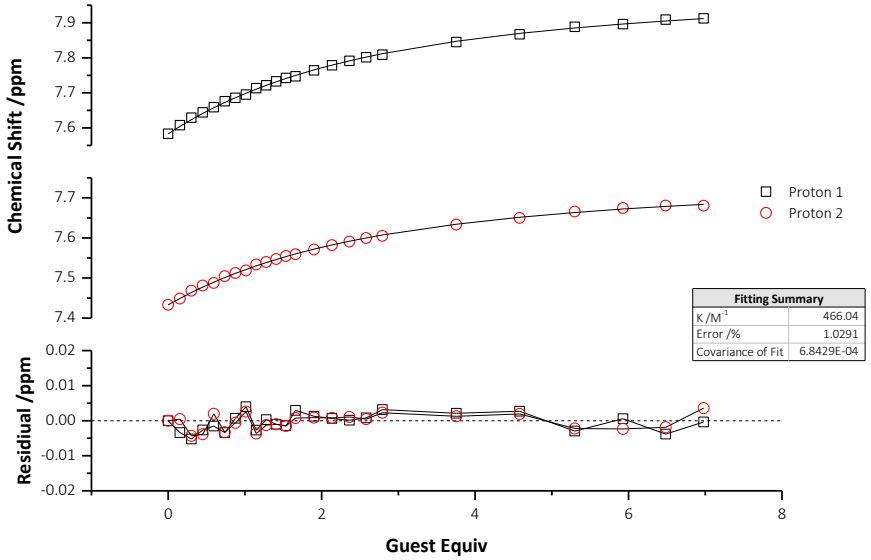


**Figure III.68** Fit plot for 1,1',1''-(nitrilotris(ethane-2,1-diyl))tris(3-(3,3,3-trifluoropropylthiourea) **104** with TBA Cl, following both NH protons (δ = 7.58, 7.43 ppm). K = 466 $M^{-1}$, error = 1.0 %.

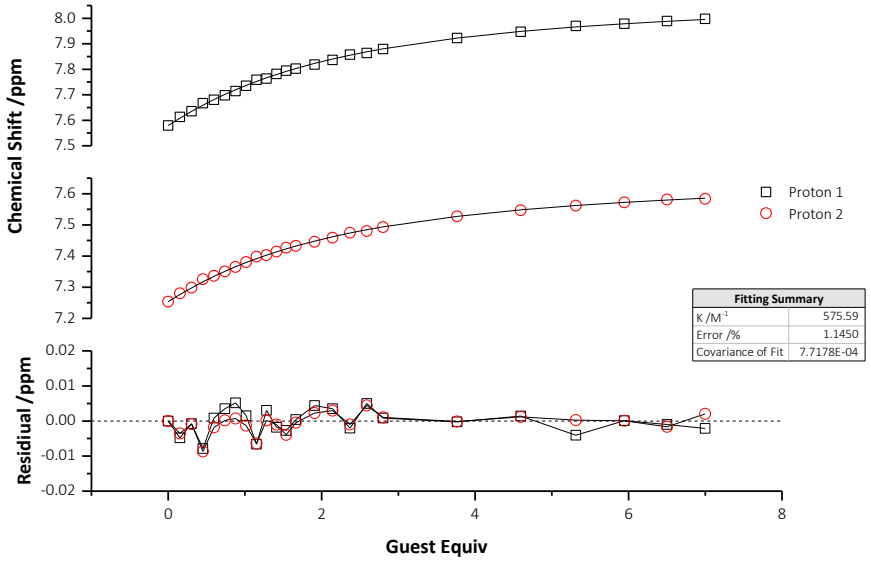


**Figure III.69** Fit plot for 1,1',1''-(nitrilotris(ethane-2,1-diyl))tris(3-(4,4,4-trifluorobutylthiourea) **105** with TBA Cl, following both NH protons (δ = 7.67, 7.33 ppm). K = 576 $M^{-1}$, error = 1.1 %.